Mechanical characterisation of Nb_3Sn Rutherford cable stacks

Von der Fakultät für Maschinenbau, Verfahrens- und
Energietechnik
der Technischen Universität Bergakademie Freiberg

genehmigte

DISSERTATION

zur Erlangung des akademischen Grades

Doktor-Ingenieur (Dr.-Ing.)

vorgelegt

von M.Sc. Felix Wolf
geboren am 03. August 1989 in Hoyerswerda

Gutachter.:
Prof. Dr.-Ing. Alfons Ams, Freiberg
Prof. Dr. rer. nat. habil. Andreas Leineweber, Freiberg

Tag der Verleihung: 28. Juli 2021

Abstract

Nb_3Sn Rutherford cables are used in CERN's superconducting 11 T dipole and MQXF quadrupole magnets, which are proposed for the instantaneous luminosity (rate of particle collisions) upgrade of the Large Hadron Collider (LHC) by a factor of five to a High Luminosity-Large Hadron Collider (HL-LHC). Nb_3Sn-based conductors are the key technology for the envisioned Future Circular Collider (FCC) with an operating magnetic dipole field of 16 T. The baseline superconductor of the LHC dipole magnets is Nb–Ti, whereas an operation above 10 T is not possible due to the current carrying performance limitations of this superconductor at higher magnetic fields. Therefore, a superconducting material such as Nb_3Sn has to be used with proven performance capabilities of 10 T and above.

The conductor choice towards Nb_3Sn-based cables affects the magnet manufacturing process, as it requires a heat treatment up to 650°C, an epoxy resin impregnation and introduces mechanical difficulties as the superconducting filaments are brittle and strain sensitive. A mechanical over loading of the filaments lead to irreversible conductor damage. The designs of 11 and 16 T magnets are supposed to push the conductor towards its mechanical and electrical performance limitations. The magnetic field induced forces on the current carrying conductor are balanced by mechanical pre-loading of the magnet. Thereby the highest controlled mechanical pre-load for the 11 T dipole magnet is set at ambient temperature. The mechanical stress limits of Nb_3Sn-based cables have been investigated at cryogenic temperatures. The material strength and stiffness of the cable insulation system, formed by glass-fibre-reinforced resin, is increased at low temperatures. The ultimate stress values, determined at cryogenic temperature, are therefore not conservative. The ultimate stress limitation of the insulated conductor is assumed to be lower at ambient temperature. The cable limitations at ambient temperature need to be known for the ongoing magnet manufacturing process and also for future design approaches. Furthermore, the compressive stress–strain behaviour of a coil conductor block at ambient temperature is the key material characteristic, in order to recalculate the stress level in the coil during the assembly process. Existing approaches using an indirect strain measurement method provide uncertainties in the low-strain regime, which is the essential strain range for a material compound consisting of major fractions composed of heat-annealed copper and epoxy resin. Compressive stress–strain data of an impregnated conductor block are required, based on a direct strain measurement system, as available data have been collected on samples based on a different strand type and insulation system. The elaborated direct strain measurements can be correlated to strain gauge data, measured directly on a coil. The stress distribution in a Nb_3Sn Rutherford cable need to be understood and validated to understand strain-induced degradation effects in the insulated conductor. This knowledge can also help to optimise the stress distribution envisioned magnet designs. The stress–strain state in the copper and Nb_3Sn phase of a loaded conductor block has to be determined experimentally.

This dissertation describes a test protocol and first elaborated results on the investigated stress limitations of a Nb_3Sn Rutherford cable under homogeneous load applied in transversal direction. The compressive stress–strain behaviour of impregnated Nb_3Sn Rutherford cable stacks was investigated experimentally. This includes a detailed report on the sample manufacturing process, measurements performed and validation of results through a comparison with the elaborated data of cable stacks extracted from a coil. The presented results from neutron diffraction measurements of loaded cable stacks allow the determination of the stress–strain level of the copper and Nb_3Sn phase in the impregnated conductor. The

relevant measured results have been recalculated with numerical calculations based on the Finite Element Method (FEM).

Kurzfassung

Supraleitende Nb_3Sn Rutherfordkabel werden in den 11 T Dipol- und MQXF Quadrupolmagneten am CERN verwendet, um die Luminosität (Rate der Partikelkollisionen) des Large Hadron Collider (LHC) für den High Luminosity-Large Hadron Collider (HL-LHC) um das Fünffache zu steigern. Des Weiteren gehören Nb_3Sn-basierte Leiter zu einer Schlüsseltechnologie für den geplanten Future Circular Collider (FCC), dessen Dipolmagnete eine magnetische Flussdichte von 16 T erreichen sollen. Die supraleitenden Kabel der LHC Dipolmagnete basieren auf Nb–Ti, mit welchen maximale Felder von um die 10 T mit Beschleunigermagneten erreicht werden können. Aus diesem Grund werden supraleitende Materialien wie Nb_3Sn verwendet, welche hohe Ströme in magnetischen Feldern über 10 T transportieren können. Die Materialauswahl der Nb_3Sn-basierten Kabel beeinflusst den Herstellungsprozess der Magnete, da eine Wärmebehandlung von bis zu 650°C sowie eine Imprägnierung mit Epoxydharz erforderlich sind. Die supraleitenden Filamente sind spröde und dehnungsempfindlich, was die Handhabung der Leiter verkompliziert. Eine mechanische Überbeanspruchung der Leiter führt zu einer unwiderruflichen Schädigung der supraleitenden Filamente. Die Entwicklungen der 11 T und 16 T Magnete sollen den Leiter an seine mechanische und elektrische Leistungsgrenze bringen. Die durch das magnetische Feld hervorgerufenen Kräfte auf den stromdurchflossenen Leiter werden mithilfe einer mechanischen Vorspannung ausgeglichen, was eine Bewegung des Leiters verhindert. Hierbei wird die größte kontrollierte Vorspannung im 11 T Magneten bei Raumtemperatur aufgebracht. Die mechanische Grenzlasten des Kabels wurden bislang nur bei kryogenen Temperaturen untersucht. Die mechanische Festigkeit und Steifigkeit der Isolierung des Kabels, bestehend aus glasfaserverstärktem Kunststoff, sind bei tiefen Temperaturen höher als bei Raumtemperatur. Somit sind die bisher ermittelten Grenzlasten nicht konservativ für den Magnetzusammenbau bei Raumtemperatur. Es wird angenommen, dass die Widerstandsfähigkeit des isolierten Leiters bei Raumtemperatur geringer ist. Der mechanische Spannungsgrenzwert ist eine wichtige Kenngröße für die Magnetherstellung sowie für zukünftige Magnetentwürfe. Weiterhin beschreibt das Spannungs–Dehnungsverhalten eines Leiterblocks wichtige Materialeigenschaften, um den Spannungszustand einer Spule während des Zusammenbaus zu berechnen. Bestehende Vorgehensweisen zur Spannungs–Dehnungsmessung beschreiben eine indirekte Dehnungsmessmethode, welche in Bereichen geringer Dehnung große Messunsicherheiten aufzeigt. Dieser Dehungsbereich ist wichtig für die Charakterisierung eines Materialsverbunds, welcher zu großen Teilen aus weichgeglühtem Kupfer und glasfaserverstärktem Kunststoff besteht. Daher wird das Spannungs–Dehnungsverhalten eines Leiterblocks, basierend auf einer direkten Dehnungsmessmethode präsentiert. Die direkten Dehnungsmessungen können mit Messungen von Dehnmessstreifen an der Spule verglichen werden, um den Spannungszustand des Leiterblocks zu bestimmen. Der Spannungszustand in einem Nb_3Sn Rutherfordkabel muss untersucht werden, um die dehnungsbasierten Schädigungsmechanismen im isolierten Kabel zu verstehen und dessen Design zu verbessern. Dieses Verständniss kann helfen, die Spannungsverteilung an zukünftigen Magneten zu optimieren. Hierzu müssen die Spannungs–Dehnungszustände des Kupfers und des Nb_3Sn eines belasteten Leiterblocks experimentell ermittelt werden. Diese Arbeit beschreibt das Testprotokoll zur Ermittlung der mechanischen Grenzbelastung eines Rutherfordkabels unter homogener Druckspannung sowie ermittelte Grenzwerte. Das Spannungs–Dehnungsverhalten von imprägnierten Nb_3Sn Rutherfordkabeln wurde experimentell bestimmt und der Einfluss des Imprägnierungsvolumenanteils auf die Gesamtsteifigkeit ermittelt. Dies beinhaltet einen detaillierten Bericht

über die Probenherstellung, das Messprotokoll sowie die Messauswertung. Die Validierung des Probenherstellungsprozesses erfolgte durch Vergleichsmessungen von Proben, welche aus einer Spule extrahiert wurden. Die präsentierten Neutronen-Diffraktionsmessungen von belasteten Kabeln erlauben es, den Spannungs–Dehnungszustand der Kupfer- und Nb_3Sn-Phase im impregnierten Leiters zu bestimmen. Die relevanten Messergebnisse wurden unter Anwendung der Finite Element Methode in ANSYS reproduziert.

Acknowledgements

The work presented in this dissertation was carried out at CERN in the framework of the Technical Doctoral Student Programme in cooperation with the Technische Universität Bergakademie Freiberg, Germany. The research was embedded in the high-field magnet program of the TE-MSC group at CERN and in the research activities of the HL-LHC project and the FCC study. I worked on the characterisation of Nb_3Sn cable stacks. Here, I thank the people who contributed in some way to this research. Daniel Schoerling, Friedrich Lackner and Christian Scheuerlein, CERN, and Prof. Alfons Ams, TUBAF, supervised this thesis and provided valuable support and guidance. Davide Tommasini, CERN, strongly supported this project. My group leader during my stay at CERN, Luca Bottura, supported this project in the TE-MSC group. My section leaders during my stay at CERN, Davide Tommasini, Gijs de Rijk and Attilio Milanese, CERN, helped me through the section budgets. Frédéric Savary, CERN, I owe a debt of gratitude for the opportunity to perform measurements in the TE-MSC-LMF facility.

I thank Patrick Ebermann for the fruitful collaboration resulting in the MATLAB script with which colourised pressure-sensitive films can be evaluated. I thank Giorgio Vallone and Jaakko Murtomaki for many discussions about finite element modelling in ANSYS® and Jeroen Van Nugteren for his support in MATLAB programming. I thank Dennis Mosbach, ITWM Kaiserslautern, for analysing and reconstructing the X-ray data. I would like to thank Philip Schwarz and Olivier Crettiez for their valuable feedback on manufacturing drawings, and Remy Gauthier, CERN, for his inputs to the vacuum tight mould design. I am grateful for the collaboration with Christian Scheuerlein for his input to the definition of measurement procedures that helped me to achieve reliable results and for the motivation to perform neutron diffraction measurements on the manufactured samples. I would like to thank Michael Hofmann, MLZ, Garchingen, for support during the diffraction experiment performance and data analysis, and Markus Lorentzon for the data analysis of the diffraction experiment. Mickael Crouvizier, CERN, prepared pictures of cross-sections of the investigated coil segments and cable stacks. I want to express my gratitude to the colleagues in the TE-MSC-LMF section, especially Sebastien Luzeux for support in arrangements in the laboratory and Guillaume Genest for manufacturing the required parts of the impregnation mould and tooling for the hydraulic press in the main workshop of CERN. I also wish to thank the team of the polymer laboratory at CERN for their technical support during sample impregnation and Jerome Fleiter who did the FRESCA measurements and Oleg Kalouguine, CERN, for providing cable samples and sharing his experience in cable handling. This thesis would have not been possible without their assistance. I thank Tim Williams for his comments on the English language.

I would like to thank my parents and grandparents for their support during my studies abroad. Special thanks goes to my wife, Bernadett Wolf, for her support and encouragement during my studies.

Contents

1. Introduction

Particle accelerators are one of the most important tools in the research domain of high-energy physics to accelerate charged particles to high energies. The discovery potential of new particles depends on the energy. In Figure 1.1 the force and stored energies of the ambitious High Energy Large Hadron Collider (HE-LHC) (20 T) and the Future Circular Collider (FCC) study (16 T) are compared with magnets designed, built and tested for colliders (RHIC, HERA, Tevatron, LHC) and Nb-Ti (SCC, MFISC) and Nb_3Sn prototypes (MSUT, MFresaca, D20).

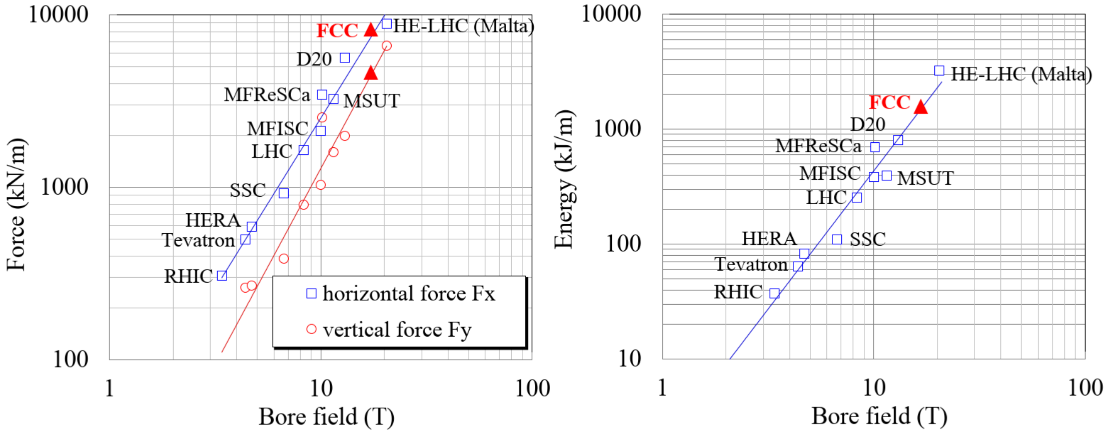

Figure 1.1.: Comparison of forces and stored energies scaled to one aperture of FCC dipoles, reported on a general scaling plot for other accelerator dipole magnets of comparable dimension [1].

The main components of modern circular particle accelerators and their functions are:

- vacuum tube, ensuring ultra-high vacuum to minimise collisions of accelerated particles with gas molecules;
- radio-frequency cavities, accelerating charged particles with an alternating electromagnetic field;
- magnet system to steer and guide the accelerated particles.

The beam energy in TeV in a circular particle accelerator follows

$$E_{\mathrm{beam}} \simeq 0.3BR, \tag{1.1}$$

where B is the magnetic field in Tesla and R is the radius of the circular curvature in kilometres. A cost-effective way of reaching high energies is the use of high-field magnets, which allow smaller machine radii and therefore smaller circumferences. Thereby, the current-carrying capability of the used conductor is a key parameter for the magnet performance as the generated magnetic field B is proportional to the current density J in the conductor:

$$B \propto J. \tag{1.2}$$

Water-cooled aluminium or copper conductors have a limited J of ~10 A/mm^2. In superconducting wires, current densities of the order of 600 A/mm^2 are typically achieved. One of the key challenges in high-field magnets with superconducting coils is the management of mechanical stress. Owing to the Lorentz forces on the conductors, a magnetic pressure P is generated in a dipole bending magnet that scales with

$$P \propto B^2 \text{ and } P \propto J^2 \text{ in the mid-plane.} \tag{1.3}$$

Past projects for high-field particle accelerators such as Tevatron, HERA and the Large Hadron Collider (LHC) [2] were employing superconducting magnets with Nb–Ti conductor technology. This technology has reached maturity with the LHC. To further increase the magnetic field, Nb_3Sn has been selected as the design choice for future machines such as CERN's High Luminosity Large Hadron Collider (HL-LHC) and is the baseline material for the conductors of the high-field magnets for the FCC 16 T magnets. Nb_3Sn has the potential to reach high magnetic fields.

The selected conductor based on Nb_3Sn, used in a high-mechanical-stress environments, is sensitive to strain [3]. For the magnet manufacturing process, it is crucial to know the mechanical behaviour and performance limitations of the conductor, embedded in a compound of insulating and impregnating material, to fulfil the design criteria.

1.1. The LHC and the HL-LHC project

The LHC

The LHC is a hadron collider with a circumference of 27 km, equipped with 1232 two-in-one superconducting dipole bending magnets that provide a nominal magnetic field of 8.33 T. They are operated at a nominal current of 11.85 kA, and an operating temperature of 1.9 K. The LHC design target for a nominal centre-of-mass energy of 14 TeV is reached at these values.

In this collider, two beams are accelerated in opposite directions and brought to collision. The machine was installed in an existing tunnel previously used for the Large Electron–Positron Collider (LEP) [4]. The LHC is divided into eight sectors. The beams intersect at four Interaction Points (IP) as shown in Figure 1.2.

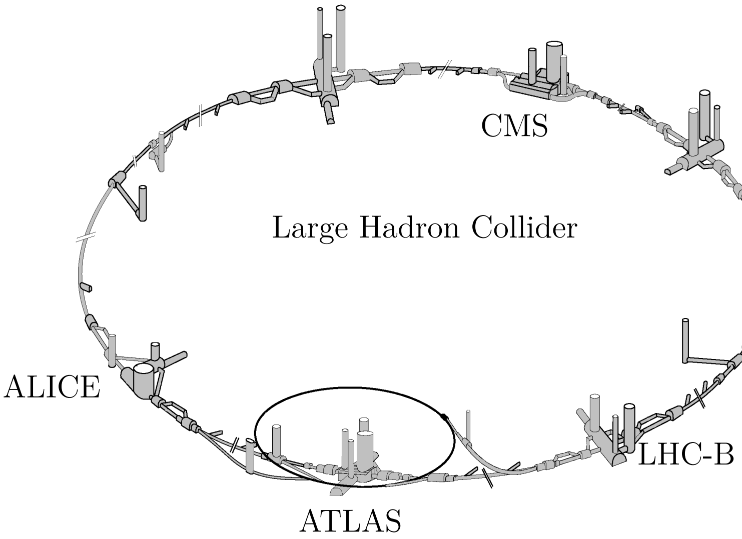

Figure 1.2.: Layout of the LHC [5].

These IPs are installed in big caverns hosting the particle-physics detectors called CMS (Compact Mueon Solenoid), ATLAS (A Toroidal LHC Apparatus), LHC-B (Large Hadron Collider Beauty) and ALICE (A Large Ion Collider Experiment). Further information about particle accelerators is provided by Landolt-Börnstein [6] and Wiedemann [7]. Superconducting magnets are described in detail by Wilson [8], Iwasa [10], Mess [11], Russenschuck [12], Brechna [13] and Schoerling and Zlobin [14].

The HL-LHC project

The HL-LHC [15] is an upgrade to the LHC, proposed to increase the instantaneous luminosity (rate of collisions) by a factor of five beyond the nominal LHC design value. Increased luminosity will provide more statistical data on the researched particles, allowing precise measurements to be performed with reduced statistical error. Brüning (2015) stated that:

> "*...running the accelerator without an additional considerable luminosity increase beyond its design value will become marginal. The running time necessary to half the statistical error in the measurements will be more than ten years..*" [16]

Therefore, the CERN council has approved this major upgrade to LHC. To achieve the defined goal, of increasing the rate of collisions at the IPs, the beam intensity has to be increased and the beam size at the IPs reduced, to increase the probability of collisions. To achieve both the higher intensities and the smaller beam size at the IPs, major upgrades in the LHC machine and its injectors are necessary. Examples include the cryogenics system, the machine protection, the inner triplet magnets and the collimation system.

In terms of superconducting magnets, a beam size reduction in an IP can be achieved by using stronger inner triplet magnets[1] with a larger aperture. The free bore of a magnet is called the aperture. Currently, the LHC inner triplet magnets have an aperture of 70 mm and a field gradient of 200 T/m. The coils are based on the Nb–Ti conductor technology with a peak field of 7 T in the coil. In HL-LHC, the large aperture inner triplet quadrupole

---

[1] Triplet: Assembly of three quadrupole magnets, used for a reduction of the optical β-functions at the IPs [12].

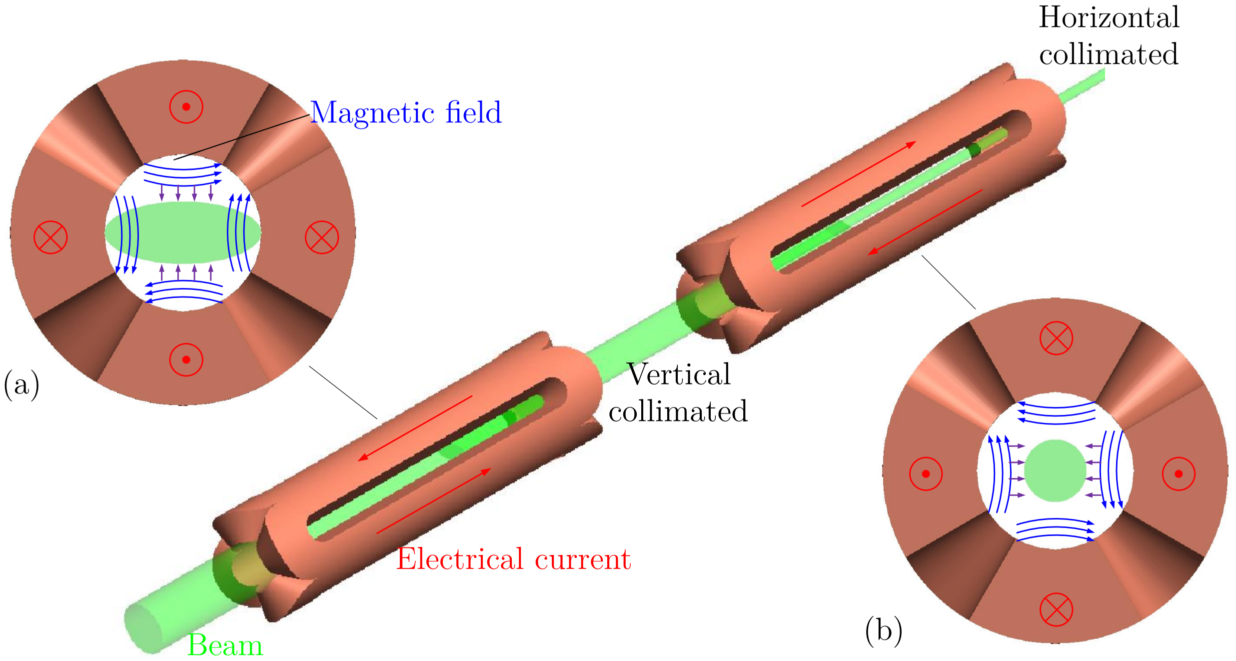

Figure 1.3.: Beam collimated by quadrupole magnets in vertical direction (a) and horizontal direction (b).

magnets have a free bore of 150 mm. The coils, wound by a Nb_3Sn based conductor, have an operating field gradient of 140 T/m with a peak field of about 10.5 T in the coil. These stronger magnets focus the particle beam as visualised in Figure 1.3.

The increased intensities of the heavy-ion beams in the HL-LHC configuration require the installation of collimators in the cold Dispersion Suppressor (DS) region of the IR7 cleaning insertion to protect the downstream dipoles [17]. This choice was taken as there is no room left for the installation of TCLDs (Target Collimator Long Dispersion suppressor) without replacing two 14.3 m long 8.33 T standard LHC main dipoles (MB) each with an assembly consisting of a pair of 5.5 m long 11 T dipoles making room for a central bypass cryostat (length 3.3 m) hosting the TCLD collimator (length 1 m).

1.2. The FCC study

The FCC study, a study for a post-LHC collider, aims to reach energy levels far beyond the range of the LHC. FCC-hh is currently aiming for a collision energy of 100 TeV [18]. The European Strategy Session states in 2013 that:

> “*to stay at the forefront of particle physics, Europe needs to be in a position to propose an ambitions post-LHC accelerator project at CERN by the time of the next Strategy update, when physics results from the LHC running at 14 TeV will be available. CERN should undertake design studies for accelerator projects in a global context, with emphasis on proton–proton and electron–positron high-energy frontier machines. These design studies should be coupled to a vigorous accelerator R&D programme, including high-field magnets and high-gradient accelerating structures, in collaboration with national institutes, laboratories and university worldwide.*” [18]

The beam energy E_{Beam} (Equation (1.1)) is proportional to the magnetic dipole field B (increasing the bending strength) and the bending radius R, in the frame of the FCC study both parameters being increased compared with the LHC. A circumference of 80 km to 100 km is housed in a new tunnel in the area of Geneva, as shown in Figure 1.4, with main bending dipoles with magnetic fields of 20 T based on high-temperature superconductor (HTS) technology to 16 T based on Nb_3Sn technology. The dipole magnet development program for FCC is focusing currently on the 16 T dipole option for cost reasons [20]. For the 16 T dipole, different design approaches are under investigation. In [14] a review of all so-far built dipole Nb_3Sn magnets is given. This review shows the magnet manufacturing process. Recent studies have emphasised a $\cos\theta$-coil design [21], block-coil design [22], common-coil design [23] and canted-$\cos\theta$-coil design [24] based on Nb_3Sn superconductors.

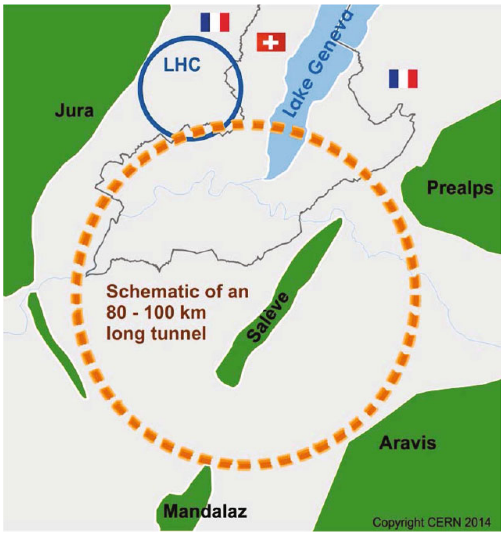

Figure 1.4.: Schematic of a 100 km tunnel for the FCC in the Lake Geneva basin [25].

1.3. Superconducting materials for accelerator magnets

To reach the previously mentioned high field in a cost-efficient way, superconductors are mandatory. In conventional iron-dominated magnets, the field is limited by the saturation of iron to about 2 T. Thanks to the effect that the electrical resistance for certain materials drops to zero as the temperature drops below a critical value T_{c}, magnetic fields way beyond 2 T can be generated. Superconductivity was discovered in 1911 by H. K. Onnes [26]. He measured the resistance of mercury versus temperature and discovered the superconducting transition at 4.20 K where within 0.01 K the resistance dropped from an easily measurable to an unmeasurably small value, as shown in Figure 1.5.

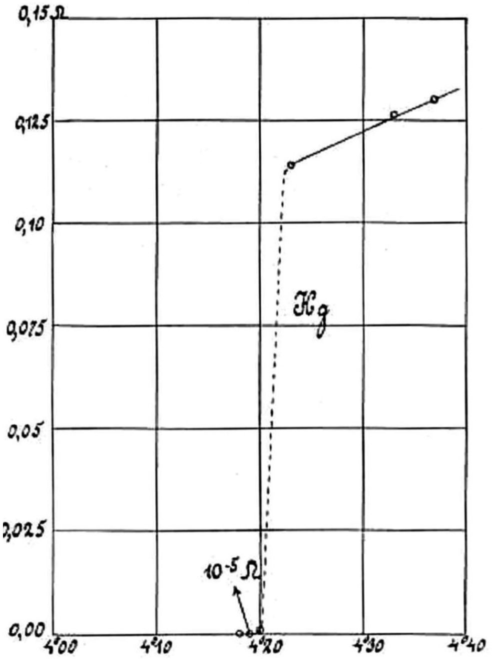

Figure 1.5.: Historic plot of resistance (Ω) versus temperature (K) for mercury from the experiment showing the superconducting transition at 4.2 K [26].

Type I superconductor

If a magnetic field is applied on a type I superconductor below a critical temperature, a surface current that shields the magnetic field is generated. This behaviour is called the Meissner–Ochsenfeld effect [27]. The phenomena was observed for type I superconducting materials such as mercury, lead and aluminium. The materials lose superconductivity if the magnetic field exceeds a critical value B_{c1}. At this state the magnetic field can no longer be shielded by the surface currents and penetrates into the material.

Type II superconductor

In addition to the type I characteristic, a type II superconductor has the capability to withstand higher magnetic fields. When exposed to a magnetic field below its critical temperature T_c, the magnetic field penetrates the material in discrete flux lines through vortices, as illustrated in Figure 1.6. The vortices allow the material to have a superconducting state in higher magnetic fields. The vortices are located at micro-structural defects in the material, which are called pinning centres. The force needed to detach a vortex from a pinning centre is called the pinning force. The transport current in a material applies a Lorentz force to the vortices. The vortex starts to move if the applied Lorentz force exceeds the pinning force. At this level the material becomes electrically resistive. This defines an upper limit that is called the critical current density J_c.

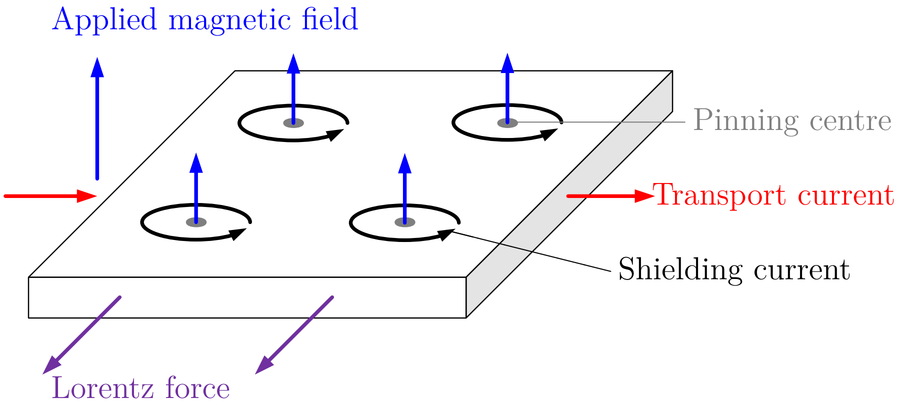

Figure 1.6.: Schematic of a type II superconductor in an applied magnetic field with the Lorentz force between the transport current and the flux lines [28].

A further limitation of a type II superconductor is the upper critical field B_{c2}. As the magnetic field increases, the vortices crowd closer together, up to a critical value where the vortices begin to overlap and the sample loses superconductivity. These parameters, the critical temperature, critical current density and critical magnetic field, define the critical surface of a conductor and define the upper theoretical performance limit of a superconducting magnet [8, 28]. Only type II superconductors are suitable for applications in high magnetic fields. Typical conductor materials used for high-field accelerator magnets are Nb–Ti and $\mathrm{Nb_3Sn}$, which characteristic properties are given in Table 1.1.

Table 1.1.: Properties of some Type II superconductors [28].

Material	Critical Temperature (K)	Critical Magnetic Field B_{c2} (T)
Nb–Ti	9.6	14.5
$\mathrm{Nb_3Sn}$	18.1	25

The critical surface for $\mathrm{Nb_3Sn}$ can be adapted with the following equations to describe the critical current density J_{c} change with respect to the temperature T and magnetic field B. In contrast to Nb–Ti, the superconducting current-carrying capability of $\mathrm{Nb_3Sn}$ is also dependent on the strain ε. The crystallographic structure of $\mathrm{Nb_3Sn}$ is known as the A15 or $\mathrm{Cr_3Si}$ type, with body-centred cubic (bcc) lattice of Sn atoms and two Nb atoms on each face of the cube as shown in Figure 1.7. The characteristic parameters of $\mathrm{Nb_3Sn}$ wires are a critical temperature $T_{\mathrm{c}}(0\,\mathrm{T}) = 18.1\,\mathrm{K}$, an upper critical field $B_{\mathrm{c20}} = 30\,\mathrm{T}$ and engineering current density $B_{\mathrm{eng}} = 700\,\mathrm{A/mm^2}$ at 15 T [30], which represents the critical current density normalised to the wire cross-section. The FCC specification is $J_{\mathrm{c}}(16\,\mathrm{T},4.2\,\mathrm{K}) = 1500\,\mathrm{A/mm^2}$ on small samples, and in large production $J_{\mathrm{c}}(16\,\mathrm{T},4.2\,\mathrm{K}) = 1000\,\mathrm{A/mm^2}$. The fit function $J_{\mathrm{c}}(T,B,\varepsilon)$ for $\mathrm{Nb_3Sn}$ in Equation (1.4) is based on the formulations of [29]:

$$J_{\mathrm{c}}(B,T,\varepsilon) = C_0\frac{B_{\mathrm{c20}}}{B}((s(\varepsilon))^{\sigma}\left[(1-t^{1.52})(1-t^2)\right]^{\alpha} b^{0.5}(1-b)^2 \tag{1.4}$$

with σ and α being close to one and C_0, α and σ being fitting parameters, B is the applied magnetic field and T the temperature. The parameter t is the so-called reduced temperature

$$t = \frac{T}{T_{\mathrm{c}}(\varepsilon)}, \tag{1.5}$$

where $T_c(\varepsilon)$ is the critical temperature, T_{c0} is the temperature at 0 T,

$$T_c(\varepsilon) = T_{c0} s(\varepsilon)^{\frac{1}{3}} \tag{1.6}$$

and s is a strain-dependent term, which further includes the first and second invariant of the axial strain sensitivity I_1 and J_2 as well the fitting parameters C_1, $C_2 = 0.5$ and $C_3 = 2$,

$$s(\varepsilon) = \frac{e^{-C_1\left(\frac{J_2+C_3}{J_2+1}\right)J_2} + e^{-C_1C_2\left(\frac{I_1^2+C_3}{I_1^2+1}\right)\frac{I_1^2}{2}}}{2}, \quad C_2 = \frac{1}{2}, \quad C_3 = 2 \tag{1.7}$$

and I_1 and J_2 are invariants of the strain tensor. The normalised magnetic field b is calculated by the upper critical field B_{c2} at the operating temperature

$$b = \frac{B}{B_{c2}(\varepsilon)}, \tag{1.8}$$

which is calculated by scaling the upper critical field at 0 K B_{c20} with the reduced temperature t and the strain function $s(\varepsilon)$ to

$$B_{c2}(T,\varepsilon) = B_{c20} s(\varepsilon)(1 - t^{1.52}). \tag{1.9}$$

The strand production requires a Nb_3Sn formation step by a reaction heat treatment (RHT), in which niobium and tin react at a temperature of about 650°C to form Nb_3Sn. Most superconducting magnets based on the Nb_3Sn conductors are manufactured by the so-called “wind and react” technology, a two-step preparation technique starting with the coil winding of an “unreacted” superconducting cable followed by a RHT of the wound coil. A technology called “react and wind” [14] imposes the coil winding after reaction. This technology requires special winding schemes, and is not discussed further in this thesis.

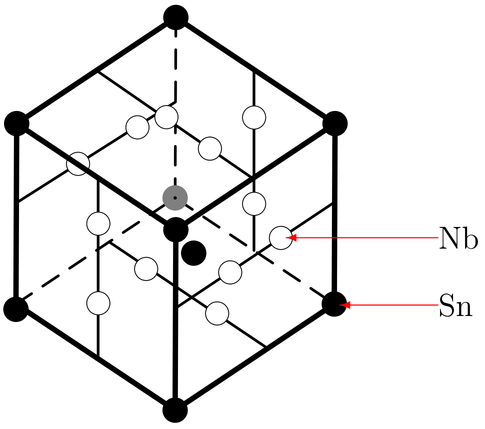

Figure 1.7.: A15 crystal structure of Nb_3Sn with Sn ions in a bcc crystal structure and niobium ions in chains along the sides of the unit cell [31].

1.4. Multi-filamentary wires and Rutherford cables

Nb_3Sn strand
Strands used for today's magnet applications consist of several superconducting filaments that are twisted and embedded in a normal low-resistivity matrix [8] with a strand diameter in the range 0.5 mm to 1.3 mm depending on the application.

A summary of the Nb_3Sn conductor development from 1960s until 2018 is given in [14]. The wire manufacturing technologies PIT (powder-in-tube) and IT (internal tin) achieved the previously stated requirements for superconducting magnet applications.

Bronze-route wires
So-called bronze-route wires are the workhorse for most applications using Nb_3Sn as solenoid magnets. The bronze-route process is based on Nb filaments placed in a Sn-rich bronze matrix in multiple rods surrounded by a high-purity copper matrix, separated by a Nb or Ta diffusion barrier. The thus produced wires have a relatively low critical current density owing to the limited content of Sn in the bronze [14].

PIT wires
The first laboratory production of PIT wires was in 1961 [32] with Nb tubes filled with crushed niobium tin powders, sealed and drawn to long wires. A reaction temperature range of 1000 °C to 1400 °C was necessary to form the superconducting Nb_3Sn phase with this simple PIT technique [33]. In a binary Nb–Sn system, the Nb_3Sn is formed by solid-state diffusion above ~930°C, where Nb_3Sn is the only stable state. The addition of Cu to a ternary system (Nb–Sn–Cu) strongly lowers the A15 phase formation temperature of Nb_3Sn to ~650°C and the diffusion path from the Cu–Sn solid solution to the Nb–Sn solid solution prevents the formation of non-superconducting phases [14]. The advanced PIT process is based on a niobium tube that was filled with grain size $NbSn_2$ powders inserted into a copper tube. The resulting cold-drawn wire could be reacted at temperatures of 650 °C to 700 °C. Large development efforts were expended by the Netherlands Energy Research Foundation (ECN) [34] followed by a further strand optimisation by Shape Metal Innovation Company (SMI) [35]. In 2006 Bruker-EAS Germany purchased the "know-how" for the PIT technology. The technology might be continued as a possible platform for future high-current density wires [14, 36].

IT wires
The IT process was introduced in 1974 [37]. Sub-elements are formed by tin cores surrounded by niobium rods, embedded in a copper matrix with a surrounding diffusion barrier of Ta. These sub-elements are re-stacked in a pure copper matrix, where the diffusion barrier prevents tin from diffusing into the pure copper matrix. This is extruded to fabricate a wire. There are several modifications of these manufacturing techniques such as the "modified jelly roll" (MJR) process [38], the hot extrusion process (HER) [39], the distributed tin process (DTP) [40], the enhanced internal tin (EIT) process [41] and the Restacked Rod Process® (RRP ®) [38] as listed in [33]. The variations differ in niobium filament design, tin distribution in the billet, sub-element design, shape and position of the diffusion barrier and the extrusion process, which all affects the strand performance. The best performance for accelerator magnet applications could be achieved so far with strands using the RRP® process [14]. The RRP® wire manufacturing process is based on the assembly of niobium filaments and pure-tin or tin-alloy rods in copper matrix to from a sub-element [38]. These

sub-elements are surrounded by a diffusion barrier to avoid tin diffusion into the copper matrix. The sub-elements are re-stacked in a copper matrix and cold drawn to the final size.

The RRP® conductor was selected as a workhorse for Nb_3Sn accelerator magnets, and at present it is the only high J_c wire available commercially. In 2016 Oxford Instruments Superconducting Technology (OST), the company holding the patents for RRP, was purchased by Bruker-EAS GmbH, the company commercially producing PIT [14]. Based on economic considerations, Bruker decided after this acquisition to discontinue the production of PIT wires.

The knowledge of the thermodynamics on the growing Nb_3Sn in Cu–Nb–Sn composite wires is incomplete. A ternary phase $Nb_{0.75}Cu_{0.25}Sn_2$ was observed in a recent study [42], which is not represented in the evaluated phase diagram. A detailed investigation of the phase equilibrium of the Cu–Nb–Sn system is currently being studied at the TU Bergakademie Freiberg with a focus on the temperature range relevant to superconducting wires [43].

The HL-LHC magnets are employing the RRP® 108/127 strand, which consists out of 108 sub-elements that form the superconducting filaments and a total of 127 elements including the copper elements in the core surrounded by a copper matrix. A detailed cross-section of a commercially available wire is shown in Figure 1.8.

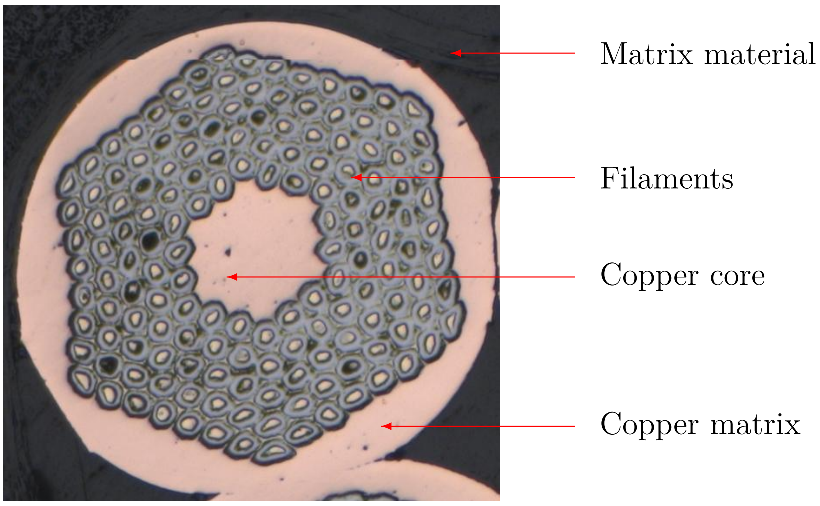

Figure 1.8.: Microscopic cross-section of a single RRP 108/127 strand from a Rutherford cable.

Rutherford-type cable

The Rutherford-type cable is a flat two-layer cable that was developed in the 1970s at the Rutherford Appleton Laboratory in Oxfordshire, UK [44]. It is a twisted fully transposed cable, consisting of a few dozen superconducting strands twisted into a flat tape-like shape. The strands are typically wound around a thin insulating stainless steel foil to improve the inter-strand resistance as explained in [45]. The wiring machine at CERN is capable of processing up to 40 strands into a Rutherford cable, the machine at Lawrence Berkeley National Laboratory can process up to 60 strands. The multistrand cable improves the flexibility to follow the curvature of the coil and it is required for achieving stability and to reduce eddy currents. A smaller radii can be wound compared with a monolithic conductor that is hard to bend [46]. The cabling process may also include a key-stoning step, where the cable is squeezed between two rollers into a wedge shape by a so-called keystone angle up to 1°, which enables the cable to follow the foreseen coil geometry. Owing to its excellent mechanical, electrical and thermal properties, Rutherford-type cable has played a crucial role in establishing Nb-Ti accelerator magnet technology and is also widely used in Nb_3Sn magnets [14]. A multistrand cable has further advantages as summarised in [28]:

- it limits the piece length for wire manufacturing (length reduction by the number of strands in the cable);
- it allows strand-to-strand current redistribution in the case of a localised defect or when a quench originates in one strand;
- it limits the number of turns and facilitates coil winding;
- it limits the coil inductance (inductance scales to the number of turns N with $1/N^2$ and a small inductance reduces the voltage to ground in the case of a quench).

The application in a superconducting coil addresses the following main issues of cable design as summarised in [28], which must be taken into account: the cable compaction to ensure mechanical stability and high overall current density, the control outer dimensions to achieve suitable coil geometry and mechanical properties, the critical current degradation due to strand and filament deformation at the cable edges and the inter-strand resistance, which should be large enough to limit field distortion by coupling currents and low enough to allow current redistribution.

Insulation system

The insulation system between the cable turns of a Nb_3Sn magnet need to withstand the reaction heat treatment (RHT) process of the conductor. The high reaction temperature precludes application of organic materials as an insulation system of the cable before the RHT, in contrast to the Nb–Ti magnet manufacturing process, which does not require a heat treatment. Commonly used materials are fibreglass braidings or tapes made of E- or S2-glass yarns. Standard E-glass contains approximately about 8 % B_2O_3 [47]. As boron interacts with neutrons during irradiation, it is unfavourable for some applications. In order to reduce possible effects of radiation, a boron-free S2-glass is used for insulation purposes. Hybrid insulation systems made from fibreglass and mica are also used to improve the insulation properties. Mica is a naturally occurring aluminosilicate mineral with good dielectric properties. Figure 1.9 shows twisted strands of a non-reacted Rutherford cable used for the 11 T magnet. The cable is surrounded by a C-shape insulation layer of mica FIROX P 636P24A (80 μm) by COGEBI a.s. and a Type 636 S2-glass yarn braiding by AGY (Advanced Glassfiber Yarns) Holding Corporation with numerous filaments of varying diameters, forming two independent insulation layers with a total thickness of 122 μm. A starch-oil sizing is used for the Type 636 S2-glass yarn to protect the glass filaments from abrasion during processing. The sizing is removed afterwards. The additional layer of insulation improves the turn-to-turn insulation between the cables.

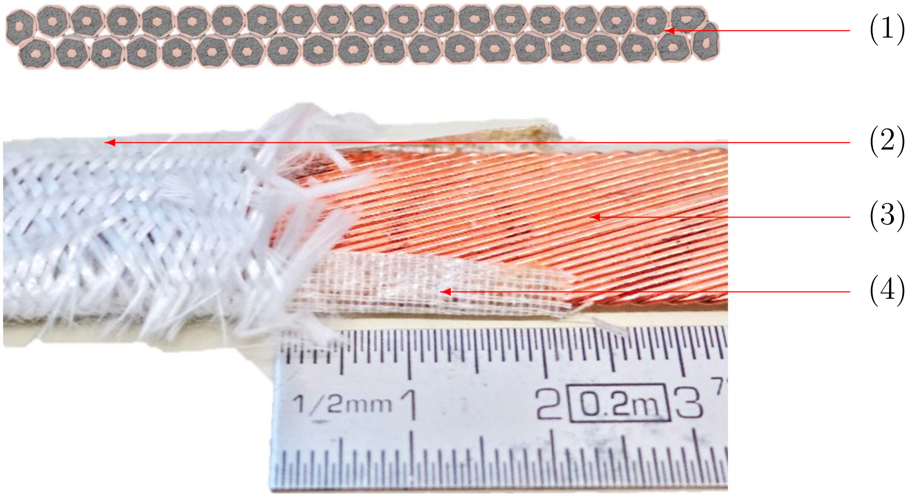

Figure 1.9.: Cross-section of a Rutherford cable (1) and photograph of a cable (3) with Mica insulation (4) and fibreglass sleeve (2).

The braiding machine and a detailed picture of a Rutherford cable during braiding is shown in Figure 1.10. The pictured cable is a MQXF cable insulated without mica. The applied yarn is a Type 933 S2 glass by AGY with numerous filaments of 9 μm diameter forming a 145 μm thick glass insulation. The Type 933 S2 glass comes with a thermally stable inorganic sizing that eases the braiding process [49]. The electrical magnet insulation is completed with the vacuum pressure impregnation of the coil with an epoxy resin, commonly CTD-101K by Composite Technology Development, Inc., chosen due its higher radiation resistance. The mechanical behaviour of the impregnation system affects the magnet performance, as it is believed that the energy released by a crack in the resin is sufficient to initiate a quench [48].

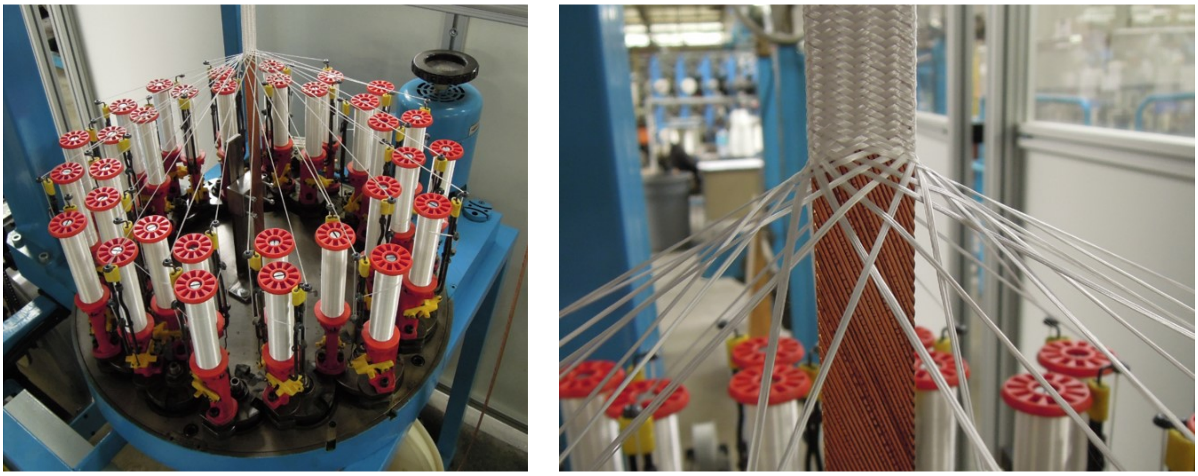

Figure 1.10.: Braiding of a Rutherford cable without mica insulation at CGP SAS. Courtesy of P. Ferracin [50].

1.5. Coil manufacturing process

Both types of superconducting magnets for HL-LHC are produced by the so-called "wind and react" technique and follow the $\cos\theta$ design. First, the insulated keystoned Rutherford cable is wound around a winding mandrel. So-called wedges are included to follow the arc shape towards an optimised cross-section, to achieve the required field quality when the magnet is in operation. After the coil winding, the coil outside is wetted with the polymer-derived ceramic (PDC) resin system CTD-1202, a ceramic binder, which makes the coil a rigid body after curing and eases the coil handling after RHT. Once treated with ceramic binder the coil undergoes a curing heat treatment, 1 hour at 80°C and 2 hours at 150°C. Afterwards, the RHT takes place where the superconducting Nb_3Sn phase in the conductor is formed. The RHT is performed in a dedicated mould, purged with argon to clean out the coil from burned organic residuals mainly sizing agents required for processing the glass-fibre insulation. The process is followed by a dedicated heat treatment, optimised for the used strand. The RHT schedule for the 11 T and MQXF magnet production is presented in Table 1.2 adapted to the used strand.

Table 1.2.: Reaction heat treatment cycle for 11 T and MQXF coils.

Plateau temperature 11 T (MQXF)	Duration 11 T (MQXF)	Temperature ramp
210°C (210°C)	48 h (48 h)	25°C/h
400°C (400°C)	48 h (48 h)	50°C/h
650°C (665°C)	50 h (75 h)	50°C/h

After a slow cool-down to room temperature, the coil is put into a leak tight mould for vacuum pressure impregnation with CTD-101K, a Diglycidyl Ether of Bisphenol-A (DGEBA) with anhydride curing agent. The impregnation mould defines the shape of the coil. The vacuum impregnation with a resin system provides mechanical support to the coil and electrical insulation of the coil and cable. The impregnation is performed in a vacuum chamber. In preparation for the impregnation, the two-component epoxy resin is degassed. The epoxy injection is performed under pressure and followed by a curing heat treatment cycle of 5 hours at 110°C and 16 hours at 125°C. The coil is ready for the magnet assembly after de-moulding from the impregnation mould. A cut segment of a dipole coil is shown in Figure 1.11.

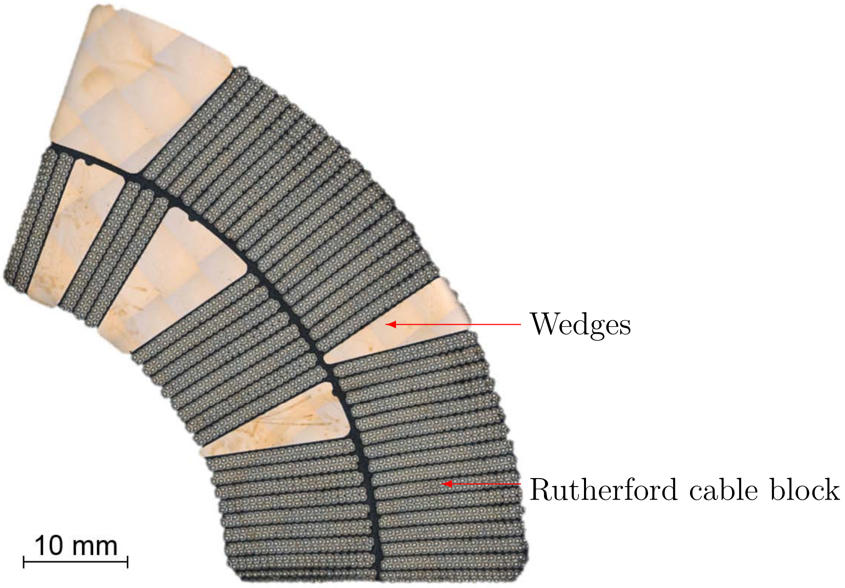

Figure 1.11.: Metallographic cross-section of one Nb_3Sn 11 T dipole coil sector showing the conductor blocks and wedges.

1.6. Magnet coil assembly

To pair coils with similar dimensions, they are measured precisely with a FaroArm® Edge 1.8 to be able to compensate dimensional differences. The magnet assembly process of the coil includes a mechanical pre-loading step, commonly done for accelerator dipole magnets with rigid laminations called collars stacked and clamped around the coils with tapered keys under the load of a press to set the pre-load at room temperature. This step is further completed with an iron yoke and a thermal shielding.

Pre-load of a magnet

The conductor in a superconducting magnet needs to be pre-stressed to ensure the desired magnetic field characteristic and to reduce the risk of quenches[2] during powering and operation. Both effects are caused by conductor movements owing to electromagnetic forces compressing the coil towards the midplane and in the outward direction. In order to ensure the mechanical stability of the conductor, the coil is pressed against a rigid support structure. In the absence of pre-load, the coil would detach from the support structure. A minimum load is selected to ensure no displacements of the coil at nominal current.

The possible conductor degradation under high stress and insulation damage define the upper pre-load limit. This limit is particularly relevant for high-field Nb_3Sn magnets where the assembly stress can cause excessive conductor degradation. Discussion of the appropriate

---

[2] A quench is the transition between the superconducting and resistive state of the material.

level of pre-stress remains ongoing. Recent analysis of manufacturing and test data from the two types of magnets of the HL-LHC project (11 T and MQXF) have shown that many magnets did not satisfy the minimum pre-loading requirement but could still reach the performance targets [51].

The Nb_3Sn magnet programs for the HL-LHC upgrade are following different pre-loading concepts. The pre-load in the MQXF quadrupole magnet [52] is achieved by using the bladder and key technology, conceptual designs to achieve the pre-load for the quadrupole magnet using collars also exist [53]. The 11 T magnet program [54] is following the collared coil technology. The bladder and key concept provides a high load with the use of an aluminum cylinder around the yoke, surrounded by a stainless steel welded shell. At room temperature, so-called bladders are inserted into the magnet and pressurised with water (<600 bar). Then precise-manufactured steel keys are inserted, keeping a load between 10 and 80 MPa as the pressure is released. The differential shrinkage during the cool down between the aluminium shell and iron yoke increases the pre-stress up to 100 MPa. This concept allows the highest stress to be applied on the conductor at cryogenic temperature.

The traditional solution to pre-load a magnet is to place thin collars around the coil and compress them at room temperature. The coil is well contained in a fixed cavity. Both collar halves are pressed together and locked with pins or keys. The applied pre-stress is about twice that needed to counteract the Lorentz forces as a part of the stress is reduced during the cool down by thermal contraction. The pre-load is defined between the clearance provided by the collars and the coil. It is crucial to know the mechanical behaviour and limitations of the conductor block embedded in an epoxy matrix under applied load at room temperature to set the desired pre-load.

The level of the desired pre-load is under discussion, owing to recent observations in both types of magnets during testing. Test results of the MQXF and 11 T magnets have shown an unloading in the winding pole, determined by strain gauges [55], indicating a magnetic pressure in the coil above the pre-load level. A varying coil pre-load has shown no evident correlation on the training[3] behaviour or magnetic field limitations. Further, it was observed that the conductor movements determined by magnetic field measurements have been less than expected by finite element models [55]. An investigation of the relation between compressive stiffness of the coil and the displacement under load might explain the smaller than expected conductor movement.

1.7. Objectives of this thesis

In this thesis, methods for the characterisation of Nb_3Sn Rutherford cables and cable stacks as an impregnated compound used for accelerator magnets are presented. There are four main achievements:

- establishment and performance of a test procedure to investigate the irreversible conductor degradation at room temperature under compressive load, determining the limiting manufacturing parameter of the applied compressive stress to 150 MPa during the magnet assembly process;

---

[3] Magnet training is a phenomenon observed during testing of superconducting magnets, when the maximum performance before a quench gradually increases in consequent quenches.

- stiffness characterisation of the coil material and representative samples identifying the effect of pre-stress variation in the coil manufacturing process on the mechanical coil behaviour with a compressive stiffness of 42 GPa at 5 MPa up to 55 GPa at 30 MPa pre-stress during reaction and impregnation;
- determination of the stress–strain state of the copper and Nb_3Sn phase in the conductor by neutron diffraction measurements performed during compressive stress–strain measurements;
- reproduction of the measurement results with finite element models, which can be used to predict the stress–strain state of the magnet during the assembly process.

2. Theory: fundamental principles

2.1. Analytical calculation: sector coil dipole

A simple representation of a dipole magnet is a sector coil. The coil sector is defined by the coil angle Φ, a free bore with inner radius R_1 called the aperture and an outer coil radius R_2. Each sector has the current density J. The radial and azimuthal magnetic field components B_r and B_Θ in the coil itself can be calculated by using the following equations:

$$\begin{aligned} B_\mathrm{r} = -\frac{2\mu_0 J_0}{\pi} \Big[& (R_2 - r)\sin\Phi \sin\Theta \\ & + \sum_{n=1}^{\infty} \left(1 - \left(\frac{R_1}{r}\right)^{2n+1}\right) \frac{r}{(2n+1)(2n-1)} \sin(2n-1)\Phi \sin(2n-1)\Theta \Big], \end{aligned} \tag{2.1}$$

$$\begin{aligned} B_\Theta = -\frac{2\mu_0 J_0}{\pi} \Big[& (R_2 - r)\sin\Phi \cos\Theta \\ & - \sum_{n=1}^{\infty} \left(1 - \left(\frac{R_1}{r}\right)^{2n+1}\right) \frac{r}{(2n+1)(2n-1)} \sin(2n-1)\Phi \sin(2n-1)\Theta \Big]. \end{aligned} \tag{2.2}$$

With respect to Equation (2.1) and (2.2) it can be seen that the magnetic field B inside the clear aperture scales linearly with the current density J of the coil

$$B \sim J. \tag{2.3}$$

A detailed derivation on the calculation of the magnetic field components is given in Appendix A. The field map using Equations (2.1) and (2.2) for a 16 T dipole is shown in Figure 2.1.

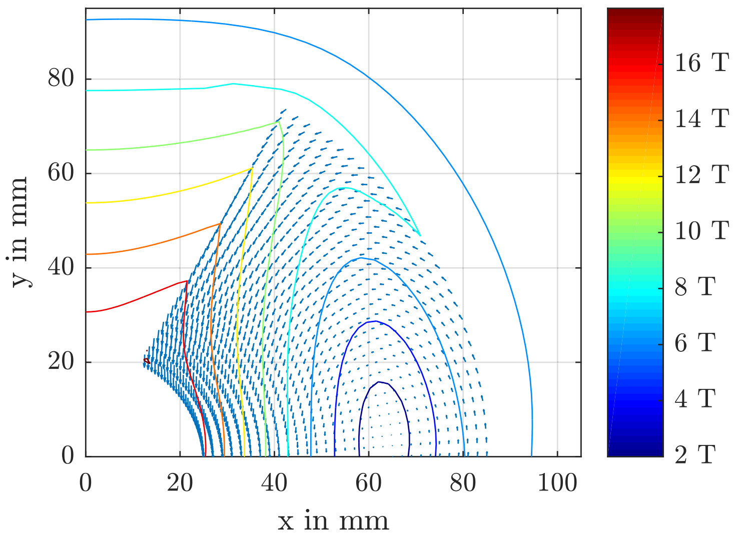

Figure 2.1.: Magnetic field and magnetic field arrows.

The resulting Lorentz force F_L in the sector coil is given by the line current I and the magnetic field B at each coil location along the unit length l:

$$F_L = I(r) \int \mathrm{d}l \times B. \tag{2.4}$$

The distribution of the Lorentz force in a sector coil is shown in Figure 2.2, indicating the force direction, and the force density to scale the force with respect to the corresponding volume element.

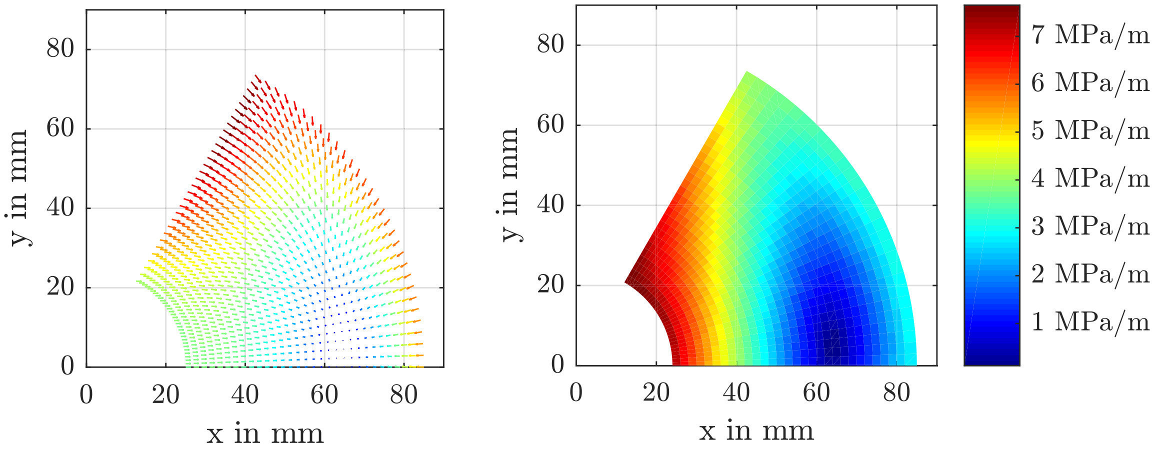

Figure 2.2.: Magnetic force distribution (left) and the force density distribution (right) in the sector coil.

The Lorentz force that acts on the coil can also be calculated analytically by

$$F_\mathrm{r} = -B_\Theta J = \frac{2\mu_0 J_0^2}{\pi} \sin\Phi \left((R_2 - r) - \frac{r^3 - R_1^3}{3r^2} \right) \cos\Theta, \tag{2.5}$$

$$F_\Theta = B_\mathrm{r} J = -\frac{2\mu_0 J_0^2}{\pi} \sin\Phi \left((R_2 - r) + \frac{r^3 - R_1^3}{3r^2} \right) \sin\Theta. \tag{2.6}$$

The azimuthal stress on the magnet mid-plane caused by the Lorentz force can be expressed by the integration of the azimuthal force components as

$$\sigma_{\Theta\mathrm{mid-plane}} = \int_0^{\pi/3} F_\Theta r \mathrm{d}\Theta = -\frac{2\mu_0 J_0^2}{\pi} \frac{\sqrt{3}}{4} r \left[(R_2 - r) + \frac{r^3 - R_1^3}{3r^2} \right], \tag{2.7}$$

for a sector coil with an angle $\Phi = 60°$. The equation for the integrated stress at the mid-plane is indicating that for a fixed magnet design with a constant current density J along the cross-section, J scales quadratic to the azimuthal mid-plane stress σ_Θ as well as the magnetic field B to

$$\sigma_\Theta \sim J^2 \quad \text{and} \quad \sigma_\Theta \sim B^2. \tag{2.8}$$

The relation relation between magnetic field and mid-plane stress in the coil is quadratic. The stress values at the mid-plane of the powered LHC dipole magnet and the 11 T dipole

Table 2.1.: Azimuthal stress at the mid-plane during powering.

Dipole magnet	Magnetic field	Mid-plane stress
LHC [56]	8.3 T	70 MPa to 75 MPa
HL-LHC 11T [54]	11 T	125 MPa to 135 MPa

magnet are listed in Table 2.1. Both magnets have a similar coil cross section, whereas the higher current density in the 11 T coil provides a higher magnetic field.

The magnet design has to respect the critical surface $J_c(T_c, B_c)$ of the conductor, limiting the current density J with respect to the magnetic field B at a critical temperature T_c. Further, the current density should be limited in order to fulfil protection requirements, preventing damage to the magnet when the magnet quenches and the conductor loses its superconducting properties as the current needs to be carried by the normal conducting material.

2.2. Mechanical behaviour of composite materials

A coil conductor block made of superconducting Nb_3Sn wires insulated with fibreglass and impregnated with an epoxy resin, as shown in Figure 2.3, is described by using models for composite materials.

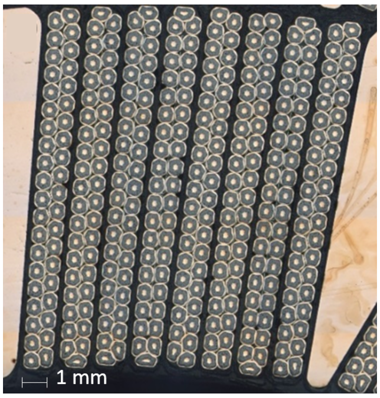

Figure 2.3.: Detailed view of a conductor block in a magnet.

Model simplifications must be made in order to describe the mechanical behaviour of composite materials. The Voigt model [57] used for composite materials, also known as the rule of mixtures (ROM), assumes an iso-strain condition[4] along the load chain in the material. The model allows an estimation of the elastic modulus E_{Voigt} of a composite with respect to the fibre modulus (E_f) and fibre volume fraction (V_f) and the corresponding matrix modulus (E_m) and matrix volume fraction (V_m)

$$E_{\mathrm{Voigt}} = E_\mathrm{f} V_\mathrm{f} + E_\mathrm{m} V_\mathrm{m}. \tag{2.9}$$

The inverse ROM, the so-called Reuss model [58], assumes iso-stress conditions[5], which

---

[4] Iso-strain: the strain is equal in fibre and matrix.

[5] Iso-stress: the stress is equal in fibre and matrix.

allows the calculation of the elastic modulus perpendicular to the fibre orientation:

$$E_{\mathrm{Reuss}} = \frac{E_{\mathrm{f}} E_{\mathrm{m}}}{E_{\mathrm{f}} V_{\mathrm{m}} + E_{\mathrm{m}} V_{\mathrm{f}}}. \tag{2.10}$$

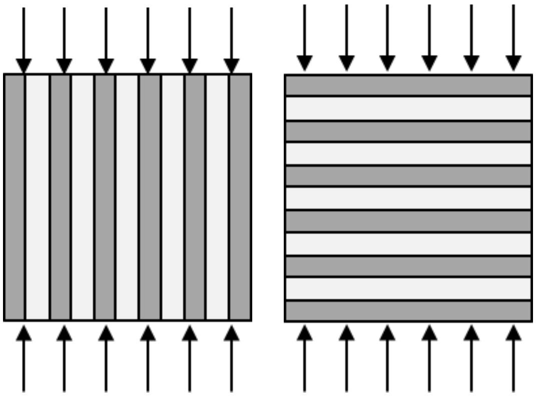

Figure 2.4.: Voigt iso-strain model (left) and Reuss iso-stress model (right).

The Reuss and Voigt models describe the theoretical limits with the assumptions of a pure iso-stress or iso-strain load scenario. The Neerfeld model describes the arithmetic average of the Voigt and Reuss model [59]:

$$E_{\mathrm{Neerfeld}} = \frac{E_{\mathrm{Voigt}} + E_{\mathrm{Reuss}}}{2}. \tag{2.11}$$

The Neerfeld model was also generalised to a linear combination of E_{Voigt} and E_{Reuss} with a weighting factor α, with the Neerfeld model for $\alpha = 0.5$,

$$E_{\mathrm{weighted}} = E_{\mathrm{Voigt}}(1-\alpha) + \alpha E_{\mathrm{Reuss}}. \tag{2.12}$$

The weighting factor α can be used as a fitting parameter as the models of Voigt and Reuss describe the extreme cases of strain and stress distribution, whereas in reality it needs to be approximated for some cases.

2.3. Failure criteria and strength hypotheses for materials

The limitation in superconducting magnets is not the yield limit of the material compound. It is defined by the strain sensitivity of filaments in a superconducting Nb_3Sn strand as shown in Equation (1.4). The failure criteria for superconducting cable is the stress limit, which causes the breakage of the superconducting filament and a permanent conductor degradation, as shown in Figure 2.5. The change of the critical current of a Nb_3Sn conductor due to stress is called critical current reduction, which is an irreversible effect caused by conductor damage. A reversible critical current reduction can be caused by stress, magnetic field or temperature influences.

Extensive test programs were performed in uniaxial stress states on strands and cables to determine the conductor limitations in different load configurations, defining the maximum

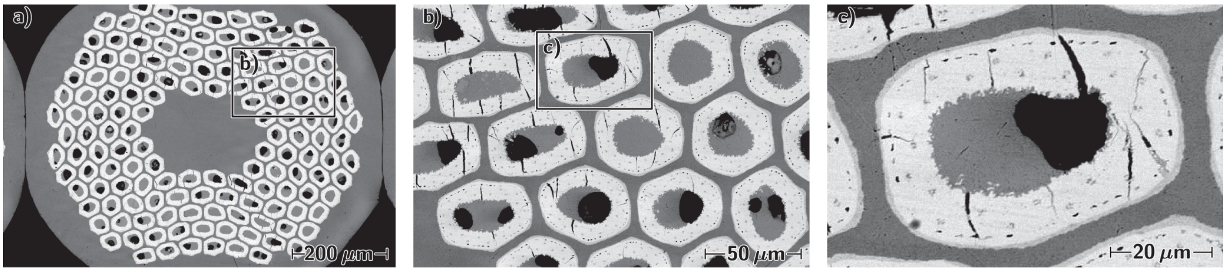

Figure 2.5.: SEM micrographs of the transverse metallographic cross-section of a 200 MPa loaded cable sample [60].

allowable stress. The concept is not linked to a yield criteria, but to the permanent conductor damage caused by the breakage of filaments. The test configurations cover the major stress states that the conductor is exposed to in a magnet, as testing all different stress states is practically impossible.

Strength hypotheses are commonly used to determine material limitations if the mechanical load is described by a multiaxial stress state. These limits have been defined for different materials, following different approaches as follows.

Principal normal stress hypotheses

This hypothesis is commonly used for brittle materials that are sensitive to the tensile stress component of the stress state, which assumes that the biggest principal stress is limiting the material performance as

$$\sigma_\mathrm{v} = \max(\sigma_1, \sigma_2, \sigma_3). \tag{2.13}$$

Shear stress hypotheses

The maximum shear stress hypothesis is used for homogeneous ductile materials, defining a more conservative approach than the equivalent stress hypotheses by von Mises,

$$\sigma_\mathrm{v} = 2\tau_\mathrm{max} = \max\left(|\sigma_1 - \sigma_2|, |\sigma_1 - \sigma_3|, |\sigma_2 - \sigma_3|\right). \tag{2.14}$$

Von Mises equivalent stress hypotheses

By the interpretation of the von Mises equivalent stress it should be taken into account that the same combination of compressive stress components can lead to an underestimation of the stress. Furthermore, the following derivation of the equivalent stress hypotheses of von Mises shows its validity only for isotropic material properties. The equivalent stress von Mises σ_v is defined in the principal axis system with the principal stress as

$$\sigma_\mathrm{v} = \sqrt{1/2\left((\sigma_1 - \sigma_2)^2 + (\sigma_1 - \sigma_3)^2 + (\sigma_2 - \sigma_3)^2\right)}. \tag{2.15}$$

The corresponding strain in the main axis can be calculated with the following equations:

$$\varepsilon_1 = \frac{1}{E}\left(\sigma_1 - \nu(\sigma_2 + \sigma_3)\right), \tag{2.16}$$

$$\varepsilon_2 = \frac{1}{E}\left(\sigma_2 - \nu(\sigma_1 + \sigma_3)\right), \tag{2.17}$$

$$\varepsilon_3 = \frac{1}{E}\left(\sigma_3 - \nu(\sigma_1 + \sigma_2)\right). \tag{2.18}$$

In the equivalent von Mises model it is assumed, that the deformation of a body can be caused by two different energies:

- U_{h}, which deforms the body in a geometric similar body (rescaled with the same shape);
- U_{sha}, which distorts the body and changes the shape.

The von Mises equivalent stress model assumes that just the shape-changing part of the energy U_{sha} leads to a material failure of a body. The inner energy U of a stressed body can be calculated with the principal stress and strain as

$$U = \frac{1}{2}(\sigma_1\varepsilon_1 + \sigma_2\varepsilon_2 + \sigma_3\varepsilon_3). \tag{2.19}$$

With Equations (2.16)–(2.18) in (2.19), the inner energy can be calculated as

$$U = \frac{1}{2E}\left(\sigma_1^2 + \sigma_2^2 + \sigma_3^2 - 2\nu(\sigma_1\sigma_2 + \sigma_1\sigma_3 + \sigma_2\sigma_3)\right). \tag{2.20}$$

The hydrostatic part of the energy is defined by the assumption that the principal stresses are equal:

$$\sigma = \sigma_1 = \sigma_2 = \sigma_3. \tag{2.21}$$

By inserting Equation (2.21) into (2.20) the hydrostatic energy U_{h} can be calculated as

$$U_{\mathrm{h}} = \frac{1-2\nu}{2E}3\sigma^2, \tag{2.22}$$

$$\sigma = \frac{3}{3}\sigma = \frac{\sigma_1 + \sigma_2 + \sigma_3}{3}, \tag{2.23}$$

$$\begin{aligned} U_{\mathrm{h}} &= \frac{1-2\nu}{6E}(\sigma_1 + \sigma_2 + \sigma_3)^2 \\ &= \frac{1-2\nu}{6E}\left(\sigma_1^2 + \sigma_2^2 + \sigma_3^2 + 2(\sigma_1\sigma_2 + \sigma_2\sigma_3 + \sigma_1\sigma_3)\right). \end{aligned} \tag{2.24}$$

The shape-changing energy U_{sha} can be calculated by subtracting the hydrostatic energy U_{h} from the total energy U,

$$U_{\mathrm{sha}} = U - U_h = \frac{1+\nu}{6E}\left((\sigma_1 - \sigma_2)^2 + (\sigma_1 - \sigma_3)^2 + (\sigma_2 - \sigma_3)^2\right). \tag{2.25}$$

In the theory of von Mises, it is assumed that the fictitious equivalent stress describes the same energy as a spatial stress state. This assumption is expressed in the following equation:

$$\sigma_1 = \sigma_{\mathrm{v}}; \quad \sigma_2 = \sigma_3 = 0. \tag{2.26}$$

With the shape-changing energy in Equation (2.25) and the fictitious one-directional stress in Equation (2.26) the following equation can be written:

$$U_{\mathrm{sha}} = \frac{1+\nu}{6E} 2\sigma_{\mathrm{v}}^2 = \frac{1+\nu}{6E} \left((\sigma_1 - \sigma_2)^2 + (\sigma_1 - \sigma_3)^2 + (\sigma_2 - \sigma_3)^2 \right). \tag{2.27}$$

From Equation (2.27) we obtain an equivalent stress σ_v, which can be calculated in the following way:

$$\sigma_{\mathrm{v}} = \sqrt{1/2\left((\sigma_1 - \sigma_2)^2 + (\sigma_1 - \sigma_3)^2 + (\sigma_2 - \sigma_3)^2\right)}. \tag{2.28}$$

The equivalent von Mises stress assumes an isotropic Young's modulus E and Poisson's ratio ν. The anisotropic material behaviour of an impregnated cable does not match with the basic assumptions for the equivalent stress theory by von Mises. It should be kept in mind that an equivalent stress can be calculated by using the principal stresses, but it is not based on the physical principle of the von Mises theory. The derivation is based on formulae taken from [61].

The equivalent stress hypotheses by von Mises is typically used in the superconducting magnet design community to evaluate macroscopic peak stresses in the coil. Thereby generalised material properties can be used for finite element models of superconducting coils. Owing to the typical force pattern in a superconducting magnet it can be shown that the principal stresses and the equivalent stress by the von Mises hypothesis are very similar [23].

In order to perform conservative stress calculations in the magnet design phase, the principal stress should be considered, as the conductor degradation is linked to the strain in any direction. As the major part of the stress is applied in transversal direction, perpendicular to the wide side of the cable, the existing test facilities for superconducting cables investigate the cable degradation under applied transversal stress. Therefore, the principal stresses should be investigated and compared with the design criteria. Currently a limit of 150 MPa at room temperature is used [60], but further investigations are ongoing.

2.4. Compressive tests

The superconducting magnet design and analysis of its structural behaviour requires knowledge of the compressive stress–strain properties, representing the stress mode of interest for the magnet manufacturing process. In order to investigate the superconducting coil behaviour, the compound of superconducting wires (Nb_3Sn and copper) and insulation material (fibreglass and epoxy) was tested to obtain average properties instead of testing the material components separately. Thereby the Standards ASTM-E9 [62], ASTM-E111 [63] and ASTM-D695 [64] for material tests were used as guidelines if applicable. The elastic slope determined from the compressive stress–strain measurements is called in the following stiffness. For an investigation focused on static elastic behaviour based on the principle of Hooke's law [65], the engineering stress (σ_{eng}) based on the initial cross-sectional area A_0 and applied load F

$$\sigma_{\mathrm{eng}} = \frac{F}{A_0}, \tag{2.29}$$

and the engineering strain ($\varepsilon_{\mathrm{eng}}$) based on the original (gauge) dimensions of specimen

$$\varepsilon_{\mathrm{eng}} = \frac{L - L_0}{L_0} = \frac{L}{L_0} - 1, \tag{2.30}$$

are employed. However, the length and cross-sectional area change in plastic regions. For an accurate definition of plastic behaviour of ductile materials by considering the actual (instantaneous) dimensions, the true stress (σ_{true}) and true strain ($\varepsilon_{\mathrm{true}}$) can be used. The true stress is calculated by the force F divided by the actual area A. By the constancy of volume

$$V = A \cdot L = A_0 \cdot L_0, \tag{2.31}$$

we can obtain the true stress with respect to the initial gauge length L_0 and the actual gauge length L

$$\sigma_{\mathrm{true}} = \frac{F}{A} = \frac{F \cdot L}{A_0 \cdot L_0} \tag{2.32}$$

and by using Equations (2.29) and (2.30) the true stress (σ_{true}) can be written as [66]

$$\sigma_{\mathrm{true}} = \frac{F}{A_0}(1 + \varepsilon_{\mathrm{eng}}) = \sigma_{\mathrm{eng}}(1 + \varepsilon_{\mathrm{eng}}). \tag{2.33}$$

The true strain ($\varepsilon_{\mathrm{ture}}$) changes in length with respect to the instant length:

$$\varepsilon_{\mathrm{ture}} = \int_{L_0}^{L} \mathrm{d}L/L = \ln(L/L_0) \quad \text{and} \quad L = (1 + \varepsilon_{\mathrm{eng}})L_0, \tag{2.34}$$

which leads to the expression [66]

$$\varepsilon_{\mathrm{ture}} = \ln(1 + \varepsilon_{\mathrm{eng}}). \tag{2.35}$$

Depending on the measurement technique used to elaborate on the engineering stress–strain curve of a material, a non-linear toe region can be observed that does not represent a property of the material. This is an artefact caused by a take up of slack, and alignment or seating of the specimen [64]. Such behaviour can be observed by using an indirect strain measurement method, increasing the uncertainty in the elastic modulus determination.

There are favourable materials existing where an elastic modulus determination can be performed in the initial loading region of the stress–strain curve with very little uncertainty, such as Ti–6Al–4V as shown in Figure 2.6. However, for unfavourable materials such as stainless steel, an uncertainty of about ±5 % was observed in the Young's modulus determination by a tensile test compared with a dynamic resonance and impulse method [67].

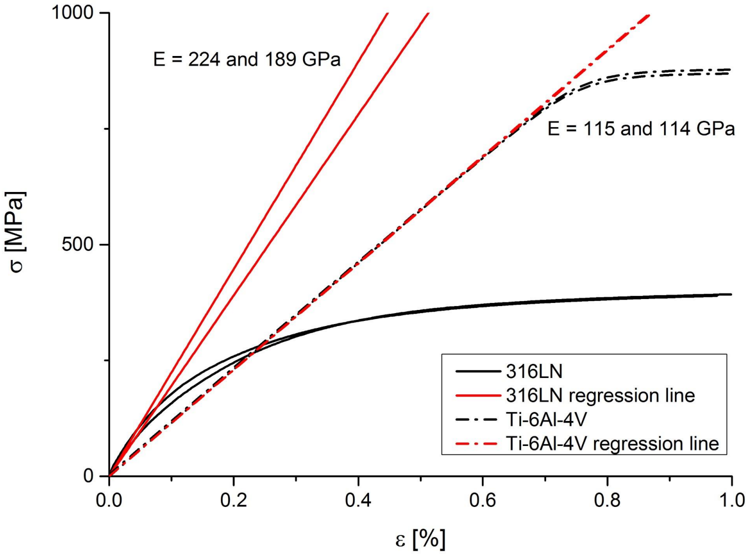

Figure 2.6.: Comparison of stainless steel 316LN and Ti–6Al–4V stress–strain curves [67].

A measurement procedure was presented by Scheuerlein [67] to determine the elastic modulus of unfavourable materials by a stress–strain measurement, where the initial elastic strain is too small for a reliable slope definition, as shown, for example, for heat-annealed copper in Figure 2.7. Thereby the slope of the unloading stress–strain curve is elaborated, which describes the elastic materials behaviour with very little uncertainty.

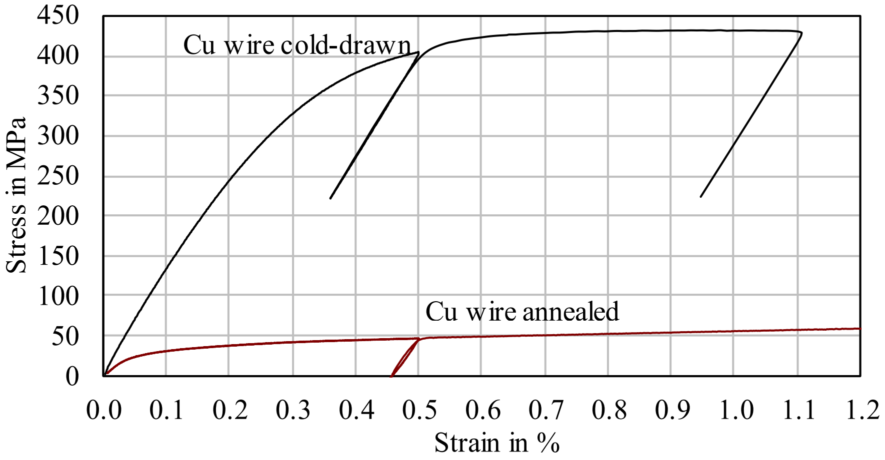

Figure 2.7.: Comparison of hard-drawn and annealed Cu wire stress–strain curves with unloading slopes for the determination of the elastic modulus [67].

In order to reduce the introduced errors with the linear fit of the measured data, the method of least squares can be used as suggested in ASTM-E111 [63]. Thereby the slope is defined from the maximum applied load in a decreasing stress range. When exceeding the yield strength of the materials, the sample strain ε in the loading phase of the stress–strain curve contains a plastic strain $\varepsilon_{\mathrm{pl}}$ and an elastic strain $\varepsilon_{\mathrm{el}}$. It is difficult to determine the elastic strain of a material with a low yield limit from the loading curve:

$$\varepsilon = \varepsilon_{\mathrm{el}} + \varepsilon_{\mathrm{pl}}, \tag{2.36}$$

whereas the elastic strain $\varepsilon_{\mathrm{el}}$ of the unloading slope can be determined with a low uncertainty as shown in Figure 2.8. Regardless of how much total strain a specimen experiences, the elastic strain is always recovered when the load is removed. The recovery (or "unload") curve is produced when the load is removed from a specimen. The amount of strain recovered during the unloading process is the elastic strain; the amount of strain that remains in the specimen after unloading is the plastic strain.

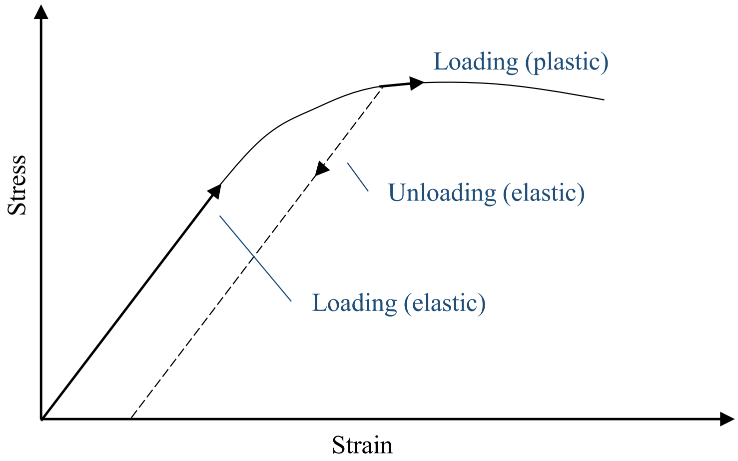

Figure 2.8.: Elastic plastic stress–strain curve [68].

Owing to the complex inner sample structure of a Rutherford cable stack, cubic samples were used instead of cylindrical samples as suggested in ASTM-E9 [62] for compressive tests. The cubic geometry also reduced the risk of sample buckling.

The following assumptions are made for the extensometer measurements in the axial compressive test [66].

- The surface strain is assumed to be similar to the internal strain.
- The stress is calculated by dividing the applied load by the cross-sectional area of the tested sample.
- The cross-sectional area is assumed to be constant over the gauge length.
- The stress is uniaxial and uniform in each cross-section along the gauge length.

2.5. Fundamental principles of Neutron scattering

Neutron diffraction measurements can be used to determine the elastic stress and strain state of complex multiphase materials by lattice crystal investigations. This method allows the stress–strain state inside a stressed material to be determined. The question of how much stress is seen by the different components of a strand inside a loaded superconducting coil may be answered by using this method.

2.5.1. Test apparatus and measurement method

The schematic layout of a standard two-axis instrument for strain measurement on a reactor neutron source is shown in Figure 2.9. The reactor facility is providing a white neutron beam that is monochromated by Bragg reflection to a specific wavelength λ from a single-crystal monochromator. The incident beam size is defined by a collimator or aperture. The neutron beam is scattered by the lattice planes on the sample and defined by a slit before the detector. The diffraction is caused by interference phenomena of the scattered beam. The intersection of incident beam and diffracted beam defines the gauge volume. The detector counts scattered neutrons through an diffraction angle 2θ. The neutron beam collimation system and detector need to be accurately positioned by about ±0.1 mm [69], in order to determine the strain by a diffraction angle shift.

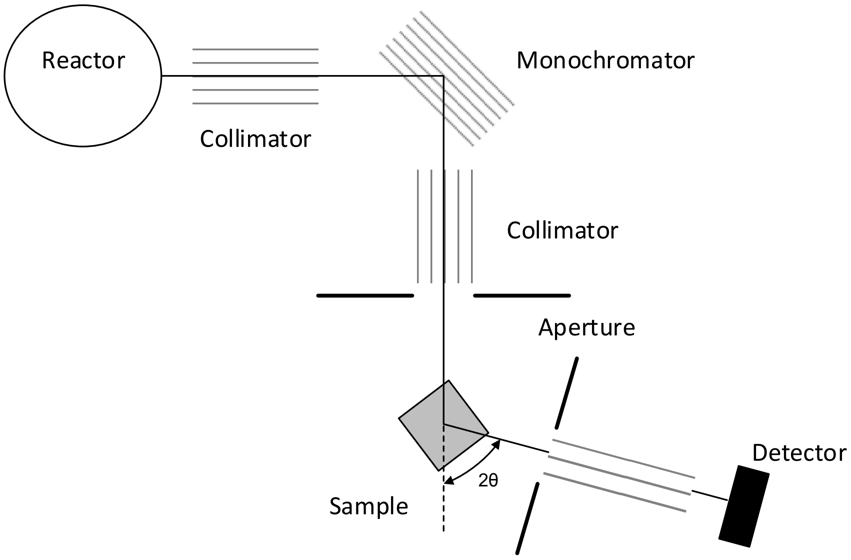

Figure 2.9.: Schematic layout for a two-axis instrument for strain measurements on a neutron source [70].

2.5.2. Lattice plane and Miller indices

A lattice plane in a crystallographic structure can be labelled with the so-called *hkl* Miller indices, specifying the lattice parameter of a lattice plane. The lattice spacing d_{hkl} of a cubic crystal can be calculated by the lattice constant a and the corresponding *hkl* indices to

$$d_{hkl} = \frac{a}{\sqrt{h^2 + k^2 + l^2}}. \tag{2.37}$$

For a known lattice constant a of a material [71], the diffraction angle 2θ observed under a wavelength λ can be allocated in the diffraction profile to a lattice plane. As the *hkl* indices increases, the detected lattice distance d_{hkl} decreases, as shown in Figure 2.10, with respect to the lattice spacing.

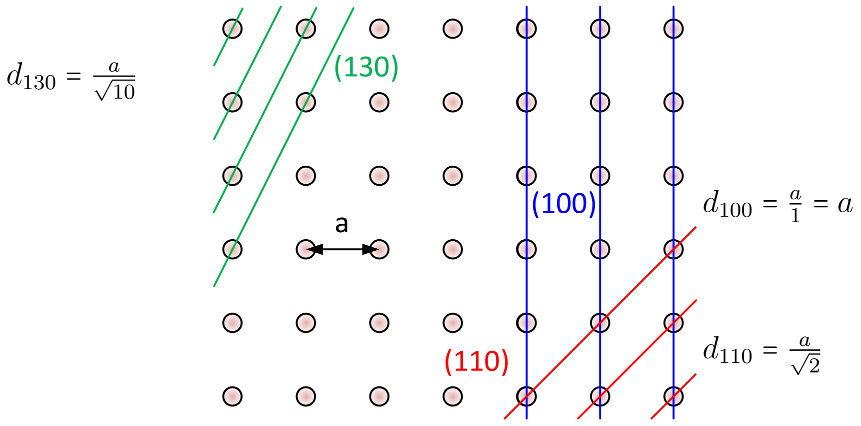

Figure 2.10.: Simplified lattice planes for the Miller indices h, k and $l = 0$.

The allocation in Equation (2.37) is valid for bcc structures such as Nb_3Sn and Nb as well as for face-centred cubic (fcc) structures as copper or aluminium. The characteristic lattice spacing for copper is summarised in Table 2.2, indicating the plane dependency of the lattice spacing. The lattice spacing is given in Ångström, which is a unit length equal to 10^{-10} m, that is one ten-billionth of a metre. Further, the diffraction intensity of each lattice plane is given, identifying favourable lattice planes.

Table 2.2.: Lattice parameter for fcc copper [71].

Miller indices hkl	Lattice spacing d (Å)	Intensity
111	2.08	7
100	1.798	6
110	1.271	5
311	1.083	6
331	0.826	4
210	0.806	3
211	0.735	3

Average unit cell $a = 3.597 \pm 0.004$ Å.

2.5.3. Bragg diffraction and interference

The diffraction of short wavelength x-ray beams by crystals was discovered in 1912 by Walther Friedrich, Paul Knipping and Max von Laue [72]. Bragg scattering or diffraction can be observed as interference phenomena on any set of lattice planes. The effect occurs if an integer multiple n of the wavelength λ of a provided beam (for example, a neutron beam) satisfies Bragg's law (Equation (2.38)) with respect to the lattice spacing d_{hkl} and scattering angle θ_{hkl}. The Bragg's law developed in 1912 by William and Lawrence Bragg [73]. The lattice spacing d_{hkl} of a crystallographic plane defines thereby the diffraction angle θ_{hkl}, indexed to a specific lattice plane, at which a diffraction occurs when a sample is illuminated by a beam with the wavelength λ to

$$n\lambda = 2d_{hkl}\sin\theta_{hkl}. \tag{2.38}$$

The geometric relation is shown schematically in Figure 2.11, visualising that interference can only be observed, if the beam path ($2d_{hkl}\sin\theta_{hkl}$) equals an integer multiple n of the wavelength λ.

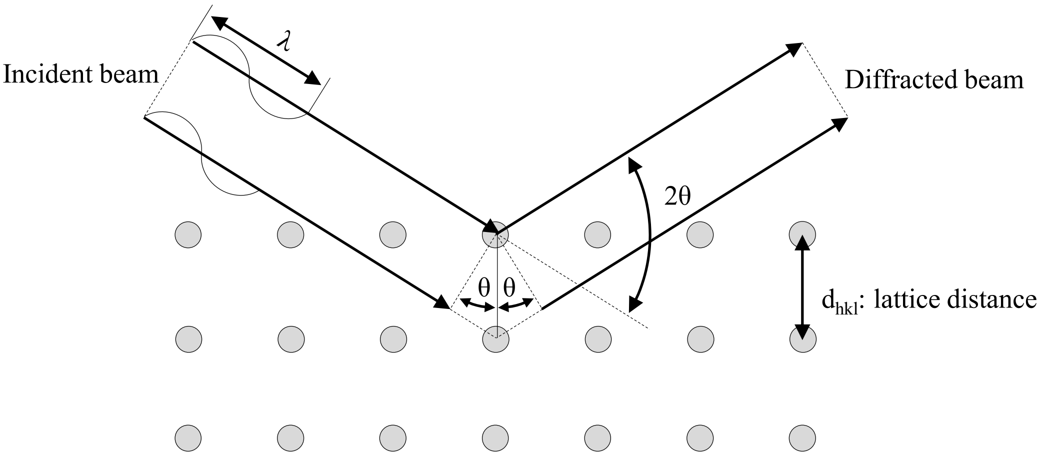

Figure 2.11.: Simplified sketch of Bragg scattering [74].

In a fixed-wavelength measurement, the incident monochromated beam is diffracted in the sample. The Bragg angles of specific lattice planes that fulfill the Bragg relation are determined by scanning over an angle range of a few degrees with a detector. A neutron diffraction peak pattern of a reference sample made out of Al7075 measured at the *Forschungs-Neutronenquelle Heinz Maier-Leibnitz* (FRM II) in a monochromated beam with a wavelength of 1.672 Å± 0.003, analysed with the software tool STeCa2 (StressTexCalculator) [75], is shown in Figure 2.12. This profile scan provides the following information with the 2θ diffraction angle on the abscissa and the number of neutron counts in the ordinate.

- Peak position: lattice stress/strain (lattice spacing changes from its stress-free state).

- Peak intensity: indicates the number of grains diffracting to a certain direction as well as the sensitivity of a plane to reflection.

- Peak shape: sub-grain structure (non-uniform diffraction related to micro-stress or defects).

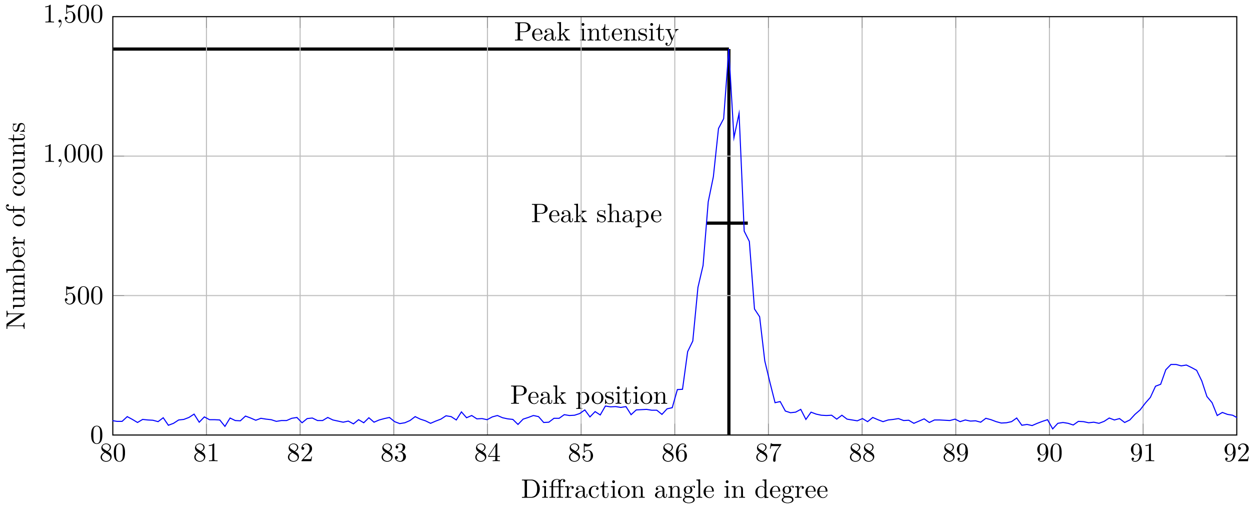

Figure 2.12.: Information in a diffraction pattern of AL7075, analysed with STECA2.

The diffraction peak profile includes information about the micro-structure and the stress state within a gauge volume. The position of a Bragg peak depends on the peak shape, diffracted spectrum and background. A single isolated peak is analysed from the measured peak pattern representing a grain family in the same orientation. It is common to perform the peak fitting with a Gaussian function. It is not recommended to analyse asymmetric or overlapping profiles, as they can indicate sample inhomogeneities, stacking faults or instrumental issues. Overlapping peaks can also be caused by multiphase materials: these can be analysed with double peak fitting strategies with the disadvantage of increasing the fit parameters and uncertainties. In order to select a reliable diffraction peak for the strain determination, the inter-granular anisotropy should be considered. The inter-granular anisotropy may affect the different strain response to the applied stress of individual crystallites or their sensitivity to inter-granular strain. In the elastic regime, the varying strain response is linear, therefore any lattice reflection can be chosen for stiffness determination. The stiffness in this occasion is not a single crystal stiffness, but a polycrystalline average. The plastic regime is indicated by a non-linear strain response to the applied stress. This non-linear strain response is a sign for a more anisotropic behaviour between the lattice planes and is unsuitable for the stiffness determination. For the stiffness and macro-scale stress determination, a reflection with small sensitivity to inter-granular strain is desired. The inter-granular strain is defined as the difference between the hkl determined diffraction strain and the strain determined by a specific elastic modulus. In order to achieve a good representation of the macroscopic stress field, it is recommended to choose lattice reflections that show a linear elastic strain response, which are less affected by inter-granular strains.

2.5.4. Diffraction-based strain calculation

The lattice strain ε_{hkl} determined by diffraction measurements can be calculated by the relation of the lattice distance d_{hkl} to the lattice distance of a stress-free sample of the material. The strain determination based on diffraction measurements determines thereby an average value over the gauge volume, in this thesis $5 \times 5 \times 5$ mm^3. In order to perform strain measurements by the diffraction method that represents the macroscopic material behaviour, a lattice *hkl* plane need to be selected which is not sensitive to inter-granular strain, showing a linear elastic behaviour. These planes give zero residual strain when completely unloaded. The strain direction, which can be determined with the diffraction experiment, is along the scattering vector, which bisects the angle between incident and diffracted beam perpendicular to the diffracting planes [69], as shown in Figure 2.11. The elastic lattice strain is determined by relating the measured lattice plane spacing to a stress-free reference value d^0_{hkl} in following the relation

$$\varepsilon_{hkl} = \frac{\Delta d_{hkl}}{d_{hkl}} = \frac{d_{hkl} - d^0_{hkl}}{d^0_{hkl}} = \frac{\sin\theta^0_{hkl}}{\sin\theta_{hkl}} - 1. \tag{2.39}$$

With the relation of the lattice distance to the diffraction angle θ under a constant wavelength under application of Bragg's law from Equation (2.38), the strain can be calculated directly with respect to the plane-related diffraction angle θ_{hkl} and the stress-free reflection θ^0_{hkl}.

Elastic regime

The lattice strain below the proportional (elastic) limit is in linear relation to the macroscopically applied stress. In this domain, any lattice reflection can be chosen for the lattice strain determination. The effects of elastic anisotropy need to be taken into account for the subsequent stress interpretation by using the correct diffraction elastic constants (DECs). The responses are linear as long as the sample has not undergone plastic deformation.

Inter-granular strain

Inter-granular strains are strain effects between grains. The origin of inter-granular strains are elastic anisotropy in elastic properties of single crystals and the plastic anisotropy if crystals do not deform homogeneously. Some grain families generate very little inter-granular strain when strained whereas others generate a more significant misfit. This misfit is due to the fact that some families of grain yield at low applied loads, whereas others are deforming only elastically. Load redistributions and non-linearities in the relation between applied stress and lattice strain [70] are thereby caused. The lattice planes are insensitive to plastic deformation, indicating a linear stress–strain response in the elastic and plastic regime. The effect of inter-granular stresses should be considered by the selection of a Bragg reflection to measure the lattice strain under uniaxial loading [70].

Plastic regime

Materials deform plastically or permanently, when the applied load exceeds the elastic limit. These effects can be observed in a diffraction experiment with a non-linear response of the determined lattice strain to the applied load. Thereby the change of the diffraction pattern can be influenced by slipped crystallites of some lattice planes, lattice reorientation or inter-granular stresses [70]. Owing to the elastic–plastic anisotropy, these effects occur at different applied stress levels for different oriented grains or lattice planes, which makes it difficult to determine exactly the initiation of plastic strain.

2.5.5. Diffraction-based stress calculation

In general, because of the tensor characteristic of stress, measurements are required in six independent orientations to completely determine the stress state at one point. However, when the principal directions are known, three orientations are sufficient to define the state of stress at a point. For the performed experiment in the neutron diffraction beam, the principal stress directions are known owing to the sample composition and the applied stress. With the determined strain data in three directions ($i = 1, 2, 3$), the macro-stresses can be calculated using Hooke's law.

The relation between the stress tensor $\boldsymbol{\sigma}$ and the strain tensor $\boldsymbol{\varepsilon}$ is defined by the stiffness matrix $\boldsymbol{C}$. The generalised Hooke's law gives the microscopic relation between the stress and strain tensor in the linear elastic regime

$$\sigma_{ij} = C_{ijkl}\varepsilon_{kl}. \tag{2.40}$$

The stress tensor $\boldsymbol{\sigma}$ can be calculated with the diffraction elastic constants (DECs) S_1, $\frac{1}{2}S_2$ [76] and the strain tensor $\boldsymbol{\varepsilon}$ and the strain tensor components ε_{kk} with respect to the Kronecker delta δ_{ij}

$$\sigma_{ij} = \frac{1}{\frac{1}{2}S_2}\left(\varepsilon_{ij} - \delta_{ij}\frac{S_1}{\frac{1}{2}S_2 + 3S_1}\varepsilon_{kk}\right). \tag{2.41}$$

The(DECs) S_1 and $\frac{1}{2}S_2$ are determining the relation between the plane-specific Young's modulus E_{hkl} and Poisson's ratio ν_{hkl}

$$S_1 = \frac{\nu_{hkl}}{E_{hkl}} \tag{2.42}$$

and

$$\frac{1}{2}S_2 = \frac{1 + \nu_{hkl}}{E_{hkl}}. \tag{2.43}$$

They can be used to determine the stress components σ_{ii} with respect to the elastic constants where $i = \mathrm{x}, \mathrm{y}, \mathrm{z}$ corresponds to the three orthogonal directions

$$\sigma_{ii} = \frac{E_{hkl}}{1 + \nu_{hkl}}\left[\varepsilon_{ii} + \frac{\nu_{hkl}}{1 - 2\nu_{hkl}}\left(\varepsilon_{\mathrm{xx}} + \varepsilon_{\mathrm{yy}} + \varepsilon_{\mathrm{zz}}\right)\right]. \tag{2.44}$$

There are different approaches existing to determine the DECs S_1 and S_2 from single-crystal values, which are summarised in Appendix B. The model suggested by Kröner in 1958 [77] is the most widely accepted approach in the community [70] to determine the DECs and is used in the following.

Self-consistent model of Kröner
The calculations of the elastic constants by Kröner in an explicit way for a cubic crystal structure that were used in the following can be found in [59] using the components of the stiffness matrix:

$$S_1^{\text{Kröner}} = S_1^B + 2S_2^B(u_1 + u_0\Gamma_{hkl}), \tag{2.45}$$

$$\frac{1}{2}S_2^{\text{Kröner}} = 2S_2^B(1 + 2u_2 + u_0(1 - 3\Gamma_{hkl})), \tag{2.46}$$

with

$$S_1^B = \frac{1}{3}\left(\frac{1}{C_0 + 3C_1 + 2C_2} - \frac{1}{2C_2^B}\right), \tag{2.47}$$

$$S_2^B = \frac{1}{4C_2^B}, \tag{2.48}$$

$$8(C_2^B)^3 + (9K + 4\gamma)(C_2^B)^2 - (3C_2(k + 4\gamma))C_2^B - 6C_2\gamma K = 0, \tag{2.49}$$

$$K = \frac{C_{11} + 2C_{12}}{3}, \tag{2.50}$$

$$\gamma = \frac{C_{11} - C_{12}}{2}, \tag{2.51}$$

where C_2^B is the positive root solution,

$$w_2 = \frac{5}{4}\left(\frac{C_0 + 3C_1 + 2C_2 + 4C_2^B}{C_0 + 3C_1 + 2C_2 + 6C_2^B}\right), \tag{2.52}$$

$$u_0 = \frac{-2C_0 w_2 C_2^B}{(C_2 - C_2^B)(C_0 + 2C_2 - 2C_2^B + 4w_2 C_2^B)}, \tag{2.53}$$

$$u_1 = \frac{C_0 + 2(C_2 - C_2^B)}{3(C_0 + 2(C_2 - C_2^B) + 4w_2 B_2^B)}, \tag{2.54}$$

$$u_2 = -\frac{(C_2 - C_2^B)}{2(C_2 - C_2^B + 2C_2^B w_2)}. \tag{2.55}$$

The single-crystal stiffness tensor coefficients are defined as $C_0 = C_{11} - C_{12} - 2C_{44}$, $C_1 = C_{12}$ and $C_2 = C_{44}$. For a cubic orthotropic crystal structure the stiffness matrix can be written as

$$C_{ij} = \begin{bmatrix} C_{11} & C_{12} & C_{13} & 0 & 0 & 0 \\ C_{21} & C_{22} & C_{23} & 0 & 0 & 0 \\ C_{31} & C_{32} & C_{33} & 0 & 0 & 0 \\ 0 & 0 & 0 & C_{44} & 0 & 0 \\ 0 & 0 & 0 & 0 & C_{55} & 0 \\ 0 & 0 & 0 & 0 & 0 & C_{66} \end{bmatrix} \tag{2.56}$$

with the symmetry conditions

$$C_{11} = C_{22} = C_{33}, C_{12} = C_{13} = C_{23} = C_{21} = C_{32} = C_{31}, C_{44} = C_{55} = C_{66}. \tag{2.57}$$

The elements of the stiffness matrix from copper and Nb_3Sn are summarized in Table 2.3. The elastic constants of Nb_3Sn (321) and Copper (220) based on the Kröner model [77] calculated by single crystal constants are summarized in Table 2.4.

Table 2.3.: Elastic constants for copper and Nb_3Sn single crystals.

	C_{11} (GPa)	C_{12} (GPa)	C_{44} (GPa)	Ref.
Nb_3Sn	253.8	112.4	39.57	[78]
Copper	168.4	121.4	75.4	[79]

Table 2.4.: Calculated elastic constants based on the Kröner model.

	E (GPa)	ν
Nb_3Sn (321)	131.2	0.363
Copper (220)	138.9	0.331

2.6. Fundamental principles of FEM

The finite element method (FEM) is a technique to numerically solve differential equations in a systematic and structured process.

> "*Finite element equations capture the characteristics of the field equations. Their derivation is based on either the governing differential equation or the global energy balance of the physical problem. The approach involving the governing differential equation is referred to as the method of weighted residuals or Galerkin's method. The approach utilizing the global energy balance is referred to as the variational method or Rayleigh-Ritz method.*"[9]

The governing equations involve physics, geometry and/or boundary conditions. In the finite element method, a given domain is treated as a collection of subdomains, and over each subdomain the governing equation is approximated by a variational method. In the domain of solid mechanics the governing equation are equilibrium equations, strain–displacement and stress–strains relations. The subdomains are defined by the discretization of a body by dividing it into an equivalent system of many smaller bodies or units (finite elements) interconnected at points common to two or more elements (nodes or nodal points) and/or boundary lines and/or surfaces. The behaviour of all elements is described by a system of equations with a stiffness matrix $[K]$, describing the property (stiffness and geometry) a displacement vector $\{u\}$, describing the behaviour and a force vector $\{F\}$, describing an resulting action

$$\left[K\right]\{u\} = \{F\}. \tag{2.58}$$

Many physical phenomena exhibit a non-linear behaviour where the linear approximation of a behaviour is not sufficient to provide satisfactory results. A non-linear structural behaviour may arise because of geometric and material non-linearities, or due to changes in the boundary conditions and structural integrity. The material non-linearity owing to plasticity (a permanent, time-independent deformation) is discussed briefly in the following. Further material non-linearities can be caused by creep, non-linear elasticity, visco-elasticity or hyper-elasticity. Examples to model and calculate non-linearities are given in [80].

A solid mechanical analysis of impregnated cable stacks as material compounds out of fibreglass, epoxy and Nb_3Sn, which by itself is a metal compound consisting of heat-annealed copper and Nb_3Sn filaments is profromed up stress levels of 200 MPa. The stress–strain state calculation of the components requires surface elements for two dimensional and solid elements for three dimensional calculations. The strand curvature and surface has to be well approximated, including the different material phases in a strand in order to study the stress–strain state of all components in a wire. Owing to the low yield strength of the single components such as annealed copper of about 50 MPa [67] or CTD-101K of about 70 MPa [81], the model has to be capable to calculate the stress–strain behaviour beyond the yield strength, whereas also the impact of the bonding between strand and epoxy resin has to be included.

Material modelling

The material model generation for elastic–plastic behaviour starts with a decomposition of the total strain ε into elastic ε_{el} and plastic ε_{pl} components as shown in Figure 2.13, identifying the reversible and irreversible strain components once exposed to a stress level A. The proportional limit identifies the stress–strain range where as the linear elastic behaviour according Hook law is valid. The yield strength σ_y is a stress level beyond the elastic limit, whereas a residual plastic strain of typically 0.2% remains after unloading. This yield criteria is defined for ductile materials where a proportional limit can not be easily defined.

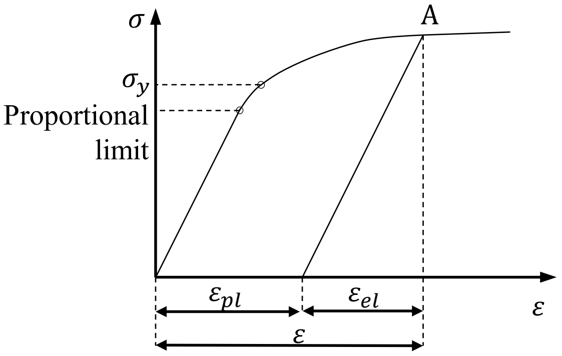

Figure 2.13.: Stress–strain curve for a ductile elastic–plastic material [82].

The essential characteristics of the plastic constitutive models are: the *yield criterion*, which defines the material state at the transition from elastic to elastic–plastic behaviour; the *flow rule*, which determines the increment in plastic strain from the increment in load; the *hardening rule*, which gives the evolution in the yield criterion during plastic deformation.

The *yield criterion* is used to relate the calculated multiaxial stress state to the uniaxial elaborated test case. Thereby a scalar value of the stress state can be compared with the uniaxial case. The von Mises yield criterion is used as an approximation of the metal and polymer components of the sample. In principal stress space, the yield surface is a cylinder with the axis along the hydrostatic line and gives a yield criterion that is independent of the hydrostatic stress. Furthermore, the Hill yield criterion [83] should be mentioned, which is an anisotropic criterion that depends on the orientation of the stress relative to the axis of anisotropy. It can be used to model materials in which the micro-structure affects the macroscopic behaviour of the material such as forged metals and composites.

The *flow rule* defines the evolution of plastic strain. Depending on the level of detail of the approximation, the stress–strain materials data can be represented by a bilinear or multilinear curve.

The *hardening rule* describes the changes of the yield surface owing to plastic deformation. Thereby, the behaviour beyond the yielding is defined. This is in contrast to elastic ideal plastic materials, which exhibit no hardening and the yield surface remains fixed. There are two basic hardening rules to describe the change of the yield surface. An *isotropic hardening* describes the increase of the yield strength in all directions by an increase of the yield surface as shown in Figure 2.14. The *kinematic hardening* model describes a translation of the yield surface. Thereby, for example, the yield strength in compression is decreased in proportion to the increase in the yield strength in tension. Most metals exhibit kinematic hardening behaviour for small strain cyclic loading.

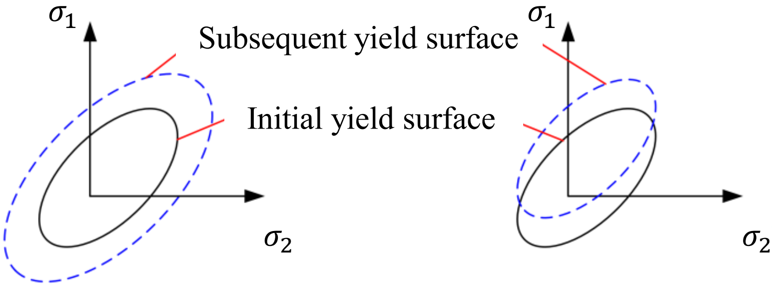

Figure 2.14.: Yield surface changes in isotropic hardening (*left*) and kinematic hardening (*right*) [82].

Element types for 2D and 3D analysis

The element type used in an FEM model defines the quality of the shape approximation and the implemented physical equations which can be addressed. The commonly used element types for structural calculations are linear or quadratic elements as shown in Figure 2.15. A linear element has only corner nodes, whereas a quadratic element also has mid-side nodes, which represents curved edges and surfaces more accurately as a linear element. Results may be achieved with fewer elements by using quadratic elements.

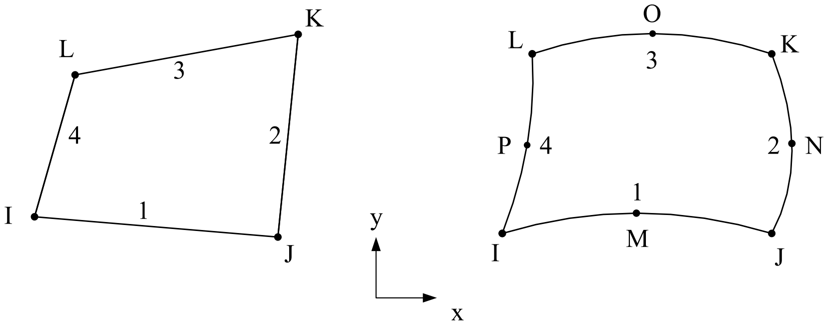

Figure 2.15.: Simplified linear (*left*) and quadratic (*right*) elements [82].

ANSYS® provides the *PLANE182* element with four nodes and the higher-order *PLANE183* element with six or eight nodes for 2D calculations. Both element types define two degrees of freedom at each node and can describe plasticity, hyper-elasticity, stress stiffening, large deflection and large strain capabilities [82].

The 3D modelling elements that are well suited to model irregular meshes are the *SOLID186* element with 20 nodes, forming a cubic structural solid or the *SOLID187* element with 10 nodes forming a tetrahedral structural solid. Both elements describe three degrees of freedom per node have the capability to describe plasticity, hyper-elasticity, creep, stress stiffening, large deflection and large strain capabilities [82].

Contact formulation

A variety of contact formulations are existing, to treat cases of changing mechanical contact between the parts of an assembly or between different faces of a single part. These elements range from simple, limited idealisations to complex and sophisticated, general-purpose algorithms. In a typical ANSYS® contact analysis, the model is first meshed with conventional elements (beam, plane or solid), and then the contact elements are created along the potential contact regions. An introduction about contact mechanics is given in [84].

ANSYS® provides two different contact elements for 2D structural calculations. Depending on the type of elements used, the contact is described by the *CONTA171* (for linear elements) or by the element *CONTA172* (for quadratic elements). The 2D contact surface elements are associated with the 2D target segment elements (*TARGE169*). The pure penalty property for contact between two rigid bodies and the augmented Lagrange property for all other contact situations is usually selected [82].

The *CONTA174* contact element is associated with the 3D target segment elements (*TARGE170*). In studying the contact between two bodies, the surface of one body is conventionally taken as a contact surface and the surface of the other body as a target surface. For rigid–flexible contact, the contact surface is associated with the deformable body and the target surface must be the rigid surface. For flexible–flexible contact, both contact and target surfaces are associated with deformable bodies. The contact and target surfaces constitute a contact pair. Hence, a target is simply a geometric entity in space that senses and responds when one or more contact elements move into a target segment element[82].

Vector principals

The orientation analysis of the principal stress and strain vectors in each node can be used to identify the orientation of the princiapl axis with respect to the global coordinate system. An angle sequence required to produce a coordinate system whose x-, y- and z-axis are the directions of maximum, middle and minimum principal stress and strain vectors can be stored in ANSYS. The angle sequence is the rotation normal to the x–y plane, normal to the y–z plane and normal to the z–x plane [82] and orients the principal coordinate system relative to the global system, which indicates that the rotation is not described by the *proper* or *classic* Euler angles, even though it is called Euler rotation [82]. The stored angles indicate the formalism of a Tait–Bryan rotation or also called cardan rotation in the German literature. Thereby, the intrinsic rotations apply to axes in the rotated coordinate system, for instance as shown in Figure 2.16, where the rotation around the z-axis, x'-axis and the y''-axis is visualised. This rotation sequence is identical to that defined in ANSYS® for the principal stress and strain vector.

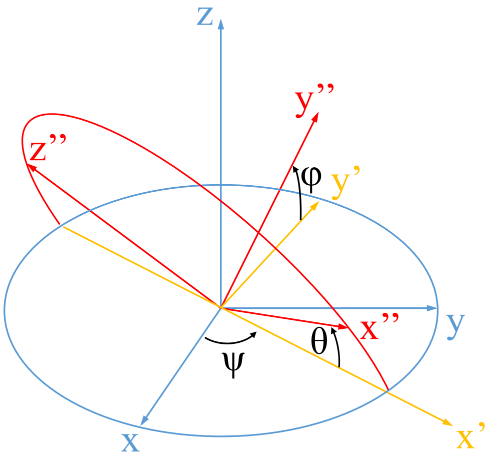

Figure 2.16.: Tait–Bryan angles for a ψ, φ and θ rotation sequence.

3. Homogeneous transversal compression of Nb_3Sn Rutherford cables

At CERN, the critical current (I_c) measurements of cables are carried out in FRESCA (Facility for the REception of Superconducting CAbles) [85], realised around 1999 for critical current acceptance of Nb–Ti cables during LHC production. In FRESCA, the current-carrying capability of a cable up to 32 kA can be tested in a magnetic background field up to 9.6 T at a temperature down to 1.9 K. The test station provides a free bore of 72 mm, called the aperture, to host the 2 m long cable samples. The test facility is used today also for the characterisation of Nb_3Sn cables. A new cable test facility is planed with the FRESCA2 superconducting magnet [14], to be commissioned in 2021. This high-field Nb_3Sn dipole magnet is designed to provide a magnetic field of 13 T in a free aperture of 100 mm, enabling tests of cables and HTS inserts in a large background field.

In order to investigate the transversal compressive stress limit of the Nb_3Sn conductor at room temperature, the standard FRESCA sample, consisting of an impregnated Nb_3Sn Rutherford cable double stack, needs to be exposed to a pressure at room temperature. The stress is then released and subsequently measured in FRESCA to test the I_c performance. The sample conditions and dimensions were defined by the FRESCA test station as sample length, stack scheme, insulation layout, impregnation system, voltage tab position and preferential press location in the high-field region of the sample. An adapted structure was used to carefully handle the sample during pressure application and transport, as the bending-induced strain should be lower than 0.5 mm/m [3].

3.1. Superconducting cable test stations

To the best of the author's knowledge, so far the only investigation of the critical current degradation of an impregnated Nb_3Sn conductor under transversal pressure at room temperature was performed in 1989 [86]. Thereby, only one multifilamentary Nb_3Sn strand of a cable compound was tested. The strand was based on the bronze route process. The bronze route technology is very different in the filament and strand design to the nowadays used RRP for strand manufacturing (see section 1.4). The test in 1989 was performed under a transversal pressure that was set at ambient temperature and kept constant during cool down to cryogenic temperature. Other test programs were performed with the maximum stress applied at cold to study the I_c performance under applied load. Test on Rutherford cables were perfromed at CERN, Switzerland [87], Twente University, The Netherlands [88] or at the National High Magnetic Field Laboratory, Florida, USA [89], [90]. The investigation of stress applied at room temperature is crucial in order to represent the magnet assembly process, as the material properties of the conductor constitutions are dependent on the temperature, for example the stiffness of the impregnation system CTD-101K increases by a factor of 1.6 during cool down to 77 K [81]. In the following section, the sample, experimental procedure and equipment are explained in detail. Detailed results of the I_c degradation measurements can be found in the literature [60].

3.2. The FRESCA test facility and specific sample holder

The sample, used for the mechanical compressive limit investigation need to be compatible with the FRESCA test facility for subsequent critical current investigations. The test station consists out of a 1.7 m long dipole magnet with a free aperture of 88 mm designed to be used as a background magnet with a maximum central field of 10 T and homogeneous field region 600 mm to perform measurements at 1.9 K [85]. The sample holder consists out of two L-shaped G10 parts, housing the impregnated cable stack, supported by a top and bottom steel bar [91]. A conceptual sketch of the FRESCA sample holder is shown in Figure 3.1. The 1.7 m long impregnated cable is clamped between two G10 parts that support the cable and insulate it electrically. The free space between cable and G10 is used for the instrumentation cabling of the voltage tabs. The parts are fixed between two 316LN stainless steel bars. The total length of the FRESCA sample holder is 2.27 m.

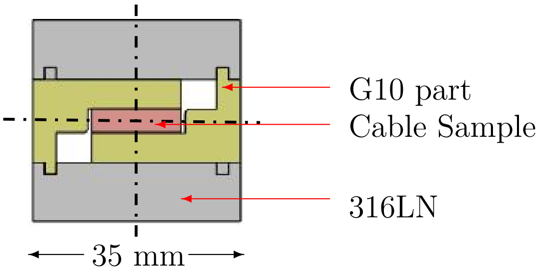

Figure 3.1.: Schematic sketch of the FRESCA sample holder.

3.3. The sample description

The first FRESCA sample

The tested sample is a 1.8 m long impregnated double stack manufactured at CERN. The used cable is similar to the 11 T CERN dipole magnet cable [92] with a width of at least 15.6 mm. The sample is designed with a central voltage tab free length of 80 mm. This voltage tab free length was used to apply pressure to the stack in the compressive test set-up. Both cables in the stack were current-carrying cables, powered in opposite direction. The cables were stacked in a way so that the keystone angles cancel each other out and generate a parallel surface. The schematic of the first sample is shown in Figure 3.2 and in the microscopic picture in Figure 3.3. Each cable is insulated with a S2-glass sleeve (0.15 mm thick) and the two-cable stack was wrapped with S2-glass tape (0.1 mm thick) and heat treated, following the 11 T dipole heat treatment cycle and vacuum impregnated with CTD-101K. No ceramic binder and no subsequent curing cycle was applied. The used fibre sleeve and tape were heat treated for 8 hours at 350°C to clean the fibres of organic residuals. The bare cable has a mid-thickness of 1.25 mm, a width of 14.7 mm and a keystoning angle of 0.79°. The Rutherford cable was made out of 40 Nb$_3$Sn 144/169 strands produced by the RRP from OST with a Cu/NCu of 1.08, and an unreacted strand diameter of 0.7 mm, transposition pitch length of 100 mm and a Residual Resistance Ratio (RRR) of 172. The impregnated double stack thickness profile variation was measured to be ± 50 µm. The sample specifications are listed in Table 3.1.

Table 3.1.: First cable stack specification.

Specification	Value
Cable	
Strand	RRP 144/169
Strand diameter	0.7 mm
Strand number	40
Keystone angle	0.79 deg
Stainless steel core (316L)	25 µm × 12 mm
Width (bare cable)	14.7 mm
Thickness (bare cable)	1.25 mm
Insulation	
S2-glass fibre sleeve	0.15 mm (without mica)
S2-glass tape wrap around the stack	0.1 mm
Impregnation	CTD-101K

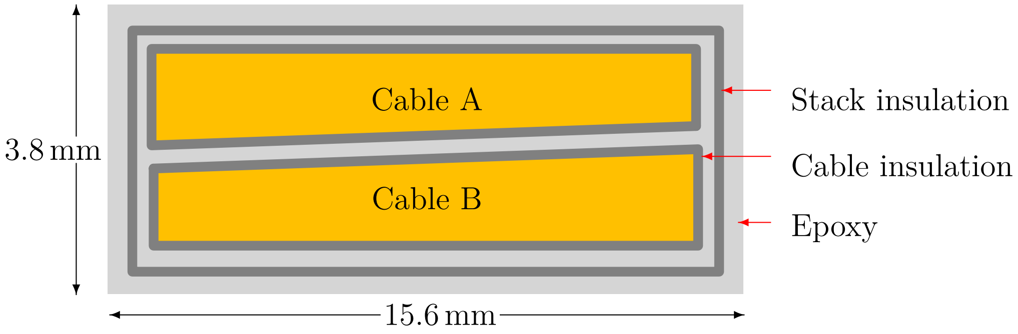

Figure 3.2.: The layout of the two stack cross-section.

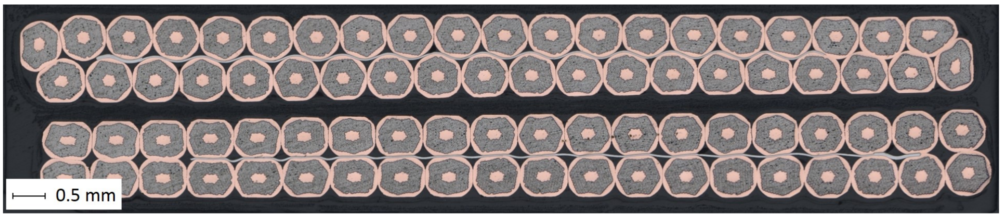

Figure 3.3.: Microscopy of the cable cross-section of the first sample stack.

A 35 cm impregnated two-cable stack sample, which was manufactured with the same procedure and using the same tooling, was used to adjust the tooling and evaluate the stress distribution for the foreseen cable study under transversal load. The thickness profile of the cable sample was measured over the sample length at three locations (top, centre and bottom), shown in Figure 3.4 at a distance of 5 mm to determine the cable geometry. Therefore, a high-resolution measuring unit Mitutoyo Litematic [93] with a resolution of 1 µm and a measuring force of 0.01 N at the contact point (carbide ball) was used, allowing the sample thickness to be determined with an accuracy of 0.5 µm. The measurement indicates a geometric variation of the sample height of about ±50 µm, as visualised in Figure 3.5. A compensation of the determined geometric variation must be taken into account for the cable compression test. In order to adapt to the geometric variation, an additional material layer between the tool and sample was needed, that was soft enough to adapt to the geometric variation and with a high enough yield point to keep integrity at loads up to 200 MPa.

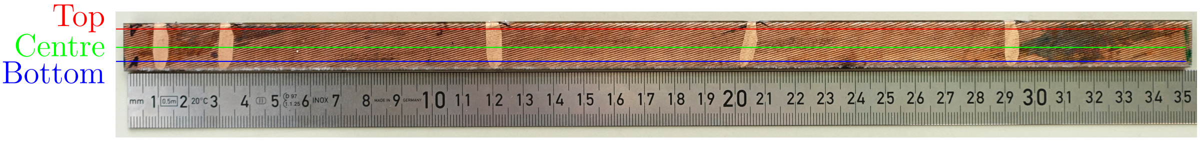

Figure 3.4.: Cable sample for thickness measurement.

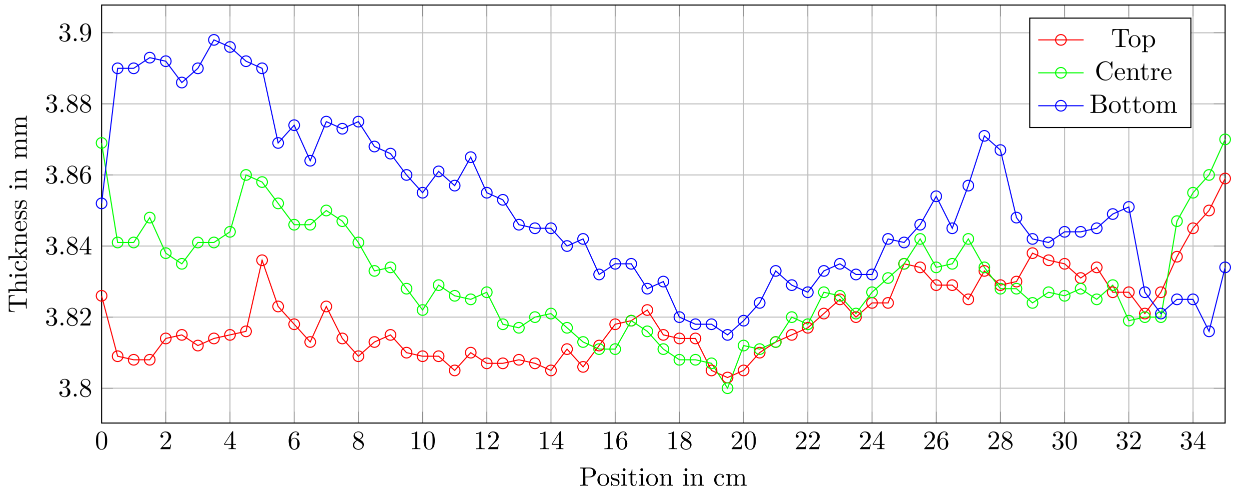

Figure 3.5.: Thickness profile of the cable.

The second FRESCA sample

Next, a cable with the properties described in Table 3.1, the 11 T standard cable, was tested with parameters summarised in Table 3.2. This cable changes during the magnet manufacturing process of the 11 T dipole prototypes. In addition, the fibreglass insulation was reinforced with a layer of 0.08 mm mica tape, building a free gap of 6.9 mm on the cable surface as shown in Figure 3.6. The cable was made of a different strand type, 40 high-performance strands 108/127 RRP[6] from OST with a strand diameter of 0.7 mm. All cable components are shown in Figure 3.7, which are extracted from a cured and reacted cable stack.

---

[6] 108/127 RRP: Restacked Rod Process with 108 Nb_3Sn sub-elements, with a total of 128 sub-elements adding the copper elements forming the core of the strand.

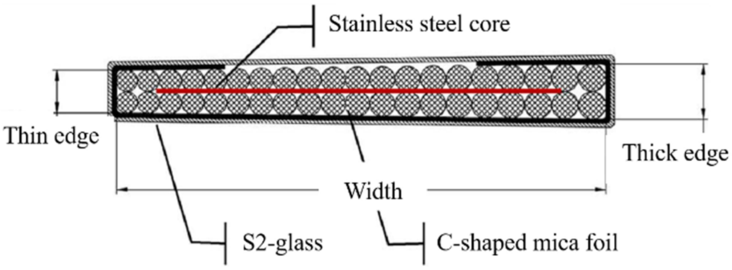

Figure 3.6.: Cross-section of a 11 T insulated cable.: in dark black, the mica foil [94].

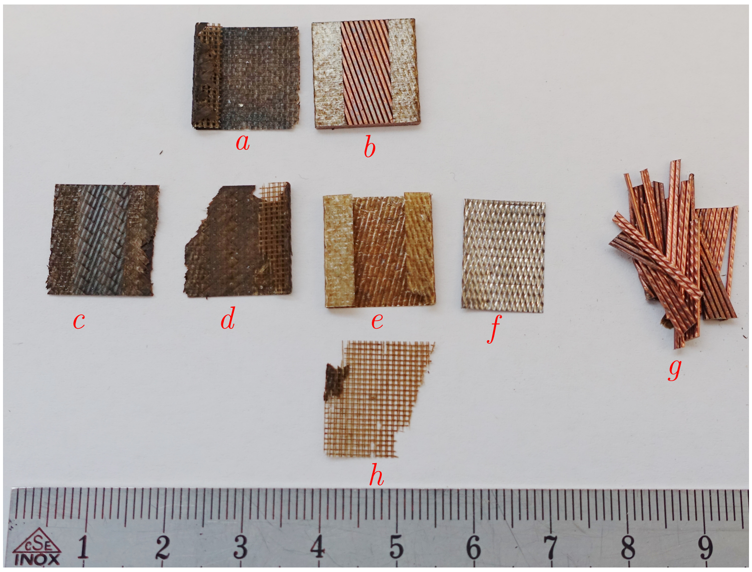

Figure 3.7.: Photograph of the extracted components identical to the second cable showing: (a), burned fibreglass; (b), cable segment with c-shaped mica; (c, d), burned fibreglass; (e), c-shaped mica; (f), stainless steel core; (g), reacted strands; and (h), fibreglass carrying grid of the mica.

Table 3.2.: Second cable stack specification.

Specification	Value
Cable	
Coil	CR07
Strand	RRP 108/127
Strand diameter	0.7 mm
Strand number	40
Keystone angle	0.79 deg
Stainless steel core (316L)	25 µm × 12 mm
Width (bare cable)	14.7 mm
Thickness (bare cable)	1.25 mm
Insulation	
Mica layer thickness	0.08 mm
Mica width	25 mm
Mica gap	6.9 mm
S2-glass fibre braiding	0.075 mm
Impregnation	CTD-101K

3.4. Experimental procedure

The experimental test routine after having prepared the sample is as follows:

1. transport the sample from the FRESCA test facility in building 163 where the virgin I_c characterisation was performed to the polyimide lab in building 180 (tensile stress $\ll 50\,\mathrm{MPa}$);
2. extract it from the FRESCA sample holder (1800 mm flat straight cable);
3. insert the cable into pressing tool and perform the press cycle;
4. re-fit the cable in the FRESCA sample holder;
5. transport the sample to the FRESCA test facility in building 163 (tensile stress $\ll 50\,\mathrm{MPa}$);
6. perform the critical current measurement in FRESCA;
7. repeat from step (1).

The cable needs to be carefully removed from the FRESCA sample holder to apply a compressive load considering the risk of damaging the sample during sample handling by bending. Therefore, a dedicated sample holder was manufactured, machined out of a 2000 mm flat straight edge (accuracy class 2) fulfilling requirements for good flatness and surface parallelism with a surface parallelism tolerance below 120 µm, a flatness tolerance below 60 µm and average surface roughness less than 1.2 µm, including alignment pins for sample positioning on the sample holder. In order to avoid sample bending by unsupported movements, the top part of the FRESCA sample holder was replaced by the sample holder foreseen for the pressure application. The so-clamped sample was shifted between the sample holders by a rotation of 180° around the longitudinal sample axis. Afterwards, the remaining part of the FRESCA sample holder could be removed without any risk of damaging the sample. In order to apply transversal stress on an impregnated Rutherford cable with a homogeneous stress distribution a dedicated tool was designed and manufactured and furthermore procedure to precisely measure the applied stress distribution was established, as explained in detail in Sections 3.5 and 3.8. To be representative for pre-load of a coil during magnet assembly, the load was applied at room temperature and kept constant for 2 min. The load was applied on the sample location on the test sample at stress values of 50, 100, 125, 150, 175 and 200 MPa. The subsequent FRESCA test requires the following restrictions on the sample preparation.

- The standard FRESCA sample design must be used (2 m long double cable stack).
- The superconducting cable must be protected against bending during sample transport.
- The transversal stress must be applied in the central high-field region.
- The applied load must not extend the central voltage tap free location of the sample (80 mm).
- The stress distribution must be as homogeneous/uniform as possible.

3.5. Review of existing contact pressure measurement system

A measurement technique needed to be defined in order to identify and improve the stress distribution between the contact surfaces of the used pressing tool and the sample. Several candidates for a contact surface stress measurement system have been investigated in order to select a robust and easily applicable system for the test scenario. The available systems can be categorised into two groups of systems, pressure-sensitive film-based systems and electrical pressure-mapping systems. An overview of film-based systems is given in Table 3.3. Most of the film-based systems work similarly to the Fuji Prescale system with colourising micro-capsules. There are two systems provided by PressureX that are based on a different principle, for a measurement range below 20 MPa.

Different post-processing software products are available, all of which are based on the interpretation of the colour values into pressure values. Few electrical pressure-mapping systems are available on the commercial market, as summarised in Table 3.4.

Table 3.3.: Overview of pressure-sensitive film-based systems.

Films	Measurement range	Post-processing system
Fuji Prescale [95]	0 MPa to 300 MPa	Fuji Analysis
EZ-Nip paper [96]	0 MPa to 7 MPa	Shoe Press Profile
Mold Align [96]	7 MPa to 41 MPa	Topaq Analysis System
PressureX-Micro Green [96]	0.05 MPa to 12.4 MPa	Point scan
PressureX-Micro [96]	0 MPa to 0.14 MPa	Auto-Nis
Surface Profiler Film [96]	0.1 MPa to 10 MPa	

Table 3.4.: Overview of electrical pressure mapping systems

System	Measurement range	Function
TekScan [97]	0 MPa to 200 MPa	Piezo-resistive
Tactylus [96]	0 MPa to 2.7 MPa	Piezo-resistive
Tactary [96]	0 MPa to 5 MPa	Capacitive
Sigma-Nip [96]	0.3 MPa to 70 MPa	Thin-film resistor

After a review of the existing commercial systems for the required stress domain of above 200 MPa, a pressure-sensitive film was chosen, as it is, to the best of the author's knowledge, the only existing system that can measure a contact stress above 200 MPa. These so-called Prescale films [98] colourise, where the density of the red colour at a given location can be correlated to the maximum amplitude of the applied pressure. The three different mono-sheet type Prescale films applicable for different pressure ranges are: MS Type (10 MPa to 50 MPa), HS Type (50 MPa to 130 MPa) and HHS Type (130 MPa to 300 MPa). Prescale films for low pressure applications are existing as well, cositing out of two measurement sheets. The spatial resolution is in the order of 0.1 mm. The pressure resolution is, depending on the type of Prescale film, between less than 2.5 MPa (up to 180 MPa) and less than 10 MPa (from 180 to 300 MPa). To analyse the pressure distribution, the Prescale films were scanned and the digital images were analysed with a dedicated, self-developed software [99]. Each pixel i is associated with a colour density level cd_i to a pressure value σ_i via a calibration function $f(cd_i)$. A calibration function is defined for each type of Prescale film. By then multiplying these stress levels by their pixel area A_p and summing them over the entire area covered by $i = 1 \ldots n$ pixels, the total force F_PS was calculated and compared with the total force of the four load cells F_LC:

$$F_\mathrm{PS} = \sum_{i=1}^{n} f(cd_i) \cdot A_p \approx F_\mathrm{LC} = \sum_{i=1}^{4} F_{\mathrm{LC_i}}. \tag{3.1}$$

Deep and very light red colour density values indicate stresses outside the measurement range of a Prescale film type. A Prescale film type with a higher or lower stress range is investigated, once the majority of the measured area is outside the stress domain of the corresponding Prescale film type. The colourized areas outside the stress domain are interpreted as zero value, to avoid a double interpretation of stresses once different Prescale film types are used in an assembly. In the measurements, the force F_PS was within 10% of the total force measured with the load cells F_LC; therefore, the overall error made by this assumption was considered acceptable. To increase the range of measurement, up to three differently ranged Prescale films were stacked, allowing a measurement range of 10 MPa to 300 MPa.

Several limitations of the film-based system were identified during the validation process of the system and the corresponding MATLAB code. There are limitations linked to the Prescale film itself such as the resolution variation, in particular for high-pressure films and the incompatibility against shear stress. Furthermore, the measurement methods include limitations that need to be considered during application. The pressure indicator is placed directly in the load train, which effects the stiffness of the assembly. A further limitation is that the system is only capable of measuring the maximal pressure during the process as a non-continuous stress indication. A disassembly and reassembly is always required in order to be able to analyse the results, which have to be within the pressure domain.

3.6. Compressive test station

A hydraulic press was selected and modified enabling a uniform well-defined compressive stress up to 200 MPa on the sample surface. The existing system was equipped with a force measurement system and a top and bottom plate, designed to exchange the press tools. The hydraulic circuit was adjusted in order to apply a controlled pressure ramp and pressure plateau. The pressing tools were aligned with stainless steel shims with respect to the load cells [100] balanced to ±5 µm and 0.125 mrad. The test station including all components is shown in Figure 3.8. It consists of a hydraulic pump with a maximum pressure of 146 bar. The hydraulic pressure is controlled by an electrical control system GEFRAN GF-Promer [101]. The reactive force of the hydraulic piston, controlled by a proportional valve, generates a maximum force of 180 kN. The test set-up was enhanced by a support structure consisting of a roller table on either side of the press to support the 2 m long sample during the test.

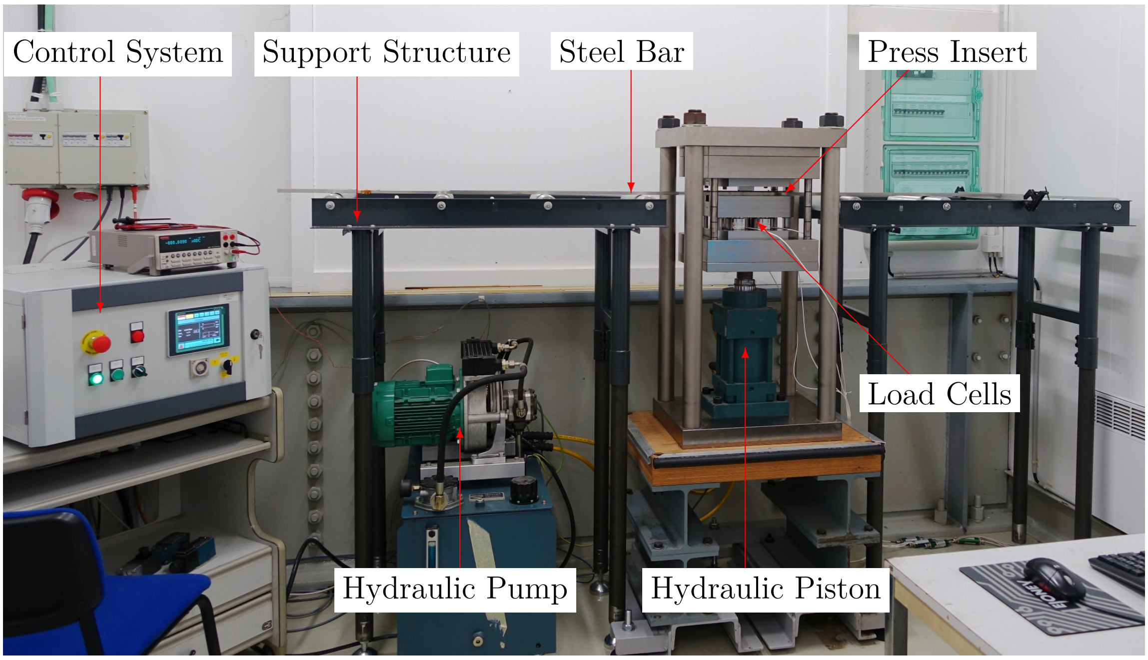

Figure 3.8.: The test set-up.

A press insert designed for arbitrary press tools is shown in Figure 3.9. The top tool holder is fixed to the structure. The bottom plate that carries the load cells and the bottom tool holder are lifted by the hydraulic piston. The bottom tool holder is free to move in the vertical direction, guided by rods in bronze slide bearings. The system was equipped with a force measurement system and a top and bottom plate, designed to exchange the press tools. In this work, a suitable press tool and a sample holder were designed.

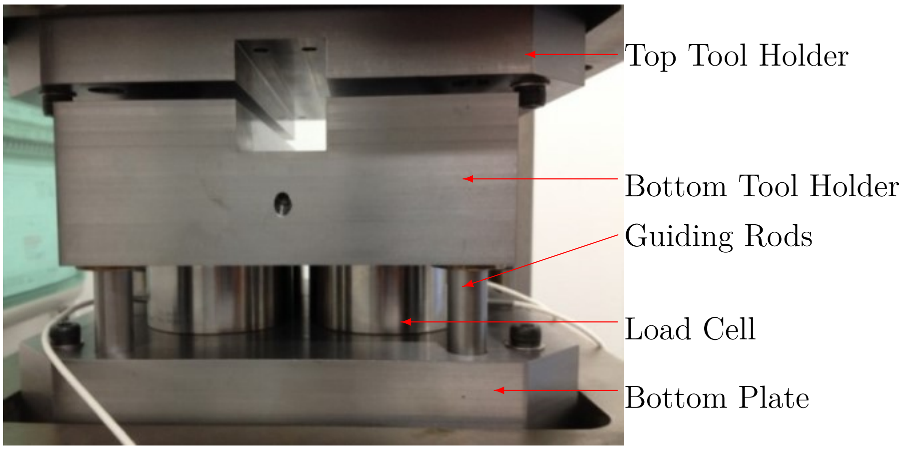

Figure 3.9.: The press insert.

Four load cells are used for the measurement achieving a symmetric stiffness of the structure (lengthwise and crosswise) with a balanced load distribution. The load cells type Burster 8526 [102] are separately connected with a USB sensor interface for strain gauges to a laboratory computer. The load cells and the USB sensor interface were delivered with a calibration certificate by the manufacturer [103, 100]. The data acquisition of the calibrated load cells was performed with the corresponding measurement software Digivison [104] and further processed in MATLAB. The specifications of the force measurement system are summarised in Table 3.5.

Table 3.5.: Load cell specification Burster type 8526 [100].

Specification	Value
Measurement range	0 kN to 200 kN
Accuracy	≤ ± 0.5 %
Sensitivity	1.0010 mV/V
Frequency	100 Hz
Year of last calibration	2016

3.7. Validation of the pressure-sensitive films

The validation of the developed analysis software was performed subsequently on the designed and manufactured set-up. Therefore, the pressure-sensitive film was placed between two hardened stainless steel pressing tools within the load line of the load cells.

A stainless steel stamp with a pressing area of 44 mm × 17 mm was pressed on a flat steel bar, both components were manufactured with high surface quality. A compressive force was applied with a hydraulic piston in a range from 0 to 180 kN with a step size of 3.5 kN. Three layers of mono-sheet pressure-sensitive films (“MS”, “HS” and “HHS”) were used as a stack between the pressing tools for each load level. The load was applied for a duration of ~2 min for each press cycle. The temperature was 25.9°C and the humidity was 29.1 % during the test.

A comparison of the force measured by the load cells F_{LC} and the integrated force F_{PS} obtained by using the Prescale film with respect to the relative analysable area A_{relative} is shown in Figure 3.10. The ratio A_{relative} is the quotient of the area within the pressure range A_{Domain} (all areas with pressure values in the domain, e.g. 10 MPa to 50 MPa for the MS type) and the total pressed area A_{Press} (defined by the press tools). This ratio defines the part of elements that are used for the contact pressure analysis

$$A_{\mathrm{relative}} = A_{\mathrm{Domain}}/A_{\mathrm{Press}}. \tag{3.2}$$

The investigated contact pressure between 10 MPa to 240 MPa is plotted in three sections in Figure 3.10 regarding the measurement ranges of the three different types of Prescale film. The dashed lines in the plot indicating a band of ±10 % of the load cell value. The Prescale film types MS (Figure 3.10(a)) and HS (Figure 3.10(b)) indicated good consistence between the load cell measurement (solid black line) and the force calculated by the integrated pressure values (red dots), if the relative domain area is above 80 %. The calculated force is in an error range of about ±10 %. The deviation between F_{LC} and F_{PS} of the HHS Prescale film type, with respect to the A_{relative} value, is higher.

The increased error of the HHS Prescale film type at high pressure values is driven by the reduced pressure resolution. The force comparison in Figure 3.10(c) indicates that the relative domain area needs to be about 90 % to be able to determine the integrated fore within an error range of ±10 % for the HHS Prescale film type.

To calculate the relative domain area, the pressed area must be known. This study shows that the sum of different forces from different film types calculated by integration should only be considered if the relative domain area is lower than 80 %. In case more than one

Prescale film paper is used, the relative domain areas of different Prescale film papers should be checked and only one value should be considered, to avoid the doubling of forces.

(*a*) MS type

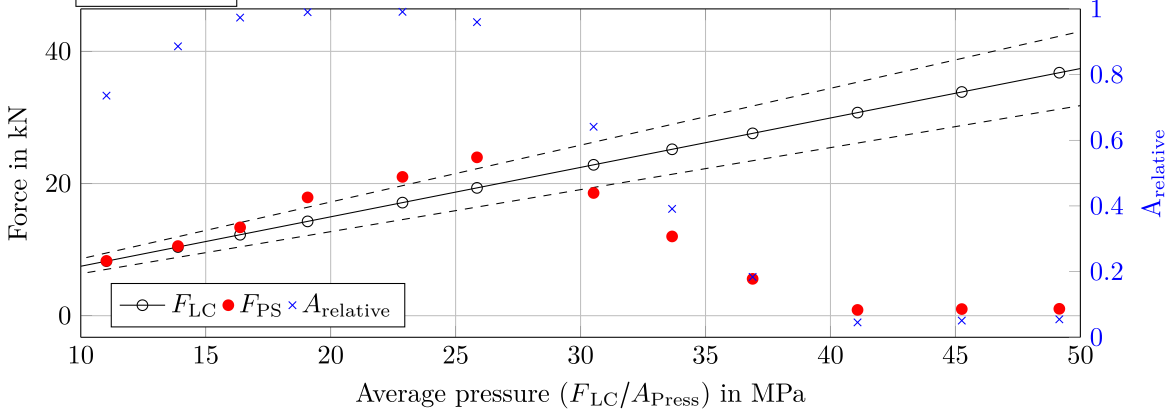

(*b*) HS type

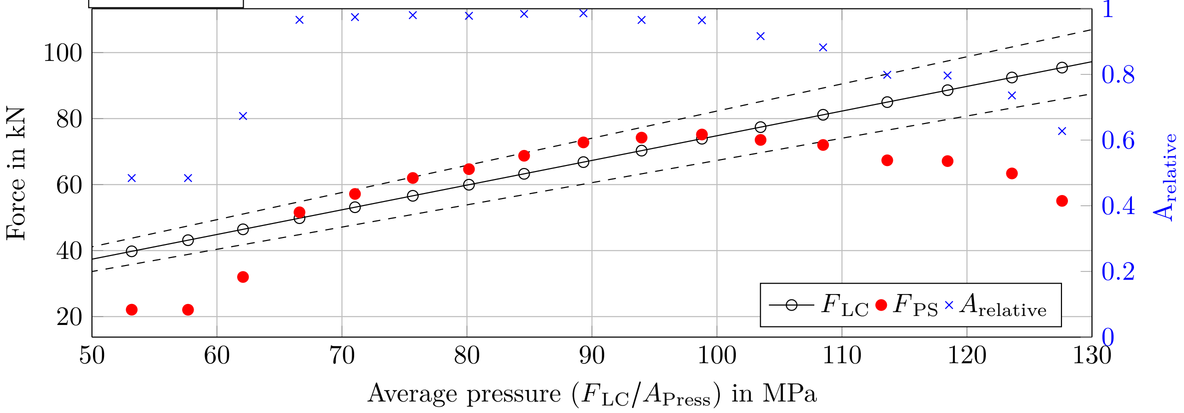

(*c*) HHS type

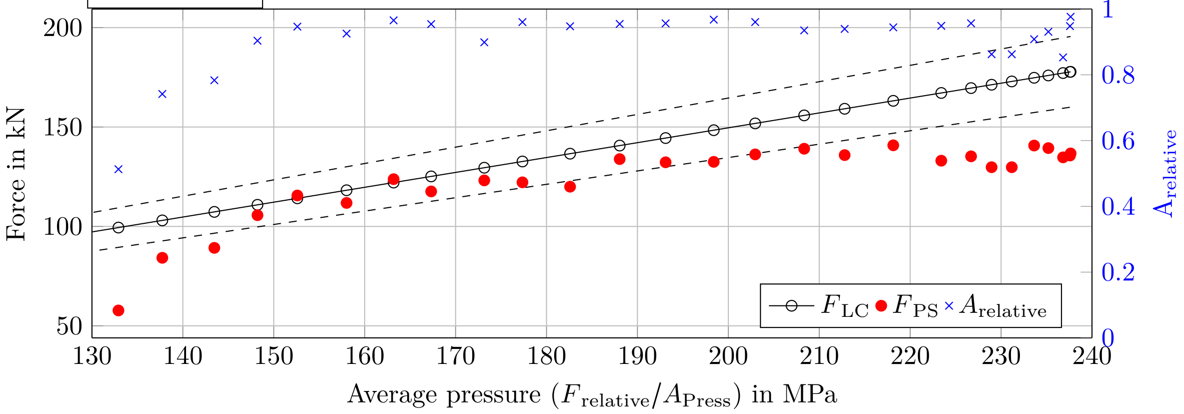

Figure 3.10.: Comparison of the force determined by load cells with the integrated force from Prescale films with respect to the relative measurement area of the films for the (*a*) MS type, (*b*) HS type and (*c*) HHS type.

3.8. Press punch

The aim of the press punch is to apply a homogeneous stress distribution with a maximal contact pressure of 230 MPa. The reaction force is generated by a hydraulic piston with a maximal force of 180 kN. With a fixed maximal force F and the cable width w the maximal contact surface pressure P is dependent only on the tool length l_{tool} and can be calculated with

$$P = \frac{F}{w \cdot l_{\mathrm{tool}}}. \tag{3.3}$$

The maximal compressive contact pressure with respect to the tool length is shown in Figure 3.11.

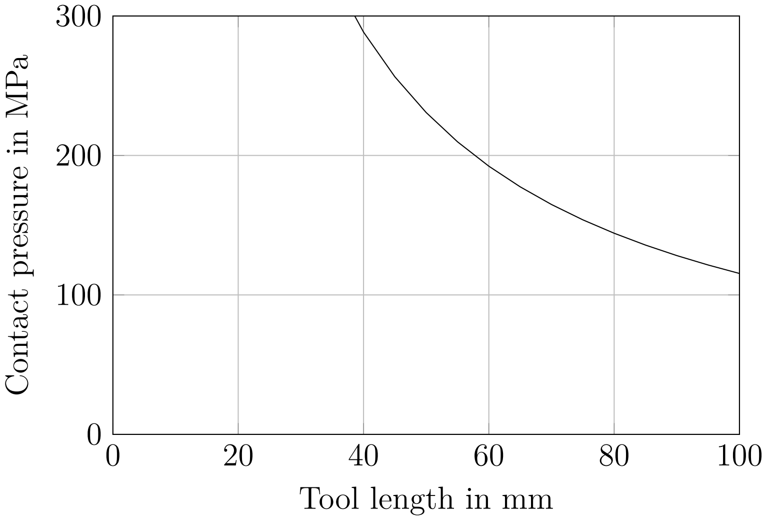

Figure 3.11.: Maximum tool length related to the contact pressure.

Stress concentrations are expected at the tool edges that need to be investigated and reduced. The stress behaviour in a contact zone can be estimated by the Hertz contact model where the radius of one contact partner is set to infinity [105]. The peak stress σ_{H} in the contact transition zone depends on the contact radius R, tool width l, the elastic modulus E_i and the Poisson ratio ν_i of the used components and the applied load F:

$$\sigma_{\mathrm{H}} = \sqrt{F \frac{2E_1 \cdot E_2}{((1-\nu_1^2) \cdot E_2 + (1-\nu_2^2) \cdot E_1) \cdot 2\pi \cdot R \cdot l}}, \tag{3.4}$$

where $i = 1, 2$ represent the punch material and the flat contact surface material, respectively. The model indicates an indirect relation between the contact radius and the resulting peak stress.

The contact transition zone was also investigated by an ANSYS® FEM model in a 2D study assuming a plane strain model with a frictionless contact behaviour. The cable was simplified by a rectangular block with a thickness of 4 mm. The contact stress distribution was investigated under a parametric study, thereby tool radius was varied. The model was calculated assuming the linear elastic material theory. The model components and boundary conditions are shown in Figures 3.12 and 3.13. The used material properties are listed in Table 3.6.

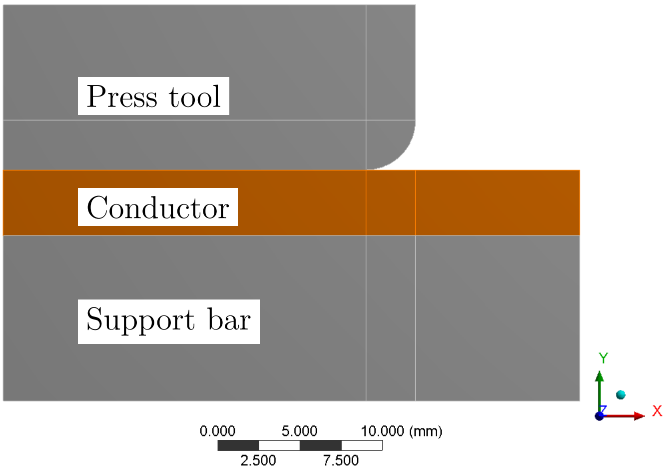

Figure 3.12.: The 2D tool radius study.

Table 3.6.: Material properties.

Component	Young's modulus	Poisson ratio
Press tool	210 GPa	0.3
Conductor	25 GPa	0.33
Support bar	210 GPa	0.3

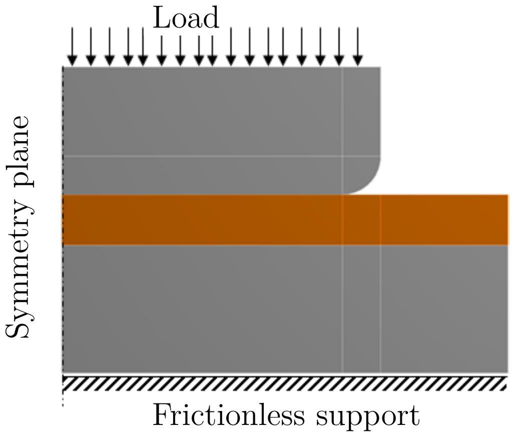

Figure 3.13.: Boundary conditions for 2D study.

The contact definition was frictionless with a symmetric behaviour. The contact formulation was based on the penalty method where the finite contact force is a product of the contact stiffness and the penetration depth. The stress distribution of the normal stress in the y direction (vertical) is shown in Figure 3.14. The edge stress concentration was investigated for different tool radii.

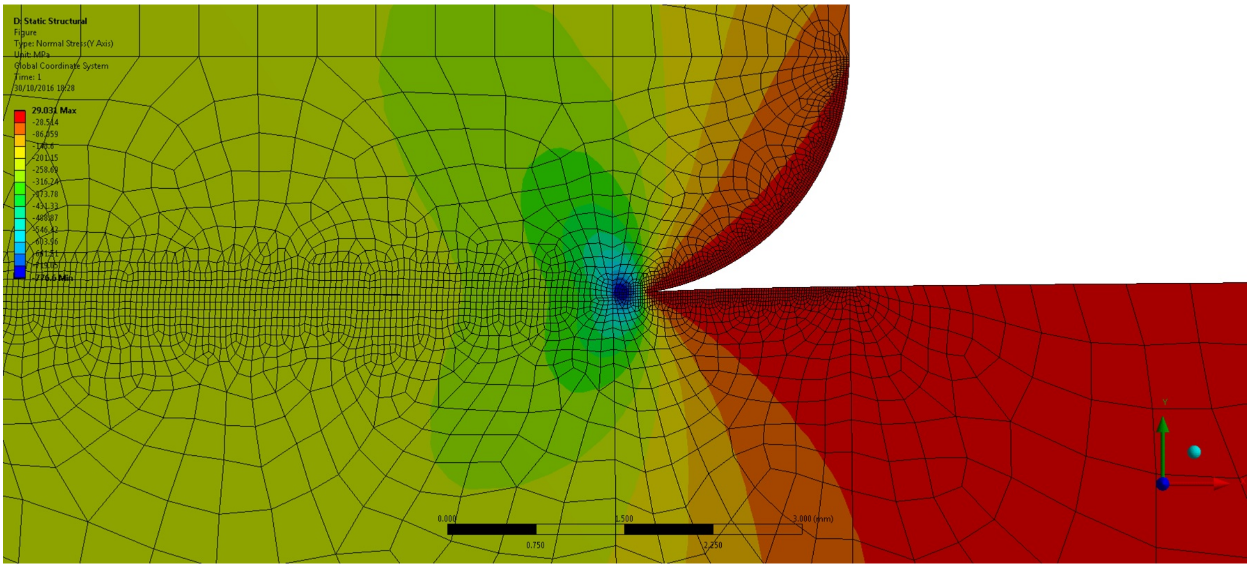

Figure 3.14.: Stress profile owing to the radius study in ANSYS.

The comparison of the normalised peak stress at the stainless steel tool edge calculated by the Hertz contact model and the FEM analysis for different radii of the pressing tool is shown in Figure 3.15. The vertical stress component σ_y along the X axis is normalised by the central stress of the tool $\sigma_y(0)$. The position $x = 0$ describes the central location on the cable. This study indicates that the stress peaks caused by edge effects can be reduced by having a radius at the tool edge. However, simulations have shown that the reduction of the stress peak is not large enough for the foreseen application.

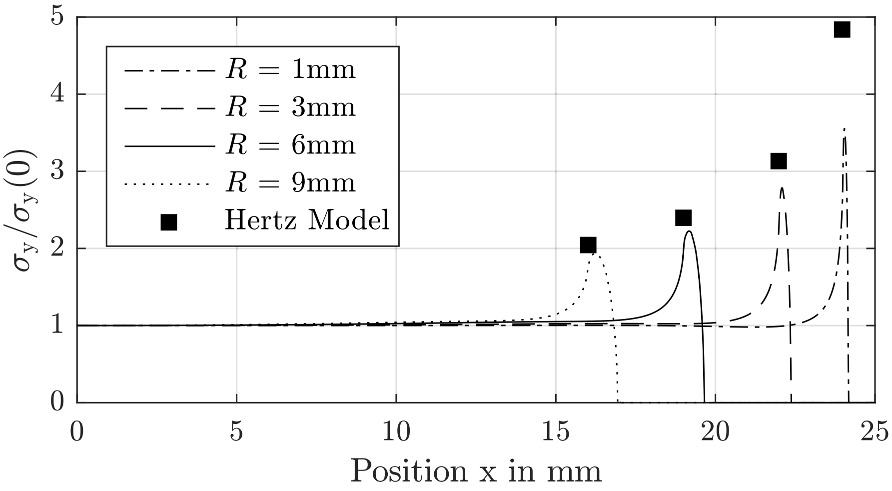

Figure 3.15.: FEM stress study at the stainless steel pressing tool edge pressing on a stainless steel plate, in comparison with normalised stress peaks calculated with the analytical Hertz contact model with radius variation.

3.9. Improvement of the contact stress distribution

The stress dependency on the pressing tool geometry was studied. A tool radius of 3 mm has been selected as it reduces stress peaks in the transition area of the contact zone by 50 % compared to a contact radius of 1 mm and keeps a well defined contact area. An increased tool radius increases the transition zone and introduces a dependency of the contact area with respect to the applied load level. The manufacturing drawing of the press tool is shown in Appendix C in Figure C.1. Furthermore, stress concentrations are caused by manufacturing-related imperfections in geometry and surface quality of the cable. To overcome these stress concentrations, further optimisations were necessary for a sufficient stress homogenisation. A 2D FEM simulation suggests that the stress peaks caused by the tool edges can be reduced by adding intermediate layers of materials with a lower stiffness between the cable and the press tool.

As the mechanical behaviour of the compound consisting of S2-glass insulation, Nb_3Sn Rutherford cable stack and impregnation was not known in detail, the selected a measurement technique for Prescale films was used to identify and improve the stress distribution between the contact surfaces. Thereby, different foil or sheet materials have been investigated between the pressing tool and sample in order to reduce stress peaks caused by sample imperfections and mechanical edge effects. The selected materials have been soft, with a relatively low elastic modulus, in order to be adaptive to the sample surface. Moreover, the inter-layer materials between press tool and sample need to have a yield strength lower than the used CTD-101K impregnation system to allow the yielding of the inter-layer and thereby a distribution of local stress peaks before yielding of the sample itself. Further, it should be high enough to have a limited flow tendency under the applied pressure to avoid an introduction of shearer stresses owing to lateral expansion. The tested foil materials are listed in Table 3.7. The Prescale film was assumed to behave similarly to the polyimide film.

Table 3.7.: Mechanical properties of shimming materials.

Material	Elastic modulus	Yield strength	Poisson ratio
$Sn_{96}Ag_4$ [106]	60.6 GPa	26 MPa	not measured
$Sn_{60}Pb_{40}$ [107]	30 GPa	33 MPa	0.4
In [108]	12.7 GPa	1.6 MPa	0.46
Polyimide foil [109]	3.1 GPa	69 MPa	0.34

Figure 3.16 shows the comparison of the relative stress variation determined experimentally by the Prescale film and by FEM simulations with polyimide foils. It is indicated by the plot that the determined peak stress at the edge is slightly lower than the calculated stress. This stress difference can be caused by the low stiffness of the Prescale film itself, which was not taken into account in the simulations.

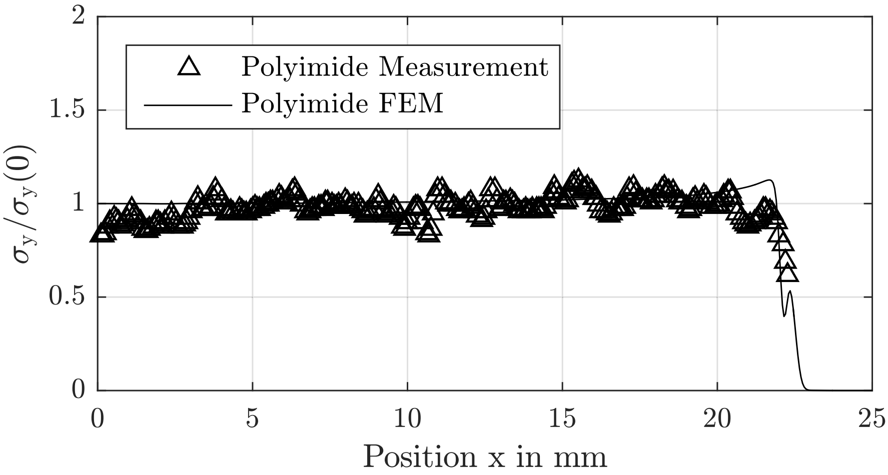

Figure 3.16.: Comparison between measurement and FEM results of the normalised stress distribution along the cable.

After improving the stress distribution in the press gap between the steel parts, the stress distribution on a real sample was measured. Several soft material were used to analyse their effect on the stress distribution. Therefore, a cable was pressed on a virgin location.

3.9.1. First test: cable pressed between the bare tools

The test cable was pressed between the bare pressing tools to analyse the initial situation. Three layers of Prescale film were placed between the cable and the top press tool to measure the stress distribution in the range 10 MPa to 300 MPa. The result of the bare tool test of the HS measurement is shown in Figure 3.17. The cable thickness profile of the cable has a large influence on the stress distribution. Figure 3.17 indicates that the applied stress spreads over a wide range, which is not acceptable. The mentioned geometric variation of the sample has an effect on the stress distribution. An asymmetric stress profile along the sample can be determined, indicating a stress variation of about 40 MPa.

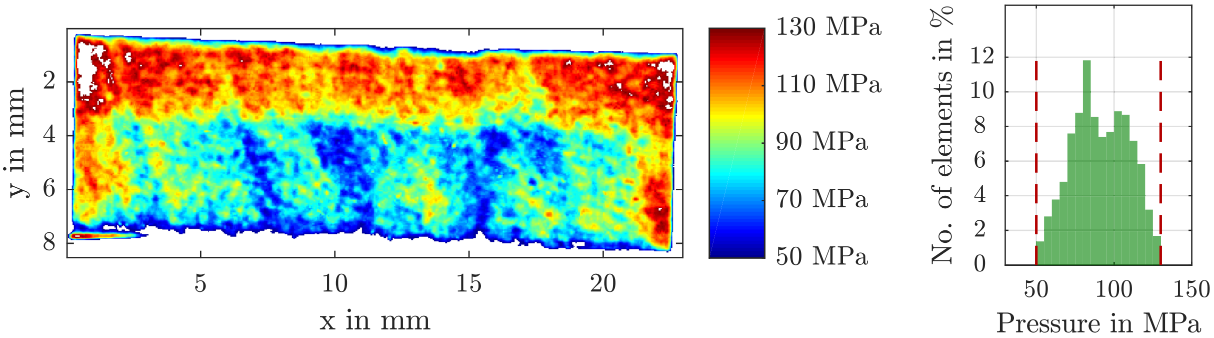

Figure 3.17.: Stress profile (*left*) and histogram (*right*) for the HS film from bare tools.

3.9.2. Second test: tool shimmed with a soft $Sn_{96}Ag_4$

The test was repeated on the next virgin location of the cable with a shim of $Sn_{96}Ag_4$ with a thickness of 0.21 mm. The shim was placed on top of the Prescale film so that it was possible to identify the applied pressure on the cable surface. The $Sn_{96}Ag_4$ shim completely covered the pressing area. The interpreted stress of the HS Prescale film is shown in Figure 3.18. Compared to the stress distribution in Figure 3.17, the stress is better distributed over the pressed area. The related histogram in Figure 3.18 also indicates a better stress distribution with a reduced curve width.

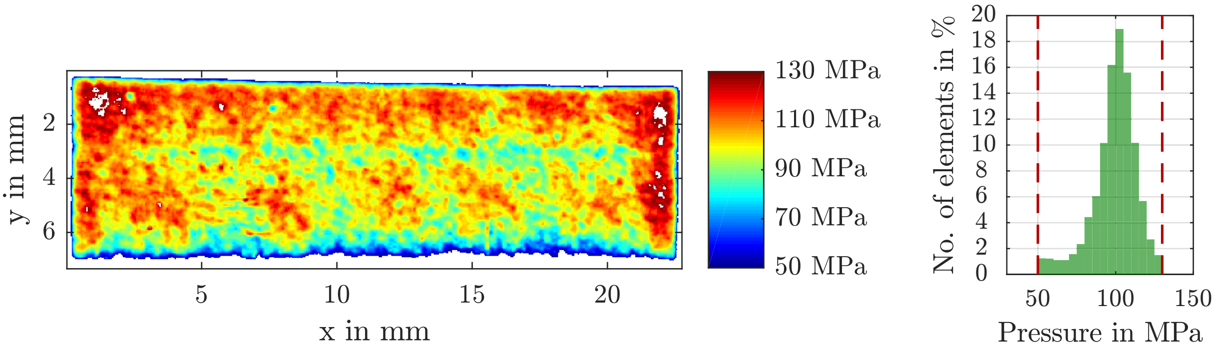

Figure 3.18.: Stress profile (*left*) and histogram (*right*) for the HS film from the tool shimmed with $Sn_{96}Ag_4$.

3.9.3. Third test: tool shimmed with a soft $Sn_{60}Pb_{40}$

The third tested shim material was a 0.12 mm layer of $Sn_{60}Pb_{40}$. The analysis of the HS Prescale film shown in Figure 3.19 compared with the $Sn_{96}Ag_4$ shim revealed a worse stress distribution. This is indicated by to the colour plot and the wide histogram in Figure 3.19.

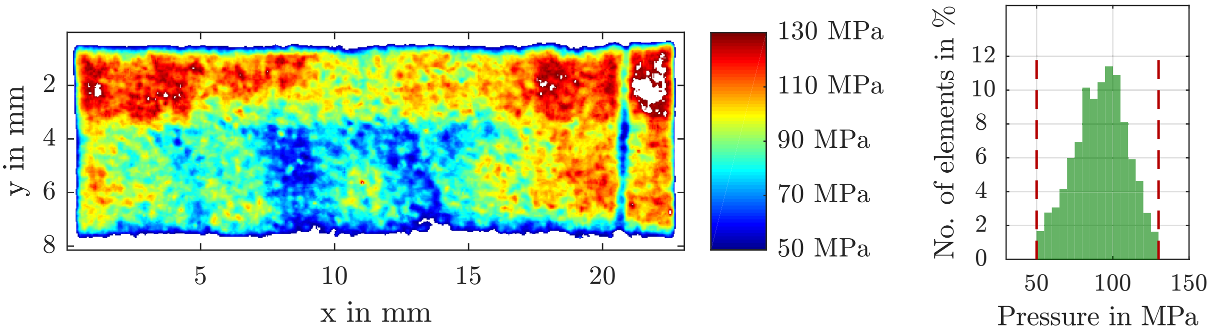

Figure 3.19.: Stress profile (*left*) and histogram (*right*) for the HS film from the tool shimmed with $Sn_{60}Pb_{40}$.

3.9.4. Fourth test: tool shimmed with a soft indium

The fourth test in this iteration was a test with a 0.18 mm soft indium shim. This test was also performed on a virgin location of the cable. The soft material can help to improve the stress distribution. As shown in Figure 3.20, where the HS Prescale film was analysed, the histogram indicates a compacted curve, but it is not sufficient to smooth out the thickness variation of the probe.

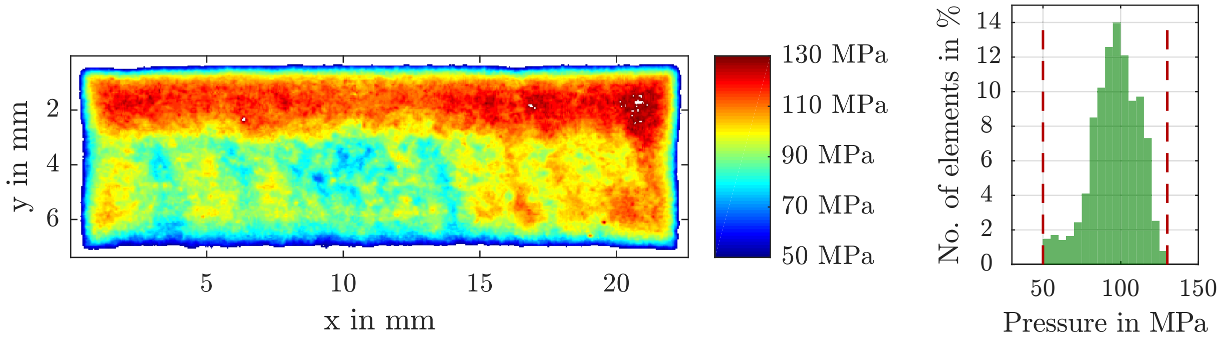

Figure 3.20.: Stress profile (*left*) and histogram (*right*) for the HS film from the tool shimmed with indium.

3.9.5. Fifth test: tool shimmed with a polyimide film

The fourth test indicated that it is possible to smooth out the stress peaks with a soft material between the press tool and the cable. Subsequently, a shimming with polyimide foil was tested. These tests were repeated several times at the same location. The cable was pressed five times with bare tools, just Prescale films placed, to generate comparable conditions for the subsequent tests with different layers of polyimide foil. The analysis of the HS Prescale film of the fifth press cycle with bare press tools is shown in Figure 3.21. The desired stress value for this test was 85 MPa to be able to interpret all stress values with one type of Prescale film. All five bare tool cycles showed the same stress distribution.

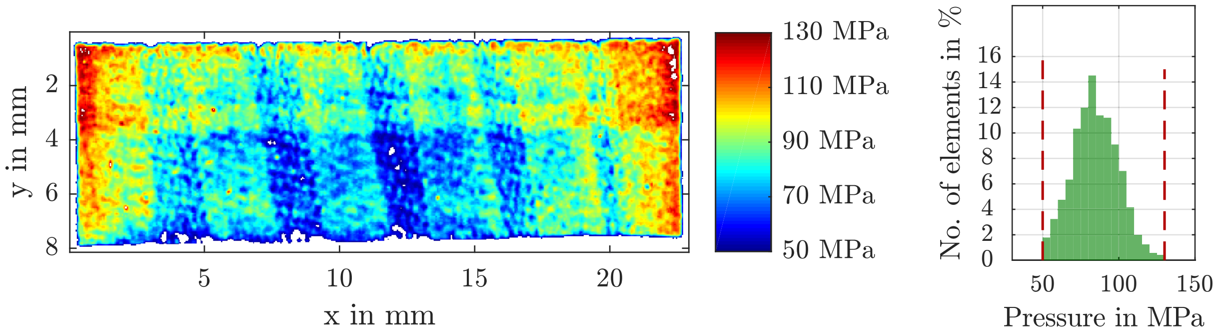

Figure 3.21.: Stress profile (*left*) and histogram (*right*) for the HS film test with bare tools after five cycles.

Subsequently the test was performed with a stack of four layers of 0.125 mm polyimide foil. The result of HS Prescale film is shown in Figure 3.22. The histogram in Figure 3.22 shows a clear reduction of the spreading of the stress values and a reduced amount of high stresses.

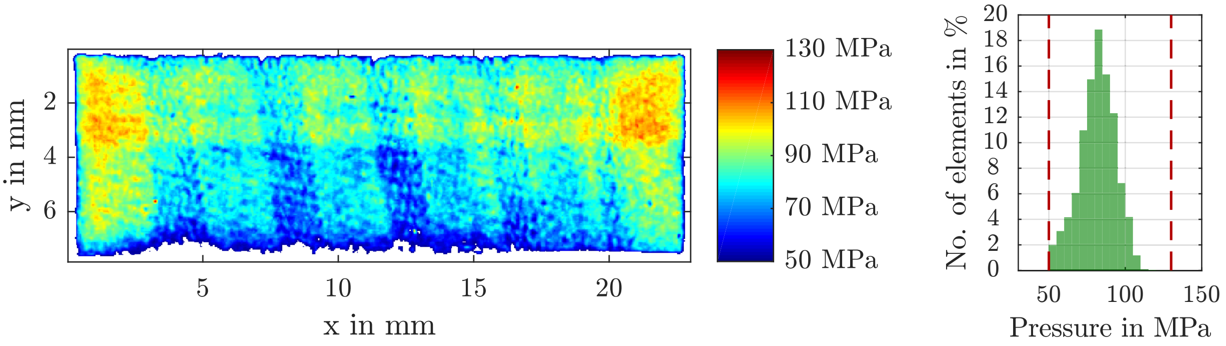

Figure 3.22.: Stress profile (*left*) and histogram (*right*) for the HS film from four layers of polyimide foil.

Whether further improvement is possible was tested by adding more layers of polyimide foil. A final test was performed with eight layers of 0.125 mm. The stress distribution shown in Figure 3.23 was accepted. The stress distribution indicates a reduction of the stress peaks at the longitudinal edges and a reduced geometric effect to the stress distribution. The related histogram shows a further improvement owing to the reduced spreading of the stress values from the desired value. The white spots in the lower edge of the stress interpretation of Figure 3.23 are small breakouts of the epoxy, which can be seen in Figure 3.24.

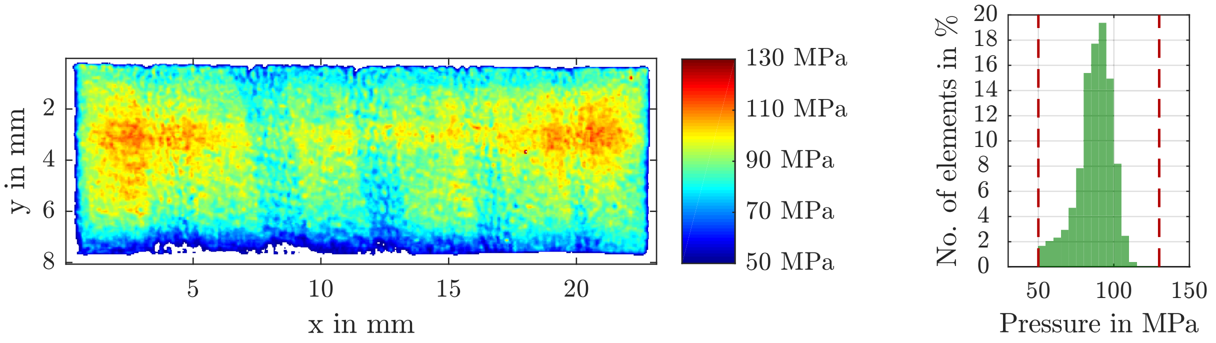

Figure 3.23.: Stress profile (*left*) and histogram (*right*) for the HS film from eight layers of polyimide foil.

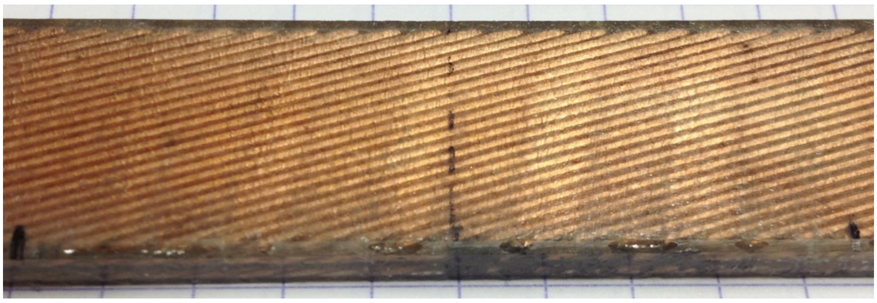

Figure 3.24.: Epoxy breakouts on the cable surface.

The final preparation of the pressed area is shown in Figure 3.25. A stack of eight layers of 0.125 mm thick polyimide foil have been used to smooth out the stress peaks. Three types of Prescale film (MS, HS and HHS) each 100 µm thick have been used to identify the stress distribution in a range of 10 MPa to 300 MPa. A shear stress at the contact surface between tool and cable can be induced owing to different lateral expansion under compressive load. The risk of shear stress is reduced by the multiple layers of polyimide foil, enabling sliding between the layers.

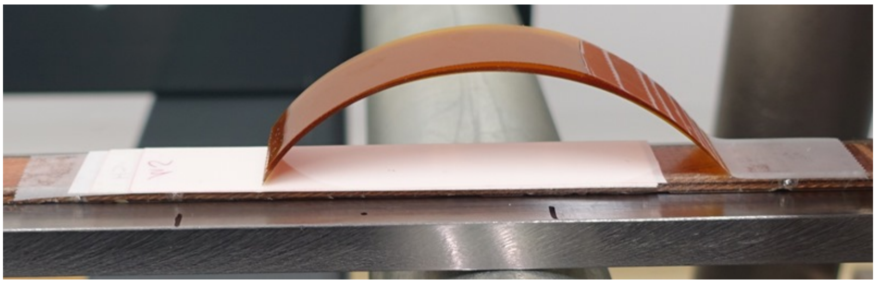

Figure 3.25.: Preparation of the pressed area with Prescale film and polyimide layers.

The final press concept for the cable degradation study is shown in Figure 3.26. The press tool with a length of 50 mm has a radius of 3 mm at the short edges and is manufactured out of hardened stainless steel. The cable is supported by a hardened stainless steel bar with a high surface quality. Three layers of Prescale film placed on top of the cable enable the compressive stress determination in a pressure range between 10 and 300 MPa.

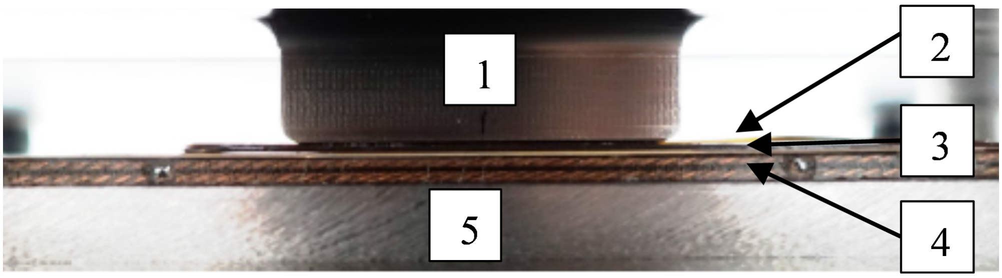

Figure 3.26.: Final press concept with stainless steel press tool with 3 mm radius (1), polyimide foil stack (2), three Prescale films (3) and impregnated double cable stack (4) on a hardened support steel bar (5).

3.10. Test results

The critical current reduction of a reacted and impregnated Nb_3Sn Rutherford cable due to applied transversal stress at room temperature was investigated. A homogeneous contact stress distribution was achieved by using eight layers of 0.125 mm polyimide film. The load was applied with a hydraulic piston and recorded with calibrated load cells, as explained in details previously. The stress distribution was determined by Prescale films of different types, stacked in the press gap to indicate the stress from 10 to 300 MPa. After each pressure application the cable was shipped to the FRESCA test station to investigate the critical current reduction. The integrated force from the Prescale films F_{PS} and the force measured by the load cells F_{LC} as well as their relative deviation with respect to F_{LC} are presented in Table 3.8. The relative deviation is calculated by taking F_{LC} as a reference value. The large measurement deviation in the load step of 150 MPa is caused by the measurement ranges of the different Prescale film types, which prevent a continuous measurement spectrum. In this case, just 60 % of the pressed area was in the measurable range.

Table 3.8.: Load cell measurements compared with integrated force from the Prescale film.

Load step	F_{LC} (kN)	F_{PS} (kN)	Deviation (%)
100 MPa	68.9	69.7	1.2
125 MPa	85.2	88.3	3.6
150 MPa	103.0	66.1	35.8
175 MPa	118.0	105.0	11.0
200 MPa	137.9	125.6	8.9

The evaluated stress distribution of the “HHS” Prescale film of the load step 175 MPa is shown in the stress plot in Figure 3.27. The analysis of these stress data in the histogram in Figure 3.28 indicates that 57.8 % of the analysed area is loaded within a stress range between 160 and 185 MPa, 13.9 % are loaded above 185 MPa and 27.8 % are loaded below 160 MPa. The data acquired by the load cells in Figure 3.28 confirm that there were no force overshoots during the press cycle and the load, which was kept constant for a duration of 2 min.

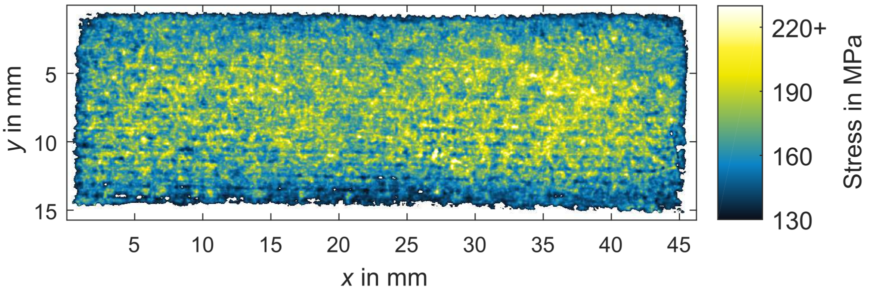

Figure 3.27.: Measured stress distribution at the step 175 MPa with Prescale film.

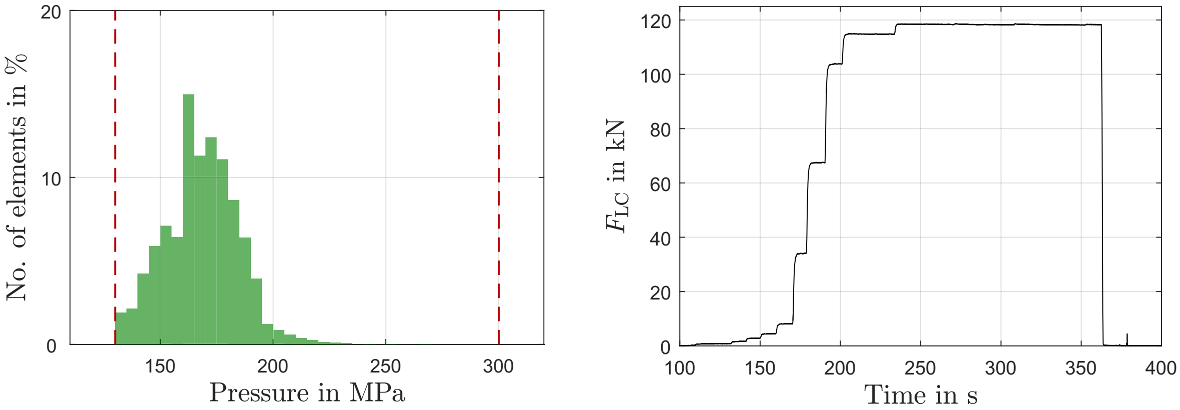

Figure 3.28.: Histogram of the applied surface pressure (*left*) and force measured by the load cells (*right*).

The first cracks in the epoxy could be found by visual inspection after an applied compressive stress of 150 MPa. The comparisoin of the cabel surface after load application of 125 MPa and 150 MPa is shown in Figure 3.29. The epoxy crack initiation started in the centre of the cable, where locally the highest surface stress was observed.

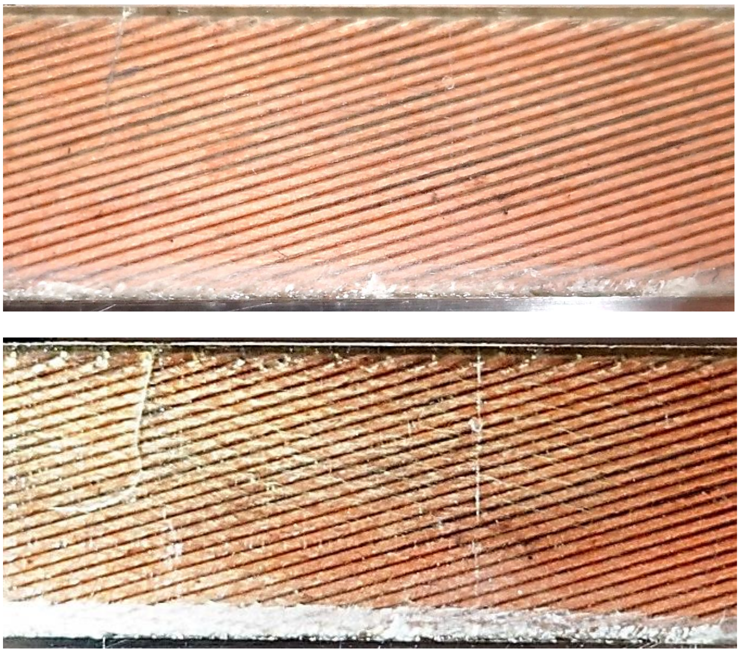

Figure 3.29.: Comparison of pictures of the pressed area of the sample after 125 MPa applied load (*top*) and after 150 MPa applied load (*bottom*) indicating cracks in the impregnation system.

Measurements in FRESCA showed that the first cable current degradation of around 3% was observed after an applied stress of 175 MPa as shown in Figure 3.30. The details of the critical current measurement can be seen in [60].

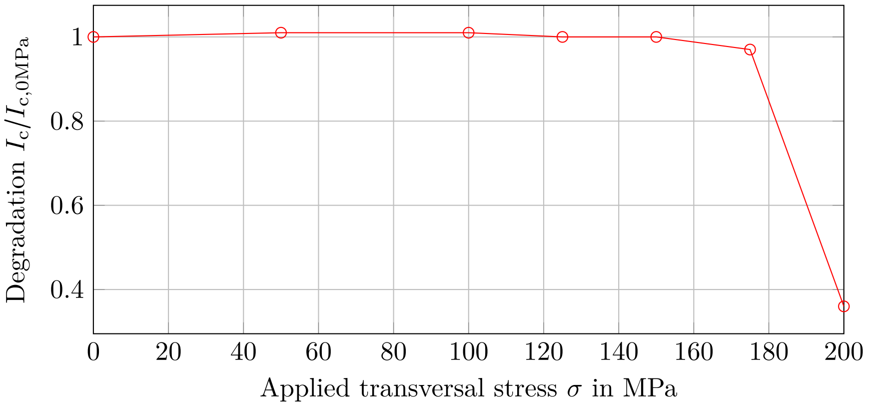

Figure 3.30.: Relative critical current reduction of the cable as a function of applied transverse stress at room temperature measured at $B_{app} = 9.6\,T$ and $T = 4.3\,K$, author's publication [60].

Further tests are foreseen with a reduced step size of 10 MPa to confirm the stress limitation and also to determine the stress limitations of different cables. The first test series has shown that the cable preparation and load application procedure is well established.

3.11. Conclusion

A test set-up has been prepared to apply a uniform compressive load to a double-stacked superconducting cable. The stress homogeneity was optimised by the press tool geometry and by adding polyimide foils between the pressing tool and the double cable stack. Prescale film was used to measure and analyse the applied stress distribution. The integrated force calculated from the Prescale film measurements is in an error range of 10 % of the force measurement performed with calibrated load cells with respect to the measurement range area of the Prescale film. The developed software to analyse Prescale films can be used in the magnet assembly process, to characterise the compressive stress. A pressing tool has been used to study the irreversible Nb_3Sn cable degradation as a function of transverse compressive stress applied at ambient temperature. Visible cracks started to propagate in the epoxy at a stress level of 150 MPa, where no permanent I_c degradation has been observed.

4. Material characterisation by a compression test

The stress–strain behaviour at room temperature of the impregnated Nb_3Sn coils is crucial for the magnet design and assembly process, especially for the introduced collared coil process where the maximum magnet pre-load is set at room temperature. This process is a displacement-based system where the pre-load is determined by the clearance between coil and stainless steel collars [112]. This study was giving direct feedback to the magnet manufacturing process as there were recent changes in the manufacturing process of the insulation system and strand used for 11 T dipole magnet production. Furthermore, this study was used to determine the effect of the cable compaction during coil production on the coil stiffness. As the samples did not comply with the standards for compressive tests (ASTM E1111), the standards were used as a guideline, but could not always be followed entirely. A direct displacement measurement system was chosen, in order to be able to represent a good contact situation, in contrast to previous studies [113, 114, 115] (based on indirect strain measurement by measuring the cross-head displacement). The presented strain measurement method has the advantage that parasitic effects due to machine compliance can be excluded and the sample elongation is recorded as the strain occurs in the sample owing to the applied load. Furthermore, the gauge length is very well defined, compared with an indirect measurement method. The use of a clip-on extensometer eases the attachment to the sample and dismounting after the test. Similar studies [116, 117] have presented results that used glued strain gauges as a direct measurement method indicating a similar shape of the stress–strain curve. The use of glued strain gauges includes a higher instrumentation effort. A previous study where the strain is measured by an indirect method [118] presents lower stiffness values, as the contact behaviour and machine compliance have a large impact on the measured stress–strain curve of a cable stack.

An experimental parametric study has been performed to measure the stiffness of so-called 11 T Rutherford cable stacks as a function of the compaction during the heat treatment and impregnation. Three different conditions of compaction during the reaction and impregnation treatments have been explored, and the cable stack stiffness is also compared with that of coil conductor blocks extracted from already powered coils coming from a short model of the 11 T magnets for the HL-LHC upgrade project. The conductor block stiffness increases with increasing applied load, and with increasing compression during the reaction heat treatment (RHT). The conductor block stiffness under axial load direction is about twice that in the transverse direction.

4.1. Test set-ups for compressive tests and validation

Hydraulic test set-up for compressive stress–strain measurements at CERN

The stress–strain measurement at CERN was performed in a hydraulic test machine [119] with an ultimate load capacity of 180 kN. A detailed description of the load measurement system can be found in Section 3.6.

The strain was measured by a direct extension measurement method by using a clip-on extensometer (Epsilon 3442-006M-010-LT) [120] with a gauge length of 6 mm and a measurement range of ±1 mm as shown in Figure 4.1. The specifications of the extensometer are summarised in Table 4.1.

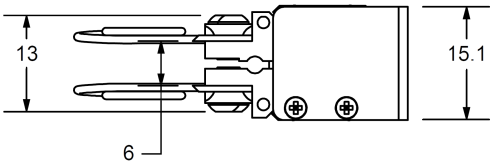

Figure 4.1.: Drawing extensometer [121].

Table 4.1.: Extensometer specification (Epsilon Technology 3442-006M).

Specification	Value
Gauge length	6 mm
Measurement range	−1 mm to 1 mm
Gauge length error	≤ ± 0.1667 %
Sensitivity	1.097 mV/V
Year of last calibration	2017

The data acquisition of the extensometer data was done with the software DSCUSB tool kit [122] in parallel to the load cell measurements on the laboratory computer and synchronised with the help of the CPU time stamp by post-processing in MATLAB. Therefore, a code was developed to adjust the measurement frequency and time shift of measurement systems in order to evaluate an engineering stress–strain curve of the measurement. The time stamp of both data files was interpreted as a global time vector. The time shift of the measurements could be identified with the help of the global time vector. The frequency adjustment was performed by an interpolation of the measured results. The interpolation points were set with respect to the data set with the lower frequency. The contact area of the compressed surface of the sample and the initial gauge length of the extensometer after mounting to the sample were defined before the stress–strain measurement, in order to subsequently evaluate the engineering stress–strain data.

In order to validate the stress–strain measurement set-up, the stress–strain curve from three reference samples out of Ti–6Al–4V has been measured. The determined Young's modulus of the reference sample was 116.4 ± 1.4 GPa. The Young's modulus of these samples has been identified previously [67] with a resonance method to be 115 GPa. Compared with the value in the literature, the stiffness of the reference sample could be determined with a deviation of less than 1 %. The longitudinal samples were used, corresponding to this paper. The ambient conditions for one validation measurement of the set-up and the initial sample specifications are summarised in Table 4.2, including also the initial diameter of the sample, measured with callipers and the gauge length of the extensometer at the beginning of the measurement.

The experiment was performed in a load-controlled mode, with a ramp rate of 50 N/s corresponding to 0.2 MPa/s. The extensometer was attached with steel springs to sample as

Table 4.2.: Measurement specifications.

Specification	Value
Cylinder height	15.04 mm
Cylinder diameter	10.06 mm
Extensometer gauge length	5.92 mm
Temperature	27.3 °C

shown in Figure 4.2. Owing to the limited access in the press gap, the extensometer needed to be mounted to the sample before it was installed in the hydraulic test machine. The contact surfaces of the press tool were coated with a lubricant to reduce effects owing to friction at the surface.

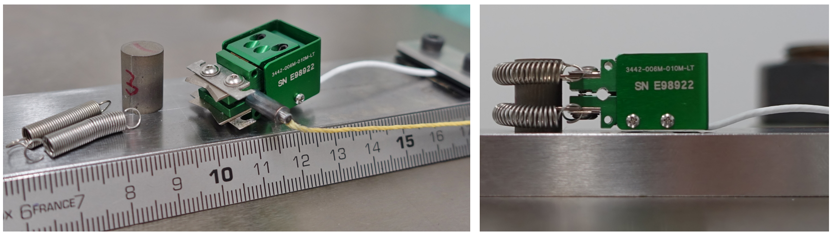

Figure 4.2.: Extensometer with fastening springs and cylindrical sample on the sample holder (*left*) and attached to the reference sample (*right*).

An example for one performed stress–strain measurement with a Ti–6Al–4V cylinder sample is shown in Figure 4.3. The good agreement between loading and unloading curve indicates a pure elastic material behaviour until a compressive load of 450 MPa. The elastic modulus determination of the plotted data was performed in the strain interval 0.3606 % to 0.25 %. An elastic modulus of 117.6 GPa was determined by a linear fit with the least-squares method giving an R^2 value of 0.99987 in the mentioned fitting interval.

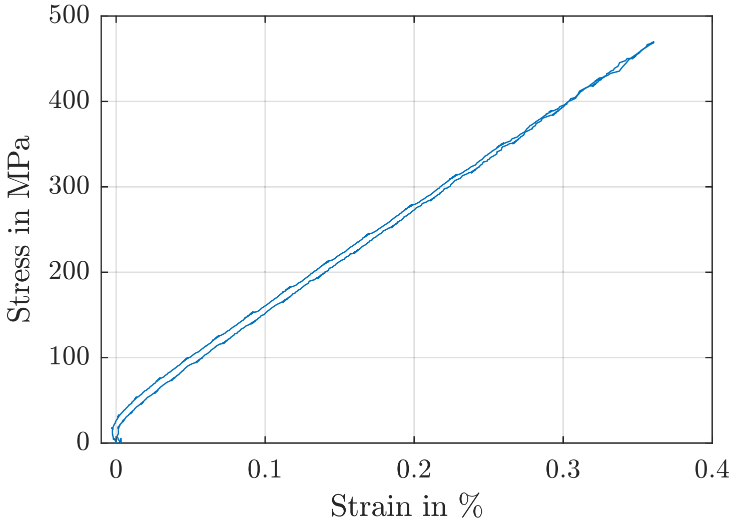

Figure 4.3.: Stress–strain measurement of a Ti–6Al–4V sample.

The results of multiple repeated validation stress–strain measurements carried out with the extensometer are summarised in Table 4.3. The Young's modulus E was always determined with a least-squares linear fitting method. The fit interval is set with respect to the strain range where the upwards and downwards data are almost identical, indicating a pure elastic deformation of the reference material. The measurement was repeated three times for each samples. The average value with one standard deviation summarise each measurement series. The average Young's modulus determined by the nine measurements is 116.4 ± 1.4 GPa for the tested material.

Table 4.3.: Overview of the measurement results.

Sample	A	B	C	Average	SD 1σ
E (GPa)	115.1	113.5	116.5	115.2	1.53
Fit strain range (%)	0.25–0.38	0.25–0.36	0.25–0.33		
E (GPa)	117.2	115.5	117.3	116.7	1.01
Fit strain range (%)	0.25–0.36	0.25–0.35	0.25–0.35		
E (GPa)	116.5	118.3	117.3	117.4	0.9
Fit strain range (%)	0.25–0.37	0.25–0.37	0.25–0.35		

Electromechanical test set-up for compressive stress–strain measurements at MLZ

An electromechanical test machine was also used to characterise the stress–strain behaviour of the cable stack samples in combination with neutron diffraction measurements, as explained in detail in Section 5. The electromechanical stress–strain measurement set-up is installed at the STRESS-SPEC material science diffractometer [123] operated by the Heinz Maier-Leibnitz Zentrum (MLZ) from the Technische Universität München, located at the thermal beam port SR-3 of the Forschungsreaktor München (FRM II). The macroscopic stress–strain measurement set-up is a load frame equipped with a load cell (HBM Type 03), a press tool guide and a spindle lifting gear powered by a step motor. The installed sample with an attached extensometer (Instron 2620-602) with an initial gauge length of 13.06 mm is shown in Figure 4.4. A special press tool has been designed, which provides enough space to attach a 13 mm clip-on extensometer to the sample with a height of 15 mm. The manufacturing drawing of the tool is shown in Appendix C in Figure C.2. The free access to the pressing gap allows the extensometer to be mounted at the sample with a pre-compression of 200 N, which corresponds to a stress level less than 1 MPa at the measured samples with a contact area of 15 mm × 15 mm. A Teflon spray was used as lubricant between the contact surfaces to reduce frictional effects during the measurements. The measurement was performed in a load-controlled mode with a load rate of 50 N/s. In addition, an initial validation test was performed with the test set-up at the MLZ with a reference sample made out of AL7075–T651. The determined elastic modulus of 72.7 GPa varies less than 1.5 % from the literature value of 71.7 GPa [124].

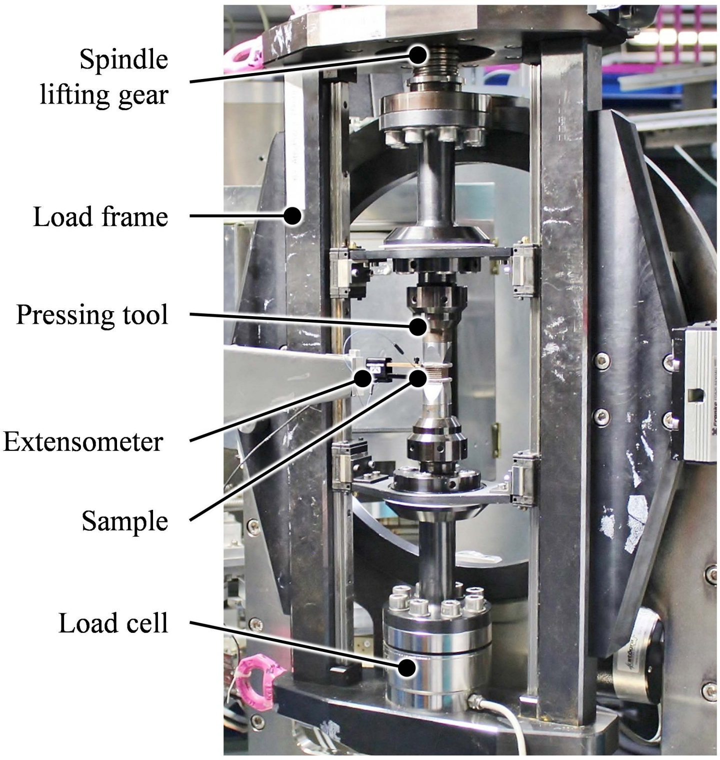

Figure 4.4.: Load frame at the MLZ for stress–strain measurements.

4.2. Sample preparation

Three different types of samples have been manufactured to study the mechanical behaviour of a coil under applied load, shown in Figure 4.5. Representative samples have been manufactured out of cables stacks, following the same manufacturing procedure of the Nb_3Sn coils. The manufactured cable stacks allowed the investigation of the stress–strain behaviour before impregnation and under varying manufacturing conditions. Furthermore cut-outs from a powered Nb_3Sn coil allow a direct comparison of the stress–strain behaviour between coil segment and representative sample. The detailed manufacturing procedures of all samples are explained in the following.

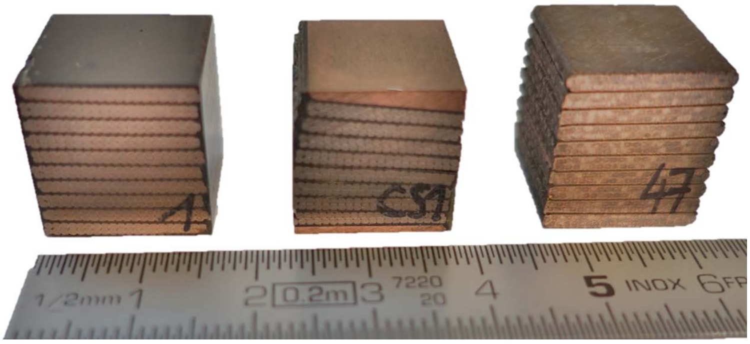

Figure 4.5.: Nb_3Sn Rutherford sample type ten-stack (*left*), coil segment (*middle*) and non-impregnated ten-stack (*right*).

The conductor used for the sample production was a Rutherford cable made out of 40 RRP-type Nb_3Sn strands from Oxford Instruments Superconducting Technology (now Bruker EAS) with a 25 µm thick stainless steel core, identical to that used for the 11 T dipole coil production. A hybrid insulation system, formed by a 80 µm thick C-shaped mica foil is wrapped around the cable and a fibreglass braiding, providing an insulation thickness of 0.15 mm at 30 MPa. The mica tape is a COGEBI FIROX [125] mica on an E-glass grid stripe. The fibreglass braiding is made from a S2-glass yarn by AGY 11 TEX[7] 636, with numerous filaments of varying diameters.

Ceramic binder application and curing

The representative cable ten-stacks were stacked with an alternating keystone angle in a specially designed mould made of stainless steel 316LN with a width of 15.5 mm and a length of 240 mm. The manufacturing drawings can be found in Appendix C in Figure C.3–C.7. The mould enabled a pre-treatment of the cable stack with a two-component ceramic binder CTD-1202A (45 %) + CTD-1202B (55 %) [126], as shown in Figure 4.6. The ceramic binder is a polymer-derived ceramic (PDC) resin used to stabilise the coil after reaction heat treatment (RHT). About 7 g were applied to the full sample length per ten-stack.

Figure 4.6.: Sideways-opened reaction mould with free access to the cables to apply the ceramic binder.

The ceramic binder was cured for 1 hour at 80°C and 2 hours at 150°C. The curing fixture was heated by two heating sleeves controlled by a laboratory power supply, equipped with a monitoring thermocouple, installed in the mould as shown in Figure 4.7.

Reaction heat treatment

The stainless steel mould was also used for the RHT of the ten-stack samples. The clearance height of the mould can be adapted by stainless steel shims with varying thickness in discrete level down to 0.01 mm in the range of 14.6 mm to 15.0 mm. This allows to vary the inter-strand void volume to be found that is subsequently filled with epoxy (in the following referred to as the non-wire volume fraction). The mould was designed to be able to keep the compressive load up to 30 MPa also at higher temperature (665°C). At this temprature levels the yield stress $R_{\mathrm{p}0.2}$ of the stainless steel drops drastically [127]. This was at the time the

---

[7] The TEX number indicates the weight in grams per kilometre. The number 636 specifies the sizing type, which is starch and oil based, required to protect the yarn during processing.

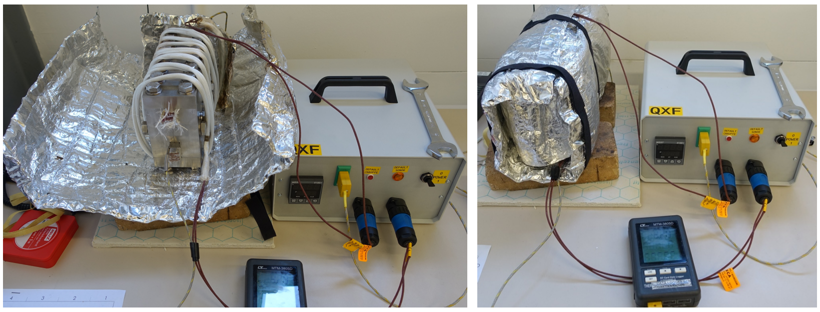

Figure 4.7.: Ceramic binder curing fixture indicating the heater and thermocouple (*left*) and operating condition with multilayer heat-resistant insulation (*right*).

target manufacturing value during RHT. The mould was symmetric in design to avoid mould or sample deformations due to unbalanced thermal-induced stresses. The sample RHT was done in parallel to a Nb_3Sn coil reaction process in the same furnaces. The heat-treatment cycle was 210°C for 48 hours, 400°C for 48 hours and 665°C for 75 hours.

Vacuum impregnation

The impregnation was performed in a custom-made aluminium mould, as shown in Figure 4.8. A stepped sealing groove enables a leak-tight impregnation under varying mould clearance. The design approach allows the compaction level to be maintained similarly to that during RHT. The manufacturing drawings of all components can be found in Appendix C Figure C.8–C.11. The silicone sealing with a diameter of 5 mm was made, corresponding to the required length, connecting the diagonal cut ends with CAF 4 by ELKEM SILICONES, a one-component silicone elastomer that cures at room temperature. The mould was coated with release agent (turpentine substitute) to reduce the bonding between epoxy and mould, in order to be able to remove the sample from the mould after impregnation. The assembled mould with inserted sample was tested to be leak tight with a vacuum pump to 95 kPa below standard pressure for 10 minutes. The mould was placed in a vacuum chamber for the impregnation after connecting all the injection tubes. The used resin CTD-101K was degassed prior to injection. The injection temperature of the resin was 55°C. The curing of the epoxy was done with a cycle given by the manufacturer for 5 hours at 110°C and 16 hours at 125°C with a temperature ramp rate of 0.5°C/min.

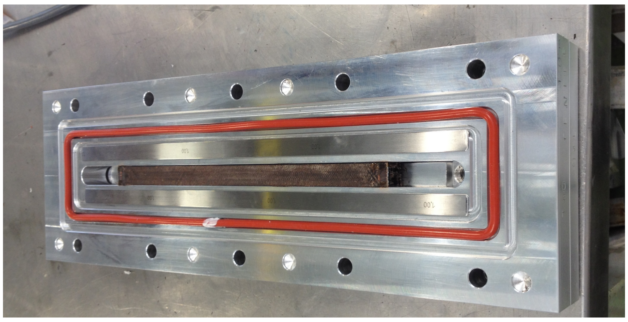

Figure 4.8.: Impregnation mould with stepped groove for the sealing and stainless steel shims to adjust the sample clearance and thereby affect the relative wire volume fraction.

Sample machining

A diamond wire saw has been used to cut ten-stack samples from bars with a total length of 240 mm, as shown in Figure 4.9, to cubic samples with an edge length of approximately 15.5 mm varying by the height of the sample. This cutting technique was chosen to reduce the risk of de-lamination by inducing cutting forces. The cubic 11 T dipole coil block was machined out of the coil after magnet cold test, containing adjacent coil wedges to compensate the keystone angle as shown in Figure 4.5.

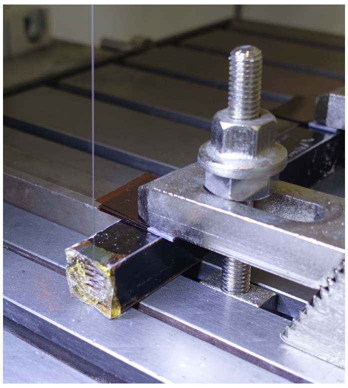

Figure 4.9.: Impregnated cable ten-stack mounted on the table of the diamond wired cutting machine.

Determination of the wire volume fraction

The wire volume fraction of each type of sample was determined by digital image analysis of high-resolution microscopic images taken from crystallographic cross-sections [128], as shown in Figure 4.10. The MATLAB code of the analysis is documented in Appendix F. The inter-cable void space filled with insulation and epoxy impregnation is referred to as non-wire volume ($V_{\mathrm{non-wire}}$) in the following. The determined wire volume fractions of the samples are summarised in Table 4.4. The geometric dimensions of each sample were defined by contact measurements with a high-resolution measuring unit (Mitutoyo, Litmeatic VL-50).

Table 4.4.: Sample overview with corresponding wire volume fraction.

ID	Sample type	V_{wire} (%)	Compaction pressure** (MPa)
A	Ten-stack impregnated	74.3	30
B	Ten-stack impregnated	72.8	15
C	Ten-stack impregnated	69.6	5
D	Conductor block from 11T dipole coil 107	75.8 ± 0.8*	30
E	Ten-stack not impregnated	n.d.	n.d.

*Uncertainty in the separation between the insulation and wire phase.

**Correlates to the not impregnated ten-stack height.

n.d. not determined

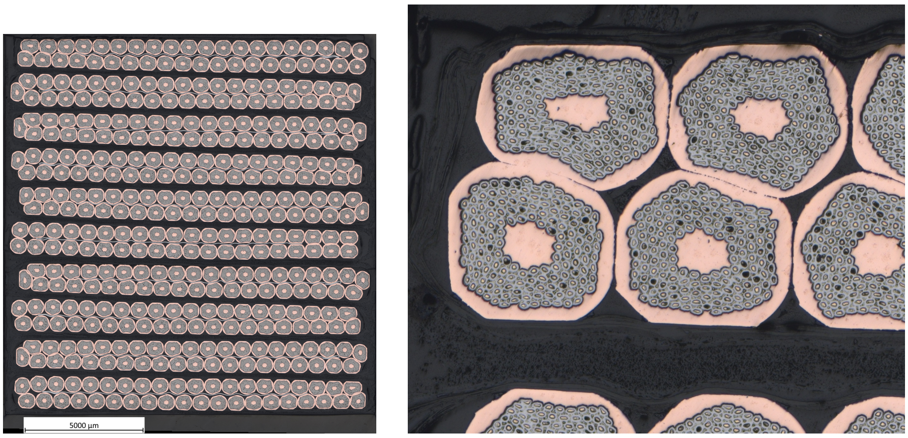

Figure 4.10.: Microscopy of the ten-stack cross-section (*left*) to determine the volume fraction with a detailed zoom of the top left corner (*right*) indicating the colour difference between strands in the insulation system.

4.3. Compressive stress–strain measurement

The compressive stress–strain measurements were performed with the two previous explained test stations in different facilities with independent measurement equipment to show the reproducibility of the elaborated results. The stress–strain measurement in both set-ups was performed in a load-control mode with a load rate of 50 N/s, which corresponds to 0.2 MPa/s for the used samples. The complex inner structure of the sample with Rutherford cable and the insulation scheme does not allow cylindrical samples to be machined as recommended for compression tests [62], without affecting the integrity of the sample at the cable edges. Instead cubic samples have been manufactured with the edge length of the cable width. This small height to cross-sectional ratio reduces buckling effects of the sample during applied load. The loaded surfaces have been coated with a PTFE (Teflon) spray before each test in order to reduce friction effects. The extensometer mounting with steel springs is shown in Figure 4.11, where three point knife edges have been pressed by the spring forces to the samples, mitigating errors in the specimen. The contact edges of the extensometer were always attached to the cut cross-section of the sample for the transversal loaded measurements and also for the radial loaded measurements. The sample orientations are defined in Figure 4.12.

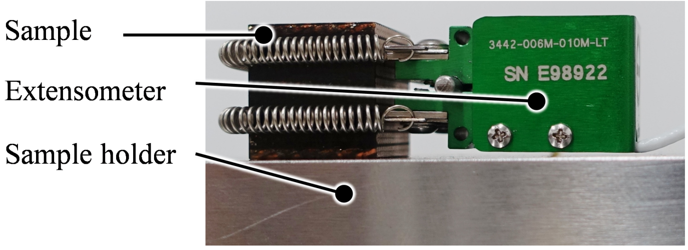

Figure 4.11.: Ten-stack sample with clip-on extensometer with 6 mm gauge length.

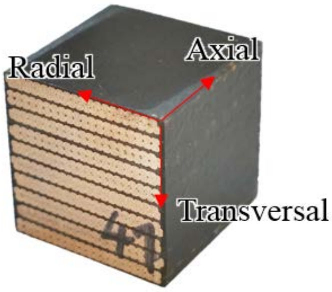

Figure 4.12.: Sample orientation of the ten-stack sample.

Initial tests have shown that the ten-stack samples do not exhibit linear elastic behaviour. Therefore, a cyclic load pattern was applied with a load increase of 15 MPa per cycle. This allowed an elastic sample behaviour to be determined, as the initial slope of the unloading engineering stress–strain curves, defined as stiffness. The Young's modulus determined with this method indicates good agreement with that determined by dynamic Young's modulus measurement methods such as resonance excitation testing [67]. This allows good reproducibility of the elastic slope determination of materials with large uncertainty from the elastic slope extracted from the loading stress–strain curve like for stainless steel AISI 316LN (1.4429, X2CrNiMoN17-13-3) or heat-annealed copper. The slope analysis was performed by using the method of least-squares [63] to determine the linear fit function, commonly used for modulus determination. All measurements have been performed at room temperature.

Ten-stack stiffness under transversal compression

The test procedure to determine the ten-stack stiffness under compression was specified, as initial compressive tests have shown that the ten-stack stiffness is strongly load and load rate dependent. Owing to this finding, all tests were performed at the same low load rate of 0.2 kN/s with incremental loading–unloading compressive stress increase. The load was kept constant at each load maximum for about 1 hour, as required from parallel neutron diffraction measurements, which is explained in detail in Section 5. The transversal compressive stress–strain curve of a cyclic loaded ten-stack sample type C (V_{wire} = 69.6%) is shown in Figure 4.13.

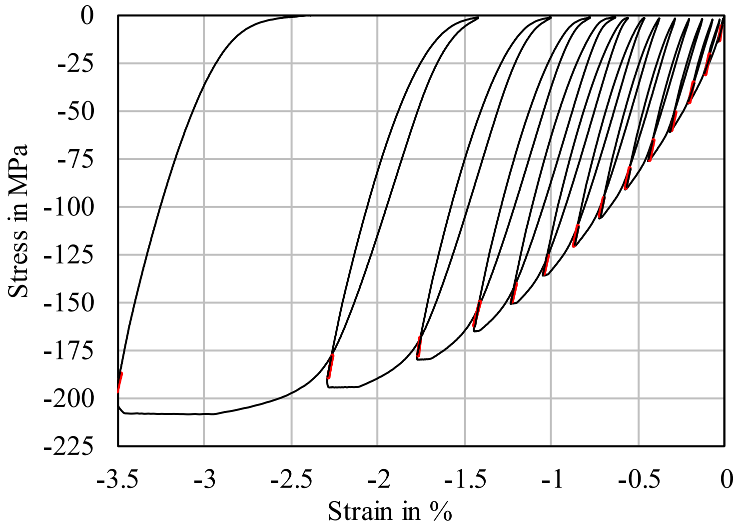

Figure 4.13.: Transverse cyclic compressive stress–strain curve of impregnated ten-stack sample type C ($V_{\mathrm{wire}} = 69.6\%$).

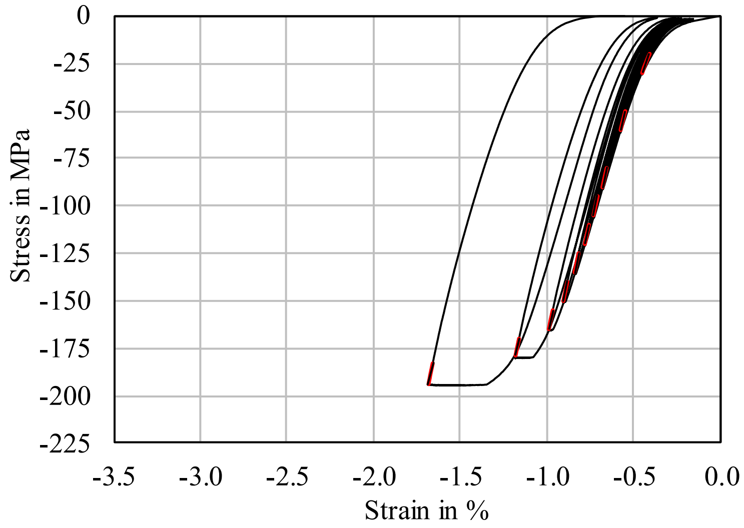

Figure 4.14.: Reloaded transverse cyclic compressive stress–strain curve of impregnated ten-stack sample type C ($V_{\mathrm{wire}} = 69.6\%$).

The incremental increase of the loading stress by 15 MPa enables us to distinguish between elastic (reversible) and plastic (irreversible) deformation. This procedure furthermore allows the load-dependent stiffness to be determined as part of the unloading curve. The shown measurement indicates a stiffness increase from 40 GPa at an unloading stress of 25 MPa to 50 GPa at 225 MPa. The loading–unloading characteristic in the stress range 0 MPa to 25 MPa of the stress–strain curve has changed as the compressive stress exceeded 135 MPa. Furthermore, a significant change of strain at constant load plateaus was observed at stress levels above 135 MPa, which is a direct observation of creep behaviour [66]. The creep behaviour indicates that the sample or components of the sample looses the strength to withstand this high load for a long time. The measurement allows a residual deformation of 0.2 % to be determined after an applied load of 75 MPa. The material compound can be represented by a bilinear curve, using the strain criteria to determine a yield point. The tangent modulus of the loading curve for a stress range of 75 MPa to 150 MPa can be determined by a linear fit to 10 GPa.

The samples were re-measured after the first incremental load cycle to study the effect of the load history on the sample stiffness. The re-measured stress–strain curve following the same test procedure is shown in Figure 4.14. The loading curve that includes the plastic and elastic material behaviour is changed significantly. However, the unloading stress–strain curves representing the elastic behaviour (stiffness) of the ten-stack sample is barely affected by the previous load cycle. The indication of creep was observed above the same load level of 135 MPa.

The transversal stiffness investigation of all impregnated samples and samples extracted from the coil segment are compared in Figure 4.15. The results indicate the average values obtained from at least three measurements. The error bars in the plot represent one standard deviation from the mean value. The stiffness results of a first load cycle like presented in Figure 4.13 is represented by full symbols in Figure 4.15. The stiffness results of a second load cycle as in Figure 4.14 are shown by empty symbols in Figure 4.15. It is shown for all samples that the effect of the load history is low when comparing the first and the second load cycle of ten-stack sample types with different wire volume fraction. The elastic behaviour in transverse direction of all samples is dependent on the load and it increases with increasing wire volume fraction in the ten-stack samples. The conductor block stiffness of the 11 T dipole coil segment (sample type D, listed in Table 4.4) corresponds well with that of the sample type A with a wire volume fraction of 74.3%, suggesting that the ten-stack samples can represent well the mechanical behaviour of a coil. Identical samples of type D were measured with both set-ups and the good agreement between the results can be seen in Figure 4.15.

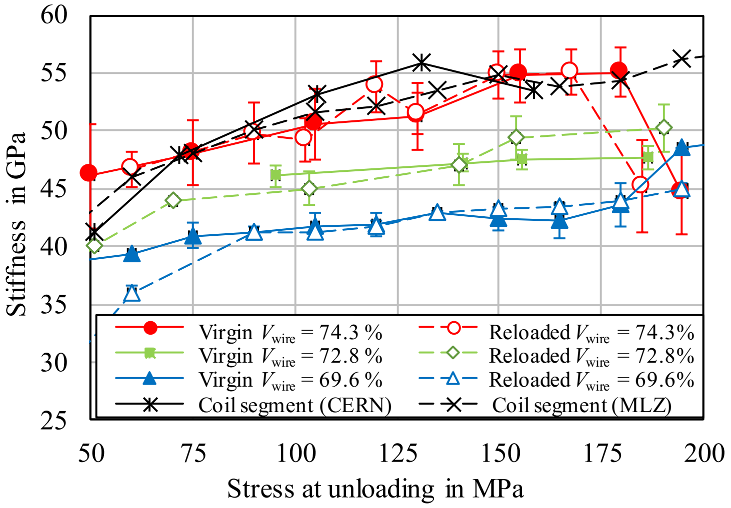

Figure 4.15.: Transverse compressive stiffness comparison of the investigated samples (type A-D) with different wire volume fraction during the first (full symbols) and second (empty symbols) load cycle.

In order to study the effect of the epoxy to the stress–strain characteristic of the samples, a non-impregnated sample type E was investigated. The sample remains in shape, due to the ceramic binder. The transversal stress–strain measurement of a virgin loaded non-impregnated ten-stack is shown in Figure 4.16. The total strain of the sample after the applied 210 MPa is about a factor 3 compared to the impregnated sample, due to the void space between the wires and the fibreglass. The measurement of this sample indicates first indications of a creep behaviour above a stress level of 75 MPa.

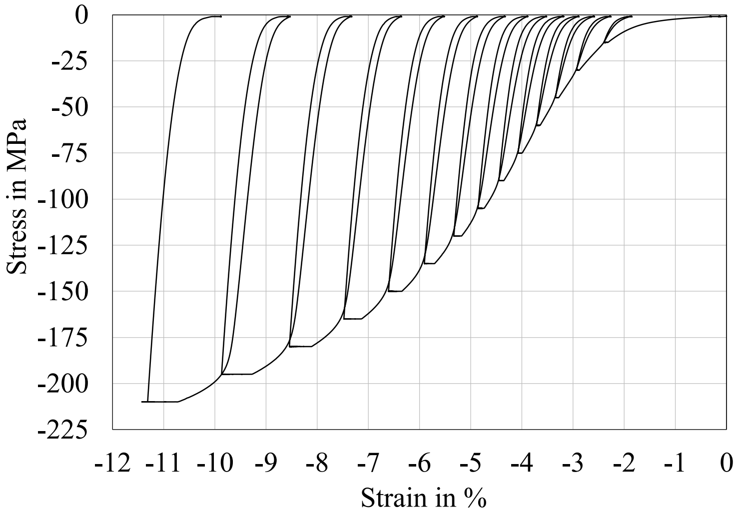

Figure 4.16.: Cycling transversal stress–strain measurement of a non-impregnated Rutherford cable stack with slope at different unloading levels.

Ten-stack stiffness under axial compression

The compressive ten-stack stiffness in axial direction was investigated by following the same procedure as in the transverse direction. The measured stress–strain curve of ten-stack sample type A ($V_{\mathrm{wire}} = 74.3\%$) in the axial load direction is shown in Figure 4.17. The stress ranges of 10 MPa used for data fitting are colourised in the plot. The linear fit equation is next to the evaluated data in the plot. Owing to the strain plot being a percentage, the slope of the linear equation needed to be divided by ten to obtain the stiffness value in gigapascal. It is remarkable that the stiffness is not dependent on the unloading–loading stress level, and there is no strong hysteresis of the unloading–loading curves.

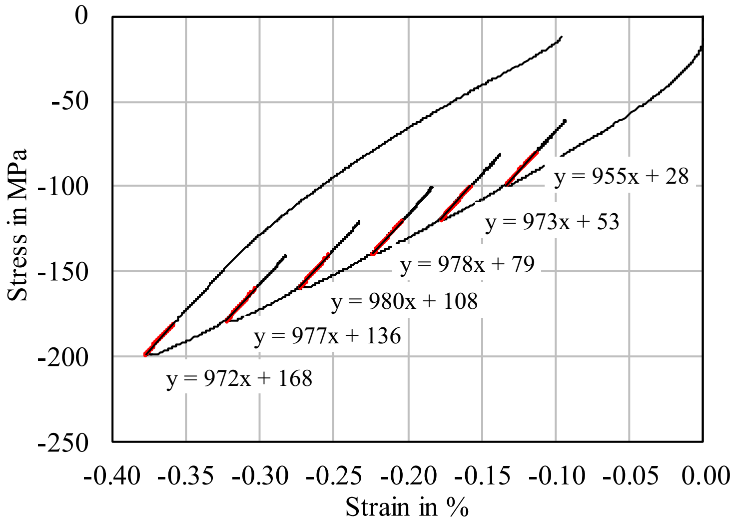

Figure 4.17.: Axial compressive stress–strain curve of ten-stack sample A (V_{wire} = 74.3%) with unloading curves at different stress levels. The linear unloading slopes are nearly load independent.

Comparison of the stiffness of ten-stack samples in different load directions

The comparison of the direction-dependent stiffness of ten-stack sample type B (V_{wire} = 72.8%) at different stress levels in the three normal load directions, axial, transverse and radial, is shown in Figure 4.18. The plot indicates the measurement of three samples per load direction. The measurement in radial direction was only possible up to 100 MPa owing to sample de-laminations above this level. The plot indicates that the sample stiffness is strongly dependent on the applied load direction. The axial stiffness of this sample type is more than twice as high as the transverse stiffness and about 1.3 times the radial stiffness.

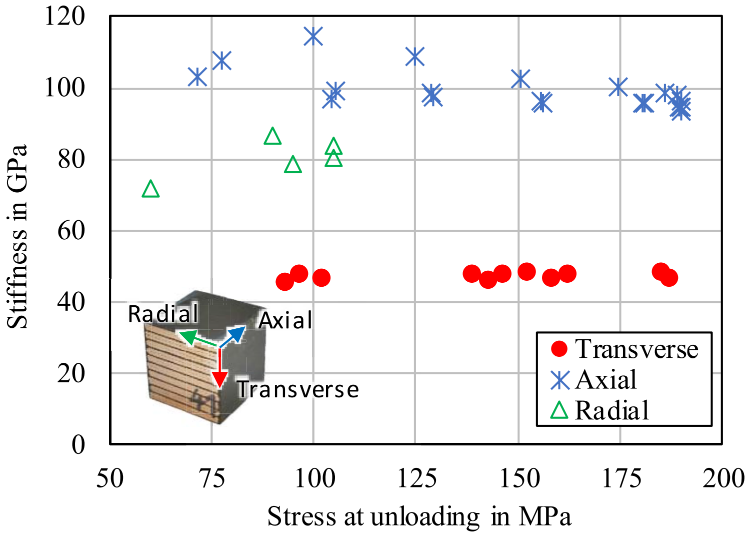

Figure 4.18.: Comparison of the ten-stack sample B stiffness with respect to the load direction ($V_{\text{wire}} = 72.8\,\%$).

4.4. Ten-stack sample stiffness estimation-based composite theories

The evaluated data from the compressive stress–strain measurements in the axial direction of two ten-stack samples with V_{wire} = 74.3% and with V_{wire} = 69.6% allow the comparison with a tensile axial stress–strain curve of a RRP-type wire (V_{wire} = 100%) [129], presented in Figure 4.19. The compressive stress–strain curves are plotted inversely, to ease the comparison with the tensile stress–strain curve. The highest stiffness was determined from the wire of 126 GPa (V_{wire} = 100%). A decreasing stiffness is observed with decreasing wire volume fraction (99.5 GPa for V_{wire} = 74.3% and 94.1 GPa for V_{wire} = 69.6%). The knowledge of the epoxy and wire volume fraction allows the stiffness to be estimated by the linear model by Voigt [57] called the rule of mixtures (ROM) E_{Voigt}, as explained in Section 2.2. Therefore, iso-strain conditions in the wire and in the epoxy impregnated inter-wire space in load direction need to be assumed. Based on the measurement an elastic modulus E_{wire}= 126 GPa can be assumed for the wire, in axial direction. The inter-wire space $E_{\mathrm{non-wire}}$ filled with epoxy resin and S2-glass insulation can be approximated with an elastic modulus of 4 GPa [81]:

$$E_{\mathrm{Voigt}} = E_{\mathrm{wire}} V_{\mathrm{wire}} + E_{\mathrm{non-wire}} V_{\mathrm{non-wire}}. \tag{4.1}$$

The stiffness estimation by the rule of mixture is included in the labels in the plot in Figure 4.19. The variation between the ROM estimation and the measurement is less than 3%, which confirms the assumptions of the ROM. Owing to the low volume fraction of epoxy and S2-glass, their effect on the ten-stack stiffness in axial direction under iso-strain conditions is minor.

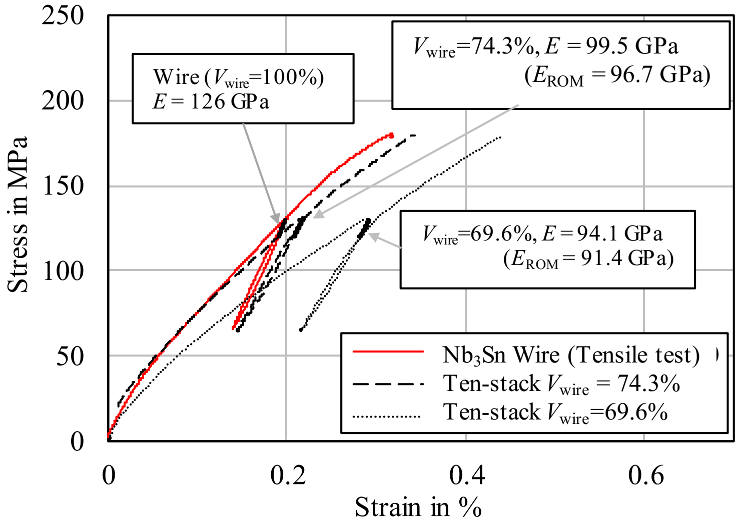

Figure 4.19.: Comparison of compressive stress–strain curves in the axial direction of ten-stack samples with different wire volume fraction with adapted axial tensile stress–strain curve of RRP-type Nb_3Sn wire [129].

In the transverse sample direction, the different material components with individual stiffness are piled in different layers. Therefore, the iso-strain assumption is not representative of the sample loaded perpendicular to the wires. The other theoretic loading extreme is represented by the Reuss model [58] or inverse ROM, which assumes an iso-stress condition to calculate the elastic modulus E_{Reuss} as

$$E_{\text{Reuss}} = \frac{E_{\text{wire}} E_{\text{non-wire}}}{E_{\text{wire}} V_{\text{non-wire}} + E_{\text{non-wire}} V_{\text{wire}}}. \tag{4.2}$$

The transverse stiffness estimation can be calculated by taking similar material assumptions as for the Voigt model. A comparison of the calculated and measured stiffness values in axial and transversal direction with respect to the wire volume fraction is presented in Figure 4.20. The calculated transverse stiffness by the Reuss model is much lower than the measured value, indicating that the stiffness estimation by using the Reuss model [58] based on the assumption of an iso-stress is not valid. Owing to the circular or elliptic shape of the wires, the stress applied to the insulation matrix and the wires is not equal everywhere. This stress distribution is against the basic assumption of the Reuss model. The weighted Neerfeld model, as introduced in Section 2.2, allows a mixed state to be described between both extreme conditions of iso-strain and iso-stress. The stiffness estimations based on the Neerfeld model with respect to the wire volume fraction is shown in Figure 4.20. The weighting factor of $\alpha = 0.17$ is based on the measurement results and need to be validated with more measurements for these type of samples. The stiffness based on the Neerfeld model is calculated as

$$E_{\text{weighted}} = E_{\text{Voigt}}(1 - \alpha) + \alpha E_{\text{Reuss}}. \tag{4.3}$$

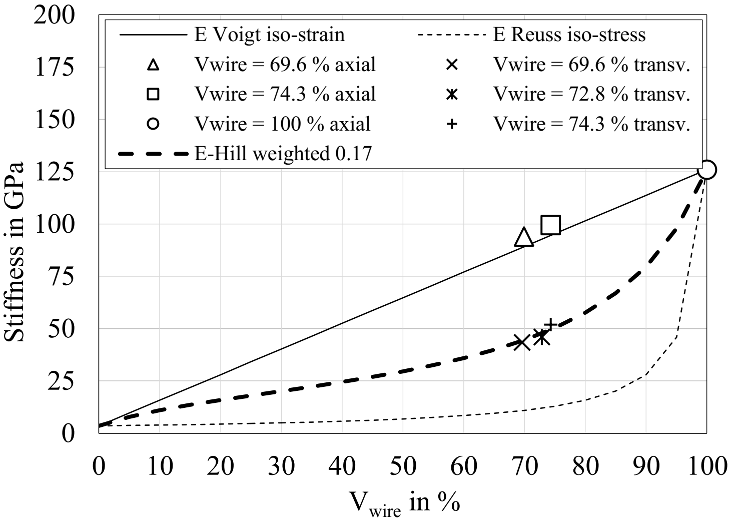

Figure 4.20.: Comparison the axial and transversal compressive stiffness determined by calculation and measurement with respect to the wire volume fraction of the samples.

4.5. Dye penetration test on loaded and unloaded samples

A dye penetration test was performed with a virgin and a transversal loaded (190 MPa) sample to investigate the presence of cracks after high-pressure application. Therefore, a water-washable fluorescent penetrant (ARDROX® 9703) was used for crack indication. The surface of both samples was dry cleaned, before application of the penetrant by brushing. A dwell period of about 10 minutes was allowed for the penetrant. Then the penetrant was removed from surfaces by water washing and the samples were dried. A fast-evaporating, non-aqueous developer (ARDROX® 9D1B) was subsequently applied. The inspection of the samples was done under ultraviolet (UV) light in a darkened area. The dye penetration test of the virgin sample indicates a crack-free surface as shown on the left in Figure 4.21. A clear indication of cracks in the inter-cable insulation system, as well as in the strand surrounding impregnation, can be seen in Figure 4.21 on the right, where the sample was exposed to a transversal pressure up to 190 MPa.

The proven existence of cracks after high load application indicate a changed internal bonding between the components of an impregnated conductor block. The stress–strain behaviour of the sample indicates first signs of creep and a change in the unloading behaviour once loaded above 135 MPa as shown in Figure 4.13 (*top*). Observations made on transversal loaded cable two stack state, that visible cracks in the insulation system start to occur in a transversal applied stress range of 125 MPa to 150 MPa, as presented in Section 3.10, which is with the stress range where changes in the mechanical behaviour are noticed.

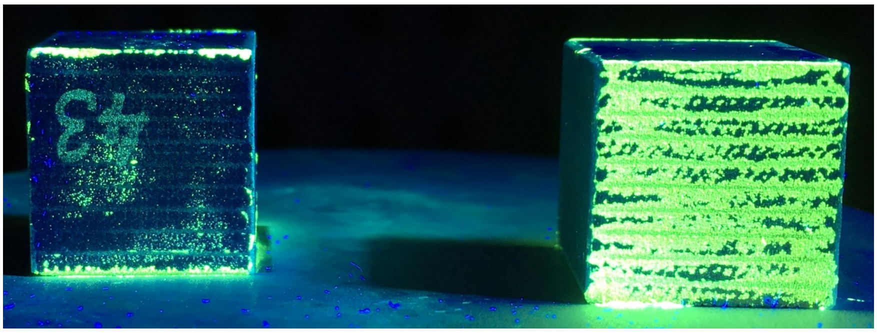

Figure 4.21.: Comparison of an virgin sample (*left*) and a sample after loading (*right*) under UV light prior application of a fluorescent penetrant.

4.6. Conclusion

A conductor block of Nb_3Sn magnet consisting of fibreglass-insulated and epoxy-impregnated Rutherford cables has an anisotropic material characteristic owing its composition of components. The characterisation of its anisotropy requires an investigation of its mechanical behaviour in its principal directions of anisotropy, which are during magnet operation also the principal stress directions of a coil. The mechanical behaviour of a composite material is strongly dependent on the ratio between fibre and matrix material, which requires a sensitivity analysis to investigate the effect of a varying fibre volume fraction to its mechanical behaviour. The volume fraction between matrix and wire is set during the magnet manufacturing process by the cavity size of the tooling, especially during RHT and impregnation.

The direction-dependent compressive stiffness of Nb_3Sn conductor blocks has been determined compressive stress–strain measurements in its three normal directions. The uncertainties of the strain measurement could be reduced by using an extensometer for a direct strain measurement method. The measurements have approved the strongly anisotropic behaviour of the conductor blocks. The highest determined sample stiffness in axial direction (about 95 GPa) is about twice that in the transversal direction and the radial stiffness is a factor of 1.3 higher than the transverse stiffness. The axial stiffness can be well predicted by the ROM, validating the assumption of iso-strain conditions in axial direction. In transversal and radial direction the determined stiffness is higher than predicted by the inverse ROM and dependent on the applied load level. The transverse stiffness increases with increasing load level. Above 135 MPa, a creep behaviour was also observed, whereas also a clear crack propagation could be identified after high load application. The transverse macroscopic stiffness and creep behaviour of a 11 T dipole coil block corresponds to that of the ten-stack samples with similar epoxy volume fraction, suggesting that the mechanical coil behaviour can be represented well by ten-stack samples.

The effect of a varying wire volume fraction of a conductor block to its compressive stiffness has been studied with specimens produced under different compaction levels during manufacturing. A transversal stiffness difference of 10 GPa was determined between samples produced under a low assembly stress of 5 MPa to those at a high assembly stress of 30 MPa.

It remains to be studied how well the test configuration of free-standing ten-stack samples can represent the conductor loading in a magnet coil, where the conductor is constrained in axial and radial directions.

5. Neutron diffraction measurements

The neutron diffraction technique is used in material sciences to determine the residual and applied stress in crystalline materials. Therefore, the deviation of inter-atomic spacing for specific planes in a gauge volume is measured. The lattice planes of a crystal act as a natural internal strain gauge inside a solid. The stress in a crystalline solid can be calculated by the relevant material elastic constants. The lattice spacing of a sample, radiated by a monochromatic neutron beam, can be calculated with respect to the Bragg diffraction relation between wavelength, diffraction angle and lattice spacing of the scattered beam, which is based on an interference phenomena. Therefore, the diffracted beam is detected and evaluated. The penetration power of neutrons enables thereby non-destructive expansion or contraction measurements up to a few centimetres depth in material in the elastic regime, which is different to X-ray diffraction measurements that can only be used in the surface region in the order of nanometres due to the small penetration depth of X-ray in matter. Variations of the experimental configuration have been developed such as continuous source experiments [130, 131] or pulsed neutron experiments [132] for residual stress–strain measurements. The experiment to determine the residual stress state used on most reactor facilities is providing a continuous monochrome neutron beam [70] as also presented in the following section.

5.1. Test set-up for neutron diffraction measurement

The present experimental work was performed at the materials science diffractometer STRESS-SPEC at the FRM II neutron source of the Heinz Maier-Leibnitz Zentrum [133]. A schematic of the experimental area with monochromator, sample table and detector is shown in Figure 5.1. A bent Si (400) monochromator was used to select a specific wavelength of 1.672 Å± 0.003 from the beam of the reactor. Owing to the deep penetration of the neutron beam, diffraction measurements could be performed in the centre of mass of cubic samples with a dimension $15 \times 15 \times 15$ mm^3. The nominal gauge volume is $5 \times 5 \times 5$ mm^3 defined by slit systems made from a neutron absorbing material (collimator made of 3 mm thick boron-based absorber and 1 mm thick cadmium) that shaped the emitted beam to a size of 5×5 mm^2. The beam in front for the detector was limited by a radial collimator with a slit of 5 mm.

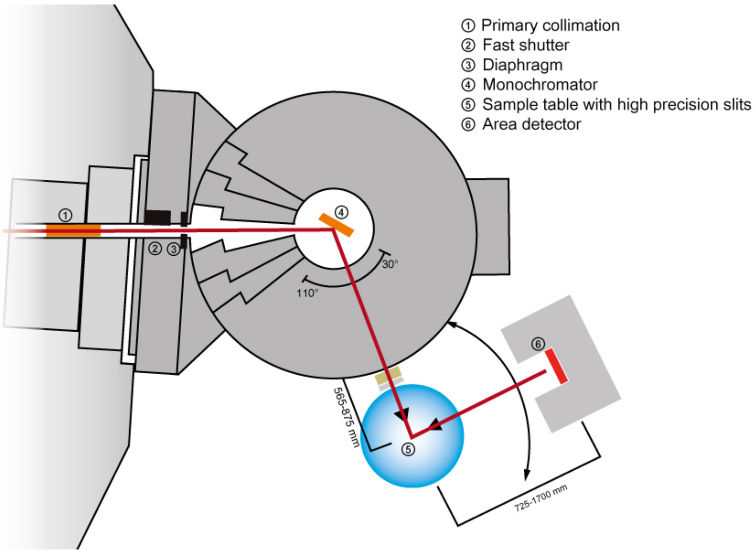

Figure 5.1.: Schematic of STRESS-SPEC [123].

A full-circle Eulerian cradle, equipped with a load frame, carried the sample and enabled the diffraction measurement in different orientations and at different load levels. With a fixed neutron source and detector, the sample was rotated in the beam, where as the applied load direction was the same, once the sample was installed.

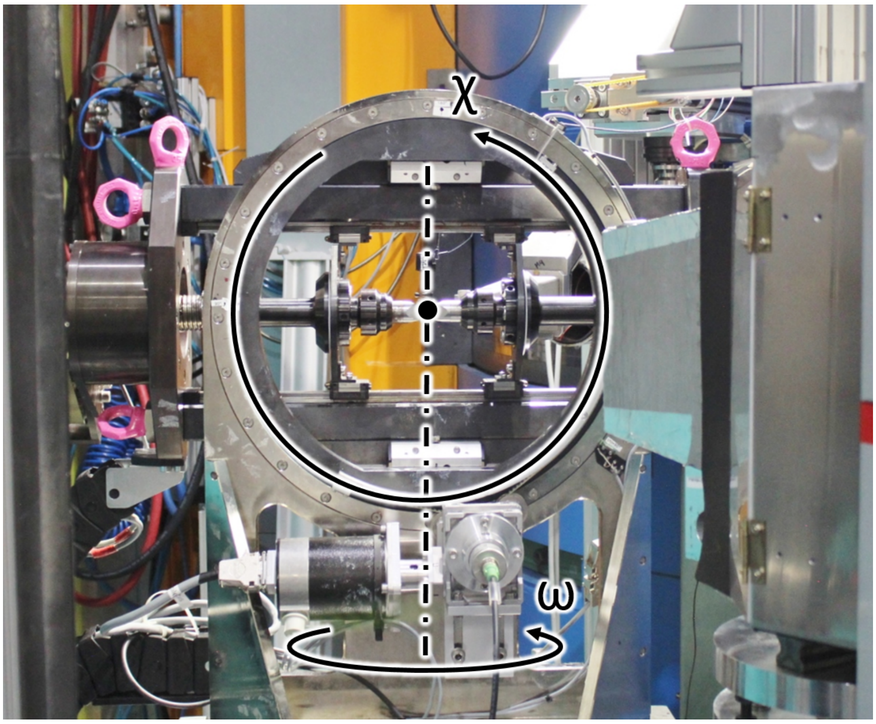

Figure 5.2.: Euler cradle.

The sample coordinate system has been defined in similarity to the cable orientation of a magnet, defining a axial, transversal and radial sample direction, which are the principal directions regarding the applied load in the Euler cradle. The lattice parameter of the samples were measured in these three principal directions. Figure 5.3 indicates the Euler angles in the cradle under uniaxial load with respect to the incident beam.

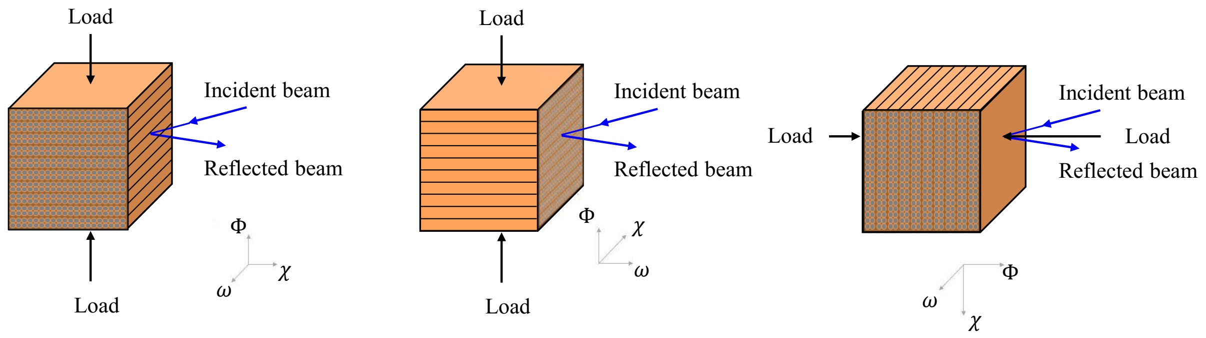

Figure 5.3.: Sample orientations in the Euler cradle with respect to the neutron beam for lattice strain measurements in radial (*left*), axial (*middle*) and transversal (*right*) direction.

The data analysis of the measurements was performed with the analysis Software “STeCa2” [75], which allows a ground correction of the calculated diffraction data to be applied. Furthermore, the Bragg peaks from the diffraction data can be selected and analysed by curve fitting to determine peak positions, peak widths and intensities.

The load frame also enables the installation of a clip-on extensometer, which allows macroscopic stress–strain measurement to be performed *in situ* to the neutron diffraction measurement. Details for the macroscopic stress–strain measurement equipment and procedure are explained in Section 4.1. In order to ease the allocation of the measured data, in the following the stress and strain values determined by the neutron diffraction method are called the lattice strain and lattice stress, as they are based on the lattice parameter changes.

5.2. The samples

Four different types of samples have been studied. Three of them are so-called ten-stack samples, introduced in Section 4.2 with all relevant manufacturing details. The fourth sample type is a $Sn_{96}Ag_4$ filled cable stack. The mechanical properties of the different used matrix materials are listed in Table 5.1.

Table 5.1.: Mechanical properties of the matrix materials.

Material	Elastic modulus	Yield strength
CTD-101K [81]	4.1 GPa	60 MPa
CTD-101K + S2 [140]	12.9 GPa	790 MPa
$Sn_{96}Ag_4$ [106]	60.6 GPa	26 MPa

A small quantity of samples was prepared to investigate the effect of the matrix material stiffness to stress–strain state of the strand in the cable stack. Therefore, samples were prepared consisting of a reacted Nb_3Sn cable ten-stack partly filled by a solder $Sn_{96}Ag_4$. The insulation from the cable has been removed, as it was not possible to fill the fibreglass voids with solder. A thin layer of solder flux Gel Mob 39 has been applied on the solder stripes and the bare cables to improve the contact between cable and solder. The so-prepared cable and solder stripes have been piled up with alternating keystone angle to a ten-stack in a specially designed mould as shown in Figure 5.4. The mould has been equipped with two heat cartridges and a thermocouple, powered and controlled by a laboratory power supply with a programmable heat plateau. The mould was heated up to 150 °C for 2 minutes to exceed the flash point of the flux (at 100°C) and further heated up for 30 seconds at 230°C to exceed the melting point of the solder (at 221°C).

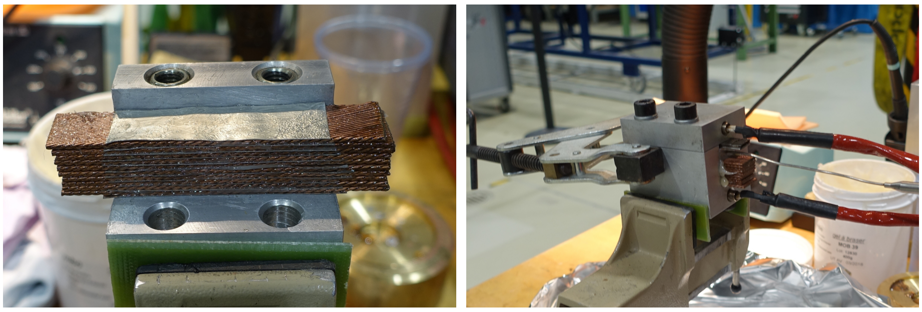

Figure 5.4.: Alternating stacked cables with solder stripes (*left*) inserted into the heat-treatment mould with heat cartridges and thermocouple for soldering (*right*).

The local sample coordinate system with respect to the cable orientation is as presented in Section 4.3 Figure 4.12 , whereas transversal is always defined as perpendicular to the wide face of the cable. The radial direction is perpendicular to the narrow side of the stacked Rutherford cables and axial is normal to the stack cutting section.

5.3. Experiment: lattice stress–strain measurements

In preparation of the sample investigation in the neutron beam, a neutron diffraction measurement of Nb_3Sn powder extracted from a Nb_3Sn 11 T 107 coil segment was performed in the range 40° to 120° to identify the scanning range for strong Nb_3Sn reflexes. A very high intensity of the diffraction from the Nb_3Sn (321) and Cu (220) lattice plane was determined at an angle of about 72.8° and 81.9° respectively. In order to reduce the scanning time, the scanned angle range was adjusted to 70.5° to 83.5° for the investigation of the ten-stack samples, which includes the Nb_3Sn (321)and the Cu (220) reflection. The Nb_3Sn (321) reflection represents well the overall Nb_3Sn strain behaviour, which has been performed in previous studies by stress-dependent synchrotron X-ray diffraction measurements [134]. The Cu (220) reflection represents the pure Cu stabiliser in the strand.

The samples were fixed in the Euler cradle with a pre-load of 0.2 kN (about 1 MPa) enabling the extensometer to be attached prior to the diffraction measurement. Measurements were performed with applied stress steps of 15 MPa, and the load rate between the stress plateaus was always 50 N/s. The acquisition time for the recording of the Nb_3Sn (321), and Cu (220) diffraction peaks in each orientation takes about 15 minutes. The Nb_3Sn (321) and Cu (220) reflections were fitted by Gaussian functions. An incoherent scattering from a vanadium scan was used as reference angle to precisely adjust the diffraction data prior the analysis. The Nb_3Sn and Cu lattice strains ε_{hkl} in transverse, axial and radial directions have been determined from the Nb_3Sn (321) and Cu (220) scattering angles θ_{hkl} according to Equation (2.39) in Section 2.5.4. The assumed stress-free scattering angles for the calculation are $2\theta_{0,\mathrm{Nb_3Sn}}$ (321) = 72.783° and $2\theta_{0,\mathrm{Cu}}$ (220) = 81.937°. The lattice stresses have been calculated according to Equation (2.41) in Section 2.5.5, assuming that the transverse, axial and radial directions are the principal stress directions in the sample. Table 5.2 summarises Young's moduli E_{hkl} and Poisson's ratio ν_{hkl} that are calculated from single-crystal constants by the Kröner model [77], which was used as it is the most widely accepted approach [133] to calculate the elastic constants.

Table 5.2.: Single-crystal elastic constants of Nb_3Sn [78] and Cu [79] with corresponding elastic constants calculated by the Kröner model.

	hkl	C_{11} (GPa)	C_{12} (GPa)	C_{44} (GPa)	E_{hkl} (GPa)	ν_{hkl}
Nb_3Sn	321	253.8	112.4	39.57	131.2	0.363
Cu	220	168.4	121.4	75.4	138.9	0.331

Results: transverse compression

The evolution of the Nb_3Sn and Cu lattice strains and stresses in a non-impregnated cable stack under transverse compression in its three principal directions are presented in Figure 5.5. Up to an external stress of 50 MPa, Nb_3Sn is under slight axial compression and Cu under slight axial tension. This difference might be caused by the thermal expansion mismatch of the different conductor constituents during cooling from the Nb_3Sn RHT temperature of 650°C. Above the external transverse stress level of 50 MPa, a similar compressive Cu lattice stress evolution is observed in the three principal directions (Figure 5.5(d)). The compressive Cu pressure in axial and radial directions imposes an axial and radial tensile stress on the Nb_3Sn filaments (Figure 5.5(c)).

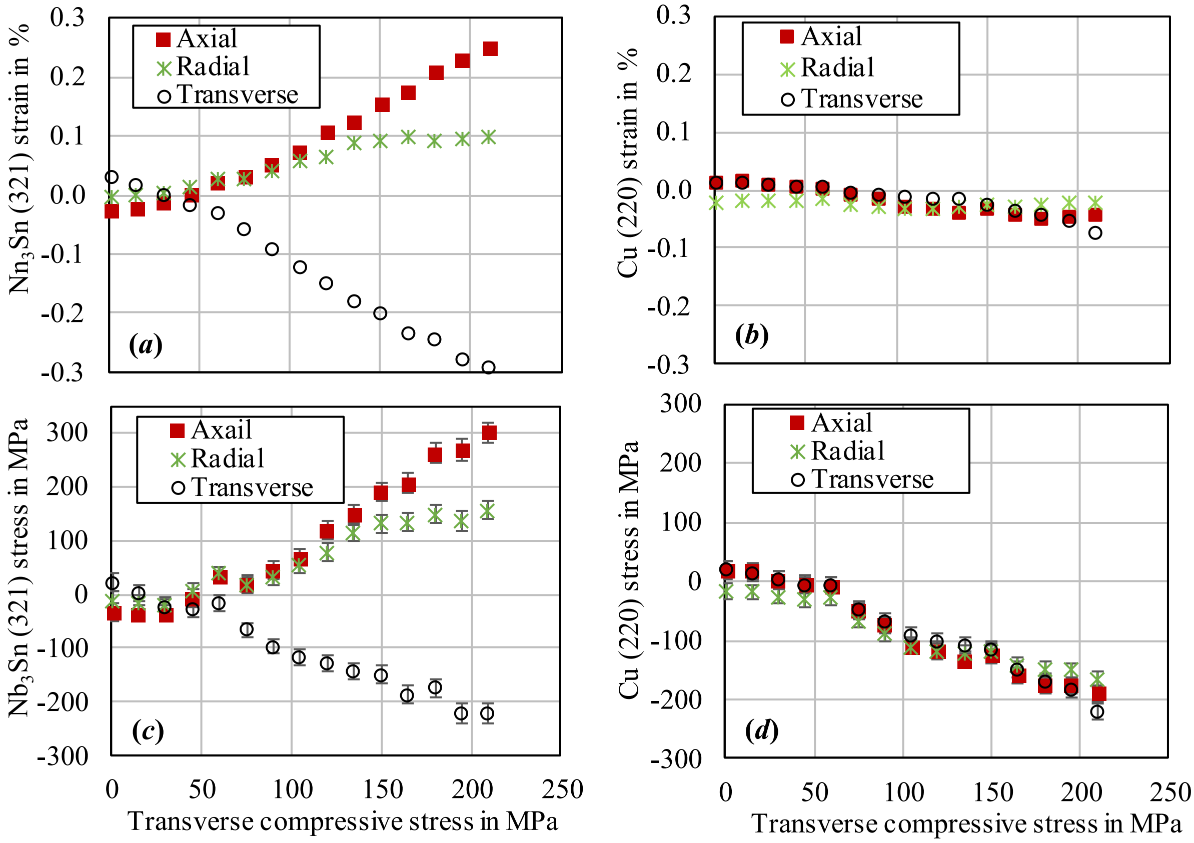

Figure 5.5.: (*a*) Nb_3Sn (321) and (*b*) Cu (220) lattice strains and (*c*) Nb_3Sn (321) and (*d*) Cu (220) stresses in non-impregnated cable stack as a function of externally applied transverse compressive stress.

In Figure 5.6 the Nb_3Sn and Cu lattice stresses in the non-impregnated cable stack are compared. In transverse direction (i.e. the loading direction), the stress determined in Nb_3Sn and Cu are nearly identical, and the transverse lattice stresses increase linearly with increasing external applied stress. The equal stress level in the Cu and Nb_3Sn indicates that the stress state in the composite is close to an iso-stress behaviour when loaded perpendicular to the flat side of the cable. The determined lattice stress of Nb_3Sn and Cu is about 20% higher than the external applied stress. The difference might be explained by the presence of about 25% porosity in the sample that does not carry load. In radial direction Nb_3Sn and Cu lattice stresses have similar magnitude, Nb_3Sn being in tension and Cu in compression. In axial direction the higher Nb_3Sn tensile stress with respect to the Cu compressive stress can be explained by comparatively smaller Nb_3Sn cross-section with respect to the Cu cross-section.

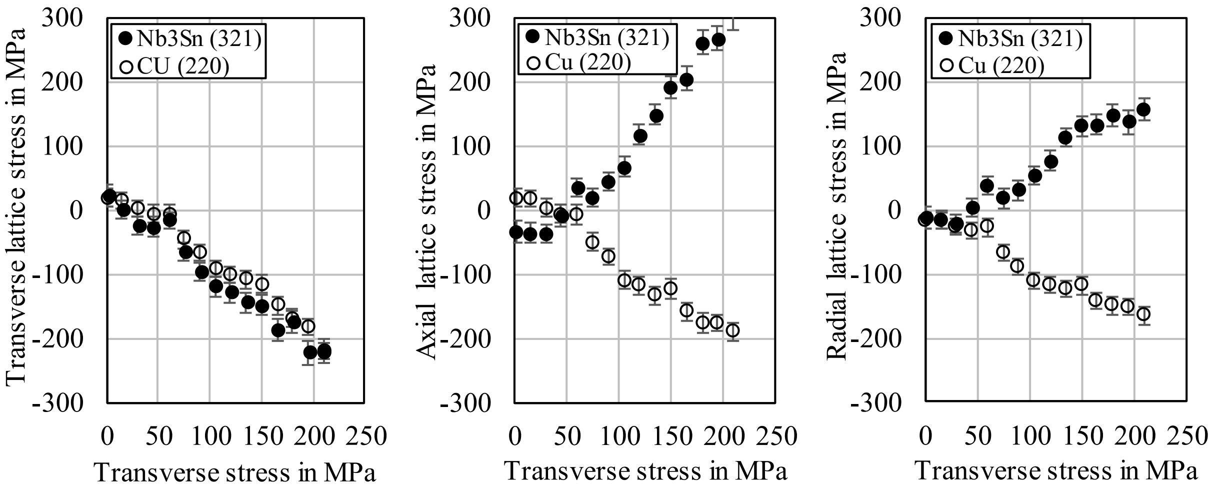

Figure 5.6.: Comparison of Nb_3Sn (321) and Cu (220) lattice stress evolution in transverse (*left*) , axial (*middle*) and radial (*right*) directions as a function of externally applied transverse compressive stress of a non-impregnated sample.

The Nb_3Sn lattice stresses shown above are average values inside the gauge volume. The maximum Nb_3Sn stresses are likely higher, as indicated by the Nb_3Sn diffraction peak broadening when the external load is increased (Figure 5.7). Nb_3Sn diffraction peak broadening indicates that the strain inhomogeneity increases, which occurs first in transverse and radial directions. When the external transverse pressure on the non-impregnated cable stack exceeds 130 MPa, Nb_3Sn (321) peak broadening is also observed in the axial direction.

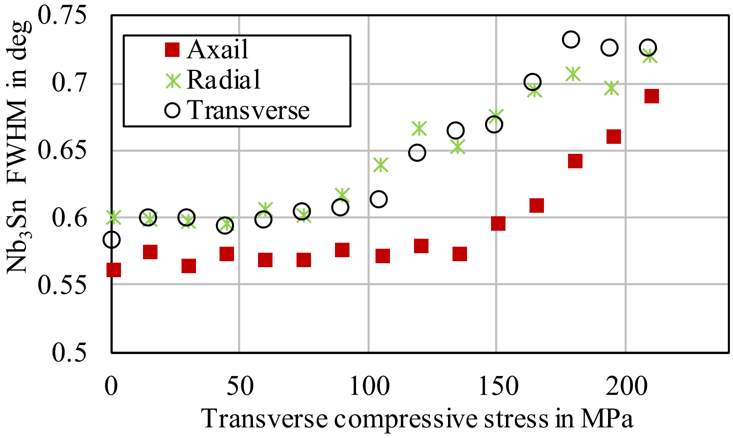

Figure 5.7.: Nb_3Sn (321) diffraction peak width evolution as a function of externally applied transverse compressive stress of a non-impregnated sample.

Results: axial compression

Figure 5.8 presents the Nb_3Sn and Cu lattice stress evolution in an impregnated cable stack under axial compressive loading. At 150 MPa applied axial pressure the axial Nb_3Sn (321) and Cu (220) lattice stresses are about 300 and 100 MPa, respectively. This stress evolution is compatible with the assumption of iso-strain conditions when the conductor is loaded in the wire direction.

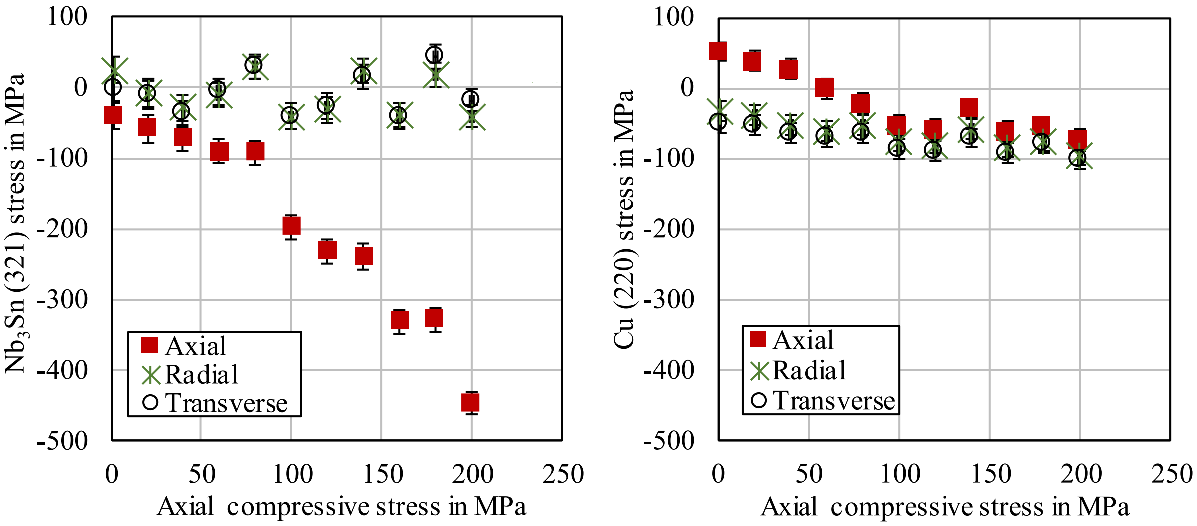

Figure 5.8.: (*a*) Nb_3Sn and (*b*) Cu lattice stresses in impregnated cable stack as a function of axial compressive stress.

The assumption of iso-strain conditions under axial load as predicted by composite theory is further confirmed by the comparison of the strain evolution of the macroscopic sample strain and the Nb_3Sn lattice strain as shown in Figure 5.9. The axial Nb_3Sn lattice strain is proportional to the axial macroscopic sample strain with a constant offset in lattice strain, which might be explained by the residual strain due to thermal processing.

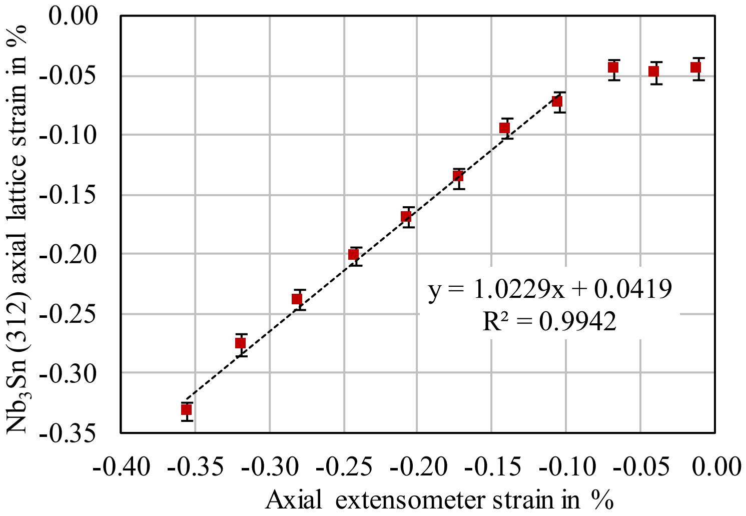

Figure 5.9.: Elastic axial strain derived from neutron diffraction data as a function of the macroscopic axial sample strain measured with an extensometer under axial applied load.

Results: impact of matrix material under transversal load

The stress-dependent neutron diffraction measurement was furthermore used to study the effect of the impregnation system of Rutherford cable stacks on the Nb_3Sn lattice strains. Therefore, the four sample types introduced in Section 5.2 are investigated under transverse load by neutron diffraction measurements. A comparison of the Nb_3Sn (321) lattice strains in the three principal directions of an epoxy-impregnated, non-impregnated, $Sn_{96}Ag_4$ filled ten-stack and an extracted coil conductor block under transverse load is shown in Figure 5.10. The Nb_3Sn lattice strains in the $Sn_{96}Ag_4$ filled ten-stack in all directions are even higher than in the non-impregnated cable stack. Lowest Nb_3Sn lattice strains have been measured in the epoxy-impregnated samples, indicating that the impregnation system can reduce the Nb_3Sn lattice strain in the conductor when the compound is exposed to high macroscopic load. The measurement furthermore indicates that at a level of 50 MPa the effect of the impregnation system on the transferred Nb_3Sn lattice strain is negligible.

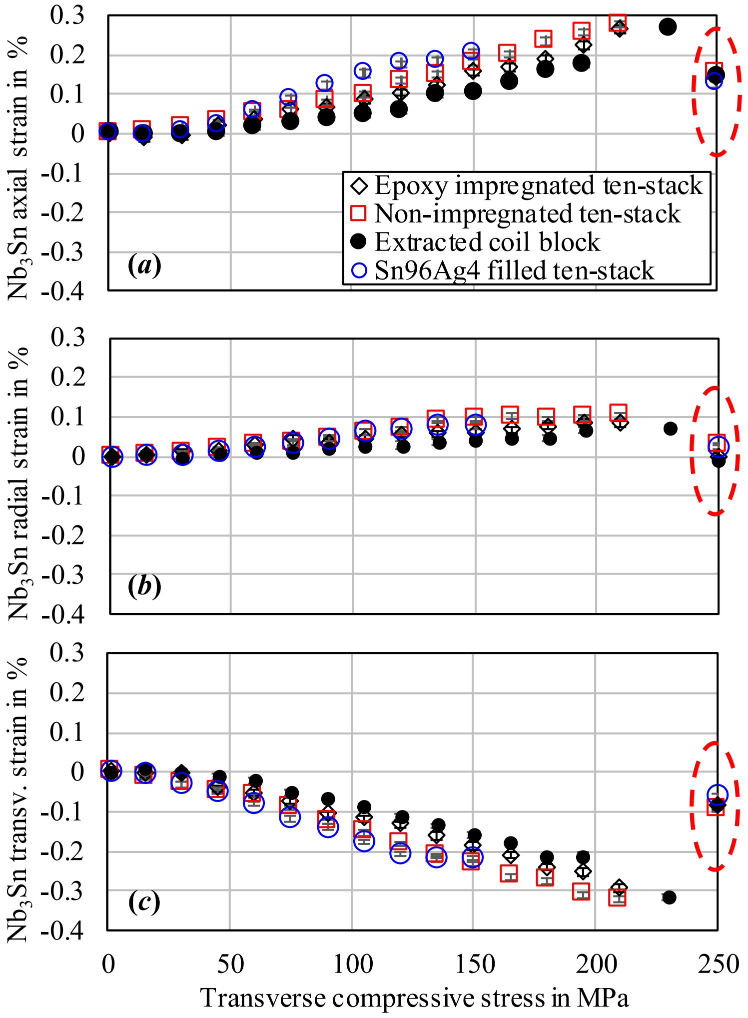

Figure 5.10.: Comparison of the Nb_3Sn (321) lattice strain evolution during application of transverse compressive stress in (*a*) axial, (*b*) radial and (*c*) transverse directions. The data points encircled with red dashed lines have been measured after releasing the external stress.

The $Sn_{96}Ag_4$ filling of the cable stack causes a strong buckling under transverse compression, as can be seen in the tomographic cross-sections shown in Figure 5.11. The cross-sections have been obtained by non-destructive X-ray μ-CT after compression tests. A very strong buckling of the $Sn_{96}Ag_4$-filled sample is observed after application of a transverse compressive stress of 150 MPa, whereas no strong buckling effect is seen in the epoxy-impregnated sample after application of 200 MPa transverse stress owing to the different behaviour of the filling material above its elastic limit in lateral expansion.

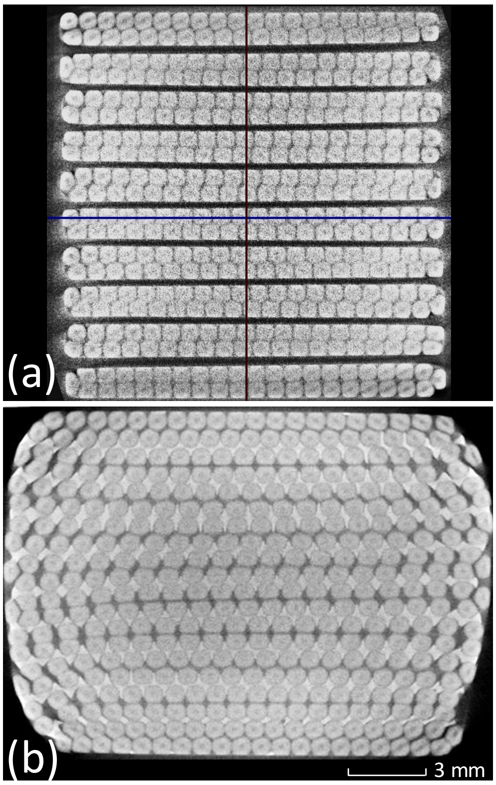

Figure 5.11.: Comparison of 11 T dipole Nb_3Sn Rutherford cable ten-stack sample tomograms (*a*) epoxy-impregnated and (*b*) partly filled with $Sn_{96}Ag_4$ solder. The epoxy-impregnated and $Sn_{96}Ag_4$-filled samples were compressed in transverse direction up to 200 and 150 MPa, respectively.

Further information about the lattice stress–strain evolution in the sample upon applied load can be achieved by analysing the diffraction peak width at half maximum above the background, the so-called full width at half maximum (FWHM) value. Thereby, changes of the FWHM value due to application of mechanical load may indicate changes of the Nb_3Sn lattice stress homogeneity [137]. A comparison of the Nb_3Sn (321) FWHM values during applied transverse compressive stress for the studied sample types is shown in Figure 5.12. A broadening of the Nb_3Sn (321) peak of the $Sn_{96}Ag_4$ solder-filled sample can be observed when the applied load exceeds 50 MPa, whereas in the epoxy-impregnated cable stacks the peak width remains constant until the load exceeds 100 MPa. It indicates that the peak width broadening and the related stress inhomogeneity can be reduced by an epoxy–fibreglass insulation system. Further it is also indicated that the effect of the insulation system at low stress levels up to 50 MPa is minor.

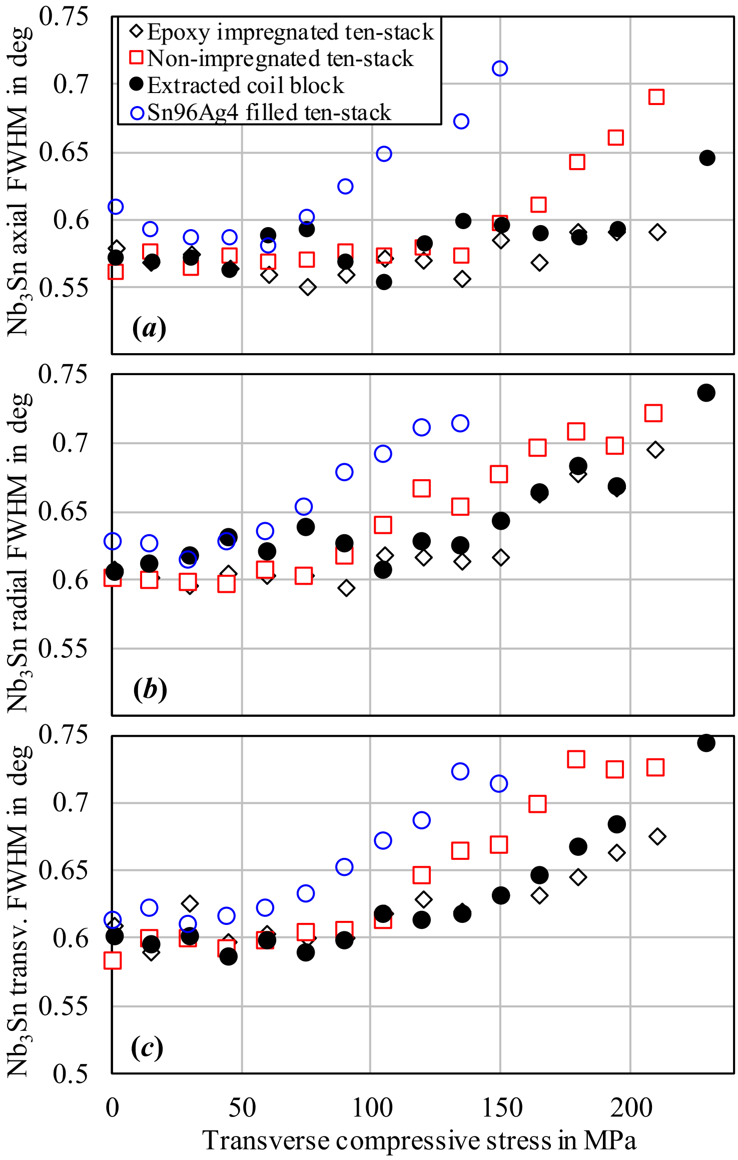

Figure 5.12.: Comparison of the Nb_3Sn (321) diffraction peak width evolution during application of transverse compressive stress in (*a*) axial, (*b*) radial and (*c*) transverse directions.

Results: cyclic loading in comparison to monotonic loading

In order to study the elastic and residual lattice stress–strain behaviour upon applied transversal load of a sample, a non-impregnated Rutherford cable stack has been exposed to cyclic transverse compressive loading. The lattice strain and lattice stress evolutions of Nb_3Sn (321) and Cu (220) are shown in Figure 5.13. The load has been increased in 15 MPa steps. After each step the load was released down to 1 MPa. The lattice Nb_3Sn (321) and Cu (220) lattice strain and stress remain almost unchanged up to a stress level of 45 MPa. Above this stress level, Cu (220) transmits an isotropic pressure that corresponds to the externally applied stress, enabling a stress above its yield limit to be applied. The Nb_3Sn filaments exert a radial and axial stress in the opposite direction to the Cu (220). When releasing the externally applied load, the Nb_3Sn and Cu lattice stresses are released in the transverse direction, but not in the axial and radial directions. The lattice of Cu (220) reaches a maximum at an applied stress level of 165 MPa, which might indicate a limit of the load-carrying capability of the copper.

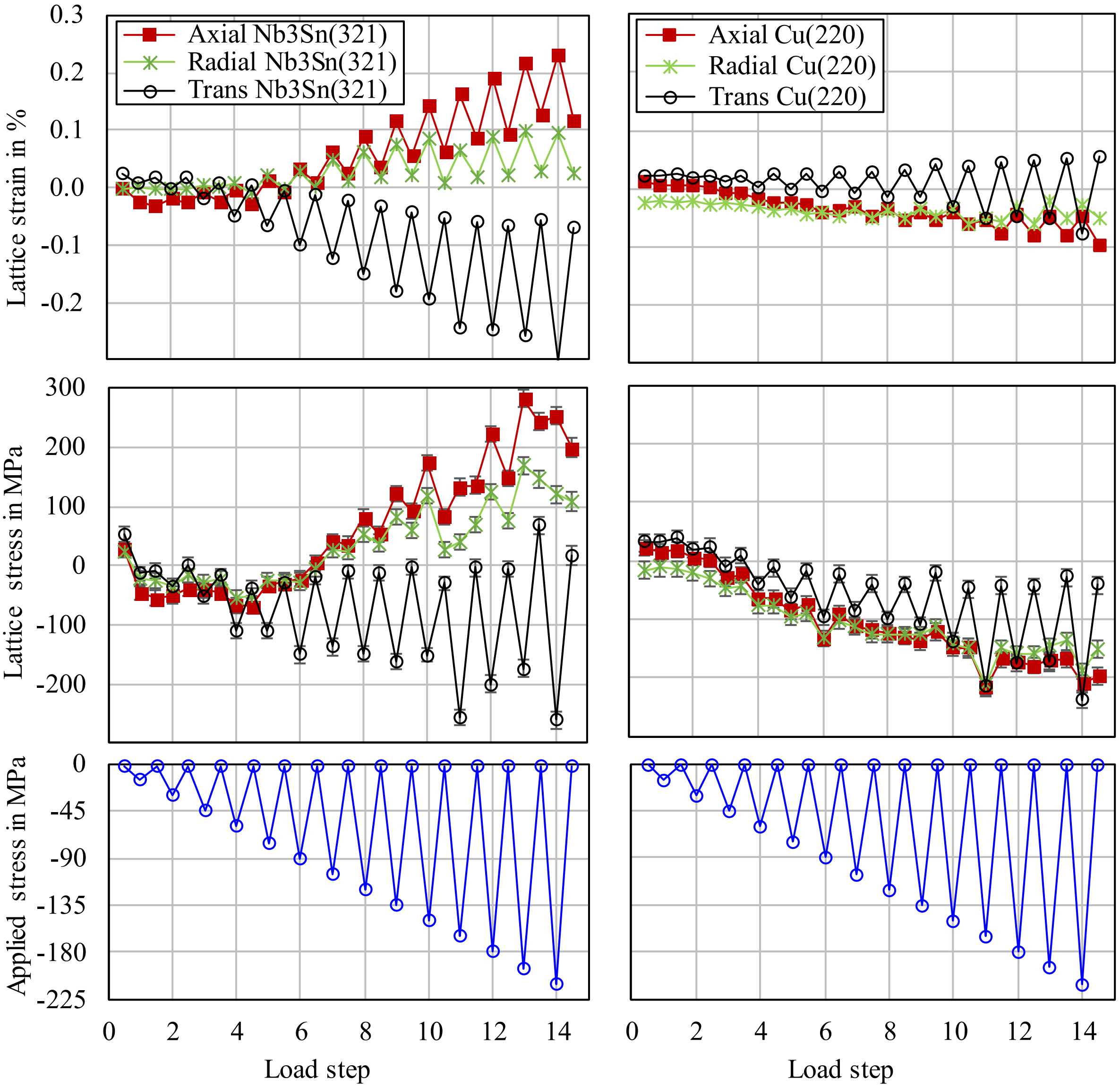

Figure 5.13.: Nb_3Sn (321) and Cu (220) lattice strain and stress evolution in axial, radial and transverse directions of non-impregnated ten-stack sample, as a function of cyclic applied transverse compressive stress. The load cycle is shown in the lower plot.

A comparison of Nb_3Sn lattice strains of non-impregnated ten-stack samples and impregnated coil conductor blocks is evaluated from monotonic and cyclic transverse stress-dependent neutron diffraction measurements in Figure 5.14. For the cyclic loading, only the strain values measured at the stress maxima are taken into account. The lattice strain of the Nb_3Sn is not affected by cyclic loading, as the same lattice strain values are observed, irrespectively of the monotonic or cyclic loading. This further indicates an excellent reproducibility of the performed experiments.

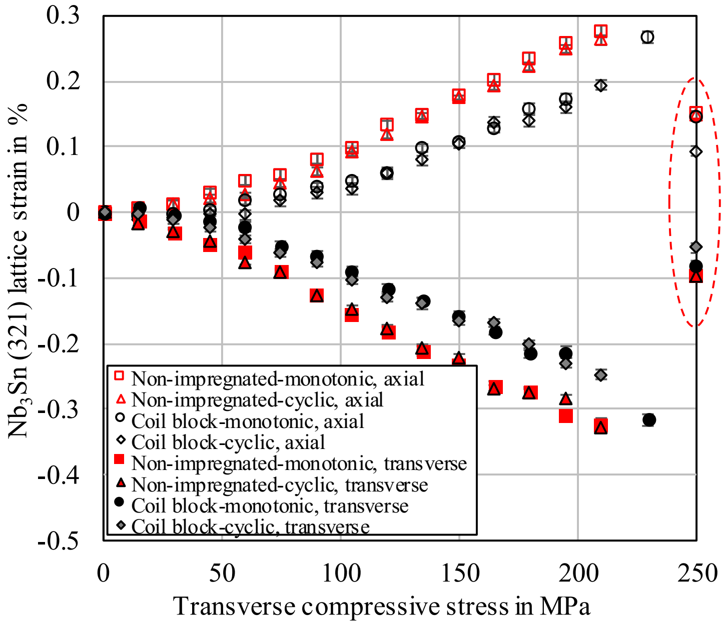

Figure 5.14.: Comparison of Nb$_3$Sn (321) transverse and axial lattice strain evolution under monotonic and cyclic loading as a function of compressive stress applied in transverse direction. The data points encircled with red dashed lines have been measured after releasing the external stress.

5.4. Conclusion

The superconducting strands in a Nb$_3$Sn conductor block are embedded in an epoxy–fibreglass matrix. The strand contains the strain-sensitive Nb$_3$Sn filaments surrounded by heat-annealed copper. A knowledge about the strain state of the copper and the superconducting filaments of a strand under external applied load are necessary to understand the stress distribution in the complex compound. These helps to optimize high field magnet designs with respect to the mechanical limits of the conductor.

A combined neutron diffraction and stress–strain measurement allows to measure the lattice stress and strain state of the Nb$_3$Sn and copper in the strand of a conductor block under applied load. The stress components are defined in the principal directions of the sample and named transversal, axial and radial direction. Measurements under transversal applied load have shown, that the Nb$_3$Sn filaments are compressed in transverse direction and under tensile stresses in radial and axial direction, which is a critical stress combination as it gives high equivalent stresses in common equivalent stress models. The copper is compressed transversally to the same level as the Nb$_3$Sn. The axial and radial stress components are also under compression to an equal stress level. The hydrostatic stress state enables the heat annealed copper to carry loads above its uni-axial yield strength. A strain inhomogeneity increase in the Nb$_3$Sn is measured beyond an applied load of 130 MPa, which indicate changes in the strain state of the Nb$_3$Sn caused by cracks. The measured stress–strain state in the strand can be used to validate stress predictions by FEM models on a strand level.

The measured complex stress state underlines the importance of a 3D model to calculate correctly the stress components in the strand. A comparison of the measured stress state in the conductor exposed to monotonic and cyclic load increase does not show a significant difference. The applied stress has to be increased in order to raise the stress in the Nb_3Sn filaments of copper. Ratcheting effects were not investigated as the load cycling as not repeated to the same stress level.

The measurements have shown that under axial applied load, the axial macroscopic strain is equal to the axial lattice strain of the copper and of the Nb_3Sn in the strand. This approval of iso-strain conditions in the axial direction supports the assumption of considering the Nb_3Sn coil as a fibre-reinforced composite in axial direction, where the Nb_3Sn filaments represent the reinforcing fibres and the copper and epoxy resin the matrix material. Thereby the stress in the Nb_3Sn is by a factor 2 higher than the axial applied sample stress, indicating that the filaments are carrying most of the axial applied load.

The Nb_3Sn strain state of samples with different strand surrounding matrix materials under transversal load have been compared. Samples with $Sn_{96}Ag_4$ filling, glass fibre resin reinforcement and non-impregnated samples are compared. The glass fibre reinforced resin matrix transfers the lowest stress to the Nb_3Sn under applied load and indicates the lowest strain inhomogeneity determined by the diffraction peak width. A good bonding and penetration between resin and strand has been observed, which improve the stress distribution. The reinforcement of the fibre glass reduces lateral expansion and increases stiffness, as fibre reinforces the resin beyond its yield strength. Even though the stiffness of $Sn_{96}Ag_4$ is by a factor five higher than the one of the reinforced resin, it is due the bad penetration behaviour and low yield strength a bad candidate to reinforce the strands. The yield strength is less than half the one of pure resin. A good candidate for a matrix material should have high stiffness and high yield strength with similar penetration behaviour as resin, in order to reduce the transferred stress on the Nb_3Sn filaments of a strand.

6. Simulation and modelling of Nb_3Sn cables

The mechanical models presented in the following are based on static structural calculations performed in ANSYS® Workbench 17.2. The observations made by macroscopic compressive stress–strain measurements of impregnated Nb_3Sn conductor blocks shall be reproduced and property driving parameters and effects shall be identified by 2D models. Therefore, the focus is on the following aspects:

- macroscopic elastic–plastic behaviour under compressive load up to a level of 200 MPa;
- increased elastic stiffness with increasing load level;
- slope change in the stress level range 15 MPa to 0 MPa while unloading;
- impact of adhesive failure between the impregnation system and strands on the stress–strain behaviour.

Three-dimensional simulations are used to validate the basic assumptions in terms of principal strain direction, which are used for the analysis of neutron diffraction data. Furthermore, the determined stress–strain state of the Nb_3Sn and copper, presented in Section 5.3, are compared with the results from 3D FEM calculations. The main aspects of investigation for the 3D numerical simulation are:

- validate the assumption of the principal strain directions;
- validate the stress state of copper and Nb_3Sn components of a strand.

6.1. The models

A 2D and a 3D modelling strategy have been used to investigate the effects that were observed during mechanical measurements as mentioned in the introduction of Section 6. The 2D model was generated based on data from a X-ray micro-computed tomography (μ-CT) of a cable two-stack. The tomography of a double keystoned cable stack was performed at the *Bundesanstalt für Materialforschung und -prüfung* (BAM), Berlin, using a μ-CT scanner with a 225 kV micro-focus X-ray tube with 6 µm focal spot size and a flat panel detector (2048 × 2048 pixels) [110]. The cable surface data were generated by a surface reconstruction from the tomographic data in collaboration with the *Fraunhofer Institut für Techno- und Wirtschaftsmathematik in Kaiserslautern* by D. Mosbach and K. Schladitz. The surface data were processed by a CAD software to generate 2D splines, representing the outer contour line of each strand. The copper core, Nb_3Sn phase and the surrounding copper phase of each strand was modelled by geometric scaling of the strand contour. The so-generated 2D model is shown in Figure 6.1.

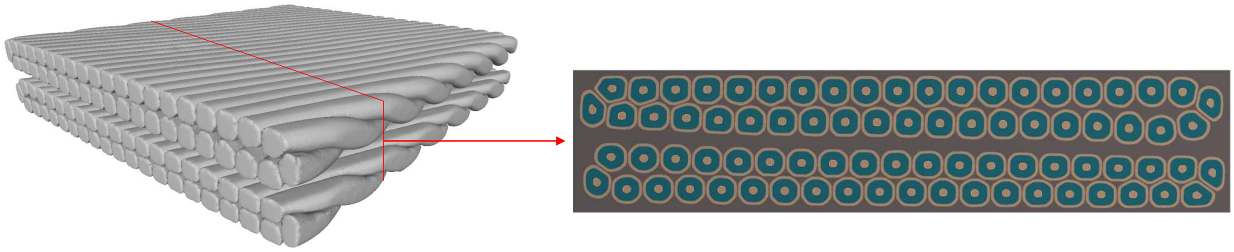

Figure 6.1.: Rutherford cable shape based on surface reconstruction (*left*) and 2D cable model (*right*).

The 3D model is based on a selected cable of a cable ten-stack, generated by multiphase extruded cylinders. The cable is represented by two layers of crossing strands respecting the cable twist pitch angle of 16.4°. The investigated area of interest in the ten-stack sample and the reconstructed model are shown in Figure 6.2.

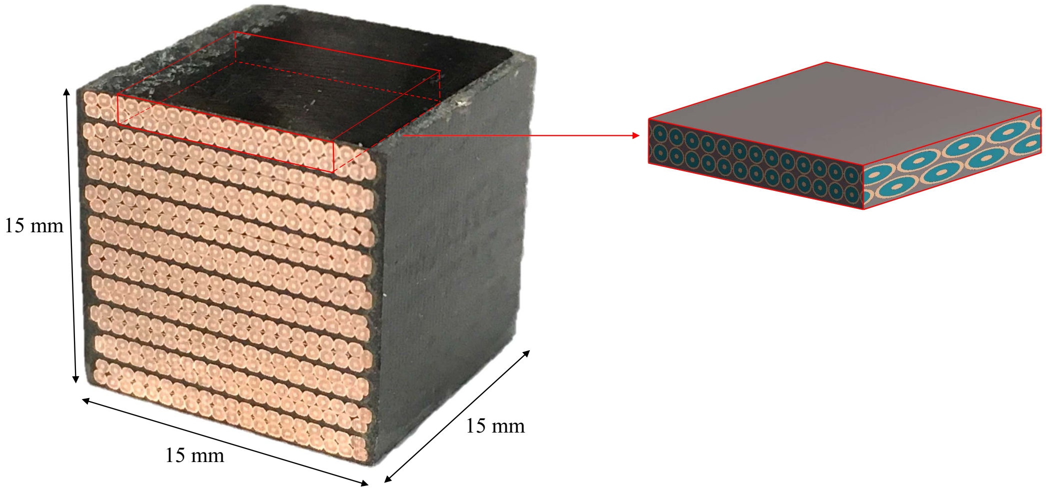

Figure 6.2.: Cable ten-stack compared with the simplified CAD-based model of a cable stack.

Model simplifications and generation

The presented 2D model of the cable is a plane strain ($\varepsilon_z = 0$) model of the cable cross-section consisting of strands with copper and superconducting phase and a surrounding epoxy matrix as suggested in previous studies [138, 139]. The twist pitch of the wound cable cannot be represented by a 2D model. However, the presented model takes into account the cross-sectional deformation of each strand and the keystoned shape of a Rutherford cable, as it is based on data from a surface reconstruction of a tomography of a Rutherford cable. The triangular surface data from the reconstruction was further processed. The STL model (Standard Triangulation Language) was sliced, to build up 2D models. The superconducting phase and the copper core have been modelled by mathematical scaling of each strand surface area with respect to the corresponding geometric centre of each strand. The geometric scaling factor of 0.82 for the outer copper boundary and 0.25 for the inner copper core was used, based on the scaling relation presented in [139]. The so-generated model including copper phase (orange) and superconducting phase (green) is shown in Figure 6.3 in comparison with a microscopic cross-section, identifying each component. The surface manipulation and geometry modelling was done with a CAD software. The presented simplified cable model neglects the 25 µm stainless steel core and the 80 µm surrounding C-shaped mica film. The model with all generated components is shown in Figure 6.4.

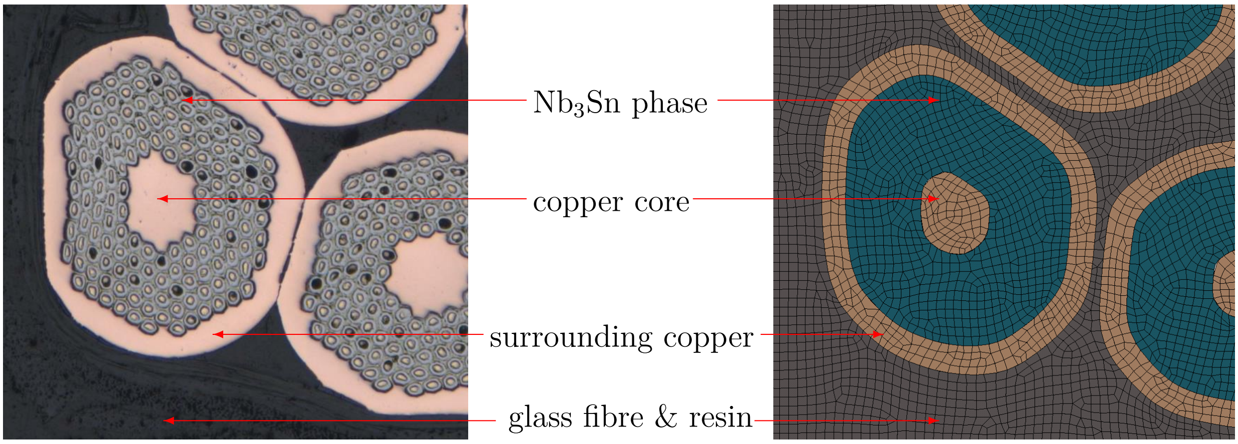

Figure 6.3.: Detailed microscopy of a cable (left) and detailed view of the 2D cable model (right) identifying all reconstructed components.

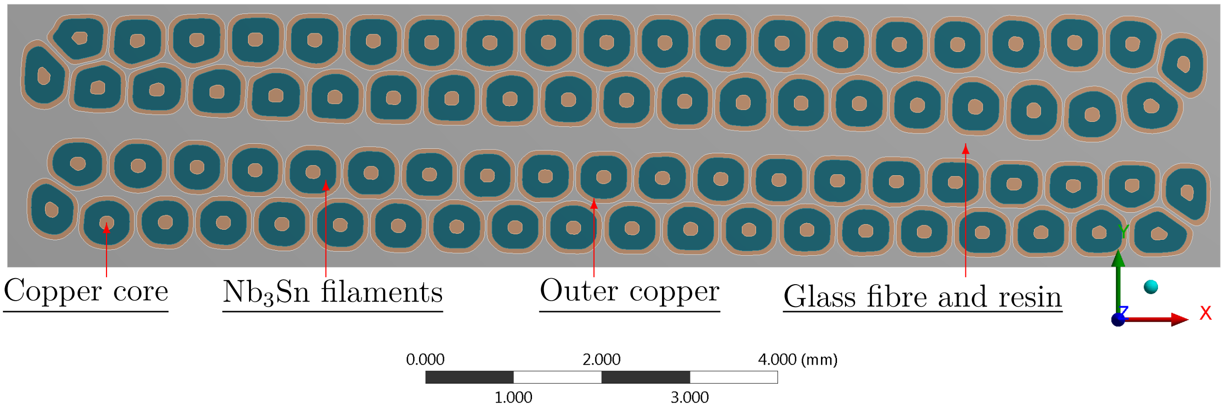

Figure 6.4.: Detailed ANSYS cable model with all generated components.

The 3D model based on extruded geometries is shown in Figure 6.5. Each strand is designed with the same scaling method as used for the 2D model to create the copper core, Nb_3Sn phase and an outer copper phase. The simplified 3D model does not represent the deformed cable edges and the keystone angle of the cable. The objective of this model is the analysis of the stress state in the central region in a sphere with 5 mm edge length, according the inspected volume by diffraction analysis in Section 5.3. The elements within the area of interest are highlighted in pink in Figure 6.6, as this region was investigated by neutron diffraction analysis.

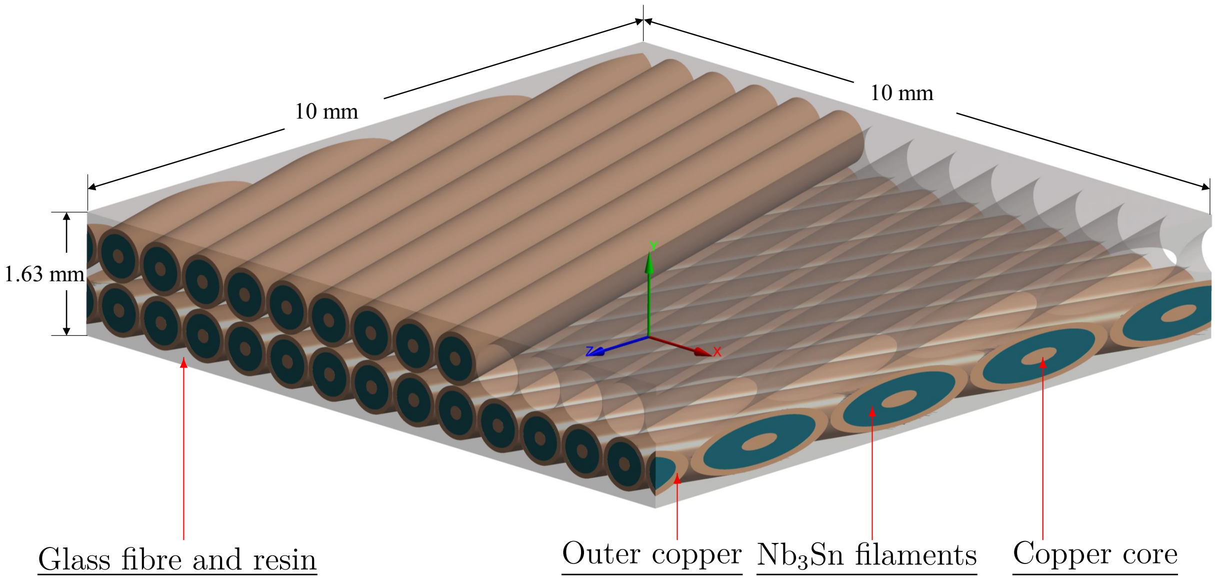

Figure 6.5.: Three-dimensional cable stack model indicating the different modelled components and the orientation with respect to the global coordinate system.

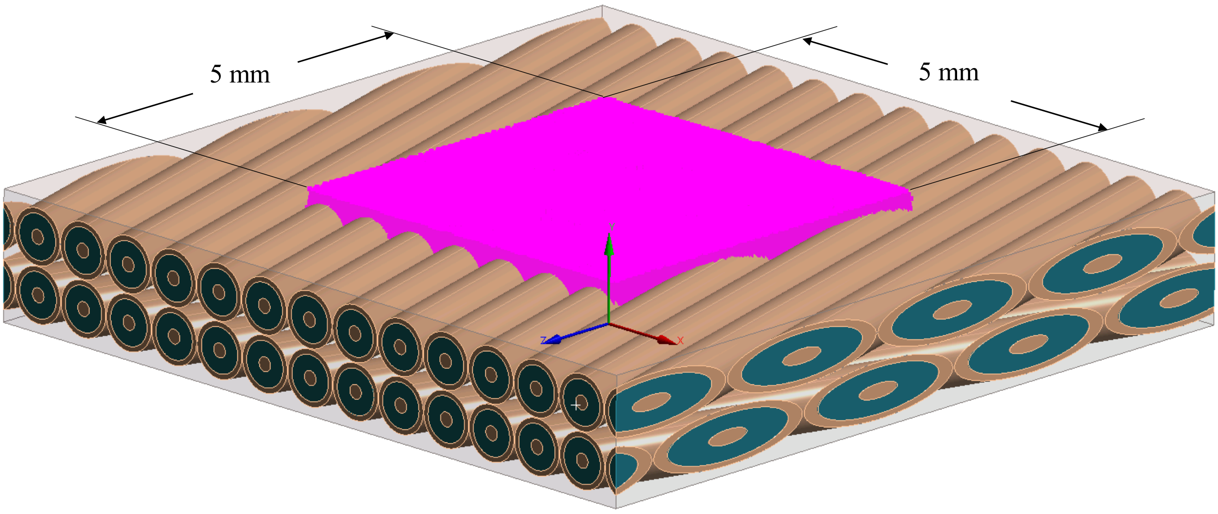

Figure 6.6.: Region of interest highlighted in pink of the 3D FEM cable model.

Material parameter

The 2D and 3D models are based on the same set of material data. The material properties of each component, used for the mechanical analysis, are summarised in Table 6.1. The copper in the strand is considered to be heat annealed, due to the RHT up to 650°C. The copper phase in the strands and the impregnations system are represented by a material model with bilinear kinematic hardening. It is assumed that the superconducting Nb_3Sn phase remains linear elastic while loading. The insulation system is represented by the stiffness of resin (CTD-101K) reinforced with compacted S2-glass fibre, as the model is investigating the stress–strain behaviour in the transverse direction (y-direction). The structur of the insulation system is introduced in Section 1.4. The effect of plastic behaviour of the impregnation system on the macroscopic stress–strain curve has been investigated by a varying tangent modulus. The von Mises yield criterion is applied on components of the conductor block which exhibit and elastic–plastic behaviour beyond its yield strength.

Table 6.1.: Material properties used in the FEM simulation.

Material	Elastic modulus	ν	Yield strength	Tangent modulus
Nb_3Sn [129]	114 GPa	0.36	300 MPa	—
Cu [67]	108 GPa	0.33	46 MPa	1.5 GPa
CTD-101K + S2 [140]	12.9 GPa	0.3	60 MPa	0.2 GPa / 1 GPa

In the 2D plain strain model, the elastic modulus E_{PS} and poison ration ν_{PS} have been adapted to compensate the stiffening of the plain strain condition to

$$E_{\mathrm{PS}} = E(1-\nu^2) \quad \text{and} \quad \nu_{\mathrm{PS}} = \frac{\nu}{1+\nu}, \tag{6.1}$$

in order to evaluate the calculated global stress-strain data of the 2D plain strain model as a representation of a free standing sample.

Mesh and element types

The mesh of the 2D model was generated by PLANE183 [82] eight-node elements in order to accurately model the curved boundary of each strand. The contact between strand and impregnation was described by CONTA172 elements (strand surface) and TARGET169 (epoxy surface) elements. The nodes of coincident surfaces are merged to ensure that a set of shared nodes is created. The mesh size was iteratively refined, as analysis with an initial mesh was performed first and then re-analysed by doubling the number of elements. As soon as the results were converging, the coarser mesh configuration is considered to be adequate. The mesh of the model used for the mechanical investigation is shown in Figure 6.7.

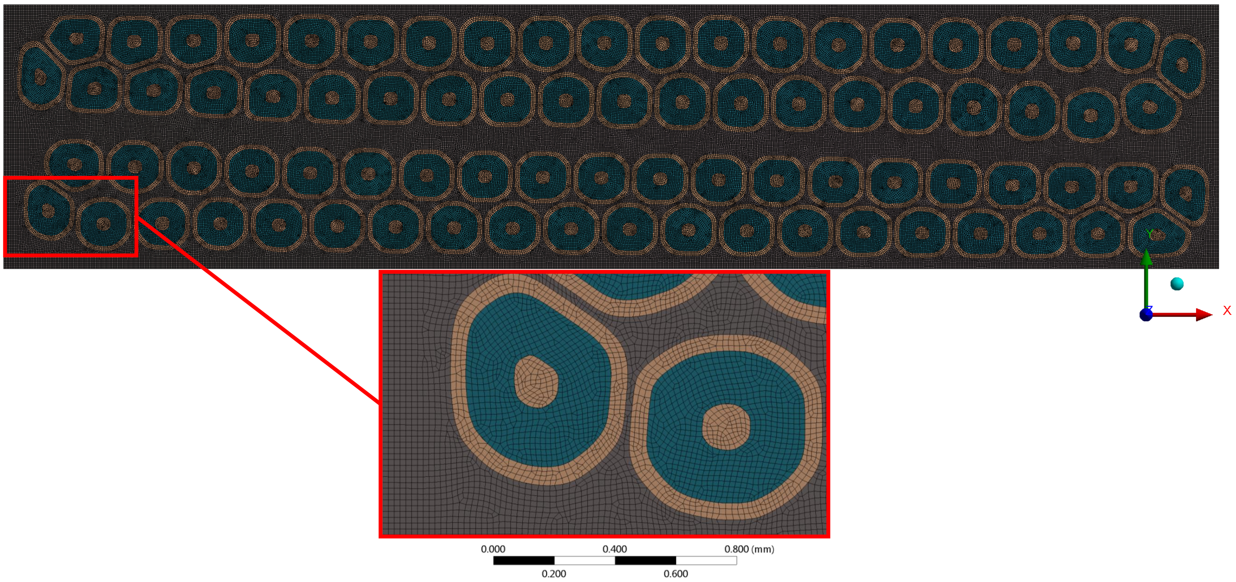

Figure 6.7.: Detailed ANSYS model indicating the shape and mesh of a single strand in a Rutherford cable based on computed tomography.

The 3D model was meshed by SOLID186 and SOLID187 [82] elements, which are higher-order 3D elements with 20 and 10 nodes, respectively. Both element types support elastic–plastic material laws and exhibit quadratic displacement behaviour. The generated mesh based on 10.481.102 nodes and 3.262.129 elements is shown in Figure 6.8. The contact between the components was described by CONTA174 elements and TARGET170 [82] by program controlled element assignment as in the 3D model all contacts are bonded.

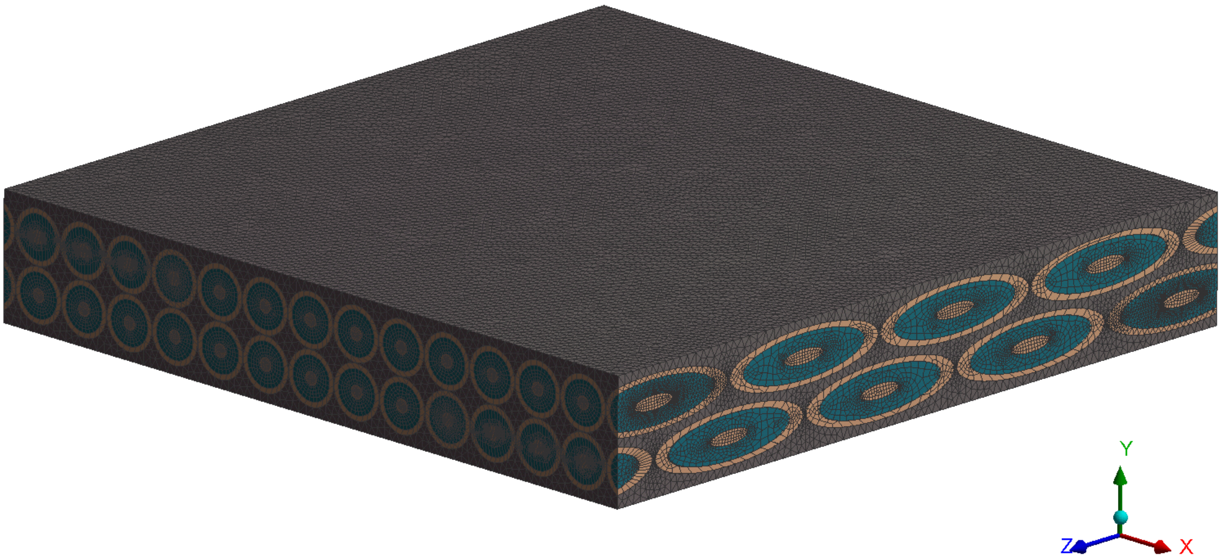

Figure 6.8.: Mesh of the 3D cable model.

Boundary conditions

The 2D model uses a frictionless bottom support with a fixed node as a boundary condition, which define the degrees of freedom in translation in x and y direction. A surface load is applied on the top edge, defined as an external force. The applied load was increased in 12 steps with a subsequent load decrease, similar to the experimental procedure, to investigate the stress–strain state at different stress levels and the macroscopic elastic–plastic behaviour of the model. The boundary conditions that are applied for the model are shown in Figure 6.9.

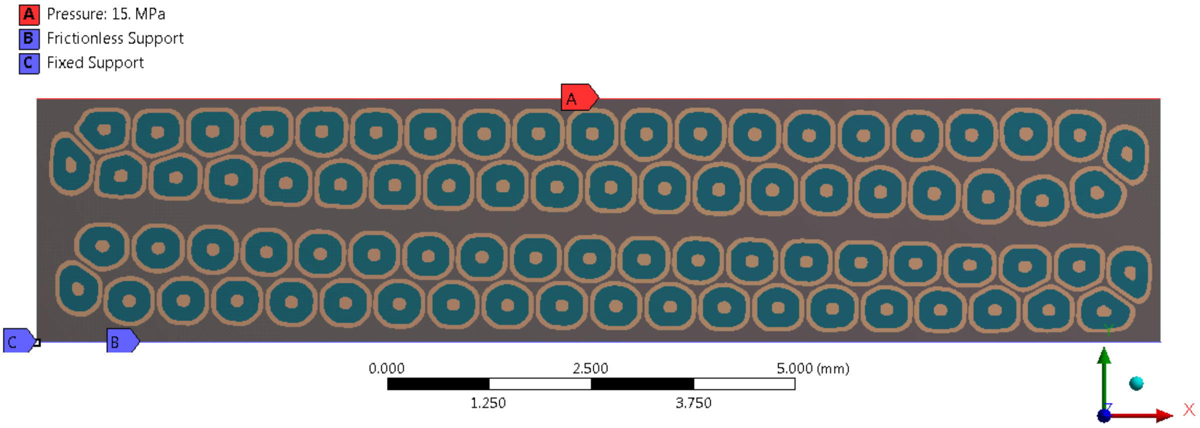

Figure 6.9.: Boundary conditions applied on the 2D cable model.

The boundary conditions, applied for the 3D model, are shown in Figure 6.10, defining a frictionless bottom support with a fixed node at the corner and an applied surface load on the top edge.

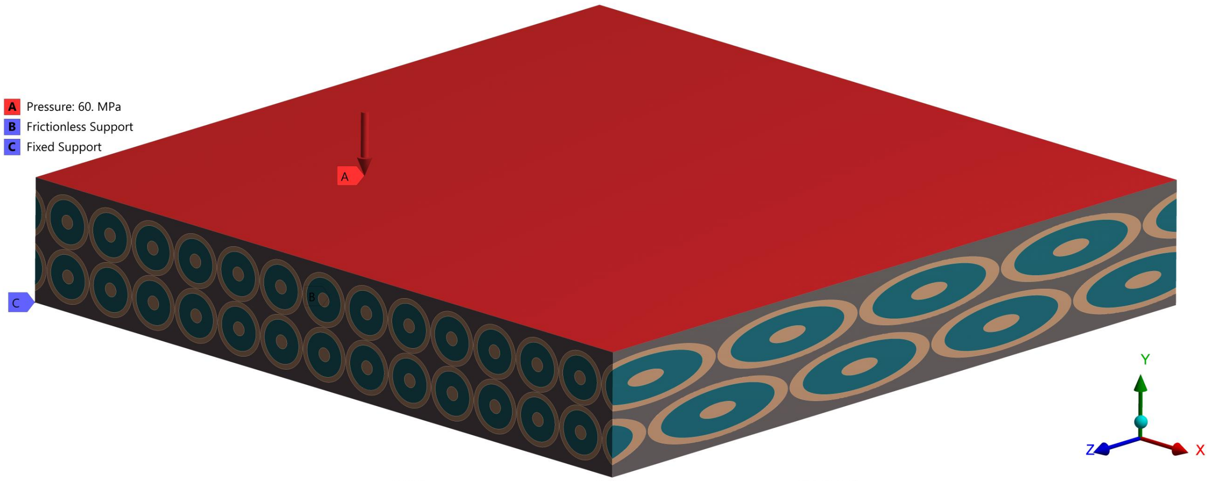

Figure 6.10.: Boundary conditions applied on the 3D cable model.

Contact modelling

The 2D model was generated to investigate whether the variations in the measured cycling stress–strain behaviour of the cable stacks are caused by a separation of strands and the impregnation system. Observations from the dye penetration test, presented in Section 4.5, lead to the assumption that the bonding behaviour between the strands and impregnation system could affect the compressive stress–strain behaviour. Therefore, two different contact definitions have been investigated in order to represent the stress–strain behaviour and the effect of generated cracks. A model with bonded contacts between each strand and the surrounding epoxy was generated, representing a perfect bonding between the strand and the surrounding matrix. The bonded contact formulation enables an ideal transfer of compressive and tensile forces, and displacements between the interfaces. The other extreme is represented by a frictionless contact formulation between the strand and surrounding matrix elements. The frictionless contact formulation represents a bonding failure between the strand and impregnation system and enables a gap opening between the components.

A perfect bonding was assumed in the 3D model, as there the focus is on the strain state of the annealed copper and Nb_3Sn under applied compressive load.

6.2. The 2D simulation results

The 2D model was used to investigate the effect of changes in the contact state between the strands and the impregnation matrix on the macroscopic stress–strain behaviour during loading and unloading. Furthermore, the influence of the plastic behaviour of the impregnation system by a varying tangent modulus on the macroscopic stress–strain behaviour was studied. The macroscopic strain was evaluated by the analysis of relative displacement changes of two vertical aligned nodes at the lower and higher central strand of the sample. The wire volume fraction $V_{\mathrm{wire}_{\mathrm{FEM}}}$ between the elaborated nodes is about 70 %. The calculated results are summarised in the following.

The 2D frictionless model

The following results are based on a model that assumes a frictionless contact between the strands and impregnation system, which represent bonding failures between strand and resin. Two models with a frictionless contact formulation between the strand and impregnation system and varying plastic behaviour (0.2 GPa and 1 GPa according Table 6.1) of the impregnation system have been investigated. The calculated compressive stress–strain curve of the model with a tangent modulus of 0.2 GPa is shown in Figure 6.11. The result of the model with a tangent modulus of 1 GPa is shown in the appendix in Figure D.1. The elastic stiffness (unloading slope) increases at different load levels in both models, to the same level. It is independent from the plastic varying tangent modulus. The tangent modulus has a dominant effect on the overall elastic–plastic stress–strain behaviour.

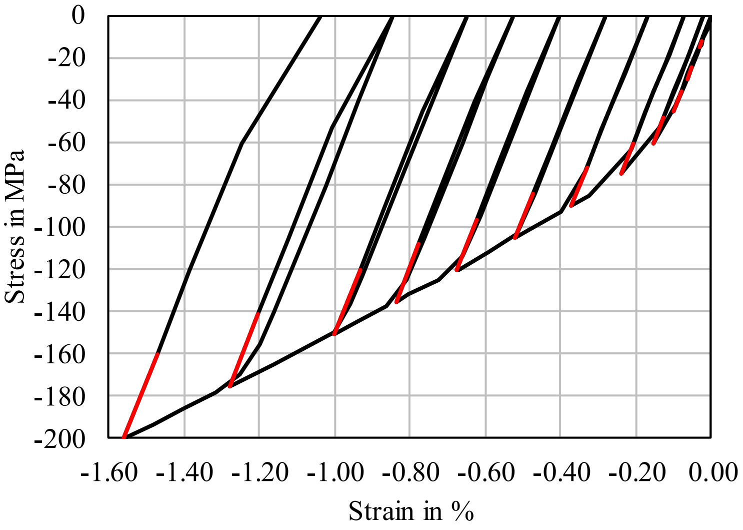

Figure 6.11.: Transverse compressive stress–strain curve from frictionless model with a tangent modulus of the impregnation system of 0.2 GPa.

The 2D bonded model

The following results are based on a model that assumes a perfect bonding between strands and the impregnation system. Two transverse compressive stress–strain curves based on simulations of 2D models with a varying tangent modulus of the impregnation system beyond the yield point are shown in the appendix in Figure D.2 and Figure D.3. The determined elastic slope of the unloading cycle is independent of the load level. The varying tangent modulus of the impregnation system does not effect the elastic stiffness. The elastic stiffness of both models is the same. The overall strain is affected by the tangent modulus of the impregnation system, which needs to be taken into account when the elastic–plastic material behaviour of the coil material should be represented. The overall strain varies about 0.2 % at a stress level of 200 MPa with a tangential modulus difference of 0.8 GPa.

A comparison of the calculated load-level-dependent elastic stiffness determined of the bonded and frictionless models is shown in Figure 6.12. The result comparison indicates the independent elastic behaviour of bonded and frictionless model from a varying plastic tangent modulus of the impregnation system. The elastic stiffness of the frictionless model is lower than that of the bonded model by about 1 GPa. Elastic stiffness of the frictionless model is dependent on the stress level, whereas the stiffness in the bonded model is independent of the stress level.

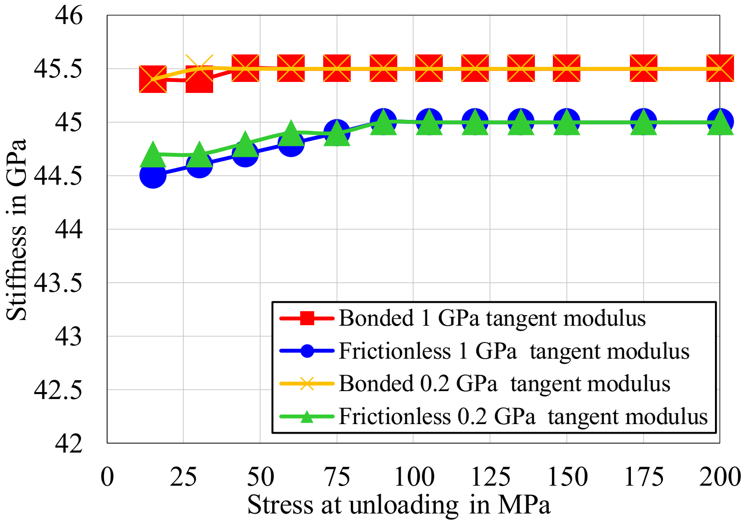

Figure 6.12.: Comparison of the load-level-dependent elastic stiffness, determined from the calculated models.

Comparison between the 2D FEM results and the measurements

A comparison of the by FEM simulation calculation stress–strain curve with to measurement is shown in Figure 6.13. The measured stress–strain curves of a sample type A with a V_{wire} of 74.3 % and a a sample type C with a V_{wire} of 69.9 % are compared to the FEM model with a frictionless strand to resin contact and a soft plastic tangent modulus of 0.2 GPa. The V_{wire} of the FEM model is about 70 %. Similar to the performed compressive test, the free-standing sample is represented by a model with free boundary conditions in radial direction. The wire volume fraction V_{wire} has an impact on the elastic-plastic behaviour of the sample. The stress–strain curve based on the FEM model agrees well with the measurement of the type A sample with a wire volume fraction of 74.3 %.

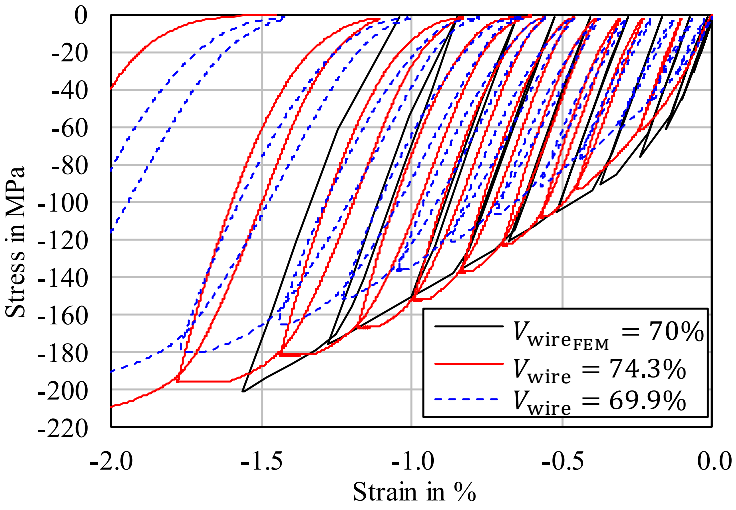

Figure 6.13.: Comparison of measured stress–strain curves of ten-stack samples type A ($V_{\mathrm{wire}} = 74.3\,\%$) and C ($V_{\mathrm{wire}} = 69.6\,\%$) to calculated curve of the FEM model.

The elastic–plastic behaviour determined by measurements above a stress level of 40 MPa, as shown in Figure 6.13, can be represented by the model by using an elastic–plastic material model for the copper and the impregnation system.

A comparison of the elastic stiffness values calculated by FEM calculated to the measured vales is shown in Figure 6.14. The elastic stiffness values of the measurements can be reproduced by the FEM model with respect to the documented material parameter. The effect of an stiffness increase with increasing stress can be recreated by a de-bonding between the strand and impregnation system. The stiffness comparison between FEM results and measurement indicates that the effect on epoxy de-bonding in the model is less than observed during the measurements.

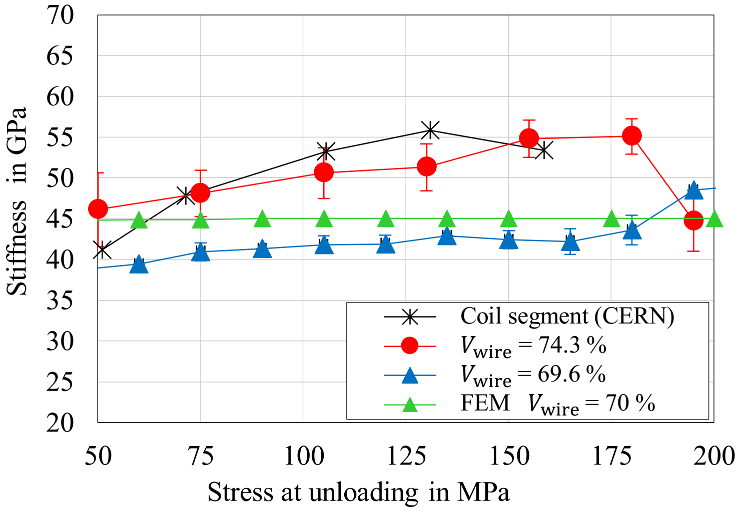

Figure 6.14.: Comparison of the stress-dependent stiffness determined by simulation and measurement.

The slope change in the unloading phase of the stress–strain curve, once exceeding 135 MPa cannot be represented by a de-bonding between the strand and the impregnation system. This effect might be in correlation to the creep behaviour that was measured at high load and could also be an indication of a relaxation at low load. The macroscopic stress–strain behaviour of an conductor block can be represented with a bilinear model, assuming an elastic stiffness of 40 GPa to 50 GPa with a yield point of 30 MPa and a tangent modulus of about 10 GPa.

6.3. The 3D simulation results

A 3D cable model has been used to investigate the stress state of a transversally loaded cable stack, presented in Section 5.3. The orientation of the principal stress vectors and the stress state in the copper and Nb_3Sn has been determined. All elaborated results are described in detail in the following.

Determination of the principal stress–strain direction
The principal stress–strain direction of the described 3D cable model has been determined at a compressive load of 100 MPa applied normal to the x–z plane of the model. Therefore, the orientation of the principal stress vectors of all 2.050.583 nodes within in a central sphere of 5×5 mm^2 through the model have been evaluated. The nodes of interest and rotational angle definition, used to identify to orientation of the principal stress vectors, with respect to the global coordinate system are shown in Figure 6.15. The orientation of the principal stress–strain vectors in ANSYS® is defined by the angle sequence ψ (around the z-axis), θ (around the x'-axis) and φ (around the y''-axis).

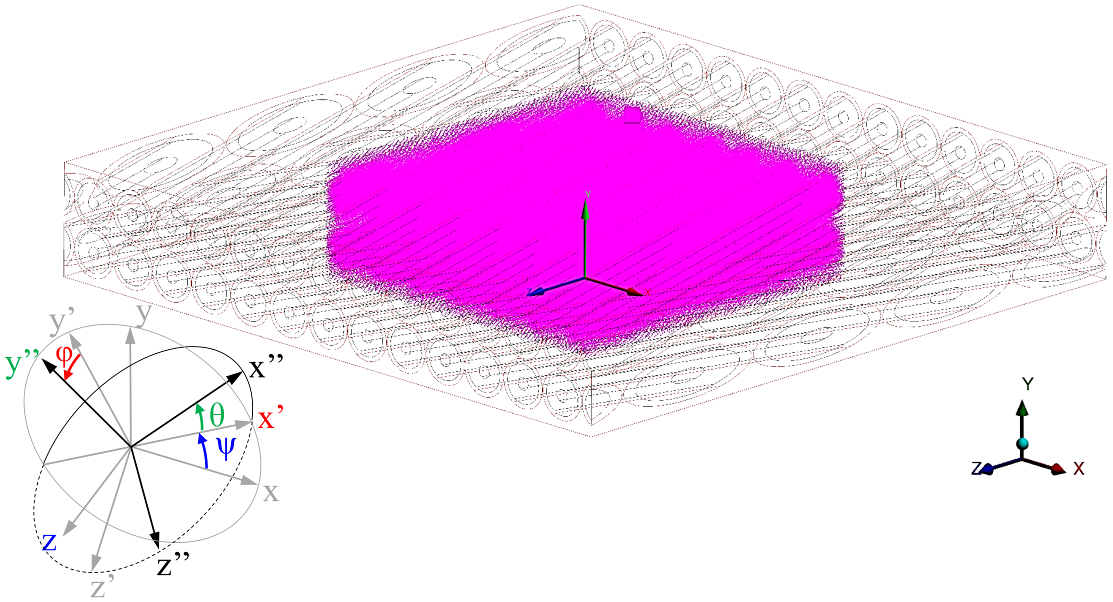

Figure 6.15.: The cable stack model with the nodes of interest highlighted in pink and the definition of rotation angles with respect to the global coordinate system.

The rotation angles ψ, θ and φ have been evaluated for all nodes in the area of interest. The results of the calculated principal stress orientation with respect to the global coordinate system is represented by histograms in Figure 6.16. The distribution rotational angles are evaluated in a spectrum between ±180°. The plot indicates that the principal directions of the majority of elements are oriented orthogonal to the global coordinate system by a rotation of about ±90°. This validates the assumption from Section 5.1 that the principal stress orientation is coaxial to the global coordinate system. This assumption is used for the evaluation of stress data from the neutron diffraction experiment, presented in Section 5.3.

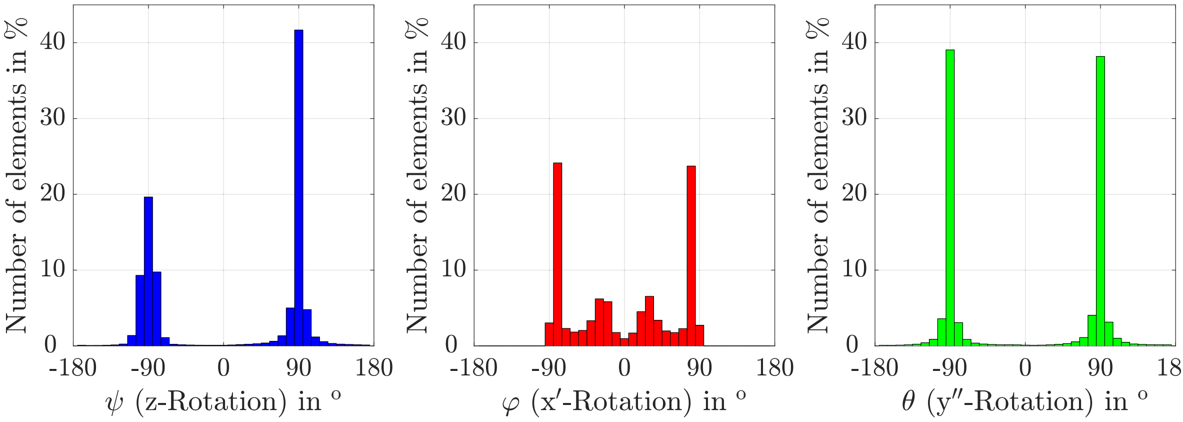

Figure 6.16.: The principal stress vector orientation of the FEM model in ψ, φ and θ.

Stress state of copper and Nb_3Sn components under transversal load

The stress state of the copper elements in the cable model has been determined by evaluating the normal stress components σ_x, σ_y and σ_z of selected copper nodes in the 5×5 mm² sphere. Thereby, the copper core and the Nb_3Sn filament surrounding copper of each strand were taken into account. The evaluated nodes are shown in Figure 6.17.

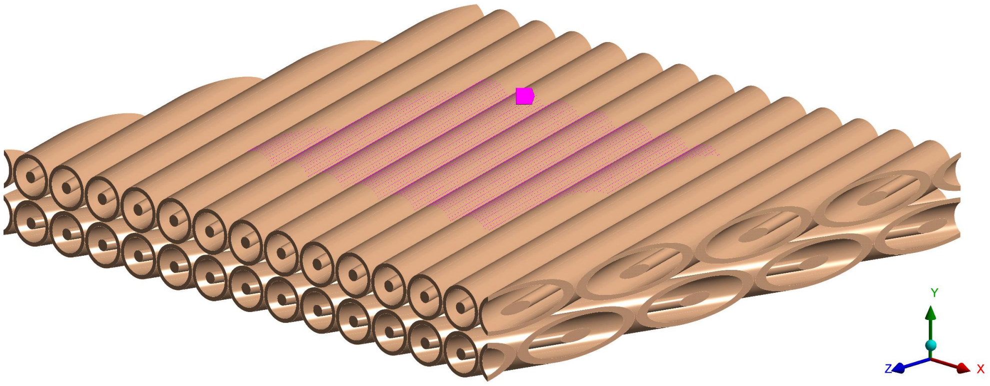

Figure 6.17.: Nodes selected for the FEM investigation of the copper components.

The determined stress states of the evaluated copper nodes under an applied compressive load of 100 MPa are shown in Figure 6.18. The three histograms indicate the statistics of the stress values, evaluated in the three normal stress directions. The colour coding of the histograms is identical to that of the global coordinates used in ANSYS®. The majority of the copper elements are in compressive load, indicated by a positive $\bar{\sigma}_x$, $\bar{\sigma}_y$ and $\bar{\sigma}_z$ value. The stress distribution in copper is very homogeneous in each direction, as the histograms are very narrow. The normal stress data are analysed by a normal distribution fitting method, marked by a black curve in each histogram, which allows a mean stress value $\bar{\sigma}$ to be identified in each direction. Thereby, one comparable mean stress value $\bar{\sigma}_x$, $\bar{\sigma}_y$ and $\bar{\sigma}_z$ for each normal stress direction is determined for each applied stress level.

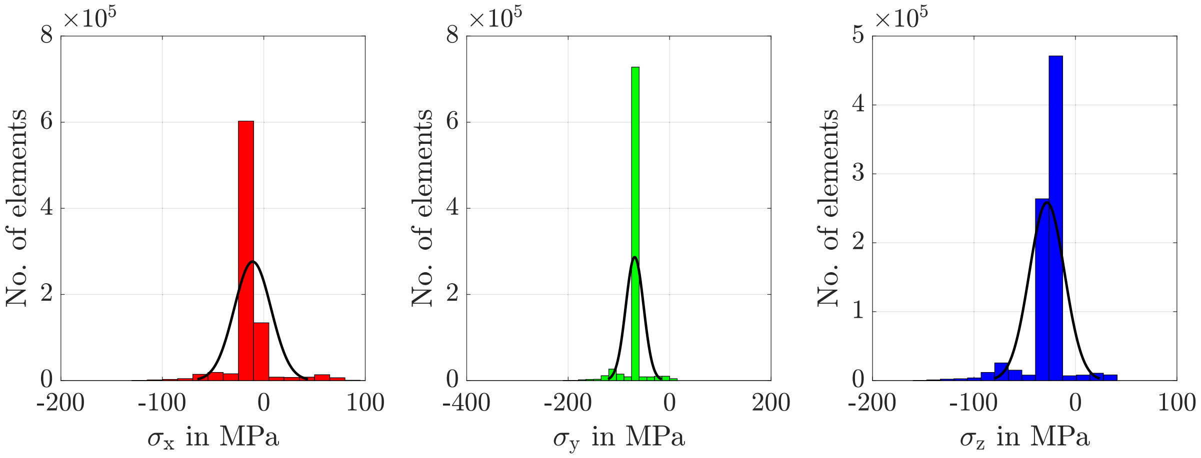

Figure 6.18.: Statistic of the normal stress distribution in the copper at 100 MPa applied load.

The evaluated mean stress values $\bar{\sigma}_x$, $\bar{\sigma}_y$ and $\bar{\sigma}_z$ in the copper under increasing compressive load up to 200 MPa are shown in Appendix E Figure E.1. The three normal stress components of the copper are under compression at each load level. The stress value of $\bar{\sigma}_y$ is highest, at about half of the applied load. The stress values of $\bar{\sigma}_x$ and $\bar{\sigma}_z$ are about half that of $\bar{\sigma}_y$.

The stress values of the Nb_3Sn elements has been evaluated by the same approach. The selected Nb_3Sn nodes within the central 5×5 mm^2 sphere are shown in Figure 6.19, highlighted in pink.

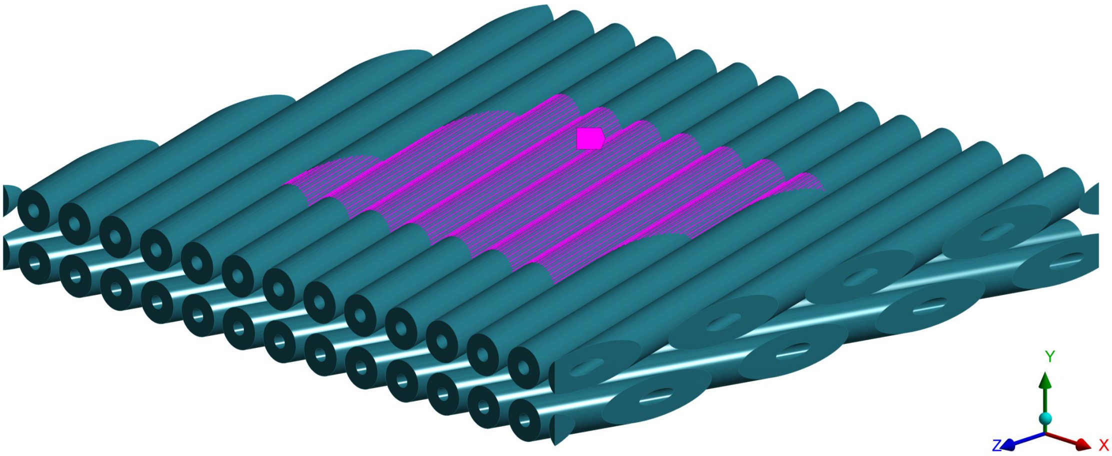

Figure 6.19.: Nodes selected for the FEM investigation of the Nb_3Sn components.

The stress states of the evaluated Nb_3Sn nodes under an applied compressive load at 100 MPa are described by the distribution of the normal stress components σ_x, σ_y and σ_z in Figure 6.20. The majority of the Nb_3Sn elements in the x and z directions identify a tensile stress state, whereas the elements in the y direction are in a compressive stress state. The stress distribution in the Nb_3Sn components is more inhomogeneous than that in the copper components, indicated by the spread of the histograms. The stress data are further processed by a normal distribution fitting method, indicated by the black curve in each histogram in Figure 6.20. A mean stress value $\bar{\sigma}_x$, $\bar{\sigma}_y$ and $\bar{\sigma}_z$ in each normal stress direction is determined, based on the data of the corresponding normal fit.

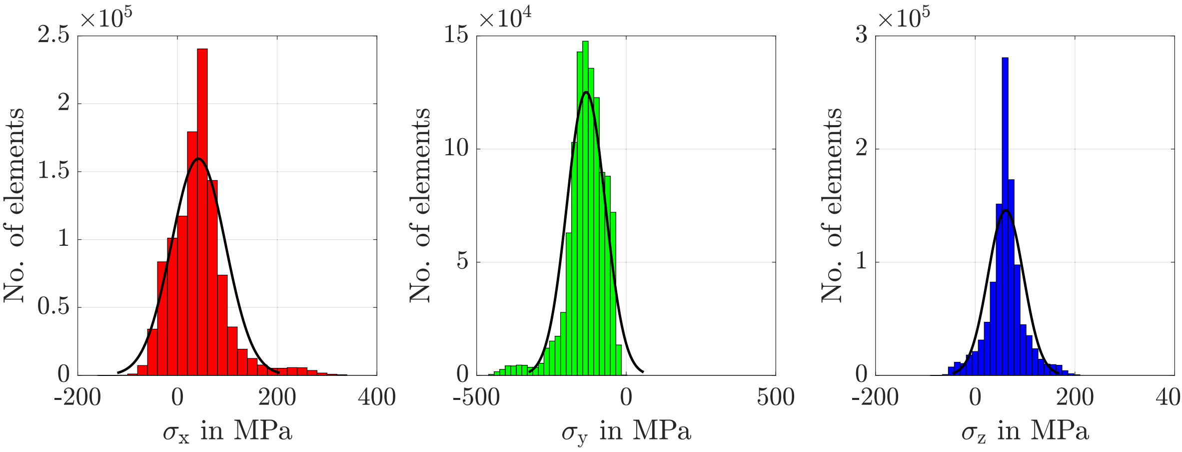

Figure 6.20.: Normal stress in the Nb_3Sn at 100 MPa applied load.

The evaluation of the mean normal stress values of all Nb_3Sn nodes within the 5×5 mm^2 sphere under monotonic compressive load up to 200 MPa is shown in the appendix in Figure E.2. The mean normal stress components $\bar{\sigma}_x$ and $\bar{\sigma}_z$ are under tensile load, whereas the mean stress values in the y direction $\bar{\sigma}_y$ exhibit a compressive stress state. The absolute value of the evaluated mean normal stress value $\bar{\sigma}_y$ is highest at each load level, about a factor of 1.5 of the applied load. The mean normal stress values $\bar{\sigma}_x$ and $\bar{\sigma}_z$ are of the same order of magnitude and about half of the $\bar{\sigma}_y$ value.

Comparison of 3D FEM results with the neutron diffraction measurements

The presented method of stress analysis allows a comparison of the FEM-based stress values with the stress values determined by a neutron diffraction experiment, presented in Section 5.3. The stress values $\bar{\sigma}_{x,\mathrm{FEM}}$, $\bar{\sigma}_{y,\mathrm{FEM}}$ and $\bar{\sigma}_{z,\mathrm{FEM}}$, determined by FEM calculation, are compared with the experimental-based stress values $\bar{\sigma}_{x,\mathrm{Exp.}}$, $\bar{\sigma}_{y,\mathrm{Exp.}}$ and $\bar{\sigma}_{z,\mathrm{Exp.}}$ in Figure 6.21 of an impregnated cable stack. The related strain values of the impregnated cable stack are shown in Figure 5.10. The assumption for the orientation of the principal strain tensor, used in the neutron diffraction, could be validated by the FEM calculation. The principal strain directions are orthogonal to the axial, radial and azimuthal defined sample orientation.

The determined stress state of the copper in a transversally loaded cable stack is in compression as determined by the neutron diffraction stress data and by the FEM calculation-based stress data. The experimental-based stresses $\bar{\sigma}_{i,\mathrm{Exp.}}$ in the copper are about twice as high as that determined by FEM calculations. The hydrostatic loading of the copper, identified by neutron diffraction measurements, is not reproduced by the presented FEM model, however all stress components are under compression.

The stress state of the Nb_3Sn components of a cable stack, determined by the neutron diffraction measurement, correlate with that determined by the FEM calculations. The determined mean stresses $\bar{\sigma}_x$ and $\bar{\sigma}_z$ are in tension whereas the mean stress $\bar{\sigma}_z$ indicates a compressive load. The load direction and the order of magnitude between the diffraction-based stress values and the FEM-based stress values correlate very well up to an applied stress level of 150 MPa. The measured stress components $\bar{\sigma}_z$ of the Nb_3Sn increases a lot above an applied stress level of 150 MPa, which is not represented by the model and might need a refinement of the model to the filament level of each strand.

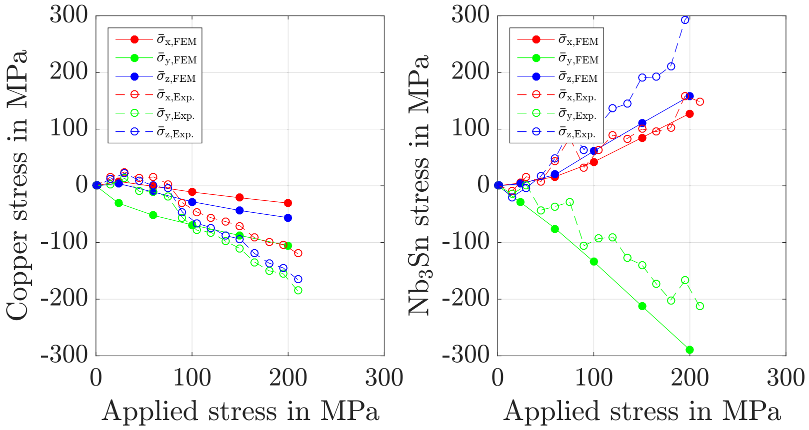

Figure 6.21.: Comparison of the calculated stress values with that determined by neutron diffraction measurements in copper (*left*) and Nb_3Sn (*right*) under transverse applied load.

6.4. Conclusion

The transversal macroscopic elastic–plastic stress–strain behaviour of an impregnated cable stack has been reproduced by 2D FEM calculations. A 2D FEM model of an insulated Rutherford cable two-stack has been generated, based on the real cable geometry reconstructed from X-ray μ-CT data. Thereby, the strand deformation caused by the cabling process could be precisely modelled as well as the deformation by the keystone angle. Each strand has been represented as multiphase metallic material embedded in a matrix, representing the insulation system. The property driving material parameters of the elastic–plastic behaviour of the cable stack under compressive load have been determined by parametric studies. Thereby, a major influence of the insulation system on the stress–strain behaviour of the cable stack was determined and compared with compressive stress–strain measurements. Minor effects such as an increase in elastic stiffness with increasing stress level and slope changes during unloading could not be reproduced by the presented model. The investigated failure between strand and insulation system did affect the elastic stiffness towards the measured effects, but not to the expected extent.

The orientation of the principal stress–strain vectors in an impregnated cable has been determined by a simplified 3D FEM cable model under transversal loading. The principal strain axes are identical to the introduced sample coordinated system. This approves the assumption, used for the data analysis of neutron diffraction measurements. Furthermore, the stress states and levels of the copper and Nb_3Sn phase in the strands of the cable stack have been calculated and compared with measurements. The calculated stress states of Nb_3Sn and copper confirm the ones measured by the neutron diffraction experiment. Nb_3Sn

is transversal under compression under transversal applied load and under tensile stress perpendicular to the applied load direction. The copper phase exhibits a compressive load in all principal directions. The stress level of the Nb_3Sn, determined by neutron diffraction measurements, agrees well with the calculation of the simplified FEM model. The stress level of the copper varies by a factor of 2–3 between calculation and measurement, depending on the direction, whereas the material properties of the copper were assumed to be similar to the one of heat annealed oxygen free copper. The copper phase in the strand might be less pure after the phase transition of the Nb_3Sn during RHT. The stress variance between measurement and calculation might be caused by the simplification of the strand which is still fare from a crystallographic level of the measurement. The designed simplified 3D FEM Rutherford cable model is based on extruded multiphase cylinders, designed with respect to copper to non-copper ratio embedded in an insulating matrix. The twist pitch angle of the cable is taken into account in the simplified design, but the stainless steel core in the cable is not modelled. However, the calculation and measurements have shown that Nb_3Sn phase of an impregnated conductor is exposed to a compressive stress under transversal applied load and under tensile stress in the lateral direction. This stress state causes a permanent conductor degradation, once the applied load exceeds 150 MPa, as shown in Section 3.10.

7. Comprehensive summary

7.1. Summary

A test procedure and the necessary test set-up have been described and tested to investigate the stress limits of a Nb_3Sn Rutherford cable under homogeneous compressive stress at ambient temperature. The stress limitation is thereby defined by the electrical performance of the cable. A hydraulic test station was modified and the homogeneity of the applied stress was optimised. The application and investigation of pressure-sensitive films enabled a quantitative analysis of the applied contact stress between tool and sample, which was validated by calibrated load cells. The studied irreversible Nb_3Sn cable degradation as a function of transverse compressive stress applied at ambient temperature helped to identify a degradation free stress limit of 150 MPa and a degradation of 3 % at 175 MPa applied stress.

The lack of experimental data on the currently used impregnated conductor lead to an extensive test campaign. The elastic stress–strain behaviour of impregnated cable stacks under compressive load has been studied in its principal strain directions. The effect of a varying wire volume fraction, representing variations in the coil compaction during the magnet manufacturing process, have been determined experimentally. A low assembly stress of 5 MPa caused a low wire volume fraction of 69.6 %. A high assembly stress of 30 MPa caused a high wire volume fraction of 74.3 %. The wire volume fractions affects the conductor block stiffness which is between 42 GPa for 69.6 % and 55GPa 74.3 %. The manufactured ten-stack samples with a wire volume fraction of 74.3 % are representative for a magnet, as validated by measurements performed with samples extracted directly from a coil segment. The direction-dependent compressive stiffness of a Nb_3Sn conductor block has been determined by compressive stress–strain measurements in its three normal directions. The compressive stress–strain measurements have been carried out by calibrated load cells in combination with a direct strain measurement with an extensometer. The measurements have approved the strong anisotropic behaviour of the conductor block. The highest determined sample stiffness in axial direction (about 95 GPa) is about twice that in the transversal direction and the radial stiffness is a factor of 1.3 that of the transverse stiffness. Above 135 MPa a creep behaviour was observed, whereas a clear crack propagation in the impregnation system could be identified after high load application with a dye ink penetration technique. The transversal macroscopic elastic–plastic stress–strain behaviour of an impregnated cable stack has been reproduced by 2D FEM calculations. The property-driving material parameters of the elastic–plastic behaviour of the cable stack under compressive load have been determined by parametric studies. Thereby, the major influence of the insulation system on the stress–strain behaviour of the cable stack was determined and compared with compressive stress–strain measurements.

The strain state in the Nb_3Sn and in the heat-annealed copper phase in an impregnated cable stack with respect to a transversal applied load has been determined experimentally. A combined neutron diffraction and stress–strain measurement allows the relation between the macroscopic applied load on a conductor block and the lattice stress and strain state of the Nb_3Sn and copper in the conductor to be investigated. The transversal stress components in the copper and in the Nb_3Sn are equal to the external applied load. Furthermore, it could be identified that the copper exhibits an isotropic pressure around the filaments. The reduction of the Nb_3Sn lattice stresses by the epoxy-impregnation system could also be validated. The stress states and levels of the copper and Nb_3Sn phase in the strands of the cable stack have been reproduced by 3D FEM models. The calculated stress states of Nb_3Sn and copper confirm the measurements by the neutron diffraction experiment. Nb_3Sn is under compression under transversal load and under tensile stress perpendicular to the applied load direction. The copper phase exhibits a compressive load in all principal directions. The stress level of the Nb_3Sn, determined by neutron diffraction measurements, agrees well with the calculation of the simplified FEM model. The stress level of the copper varies by a factor of 2–3 between calculation and measurement, depending on the direction.

7.2. Critical review

In this work, a practical approach has been described to investigate the stress limits of impregnated Nb_3Sn cable during load application at ambient temperature. The elaborated limit of 150 MPa homogeneous compressive stress on the conductor at ambient temperature defines an important design criteria for high field superconducting Nb_3Sn magnets. The pre-loading concept of the 11 T dipole magnet requires per design a compressive stress of 126 MPa on the conductor during collaring at ambient temperature [54]. The stress margin is about 15 % prior permanent conductor degradation. Future high field magnet designs beyond 11 T require a conductor with an increased stress capability at ambient temperature or a different pre-loading concept to balance the magnetic forces during powering. The used measurement method based on pressure sensitive films allows determine the average applied stress of the contact, peak stresses, integrated applied force and the stress distribution with one measurement. The stress concentrations and load unbalances on the stress sensitive filaments can cause a permanent conductor damage during the magnet assembly. The knowledge of the contact stress during magnet assembly gives a valuable feedback for the magnet designer. This measurement method has already been implemented in the manufacturing process of model magnets during the assembly [94]. The stress pattern is measured at the highest applied load and requires always a disassembly to access the pressure sensitive film which is a major limitation of this technique.

A precise and robust measurement protocol has been presented, to characterise the compressive stress–strain behaviour of a conductor block based on a direct strain measurement method. Significant stiffness differences could be determined on samples which varied by a wire volume fraction of 4.7 %. The proposed bilinear material model can be used for calculations at ambient temperature, which is an important condition for a collared coil. At this stage, it is not possible to calculate the stress state at cryogenic temperature as thermal contraction and stiffness are not measured yet. The measured values represent the material behaviour of an impregnated coil conductor block. All contact driven displacements which occur during a magnet assembly at contact interfaces of a coil due to geometric imperfections or surface roughness are not taken into account in the described measurements.

The presented measurement method of stresses in the Nb_3Sn and copper phase allow to validate FEM models on strand and filament level. The strain state orientation and order of magnitude could be calculated correctly by a simplified 3D models based on simple material models. A refined approximation of the strand geometry to a filament level could explain the stress deviation between measurement and calculation. The calculations and measurements have shown that the copper phase has an dominant impact on the stress state of the Nb_3Sn.

7.3. Next steps

The presented protocol to investigate the irreversible critical current degradation of Nb_3Sn cables under transversal applied load is used as a baseline for further test campaigns [141], to investigate cable candidates for future magnet applications. The use of pressure sensitive films remains a powerful and cost effective tool for the analysis of a compressive contact stress state, which is heavily used in the magnet development process. There are efforts at CERN to manufacture and improve capacitive load gauges [142] and to introduce them into a magnet mock-up as an online contact stress monitoring system up to 150 MPa, which can be effectively used at cryogenic temperature as well. Compressive stress–strain measurements at cryogenic temperature are planned to complete the parameter set for the calculation of the mechanical behaviour of a collared coil-type magnet during coll down and powering at cold. The observed creep behaviour starting at a stress level of 135 MPa should be taken into account for a future magnet design of high-field magnets where the preloaded might be beyond 135 MPa. The equally occurring stress relaxation could cause a loss of pre-stress in the magnet. The mechanical properties and limitations of the insulations system as composite consisting out of resin reinforced glass fibre and a mica tape need to be further investigated, as an increased stiffness of the insulation system can reduce the stress transferred to the Nb_3Sn filament.

Appendix

A. Calculation of the magnetic field components in a sector coil without iron

Introduction
The nabla operator ∇ is a differential operator of the following form:

$$\nabla = \left(\frac{\partial}{\partial x}, \frac{\partial}{\partial y}, \frac{\partial}{\partial z}\right) \tag{A.1}$$

The derivative can be written also in this way

$$\frac{\partial A_a}{\partial x} = A_{a,x}. \tag{A.2}$$

The magnetic field has to be calculated in a region which is free of any currents and magnetisation materials. For this assumptions the following equations are valid. The divergence of the magnetic field B is zero (Gauss law)

$$\nabla \cdot \vec{B} = 0, \tag{A.3}$$

and the rotation of the magnetic field is zero if the current density is zero (Ampere's law)

$$\nabla \times \vec{B} = 0. \tag{A.4}$$

The magnetic field B can be calculated by the rotation of the vector potential A

$$\vec{B} = rot\vec{A} = \nabla \times \vec{A} = \begin{bmatrix} \partial A_{z,y} - \partial A_{y,z} \\ \partial A_{x,z} - \partial A_{z,x} \\ \partial A_{y,x} - \partial A_{x,y} \end{bmatrix} = \begin{bmatrix} B_x \\ B_y \\ B_z \end{bmatrix}. \tag{A.5}$$

The vector potential has just the A_z component for the 2D-problem. The x, y- components of the magnetic field can be computed as:

$$B_x = \frac{\partial A_z}{\partial y}; \qquad B_y = -\frac{\partial A_z}{\partial x}. \tag{A.6}$$

The magnetic field B can be also calculated in cylinder coordinates (r, Θ, z) in the following way:

$$\vec{B} = rot\vec{A} = \nabla \times \vec{A} = \begin{bmatrix} \frac{1}{r}\partial A_{z,\Theta} - \partial A_{\Theta,z} \\ \partial A_{r,z} - \partial A_{z,r} \\ \frac{1}{r}\partial(rA_{\Theta,r}) - \frac{1}{r}\partial A_{r,\Theta} \end{bmatrix} = \begin{bmatrix} B_r \\ B_\Theta \\ B_z \end{bmatrix}. \tag{A.7}$$

Similar to the equation (A.6), the vector potential has just the A_z component. The r, Θ-components of the magnetic field can be computed as:

$$B_r = \frac{1}{r}\frac{\partial A_z}{\partial \Theta}; \qquad B_\Theta = -\frac{\partial A_z}{\partial r}. \tag{A.8}$$

For a single current wire we can calculate the magnetic field in cylinder coordinates (r, Θ, z) with respect to the current I, the magnetic permeability μ_0 and an arbitrary radius r around the wire:

$$B_\Theta = \frac{\mu_0 I}{2\pi r}. \tag{A.9}$$

For the 2D-problem, the z-component of the vector potential A can be defined with respect to equation (A.8) and (A.9) to

$$\partial A_z(r, \Theta) = -\int B_\Theta \partial r = -\frac{\mu_0 I}{2\pi} \ln\left(\frac{r}{a}\right), \tag{A.10}$$

where a is just an arbitrary length to make the argument of the logarithm dimensionless. If the position of the current is changed, it is possible to calculate the field at an arbitrary position P, see Figure A.1.

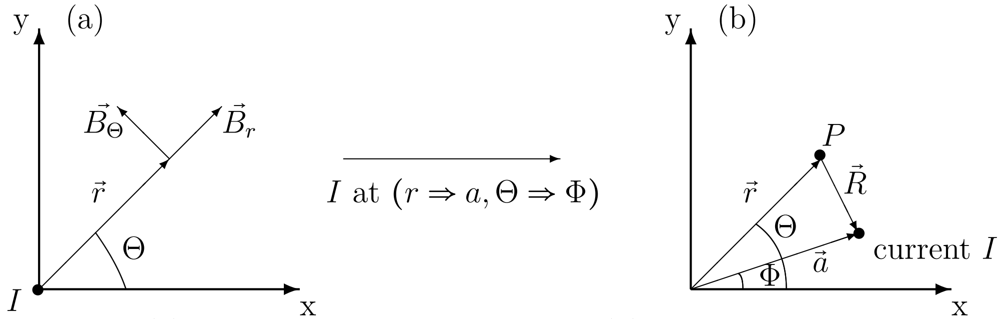

Figure A.1.: (a) The magnetic field in a wire. (b) Field calculation at a point P.

In this case the current I is parallel to the z-axis and located at some point $(r \Rightarrow a,\ \Theta \Rightarrow \Phi)$ in the r, Θ-plane. The vector potential A at the point $P(r, \Theta)$ can be calculated with respect to the vector $\vec{R}$ and $\vec{a}$ shown in Figure A.1b. With respect to $r < a$ the vector potential can be calculated inside the aperture

$$A_z(r, \Theta) = -\frac{\mu_0 I}{2\pi} \ln\left(\frac{R}{a}\right). \tag{A.11}$$

With the help of the cosine rule

$$|\vec{a} - \vec{b}|^2 = |\vec{a}|^2 + |\vec{b}|^2 - 2|\vec{a}||\vec{b}| \cos \sphericalangle \vec{a}, \vec{b}, \tag{A.12}$$

it is possible to calculate the vector $\vec{R}$ like this

$$|\vec{R}|^2 = |\vec{r}|^2 + |\vec{a}|^2 - 2|\vec{r}||\vec{a}| \cos(\Theta - \Phi). \tag{A.13}$$

The cosine can also be an expression of the exponential function

$$\cos z = \frac{e^{iz} + e^{-iz}}{2}, \tag{A.14}$$

so that $\vec{R}$ can also be calculated by using the equation (A.13) and the exponential function (A.14)

$$|\vec{R}|^2 = |\vec{r}|^2 + |\vec{a}|^2 - 2|\vec{r}||\vec{a}| \cdot \frac{1}{2}\left(e^{i(\Theta-\Phi)} + e^{-i(\Theta-\Phi)}\right). \tag{A.15}$$

This expression can be rearranged to the equation

$$\frac{|\vec{R}|^2}{|\vec{a}|^2} = \left(1 - \frac{|r|}{|a|}e^{i(\Theta-\Phi)}\right)\left(1 - \frac{|r|}{|a|}e^{-i(\Theta-\Phi)}\right) \tag{A.16}$$

and with the use of the logarithm to

$$2\ln\frac{|\vec{R}|}{|\vec{a}|} = \ln\left(1 - \frac{|r|}{|a|}e^{i(\Theta-\Phi)}\right) + \ln\left(1 - \frac{|r|}{|a|}e^{-i(\Theta-\Phi)}\right). \tag{A.17}$$

The equation (A.17) is similar to the basic equation of the Taylor polynomial

$$\ln(1-x) = -\sum_{n=1}^{\infty}\frac{x^n}{n}. \tag{A.18}$$

So the Taylor polynomial for the current problem is

$$\ln\frac{|\vec{R}|}{|\vec{a}|} = -\frac{1}{2}\sum_{n=0}^{\infty}\frac{1}{n}\left(\frac{r}{a}\right)^n e^{in(\Theta-\Phi)} - \frac{1}{2}\sum_{n=0}^{\infty}\frac{1}{n}\left(\frac{r}{a}\right)^n e^{-in(\Theta-\Phi)}. \tag{A.19}$$

By using the Euler's formula

$$e^{ix} = \cos x + i\sin x, e^{-ix} = \cos x - i\sin x \tag{A.20}$$

the equation (A.19) can be rearranged to the following expression where the sinus parts of the equation cancel each other:

$$\ln\frac{|\vec{R}|}{|\vec{a}|} = -\sum_{n=1}^{\infty}\frac{1}{n}\left(\frac{r}{a}\right)^n \cos n(\Theta-\Phi). \tag{A.21}$$

The equation (A.21) can be added to the equation (A.11) and the vector potential for $r < a$ can be calculated as a Taylor series

$$A_z(r,\Theta) = \frac{\mu_0 I}{2\pi}\sum_{n=1}^{\infty}\frac{1}{n}\left(\frac{r}{a}\right)^n \cos\left[n\left(\Theta-\Phi\right)\right]. \tag{A.22}$$

Polynomial function properties: The vector potential can be reduced because of the symmetric current distribution to the y-axis in a dipole see Figure A.2. The current distribution $I(-x) = -I(x)$ is an odd function so in the sum series are just odd n

$$A_z(r,\Theta) = \frac{\mu_0 I}{2\pi}\sum_{n=1,3,5...}^{\infty}\frac{1}{n}\left(\frac{r}{a}\right)^n \left[\cos\left(n\Theta\right)cos(n\Phi) + \sin\left(n\Theta\right)\sin\left(n\Phi\right)\right] \tag{A.23}$$

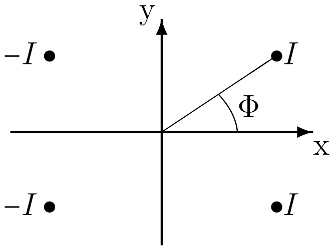

Figure A.2.: Current distribution for a dipole.

Trigonometric polynomial properties: The current distribution depends on the angle Φ. In this case $I(\Phi) = I(-\Phi)$ is a even function, the sinus part of the sum for the calculated vector potential in the equation (A.23) disappear, because of the symmetric to the x-axis

$$A_z(r,\Theta) = \frac{\mu_0 I}{2\pi} \sum_{n=1,3,5\ldots}^{\infty} \frac{1}{n} \left(\frac{r}{a}\right)^n \left[\cos(n\Theta)\cos(n\Phi)\right]. \tag{A.24}$$

The shown current distribution in Figure A.2 shows that, the current I has to be counted four times. The vector potential for the dipole magnet can therefore be calculated by using:

$$A_z(r,\Theta) = \frac{2\mu_0 I}{\pi} \sum_{n=1,3,5\ldots}^{\infty} \frac{1}{n} \left(\frac{r}{a}\right)^n \left[\cos(n\Theta)\cos(n\Phi)\right]. \tag{A.25}$$

The current I can be calculated by the current density J and the corresponding surface A

$$I = J \cdot A. \tag{A.26}$$

The magnetic vector potential can also be calculated by using equation (A.25) and (A.26) with respect to the current density by using the surface of a dipole magnet shown in Figure A.3

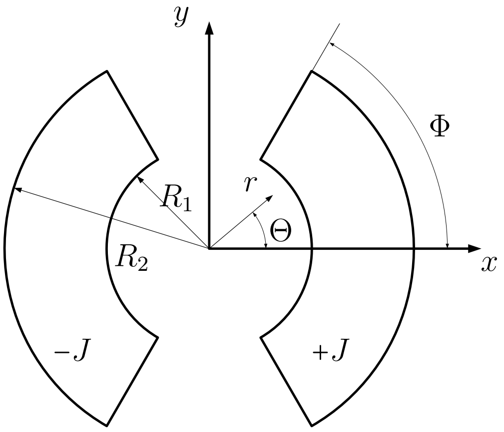

Figure A.3.: Cross-section of a sector coil.

$$A_z(r,\Theta) = \frac{2\mu_0 J}{\pi} \sum_{n=1,3,5\ldots}^{\infty} \frac{1}{n} \int_0^{\Phi_1} \int_{R_1}^{R_2} \left(\frac{r}{a}\right)^n \cos(n\Theta)\cos(n\Phi) a \; da \; d\Phi. \tag{A.27}$$

After integrating the surface the vector potential is

$$A_z(r,\Theta) = \frac{2\mu_0 J}{\pi} \sum_{n=1,3,5...}^{\infty} \frac{r^n}{n^2(2-n)} \cos(n\Theta) \sin(n\Phi) \left(R_2^{(2-n)} - R_1^{(2-n)}\right). \tag{A.28}$$

With respect to the equation (A.8) and (A.28) the tangential components of the magnetic field can be calculated as

$$B_{n\Theta} = -\frac{\partial A_z}{\partial r} = -\frac{2\mu_0 J}{\pi} \sum_{n=1,3,5...}^{\infty} \frac{r^{n-1}}{n(2-n)} \cos(n\Theta) \sin(n\Phi) \left(R_2^{(2-n)} - R_1^{(2-n)}\right), \tag{A.29}$$

as well as the radial field components:

$$B_{nr} = \frac{1}{r}\frac{\partial A_z}{\partial \Theta} = \frac{2\mu_0 J}{\pi} \sum_{n=1,3,5...}^{\infty} \frac{r^{n-1}}{n(2-n)} \sin(n\Theta) \sin(n\Phi) \left(R_2^{(2-n)} - R_1^{(2-n)}\right). \tag{A.30}$$

The absolute field value can be calculated by:

$$B_n = \sqrt{(B_{nr})^2 + (B_{n\Theta})^2}. \tag{A.31}$$

In the center line of the aperture at $\Theta = 0°$, the magnetic field reduces to tangential field components. In general the magnetic dipole component and the first multipoles at $\Theta = 0°$ can be calculated as

$$B_1(\Phi) = -\frac{2\mu_0}{\pi} J \left(R_2 - R_1\right) \sin(\Phi), \tag{A.32}$$

$$B_3(\Phi) = -\frac{2\mu_0}{\pi} J \frac{r^2}{3} \sin(3\Phi) \left(R_2^{-1} - R_1^{-1}\right), \tag{A.33}$$

$$B_5(\Phi) = -\frac{2\mu_0}{\pi} J \frac{r^4}{15} \sin(5\Phi) \left(R_2^{-3} - R_1^{-3}\right), \tag{A.34}$$

$$B_7(\Phi) = -\frac{2\mu_0}{\pi} J \frac{r^6}{35} \sin(7\Phi) \left(R_2^{-5} - R_1^{-5}\right) \tag{A.35}$$

Therefore the multipole coefficients can be calculated as

$$b_3(\Phi) = \frac{B_3}{B_1} = -\frac{r^2 \sin(3\Phi)}{3\ R_2\ R_1 \sin\Phi} \tag{A.36}$$

$$b_5(\Phi) = \frac{B_5}{B_1} = -\frac{\left(R_2^2 + R_2 R_1 + R_1^2\right) r^4 \sin(5\Phi)}{15\ R_2^3\ R_1^3 \sin\Phi} \tag{A.37}$$

$$b_7(\Phi) = \frac{B_7}{B_1} = \frac{\left(\frac{1}{R_2^5} - \frac{1}{R_1^5}\right) r^6 \sin(7\Phi)}{35(R_2 - R_1)\sin\Phi} \tag{A.38}$$

Owing to symmetry, the skew components ($n = 2, 4, 6, \ldots$) do not exist and with a coil angle of $\Phi = 60°$ the sextupole term $n = 3$ vanishes. For such a coil simplification, the magnetic field in the centre line of the aperture at $\Theta = 0°$, is dominated by the vertical dipole field component:

$$B_1 = \frac{\mu_0}{\pi} J \left(R_2 - R_1\right) \sqrt{3}. \tag{A.39}$$

With respect to Equation (A.39) it can be seen that the magnetic field B inside the clear aperture scales linearly with the current density J of the coil

$$B \sim J. \tag{A.40}$$

This derivation based on formulas taken from [143].

Magnetic field in a coil

In order to calculate the magnetic forces in a coil, the magnetic field inside the coil need to be calculated as well. The magnetic field inside a coil segment can be calculated with respect to the Biot–Savart law. The azimuthal magnetic field component B_{Θ_i}, surrounding a current I_i in a medium with the permeability μ_0, can be calculated at each distance r with the following formula:

$$B_{\Theta_i} = \frac{\mu_0 I_i}{2\pi r}. \tag{A.41}$$

To assume a constant current density J, each coil sector is separated by the radial discretisation dr and the azimuthal discretisation $d\varphi$. For each resulting area A_i, a corresponding line current I_i is calculated with respect to a constant current density J:

$$I_i = J \cdot A_i. \tag{A.42}$$

In this way, the magnetic field can be calculated at each location, based on the generated line currents.

B. Approaches for the determination of diffraction elastic constants from single-crystal values

There are different approaches to determine the diffraction elastic constants (DECs) S_1 and S_2 from single-crystal values, which are summarised in the following.

Voigt

The Voigt model assumes that all grains have the same state of strain. The calculated DECs are independent of the *hkl* planes and can be calculated from elements of the compliance tensor S_{ijkl} [144]

$$S_1^{\text{Voigt}} = \frac{2S_0(S_{11} + 2S_{12}) + 5S_{12}S_{44}}{6S_0 + 5S_{44}}, \tag{B.1}$$

$$\frac{1}{2}S_2^{\text{Voigt}} = \frac{5(S_{11} - S_{12})S_{44}}{6S_0 + 5S_{44}} \tag{B.2}$$

with

$$S_0 = S_{11} - S_{12} - \frac{S_{44}}{2}. \tag{B.3}$$

Reuss

The Reuss model assumes that all grains have the same state of stress, which introduces discontinuities at the grain boundaries [144]. The calculated DECs are *hkl*-dependent and can be calculated with elements of the compliance matrix S_{ij} as

$$S_1^{\text{Reuss}} = S_{12} + S_0\Gamma_{hkl} \tag{B.4}$$

and

$$\frac{1}{2}S_2^{\text{Reuss}} = S_{11} - S_{12} - 3S_0\Gamma_{hkl} \tag{B.5}$$

with S_0 from Equation (B.3) and the lattice plane related factor Γ_{hkl} corresponding to the Miller indices *hlk* with

$$\Gamma_{hkl} = \frac{h^2k^2 + k^2l^2 + h^2l^2}{(h^2 + k^2 + l^2)^2}. \tag{B.6}$$

Neerfeld–Hill [145]

The Hill model (also called the Neerfeld–Hill model) is based on the proof that the Voigt and Reuss models are the theoretical limits and the measured values of elastic moduli are usually between them. This model is simply the arithmetic average of the DECs of both models [144]:

$$S_1^{\text{Hill}} = \frac{(S_1^{\text{Reuss}} + S_1^{\text{Voigt}})}{2} \tag{B.7}$$

$$\frac{1}{2}S_2^{\text{Hill}} = \frac{\frac{1}{2}S_2^{\text{Voigt}} + \frac{1}{2}S_2^{\text{Reuss}}}{2}. \tag{B.8}$$

C. Manufacturing drawings

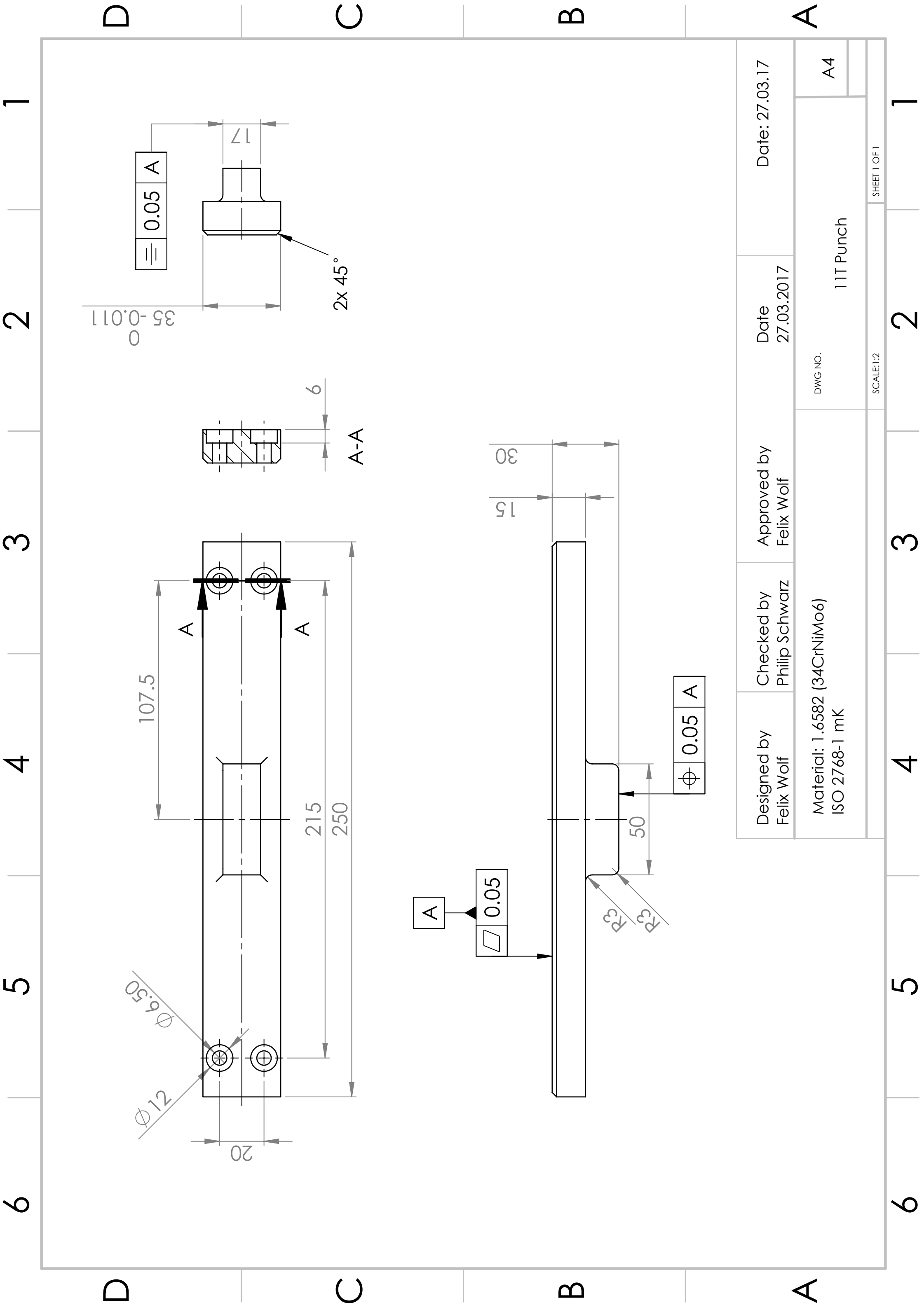

Figure C.1.: :Manufacturing drawing of press tool.

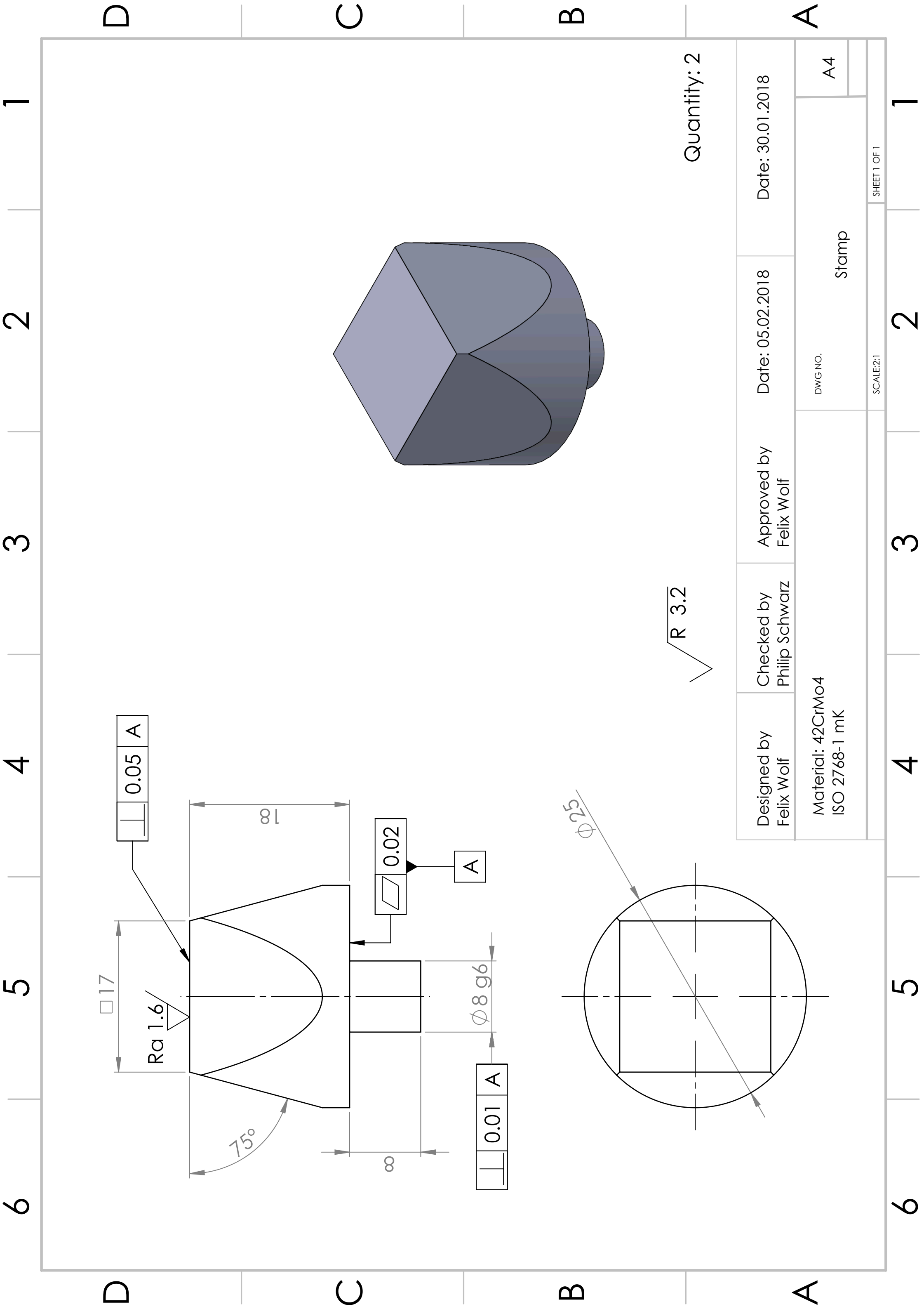

Figure C.2.: Manufacturing drawing of the stamp for the MLZ set-up.

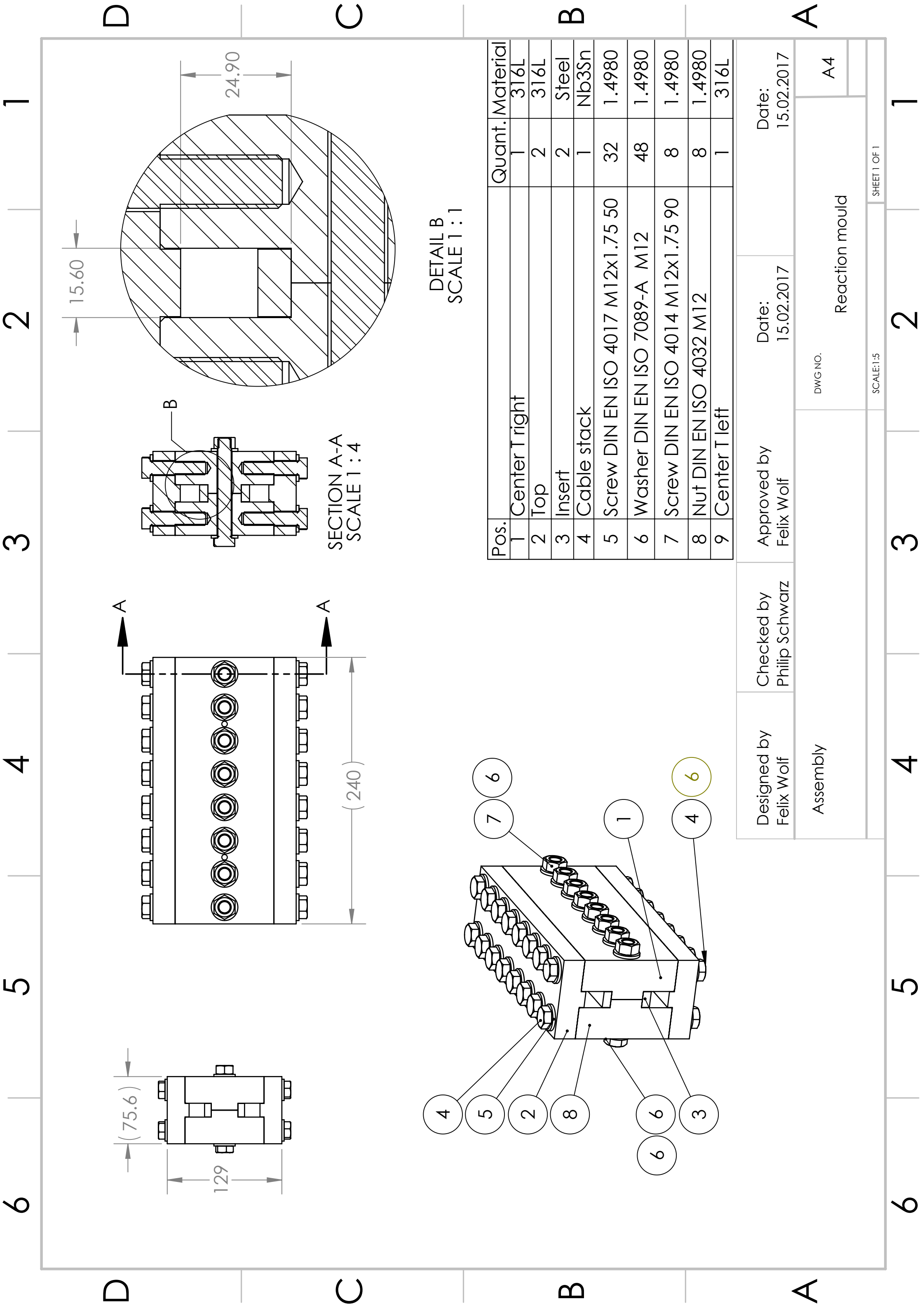

Pos.		Quant.	Material
1	Center T right	1	316L
2	Top	2	316L
3	Insert	2	Steel
4	Cable stack	1	Nb3Sn
5	Screw DIN EN ISO 4017 M12x1.75 50	32	1.4980
6	Washer DIN EN ISO 7089-A M12	48	1.4980
7	Screw DIN EN ISO 4014 M12x1.75 90	8	1.4980
8	Nut DIN EN ISO 4032 M12	8	1.4980
9	Center T left	1	316L

Figure C.3.: Assembly drawing of the reaction mould.

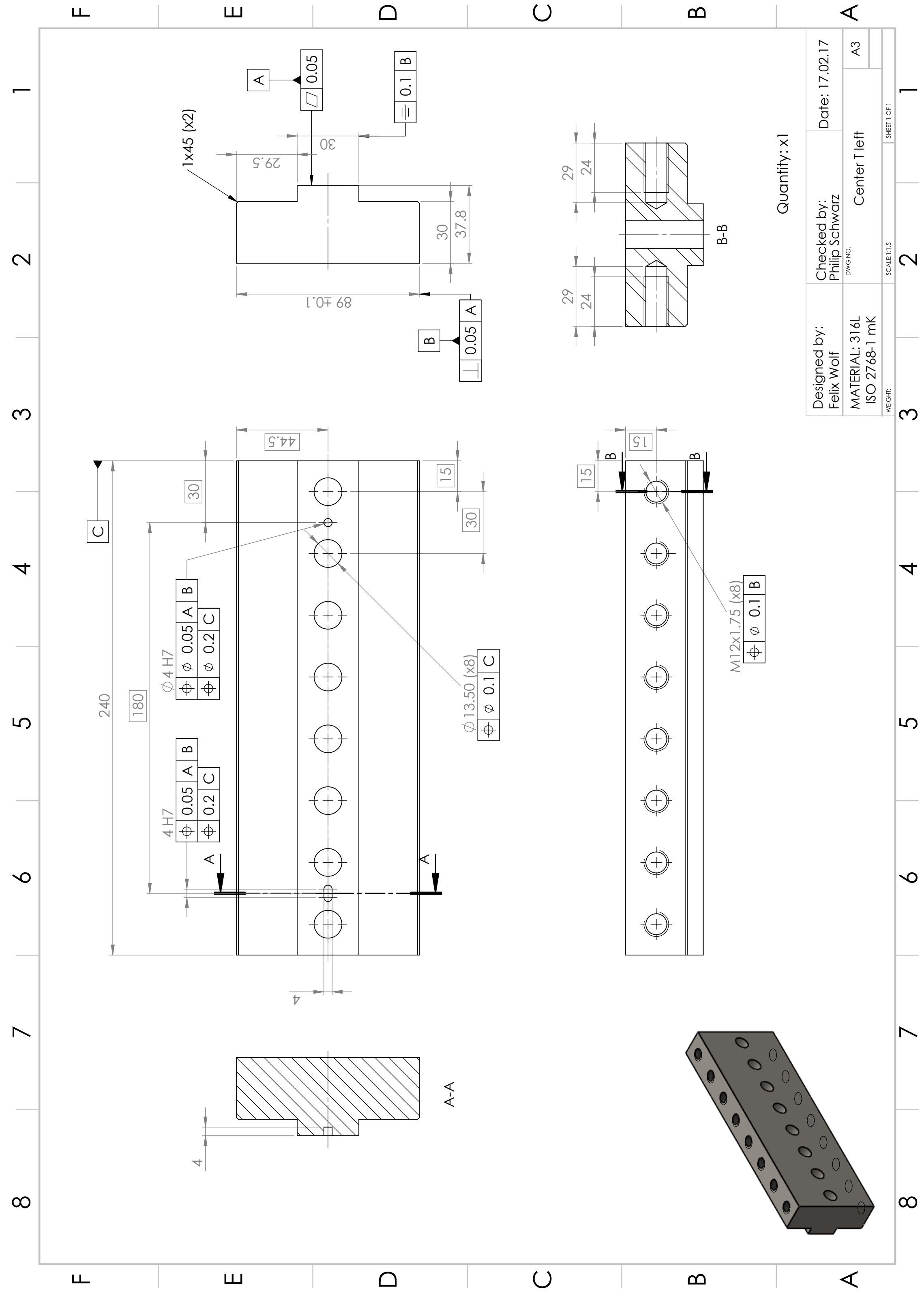

Figure C.4.: Manufacturing drawing of the heat-treatment mould left centre part.

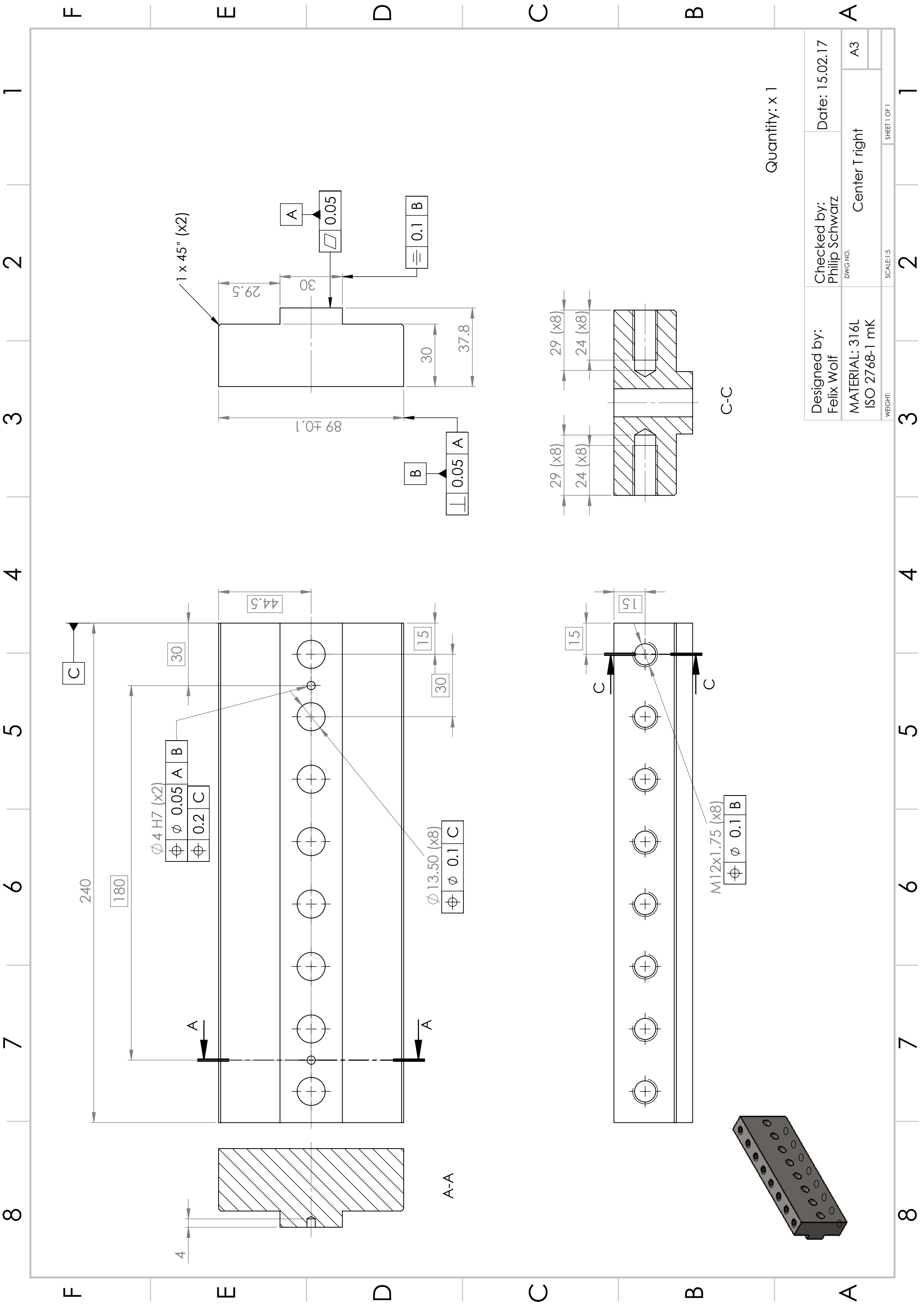

Figure C.5.: Manufacturing drawing of heat-treatment mould right centre part.

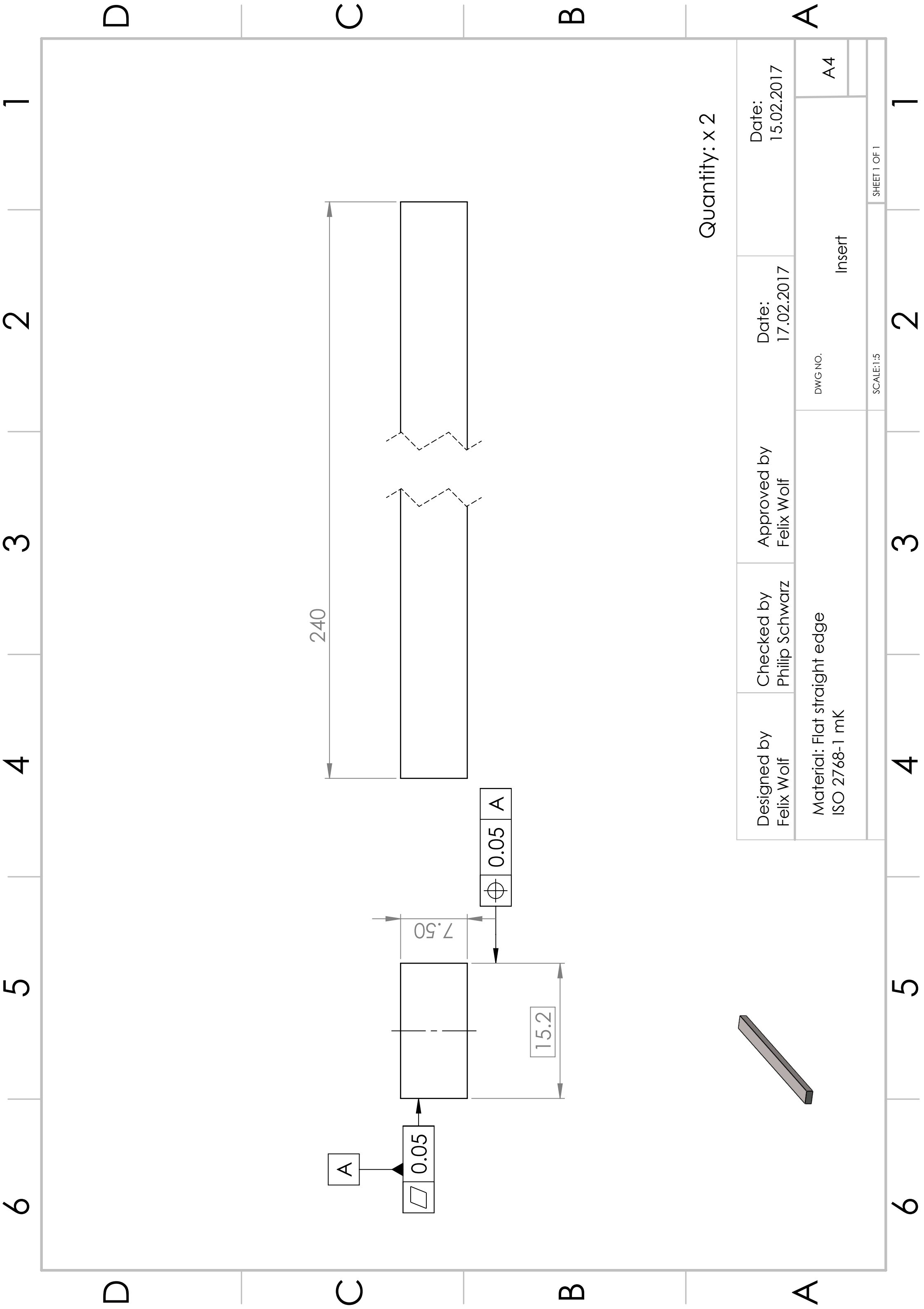

Figure C.6.: Manufacturing drawing of the insert for the heat-treatment mould.

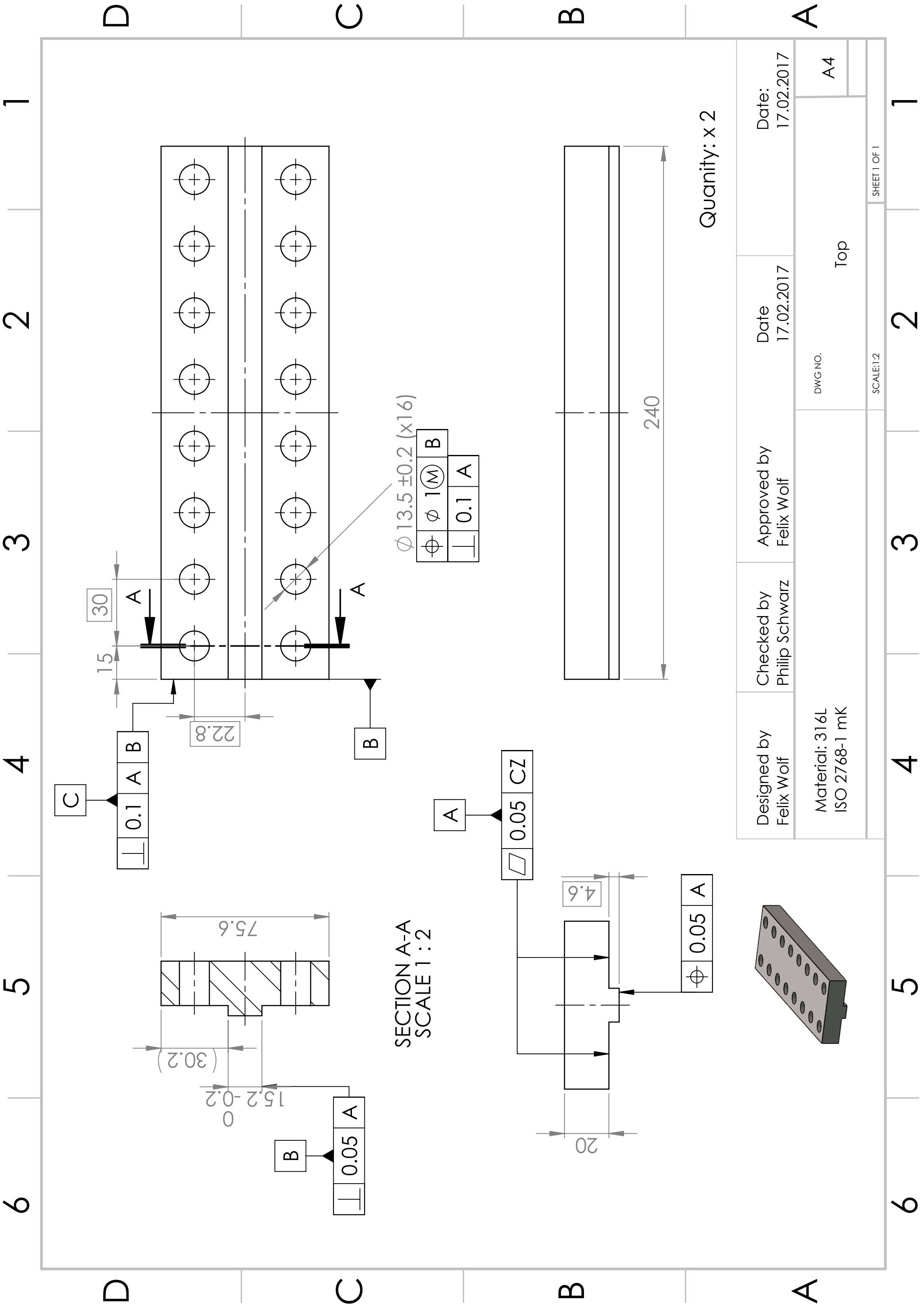

Figure C.7.: Manufacturing drawing of the heat-treatment mould top part.

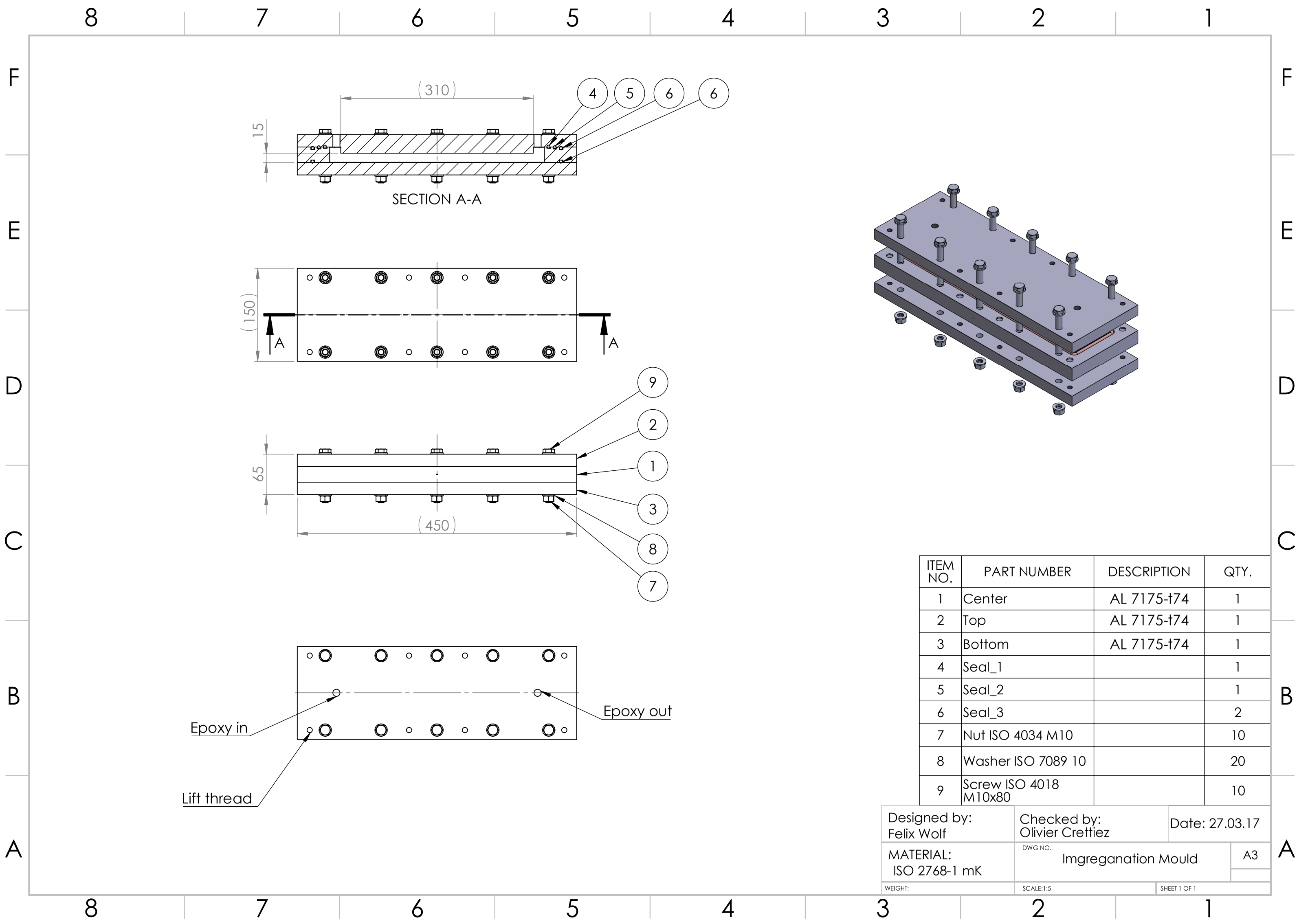

ITEM NO.	PART NUMBER	DESCRIPTION	QTY.
1	Center	AL 7175-t74	1
2	Top	AL 7175-t74	1
3	Bottom	AL 7175-t74	1
4	Seal_1		1
5	Seal_2		1
6	Seal_3		2
7	Nut ISO 4034 M10		10
8	Washer ISO 7089 10		20
9	Screw ISO 4018 M10x80		10

Designed by: Felix Wolf	Checked by: Olivier Crettiez	Date: 27.03.17
MATERIAL: ISO 2768-1 mK	DWG NO. Imgreganation Mould	A3
WEIGHT:	SCALE:1:5	SHEET 1 OF 1

Figure C.8.: Assembly drawing of the impregnation mould.

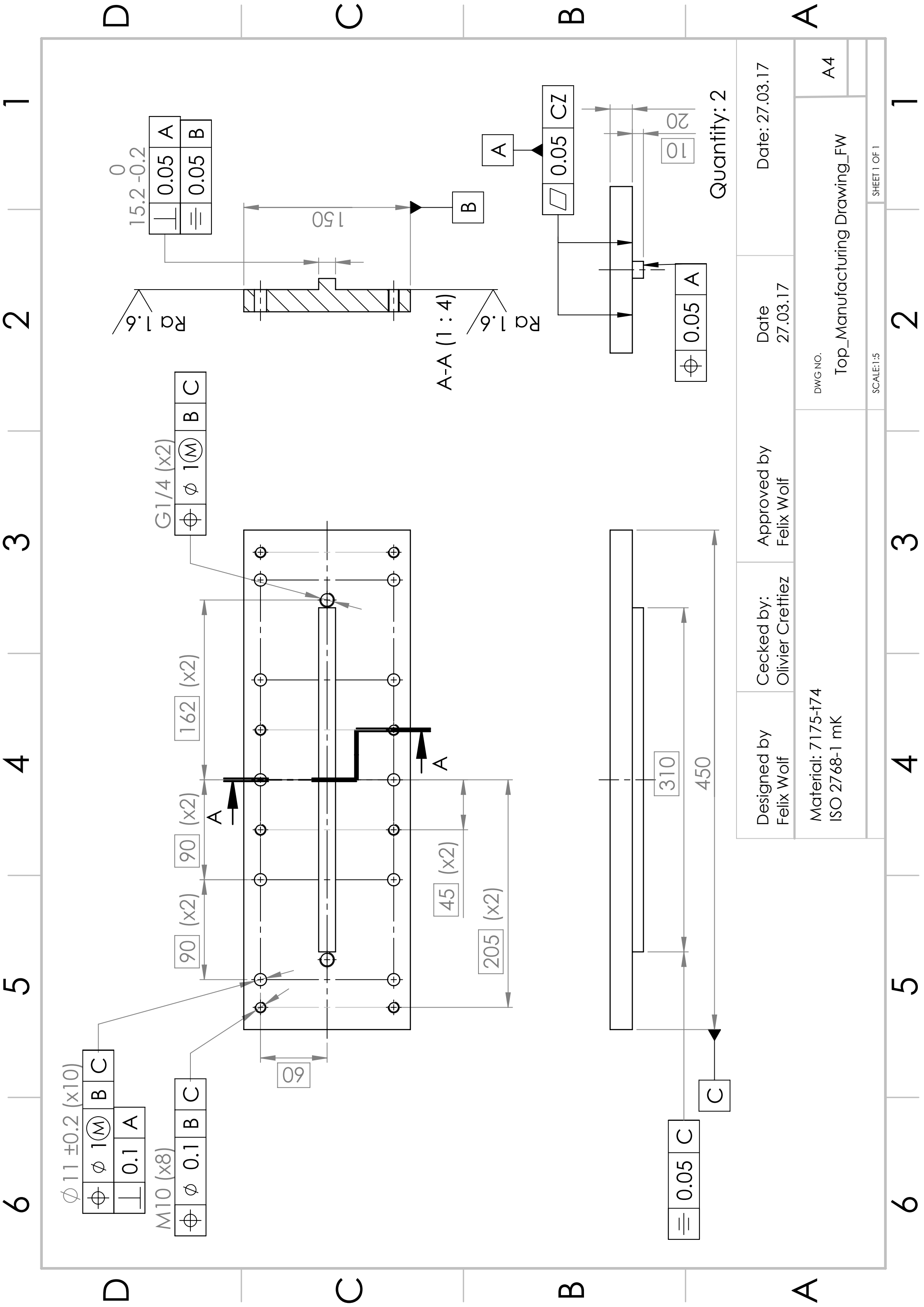

Figure C.9.: Manufacturing drawing of the top part of the impregnation mould.

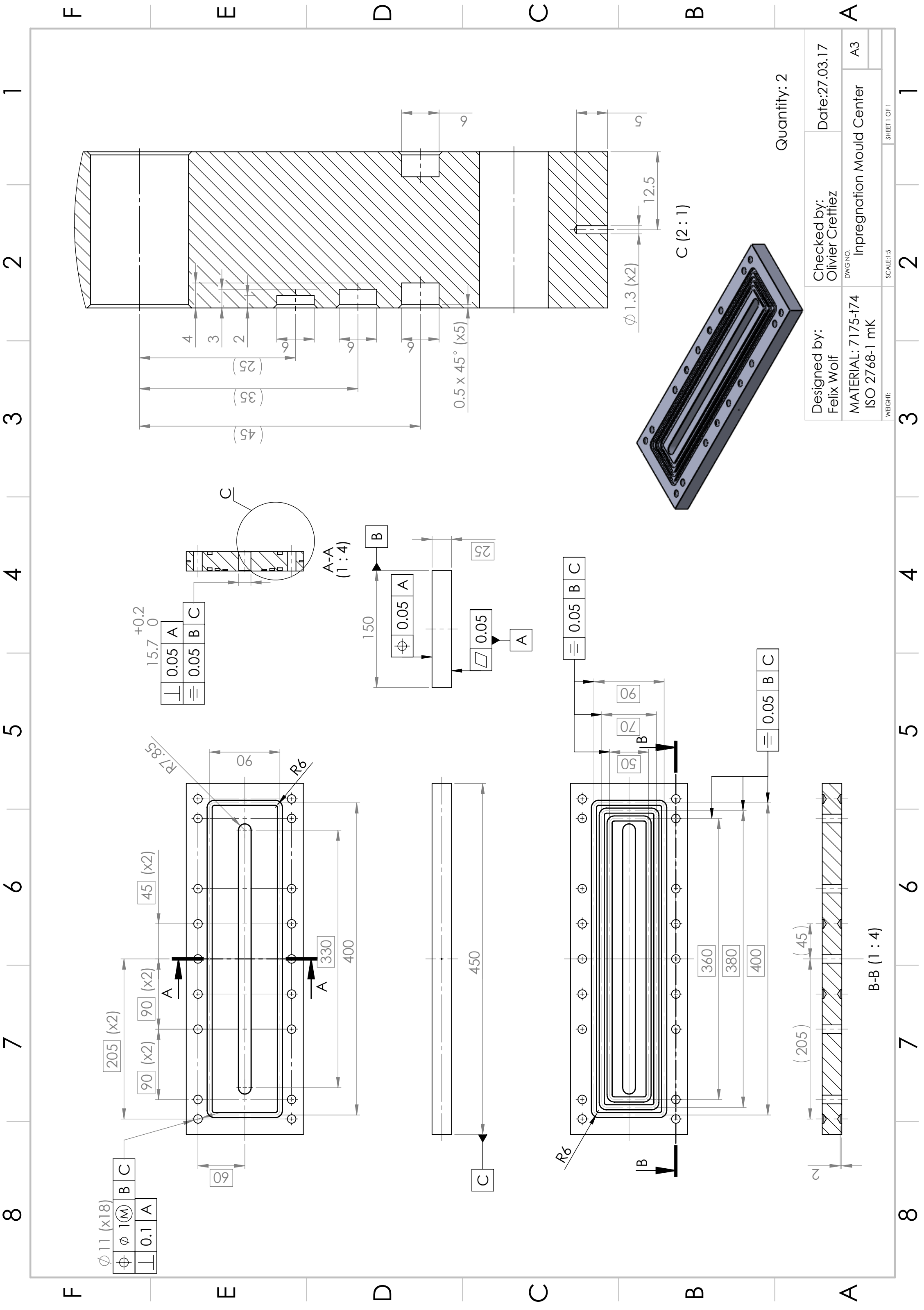

Figure C.10.: Manufacturing drawing of the centre part of the impregnation mould.

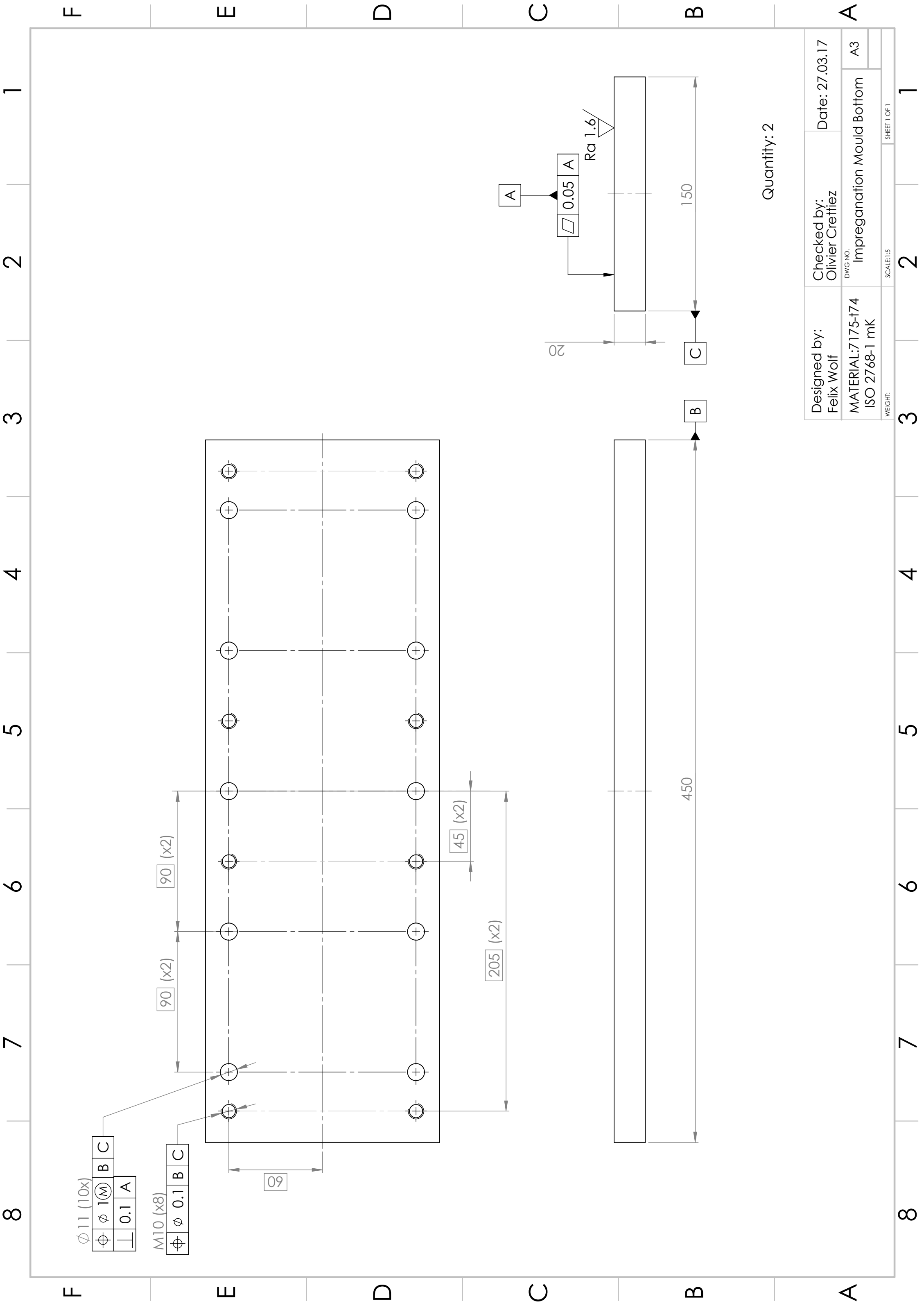

Figure C.11.: Manufacturing drawing of the bottom part of the impregnation mould.

D. FEM calculation results of the 2D model

The calculated stress-strain curves of the 2D FEM model with varying contact definition and plastic material behaviour are shown in the following. The results of the model with a frictionless contact between strand and resin are shown in Figure D.1. The tangent modulus of the matrix material is increased to 1 GPa. The stress strain curves of models with a bonded strand to matrix contact are shown in Figure D.2 and Figure D.3, where the tangent modulus of the resin is varied between 0.2 GPa and 1 GPa. The relevant results are discussed in Section 6.2.

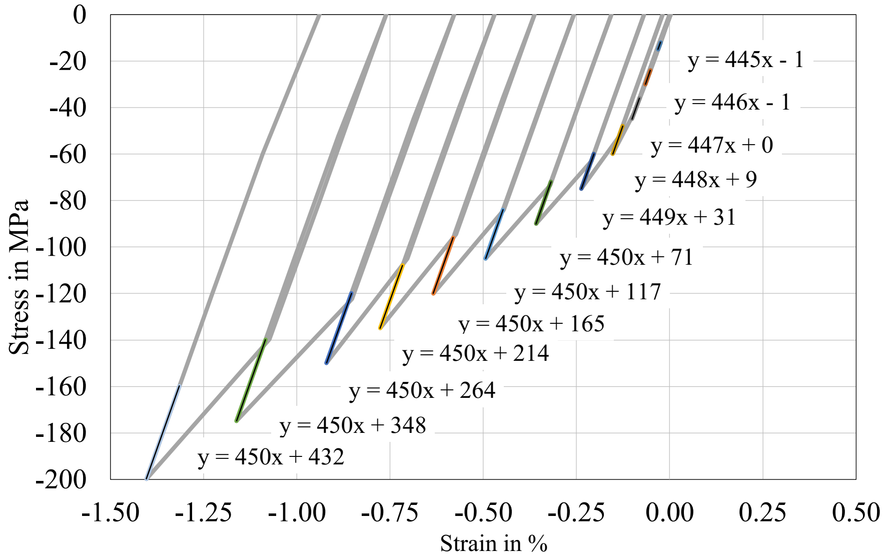

Figure D.1.: Transverse compressive stress–strain curves from frictionless models with a varying tangent modulus of the impregnation system of 1 GPa.

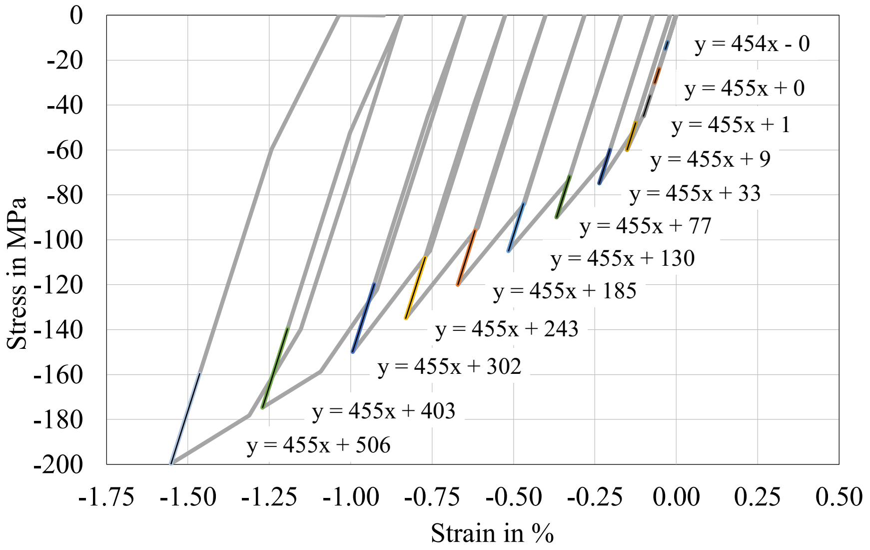

Figure D.2.: Transverse compressive stress–strain curves from bonded models with tangent modulus of the impregnation system of 0.2 GPa.

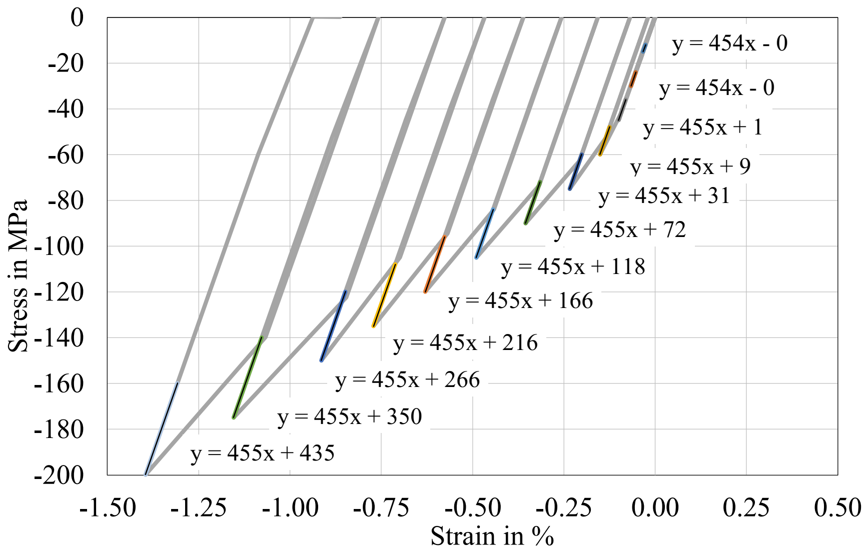

Figure D.3.: Transverse compressive stress–strain curves from bonded models with a tangent modulus of the impregnation system of 1 GPa.

E. FEM calculation results of the 3D model

The mean normal stress values, calculated in the 3D model, of the copper and Nb_3Sn nodes at different applied stress levels are shown in Figure E.1 and Figure E.2.

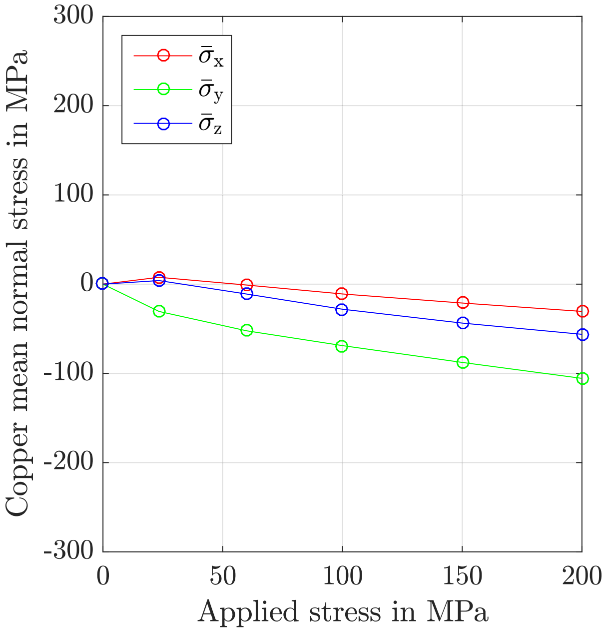

Figure E.1.: Comparison of evaluated mean normal stress values of the copper nodes under increased applied compressive load.

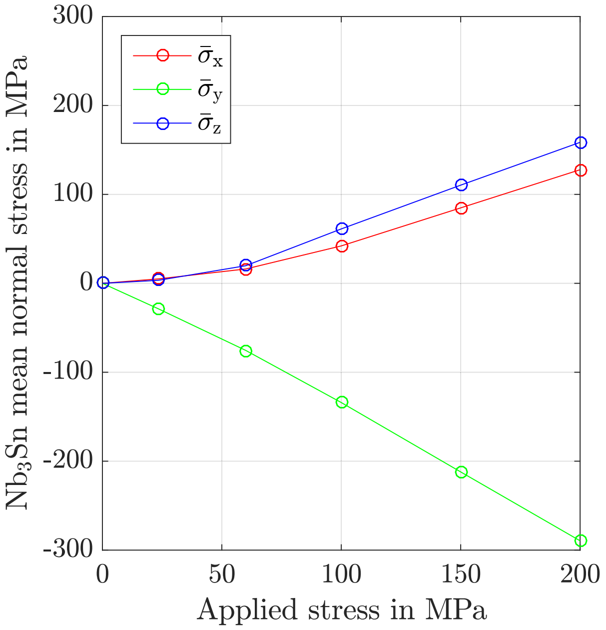

Figure E.2.: Normal stresses in the Nb_3Sn components at increased applied load.

F. Source Codes

Listing 1: StressStrainAnalysis.m

```
clear all;
clc;
close all;

%% define files
Samplename='CU540008';

l=15.0246; % sample length in [mm]
h=15.016; % sample height in [mm]
area=l*h;

% Force measurment files
f1='09_14_02_272.01.measML'; % in [kN]
f2='09_14_02_273.02.measML'; % in [kN]
f3='09_14_02_275.03.measML'; % in [kN]
f4='09_14_02_276.04.measML'; % in [kN]

% Exteniometer displacement files
displ_ext = 'displ_CU54008_T.csv';
displ_zero_ext=-0,02563; % in [mm]

%% Read data

%%%%%%%%%%%%%%%%%%%%%%%%%%%%%%%%%
%                               %
%      Read Load cell data      %
%                               %
%%%%%%%%%%%%%%%%%%%%%%%%%%%%%%%%%

%Read Force File 1

hh=str2double(f1(1:2));
mm=str2double(f1(4:5));
ss=str2double(f1(7:8));
ms=str2double(f1(10:12));

force_1=fopen(f1,'r');
% count number of lines
Nline = 1;
tline = fgetl(force_1);
while ischar(tline)
    Nline = Nline+1;
    tline = fgetl(force_1);
end

% allocate output
step = zeros(Nline-30,1);
seconds = zeros(Nline-30,1);
data_1 = zeros(Nline-30,1);
milisec = zeros(Nline-30,1);

 frewind(force_1);
 for n=1:16
 fgetl(force_1);
 end

for i=1:Nline-30
    tline = fgetl(force_1);
    id1 = find(tline=='=',1,'first');
    step(i) = str2double(tline(1:id1-1));
    id2 = find(tline=='.',1,'first');
    seconds(i) =str2double(tline(id1+1:id2-1));
    id3 = find(tline==';',1,'first');
    milisec(i)=str2double(tline(id2+1:id3-1));
    data_1(i) = str2double(tline(id3+1:end));
```

```
end

% data_1=sgolayfilt(data_1,3,7);

for i=1:1:length(data_1)-1
    if abs(data_1(i)-data_1(i+1))>0.3;
    data_1(i)=data_1(i+2);
    else
        data_1(i)=data_1(i);
    end
end

t_f_1 = hh*60*60 + mm*60 + ss + ms*1e-3 + seconds+ milisec*1e-5;
t_f_1_sec=t_f_1-t_f_1(1);


% Read Force File 2

hh=str2double(f2(1:2));
mm=str2double(f2(4:5));
ss=str2double(f2(7:8));
ms=str2double(f2(10:12));

force_2=fopen(f2,’r’);
% count number of lines
Nline = 1;
tline = fgetl(force_2);
while ischar(tline)
    Nline = Nline+1;
    tline = fgetl(force_2);
end

% allocate output
step = zeros(Nline-30,1);
seconds = zeros(Nline-30,1);
data_2 = zeros(Nline-30,1);
milisec = zeros(Nline-30,1);

 frewind(force_2);
 for n=1:16
 fgetl(force_2);
 end


for i=1:Nline-30
    tline = fgetl(force_2);
    id1 = find(tline==’=’,1,’first’);
    step(i) = str2double(tline(1:id1-1));
    id2 = find(tline==’.’,1,’first’);
    seconds(i) =str2double(tline(id1+1:id2-1));
    id3 = find(tline==’;’,1,’first’);
    milisec(i)=str2double(tline(id2+1:id3-1));
    data_2(i) = str2double(tline(id3+1:end));
end

% Peak filer

for i=1:1:length(data_2)-1
    if abs(data_2(i)-data_2(i+1))>0.3;
    data_2(i)=data_2(i+2);
    else
        data_2(i)=data_2(i);
    end
end

t_f_2 = hh*60*60 + mm*60 + ss + ms*1e-3 + seconds+ milisec*1e-5;
t_f_2_sec=t_f_2-t_f_2(1);


% Read Force File 3
```

```


hh=str2double(f3(1:2));
mm=str2double(f3(4:5));
ss=str2double(f3(7:8));
ms=str2double(f3(10:12));

force_3=fopen(f3,'r');
% count number of lines
Nline = 1;
tline = fgetl(force_3);
while ischar(tline)
    Nline = Nline+1;
    tline = fgetl(force_3);
end

% allocate output
step = zeros(Nline-30,1);
seconds = zeros(Nline-30,1);
data_3 = zeros(Nline-30,1);
milisec = zeros(Nline-30,1);

 frewind(force_3);
 for n=1:16
 fgetl(force_3);
 end



for i=1:Nline-30
    tline = fgetl(force_3);
    id1 = find(tline=='=',1,'first');
    step(i) = str2double(tline(1:id1-1));
    id2 = find(tline=='.',1,'first');
    seconds(i) =str2double(tline(id1+1:id2-1));
    id3 = find(tline==';',1,'first');
    milisec(i)=str2double(tline(id2+1:id3-1));
    data_3(i) = str2double(tline(id3+1:end));
end

% % data_3=sgolayfilt(data_3,3,7);

for i=1:1:length(data_3)-1
    if abs(data_3(i)-data_3(i+1))>0.3;
    data_3(i)=data_3(i+2);
    else
        data_3(i)=data_3(i);
    end
end

t_f_3 = hh*60*60 + mm*60 + ss + ms*1e-3 + seconds+ milisec*1e-5;
t_f_3_sec=t_f_3-t_f_3(1);



% Read Force File 4


hh=str2double(f4(1:2));
mm=str2double(f4(4:5));
ss=str2double(f4(7:8));
ms=str2double(f4(10:12));

force_4=fopen(f4,'r');
% count number of lines
Nline = 1;
tline = fgetl(force_4);
while ischar(tline)
    Nline = Nline+1;
    tline = fgetl(force_4);
```

```
end

% allocate output
step = zeros(Nline-30,1);
seconds = zeros(Nline-30,1);
data_4 = zeros(Nline-30,1);
milisec = zeros(Nline-30,1);

 frewind(force_4);
 for n=1:16
 fgetl(force_4);
 end

for i=1:Nline-30
    tline = fgetl(force_4);
    id1 = find(tline=='=',1,'first');
    step(i) = str2double(tline(1:id1-1));
    id2 = find(tline=='.',1,'first');
    seconds(i) =str2double(tline(id1+1:id2-1));
    id3 = find(tline==';',1,'first');
    milisec(i)=str2double(tline(id2+1:id3-1));
    data_4(i) = str2double(tline(id3+1:end));
end
% data_4=sgolayfilt(data_4,3,7);

for i=1:1:length(data_4)-1
    if abs(data_4(i)-data_4(i+1))>0.3;
    data_4(i)=data_4(i+2);
    else
        data_4(i)=data_4(i);
    end
end

t_f_4 = hh*60*60 + mm*60 + ss + ms*1e-3 + seconds+ milisec*1e-5;
t_f_4_sec=t_f_4-t_f_4(1);

%%%%%%%%%%%%%%%%%%%%%%%%%%%%%%%%%%%%%%%%%
%                                       %
% Read Extensiometer Displacement Data  %
%                                       %
%%%%%%%%%%%%%%%%%%%%%%%%%%%%%%%%%%%%%%%%%


% open file for reading
displ_ext = fopen(displ_ext,'r');

% count number of lines
Nline = 1;
tline = fgetl(displ_ext);
while ischar(tline)
    Nline = Nline+1;
    tline = fgetl(displ_ext);
end

% allocate output
hour = zeros(Nline,1);
minute = zeros(Nline,1);
seconds = zeros(Nline,1);
milisec = zeros(Nline,1);
data = zeros(Nline,1);

% walk over file again
frewind(displ_ext);
for i=1:Nline
    tline = fgetl(displ_ext);
    id1 = find(tline==':',1,'first');
    id2 = find(tline==':',1,'last');
    id3 = find(tline==',',1,'first');
    id4 = find(tline==',',1,'last');
    hour(i) = str2double(tline(id1-2:id1-1));
```

```
    minute(i)= str2double(tline(id1+1:id2-1));
    seconds(i) = str2double(tline(id2+1:id3-1));
    milisec(i) = str2double(tline(id3+1:id4-1));
    data_d(i) = str2double(tline(id4+1:end));
end
data_d(end)=[ ];
d_ext=data_d; % in [mm]
%t_f = hour*60*60 + minute*60 + seconds + milisec*1e-3;
ts=seconds(1:100)-seconds(1);   %timeshift
n=length(ts(ts==0));            %Element for timeshift

t_d = hour(1)*60*60 + minute(1)*60 + seconds(1) + (milisec+(1000-milisec(n)))*1e-3;
t_d(end)=[ ];

%% Calculation

% Convert force values to SI unit
data_1=(data_1)*1000 %in [N]
data_2=(data_2)*1000 %in [N]
data_3=(data_3)*1000 %in [N]
data_4=(data_4)*1000 %in [N]



%Generate time vector of the force measurement
L=min([length(data_1) length(data_2) length(data_3) length(data_4)]);
data_fsum=data_1(1:L)+data_2(1:L)+data_3(1:L)+data_4(1:L);
t_f=t_f_4(1:L);
t_f_sec_0=t_f-t_f(1);   % adjust to time zero
t_f_sec=t_f;

% adjust Ext. -time to zero
t_ext_sec_0=t_d-t_d(1);
t_ext_sec=t_d;
d_ext=data_d;

%
% Identify time basis for interpolation and generate interpolated data vector %

% time basis
t_basic=[];
l_tf=length(t_f_sec);
l_te=length(t_ext_sec);

% find shortes time vector
    if l_tf<l_te
     % Time Basis Froce
     t_basic=t_f_sec;
     %Interpolation
     % Force
     data_f_i=data_fsum; %Displacement interpolation an jeder Kraft stelle
     %Extensiometer
     d_ext_i=interp1(t_ext_sec,d_ext,t_basic);

    else
    % Time basis Extenso
        t_basic=t_ext_sec;
     %Interpolation
     % Force
     data_f_i=interp1(t_f_sec,data_fsum,t_basic); %Displacement interpolation an jeder Kraft stelle
     %Extensiometer
     d_ext_i=d_ext;

    end

t_basic=t_basic-t_basic(1);


%                %
```

```
%   Time shifts %
%               %

    if t_f_sec(1)>t_ext_sec(1)
    p_ext_sec=find(t_ext_sec>t_f_sec(1));
    p_ext_sec(1);

    t_ext_sec_short=t_ext_sec;
    t_ext_sec_short(1:p_ext_sec(1))=[]; % reduce  Ext time vector
    t_ext_sec_short=t_ext_sec_short-t_ext_sec_short(1);
    d_ext_short=d_ext;
    d_ext_short(1:p_ext_sec(1))=[]; % reduce Ext data vector
    t_f_sec_short=t_f_sec;
    t_f_sec_short=t_f_sec_short-t_f_sec_short(1);
    data_fsum_short=data_fsum;

    else
    %         'T_ext=startseit'
    p_f_sec=find(t_f_sec>t_ext_sec(1));
    p_f_sec(1);

    t_f_sec_short=t_f_sec;
    t_f_sec_short(1:p_f_sec(1))=[]; % Froce vektor kuerzen
    t_f_sec_short=t_f_sec_short-t_f_sec_short(1);
    data_fsum_short=data_fsum;
    data_fsum_short(1:p_f_sec(1))=[]; % Froce vektor kuerzen

    t_ext_sec_short=t_ext_sec;
    t_ext_sec_short=t_ext_sec_short-t_ext_sec_short(1);
    d_ext_short=d_ext;
    end

%Stress - strain calculation extensometer based
format long
stress=data_f_i/(area);  % in MPa
strain_ext=(-1)*d_ext_i'/(6+displ_zero_ext); % in [-]

%% PLOT

f=figure;

plot(strain_ext*100,stress);
xlabel('Strain␣in␣$\%$','interpreter','latex')
ylabel('Stress␣in␣MPa','interpreter','latex')
%hold on
grid on
grid minor
%title(['Stress - Strain (Ext. based) ',Samplename])
ylim([0,500])
xlim([0,0.4])


%close all;
```

Listing 2: VolumeFraction.m

```
clear all
close all

% Read image
A=imread('CableStack_1_Cable.jpg');

% Analysis colour profile
figure
imshow(A)
figure
histogram(A)
ylabel('No.␣of␣elements')
xlabel('Grey␣scale␣value')

```

```
B=A(A<69);
Bsize=size(B);
Insulation=Bsize(1)/3
white=A(A==255);
white_size=size(white);
Copper=white_size(1)/3
Element_size=size(A);
Elements=Element_size(1)*Element_size(2)
NonCuElem=Elements-Copper
Insul_ratio=Insulation/NonCuElem
Strand_ratio=1-Insul_ratio
A(A<69)=255;
%A(160<A & A<240)=0;
figure
imshow(A)
figure
histogram(A)
ylabel('No.␣of␣elements')
xlabel('Grey␣scale␣value')
```

List of Abbreviations

μ-CT micro-Computed Tomography

ALICE A Large Ion Collider Experiment

ATLAS A Toroidal LHC Apparatus

CMS Compact Mueon Solenoid

CPU Central Processing Unit

DECs Diffraction Elastic Constants

DS Dispersion Suppressor

FCC Future Circular Collider

fcc face-centred cubic

FEM Finite Element Method

FRESCA Facility for the REception of Superconducting CAbles

FWHM Full Width at Half Maximum

HE-LHC High Energy-Large Hadron Collider

HL-LHC High Luminosity-Large Hadron Collider

HTS High-Temperature Superconductor

IP Interaction Point

IT Internal Tin

LEP Large Electron-Positron Collider

LHC Large Hadron Collider

LHC-B Large Hadron Collider Beauty

PDC Polymer-Derived Ceramic

PIT Powder-in-Tube

PTFE Polytetrafluoroethylene

RHT Reaction Heat Treatment

ROM Rule of Mixtures

RRP ® Restacked Rod Process®

STL Standard Triangulation Language

TCLDs Target Collimator Long Dispersion suppressor

UV ultraviolet

List of Tables

List of Figures

List of author’s publications

Publications with major contributions of the author

- F. Wolf, *et al.*, “Characterization and manufacturing validation of CERN capacitive load gauges technology,” tech. rep. EDMS: 2330901, CERN, 2020.

- C. Barth, G. Lenoir, J. Fleiter, G. Peiro, F. Wolf, and A. Ballarino, “Behavior of Nb_3Sn-RRP Rutherford cable under increasing compressive stress applied at RT,” *IEEE Transactions on Applied Superconductivity*, to be published in 2020.

- F. Wolf, C. Scheuerlein, M. Lorentzon, B. Katzer, M. Hofmann, W. Gan, F. Lackner, D. Schoerling, D. Tommasini, F. Savary and L. Bottura, “Effect of Applied Compressive Stress and Impregnation Material on Internal Strain and Stress State in Nb_3Sn Rutherford Cable Stacks,” *IEEE Transactions on Applied Superconductivity*, vol. 29, no. 5, pp. 1–5, 2019.

- F. Wolf, F. Lackner, M. Hofmann, C. Scheuerlein, D. Schoerling and D. Tommasini, “Effect of Epoxy Volume Fraction on the Stiffness of Nb_3Sn Rutherford Cable Stacks,” *IEEE Transactions on Applied Superconductivity*, vol. 29, no. 5, pp. 1–6, 2019.

- P. Ferracin, L. Bottura, N. Bourcey, M. Daly, A. Devred, S. I. Bermudez, J. F. Troitino, S. Ferradas Troitino, P. Grosclaude, M. Guinchard, C. Loffler, E. Nilsson, J. C. Perez, J. L. R. Fernandez, F. Savary, G. Vallone, and F. Wolf, “Mechanical analysis of the collaring process of the 11 T dipole magnet,” *IEEE Transactions on Applied Superconductivity*, vol. 29, no. 5, pp. 1–5, 2019.

- C. Scheuerlein, F. Wolf, M. Lorentzon, and M. Hofmann, “Direct measurement of Nb_3Sn filament loading strain and stress in accelerator magnet coil segments,” *Supercond. Sci. Technol*, 2018.

- F. Wolf, P. Ebermann, F. Lackner, D. Mosbach, C. Scheuerlein, K. Schladitz and D. Schoerling, “Characterization of the stress distribution on Nb_3Sn Rutherford cables under transverse compression,” *IEEE Transactions on Applied Superconductivity*, vol. 28, no. 3, pp. 1–6, 2018.

- P. Ebermann, J. Bernardi, J. Fleiter, F. Lackner, F. Meuter, M. Pieler, C. Scheuerlein, D. Schoerling, F. Wolf, A. Ballarino, L. Bottura, D. Tommasini, F. Savary and M. Eisterer, “Irreversible degradation of Nb_3Sn Rutherford cables due to transverse compressive stress at room temperature,” *Superconductor Science and Technology*, vol. 31, 065009, 2018.

- U. M. Kelly, S. Richter, C. Redenbach, K. Schladitz, C. Scheuerlein, F. Wolf, P. Ebermann, F. Lackner, D. Schoerling and D. Meinel, “Nb_3Sn Wire Shape and Cross-Sectional Area Inhomogeneity in Rutherford Cables,” *IEEE Transactions on Applied Superconductivity*, vol. 28, no. 4, pp. 1–5, 2018.

- J. van Nugteren, F. Wolf, J. S. Murtomäki, G. Kirby, G. de Rijk, H. T. Kate and L. Rossi, "Idealized Coil Cross Sections With Minimized Conductor Area for High Field Dipoles," *IEEE Transactions on Applied Superconductivity*, vol. 28, no. 3, pp. 1–5, 2018.
- J. S. Murtomäki, G. Kirby, J. van Nugteren, P. Contat, O. Sacristan-de-Frutos, J. Fleiter, F. Pincot, G. de Rijk, L. Rossi, J. Ruuskanen, A. Stenvall and F. Wolf, "10 kA Joints for HTS Roebel Cables," *IEEE Transactions on Applied Superconductivity*, vol. 28, no. 3, pp. 1–6, 2018.
- P. Ebermann and F. Wolf, "Evaluation script for analysing pressure measurement films with office scanners," tech. rep., CERN, 2017.

General project publications

- D. Schoerling, D. Arbelaez, B. Auchmann, M. Bajko, A. Ballarino, E. Barzi, G. Bellomo, M. Benedikt, S. Izquierdo Bermudez, B Bordini, L. Bottura, L. Brouwer, P. Bruzzone, B. Caiffi, S. Caspi, A. Chakraborti, E. Coatanea, G. de Rijk, M. Dhalle, M. Durante, P. Fabbricatore, S. Farinon, H. Felice, A. Fernandez, I. Fernandez, P. Gao, B. Gold, T. Gortsas, S. Gourlay, M. Juchno, V. Kashikhin, C. Kokkinos, S. Kokkinos, K. Koskinen, F. Lackner, C. Lorin, K. Loukas, A. Louzguiti, K. Lyytikainen, S. Mariotto, M. Marchevsky, G. Montenero, J. Munilla, I. Novitski, T. Ogitsu, A. Pampaloni, J. C. Perez, C. Pes, C. Petrone, D. Polyzos, S. Prestemon, M. Prioli, A. M. Ricci, J. M. Rifflet, E. Rochepault, S. Russenschuck, T. Salmi, I. A. Santillana, F. Savary, C. Scheuerlein, M. Segreti, C. Senatore, M. Sorbi, M. Statera, A. Stenvall, L. Tavian, T. Tervoort, D. Tommasini, F. Toral, R. Valente, G. Velev, A. Verweij, S. Wessel, F. Wolf, F. Zimmermann and A. V. Zlobin, "The 16 T dipole development program for FCC and HE-LHC," *IEEE Transactions on Applied Superconductivity*, vol. 29, pp. 1–9, August 2019.
- D. Tommasini, D. Arbelaez, B. Auchmann, H. Bajas, M. Bajko, A. Ballarino, E. Barzi, G. Bellomo, M. Benedikt, S. Izquierdo Bermudez, B. Bordini, L. Bottura, L. Brower, M. Buzio, B. Caiffi, S. Caspi, M. Dhalle, M. Durante, G. deRijk, P. Fabbricatore, S. Farinon, P. Ferracin, P. Gao, S. Gourlay, M. Juchno, V. Kashikhin, F. Lackner, C. Lorin, M. Marchevsky, V. Marinozzi, T. Martinez, J. Munilla, I. Novitski, T. Ogitsu, R. Ortwein, J. C. Perez, C. Petrone, S. Prestemon, M. Prioli, J. Rifflet, E. Rochepault, S. Russenschuck, T. Salmi, F. Savary, D. Schoerling, M. Segreti, C. Senatore, M. Sorbi, A. Stenvall, E. Todesco, F. Toral, A. P. Verweij, S. Wessel, F. Wolf and A. V. Zlobin, "Status of the 16 T Dipole Development Program for a Future Hadron Collider," *IEEE Transactions on Applied Superconductivity*, vol. 28, no. 3, pp. 1–5, 2018.
- D. Tommasini, B. Auchmann, H. Bajas, M. Bajko, A. Ballarino, G. Bellomo, M. Benedikt, S. I. Bermudez, B. Bordini, L. Bottura, M. Buzio, M. Dhalle, M. Durante, G. de Rijk, P. Fabbricatore, S. Farinon, P. Ferracin, P. Gao, F. Lackner, C. Lorin, V. Marinozzi, T. Martinez, J. Munilla, T. Ogitsu, R. Ortwein, J. Perez, M. Prioli, J. Rifflet, E. Rochepault, S. Russenschuck, T. Salmi, F. Savary, D. Schoerling, M. Segreti, C. Senatore, M. Sorbi, A. Stenvall, E. Todesco, F. Toral, A. P. Verweij, G. Volpini, S. Wessel and F. Wolf, "The 16 T Dipole Development Program for FCC," *IEEE Transactions on Applied Superconductivity*, vol. 27, no. 4, pp. 1–5, 2017.

Bibliography

[1] D. Schoerling, *et al.*, “Strategy for superconducting magnet development for a future hadron–hadron circular collider at CERN,” *Conference: The European Physical Society Conference on High Energy Physics*, p. 517, March 2016.

[2] L. R. Evans, “The Large Hadron Collider - present status and prospects,” *IEEE Transactions on Applied Superconductivity*, vol. 10, pp. 44–48, March 2000.

[3] L. Bottura and A. Godeke, “Superconducting materials and conductors: Fabrication and limiting parameters,” *Reviews of Accelerator Science and Technology*, vol. 5, pp. 25–50, 2012.

[4] S. Myers, *The LEP Collider, from design to approval and commissioning.* John Adams’ Lecture, Geneva: CERN, 1991.

[5] J.-L. Caron, “Layout of the LEP tunnel including future LHC infrastructures..” AC Collection. Legacy of AC. Pictures from 1992 to 2002, February 1997.

[6] H. Schopper and S. Myers, eds., *Landolt–Börnstein - Group I Elementary Particles, Nuclei and Atoms Elementary Particles - Accelerators and Colliders*, vol. 21. Springer-Verlag Berlin Heidelberg, 2013.

[7] H. Wiedemann, *Particle Accelerator Physics.* Springer, 1993.

[8] M. Wilson, *Superconducting Magnets.* Clarendon Press, 1983.

[9] E. Madenci and I. Guven, *The Finite Element Method and Applications in Engineering Using ANSYS.* Springer US, 2015.

[10] Y. Iwasa, *Case Studies in Superconducting Magnets.* Springer Science, 2nd edn., 2009.

[11] K.-H. Mess, P. Schmüser, and S. Wolff, *Superconducting Accelerator Magnets.* World Scientific, 1996.

[12] S. Russenschuck, *Field Computation for Accelerator Magnets: Analytical and Numerical Methods for Electromagnetic Design and Optimization.* Wiley, 2010.

[13] H. Brechna, *Superconducting Magnet Systems.* Springer-Verlag Berlin Heidelberg, 1973.

[14] D. Schoerling and A. Zlobin, eds., *Nb_3Sn Acclerator Magnets: Designs, Technologies, Performance.* Springer, 2019.

[15] G. Apollinari, *et al.*, *High-Luminosity Large Hadron Collider (HL-LHC): Technical Design Report V. 0.1.* CERN Yellow Reports: Monographs, Geneva: CERN, 2017.

[16] O. Brüning and L. Rossi, *The High Luminosity Large Hadron Collider: The New Machine for Illuminating the Mysteries of Universe.* Advanced Series on Directions, World Scientific, 2015.

[17] D. Schoerling *et al.*, "Installation of the 11 T dipole full assembly in LHC P7 (HL-LHC WP11)," tech. rep., CERN, 2019.

[18] Future Circular Collider, *Conceptual Design Report*, Jan. 2019. https://fcc-cdr.web.cern.ch.

[19] Sensor Products, Inc., "Tactilus Nano-Polymer Core, H-series Sensor" http://www.sensorprod.com/tactile-surface-sensor.php. Sensor Products, Inc, May 2017.

[20] D. Schoerling, *et al.*, "The 16 T dipole development program for FCC and HE-LHC," *IEEE Transactions on Applied Superconductivity*, vol. 29, pp. 1–9, August 2019.

[21] R. Valente, *et al.*, "Baseline design of a 16 T cos θ bending dipole for the Future Circular Collider," *IEEE Transactions on Applied Superconductivity*, pp. 1–1, 2019.

[22] M. Segreti, *et al.*, "2-D and 3-D design of the block-coil dipole option for the Future Circular Collider," *IEEE Transactions on Applied Superconductivity*, vol. 29, pp. 1–4, Aug 2019.

[23] F. Toral, J. Munilla, and T. Salmi, "Magnetic and mechanical design of a 16 T common coil dipole for an FCC," *IEEE Transactions on Applied Superconductivity*, vol. 28, pp. 1–5, April 2018.

[24] G. Montenero, *et al.*, "Coil manufacturing process of the first 1-m-long canted–cosine–theta (cct) model magnet at PSI," *IEEE Transactions on Applied Superconductivity*, vol. 29, pp. 1–6, August 2019.

[25] M. Benedikt and F. Zimmermann, "Towards future circular colliders," *Journal of the Korean Physical Society*, vol. 69, pp. 893–902, September 2016.

[26] H. K. Onnes, "Sur les resistances electriques," *Communications from the Physical Laboratory of the University of Leiden*, vol. 29, pp. 1–11, 1911.

[27] W. Meissner and R. Ochsenfeld, "Ein neuer effekt bei eintritt der supraleitfähigkeit," *Natrurwissenschaften*, vol. 21, pp. 787–788, 1933.

[28] P. J. Lee, ed., *Engineering Superconductivity.* Wiley–IEEE Press, 2001.

[29] B. Bordini, *et al.*, "An exponential scaling law for the strain dependence of the Nb_3Sn critical current density," *Superconductor Science and Technology*, vol. 26, p. 075014, May 2013.

[30] J. A. Parrell, *et al.*, "High field Nb_3Sn conductor development at Oxford Superconducting Technology," *IEEE Transactions on Applied Superconductivity*, vol. 13, pp. 3470–3473, June 2003.

[31] W. Klose and A. Müller, *Supraleitende A15-phasen*, pp. 599–625. Berlin, Heidelberg: Springer Berlin Heidelberg, 1972.

[32] J. E. Kunzler, *et al.*, “Superconductivity in Nb_3Sn at high current density in a magnetic field of 88 kGauss,” *Phys. Rev. Lett.*, vol. 6, p. p. 89, 1961.

[33] E. Barzi and A. V. Zlobin, “Research and development of Nb_3Sn wires and cables for high-field accelerator magnets,” *IEEE Transactions on Nuclear Science*, vol. 63, pp. 783–803, April 2016.

[34] E. Homsveld *et al.*, “Development of ECN-type Nb_3Sn wire towards smaller filament size,” *Advances in Cryogenic Engineering*, vol. 34, p. 493, 1987.

[35] J. H. Londenhovius, *et al.*, “Progress in the development of Nb_3Sn conductors based on the “Powder in tube" method with finer filaments,” *IEEE Transactions on Applied Superconductivity*, vol. 9, pp. 1451–1454, June 1999.

[36] X. Xu, X. Peng, *et al.*, “Achievement of FCC specification in critical current density for Nb_3Sn superconductors with artificial pinning centers,” *arXiv:1903.08121*, submitted for publication, 2019.

[37] Y. Hashimoto, K. Yoshizaki, and M. Tanaka, “Processing and properties of superconducting Nb_3Sn filamentary wires,” *Proc. 5th Int. Cryo. Eng. Conf., Kyoto, Japan*, p. 332, 1974.

[38] J. Parrell, *et al.*, “Nb_3Sn conductor development for fusion and particle accelerator,” *Adv Cryo Eng (Materials) 50B:369–375*, 2004.

[39] J. C. McKinnell, *et al.*, “Fully bonded internal-tin, niobium–tin Nb_3Sn conductor development at Oxford Superconducting Technology,” *IEEE Transactions on Applied Superconductivity*, vol. 7, pp. 1360–1363, June 1997.

[40] M. Wake, *et al.*, “Development of high current density conductor with distributed tin configuration,” *Adv. Cryo. Eng.,*, vol. 50B, pp. 410–416, 2004.

[41] M. Durante, *et al.*, “Development of a Nb_3Sn multifilamentary wire for accelerator magnet applications,” *Physica C: Superconductivity*, vol. 354, no. 1, pp. 449–453, 2001.

[42] S. Martin, *et al.*, “The crystal structure of (Nb0.75Cu0.25)Sn2 in the Cu–Nb–Sn system,” *Intermetallics*, vol. 80, pp. 16–21, 2017.

[43] A. Ballarino, *et al.*, “The CERN FCC conductor development program: A worldwide effort for the future generation of high field magnets,” *IEEE Transactions on Applied Superconductivity*, VOL. 29(5), 6001709, 2019.

[44] G. Gallagher-Daggitt, “Superconductor cables for pulsed dipole magnets,” *Technical report, Rutherford High Energy Laboratory Memorandum*, 1973.

[45] J. D. Adam, *et al.*, “Rutherford cables with anisotropic transverse resistance,” *IEEE Transactions on Applied Superconductivity*, vol. 7, pp. 958–961, June 1997.

[46] R. M. Scanlan, J. Royet, and R. Hannaford, "Fabrication of Rutherford-type superconducting cables for construction of dipole magnets," Lawrence Berkeley Lab., CA (USA), vol. BL-24321; CONF-880653-1, 1988.

[47] H. S. Katz and J. V. Milewski, *Handbook of fillers and reinforcements for plastics*. New York: Van Nostrand Reinhold Co, 1978.

[48] A. V. Tollestrup, "Superconducting magnets," *AIP Conf. Proc.*, vol. 87, pp. 699–804, 1982.

[49] AGY Holding Corp., "Product information 933 S-2 Glass® Yarn," https://www.agy.com/wp-content/uploads/2014/03/933_S-2_Yarn-Aerospace.pdf, 2013.

[50] P. Ferracin, *et al.*, "QXF cable insulation at CERN." Joint LARP/CM20 HiLumi meeting Napa Valley, CA, USA, April 2013.

[51] E. Todesco, *et al.*, "Quench performance and coil preloading in HL-LHC Nb_3Sn magnets," *submitted for publication 2019.*

[52] P. Ferracin, *et al.*, "Development of MQXF: The Nb_3Sn low-βquadrupole for the Hi-Lumi LHC," *IEEE Transactions on Applied Superconductivity*, vol. 26, pp. 1–7, June 2016.

[53] C. Kokkinos and M. Karppinen, "High gradient Nb_3Sn quadrupole demonstrator MKQXF engineering design," *IEEE Transactions on Applied Superconductivity*, vol. 28, pp. 1–8, April 2018.

[54] M. Karppinen *et al.*, "Design of 11T twin-aperture dipole demonstrator magnet for LHC upgrades," *IEEE Trans. App. Supercond.*, vol. 22, no. 3, 2012.

[55] E. Todesco, *et al.*, "Preload and training in Nb_3Sn magnets for particle accelerators." Applied Superconductivity Conference, Seattle, WA, 2018.

[56] O. S. Brüning, P. Collier, and P. Lebrun, *et al.*, "LHC Design Report", *CERN Yellow Reports: Monographs*, Geneva, 2004.

[57] W. Voigt, "Über die Beziehung zwischen den beiden Elasticitätsconstanten isotroper Körper," *Annalen der Physik*, vol. 274, no. 12, pp. 573–587, 1889.

[58] A. Reuss, "Berechnung der Fließgrenze von Mischkristallen auf Grund der Plastizitätsbedingung für Einkristalle," *ZAMM - Journal of Applied Mathematics and Mechanics / Zeitschrift für Angewandte Mathematik und Mechanik*, vol. 9, no. 1, pp. 49–58, 1929.

[59] C. E. Murray, "Equivalence of Kröner and weighted Voigt–Reuss models for X-ray stress determination," *Journal of Applied Physics*, vol. 113, no. 15, 153509, 2013.

[60] P. Ebermann, *et al.*, "Irreversible degradation of Nb_3Sn Rutherford cables due to transverse compressive stress at room temperature," *Superconductor Science and Technology*, vol. 31, 065009, 2018.

[61] R. V. Mises, “Mechanik der plastischen Formänderung von Kristallen,” *ZAMM - Journal of Applied Mathematics and Mechanics / Zeitschrift für Angewandte Mathematik und Mechanik*, vol. 8, pp. 161–185, 1928.

[62] ASTM International, “ASTM-E9 Standard test methods of compression testing of metallic materials at room temperature,” 2018.

[63] ASTM International, “ASTM-E111 Standard test method for Young’s modulus, tangent modulus, and chord modulus,” 2004.

[64] ASTM International, “ASTM-D695 Standard test method for compressive properties of rigid plastics,” 2015.

[65] R. Hooke, *Lectures de Potentia Restitutiva, Or of Spring Explaining the Power of Springing Bodies.* Cutlerian lecture, John Martyn, 1678.

[66] J. R. Newby *et al.*, *ASM Handbook Volume 8 Mechanical testing.* ASM International, 1992.

[67] C. Scheuerlein, *et al.*, “Mechanical properties of the HL-LHC 11 T Nb_3Sn magnet constituent materials,” *IEEE Transactions on Applied Superconductivity*, vol. 27, no. 4, 2017.

[68] E. J. Hearn, *Mechanics of materials.*, vol. 2. Oxford: Butterworth-Heinemann, 1997.

[69] ISO, “ISO/TS 21432 Non-destructive testing, standard test method for determining residual stresses by neutron diffraction,” 2005.

[70] M. T. Hutchings *et al.*, *Introduction to the Characterization of Residual Stress by Neutron Diffraction.* Taylor and Francis Group, LLC, 2005.

[71] W. P. Davey, “Precision measurements of the lattice constants of twelve common metals,” *Phys. Rev.*, vol. 25, pp. 753–761, Jun 1925.

[72] W. Friedrich and and P. Knipping and M. von Laue, “Interferenz-Erscheinungen bei Röntgenstrahlen,” München Sitzungsberichte: 14, 1912.

[73] W. L. Bragg, “The diffraction of short electromagnetic waves by a crystal,” *Proc Camb. Phil. Soc.*, vol. 17, p. 43, 1914.

[74] A. J. Hurd and R. L. McGreevy, *Neutron applications in earth, energy and environmental sciences.* Neutron Scattering Applications and Techniques, Dordrecht: Springer, 2008.

[75] R. E. Brydon, *et al.*, “Stress and texture calculator STECA, version 2,” 2018.

[76] I. Noyan and J. Cohen, *Residual stress: measurement by diffraction and interpretation.* Materials Research and Engineering, Springer, 1987.

[77] E. Kröner, “Berechnung der elastischen Konstanten des Vielkristalls aus den Konstanten des Einkristalls,” *Zeitschrift für Physik*, vol. 151, pp. 504–518, August 1958.

[78] K. Keller and J. Hanak", "Lattice softening in single crystal Nb_3Sn"," *Physics Letters*, vol. 21, no. 3, pp. 263–264, 1966.

[79] W. C. J. Overton and J. Gaffney, "Temperature variation of the elastic constants of cubic elements. I. Copper," *Phys. Rev.*, vol. 98, no. 969, 1955.

[80] E. Madenci and I. Guven, *The Finite Element Method and Applications in Engineering Using ANSYS®*. Berlin, Heidelberg: Springer-Verlag, 2007.

[81] C. Scheuerlein, *et al.*, "Thermomechanical properties of polymers for use in superconducting magnets," *for submission to IEEE Transactions on Applied Superconductivity*, 2018.

[82] ANSYS 17.2, *Release 17.2 Documentation for ANSYS Workbench.* © 2016 SAS IP, Inc., 2016.

[83] R. Hill, *New York: The Mathematical Theory of Plasticity.* Oxford University Press, 1983.

[84] P. Wriggers, *Computational Contact Mechanics.* Springer Berlin Heidelberg, 2006.

[85] A. Verweij *et al.*, "1.9 K test facility for the reception of the superconducting cables for the LHC," *IEEE Transactions on Applied Superconductivity,* vol. 9, part 2, pp. 153-–156, June 1999.

[86] B. Jakob and G. Pasztor, "Effect of transverse compressive stress in the critical current of cabled Nb_3Sn conductor," *IEEE Transactions on Magnetics*, vol. 25, no. 2, March 1989.

[87] B. Bordini *et al.*, "Critical current measurements of high-J_c Nb_3Sn Rutherford cables under transverse compression," *IEEE Transactions on Applied Superconductivity*, 2014. vol. 24, no. 3, 9501005, Jun. 2014.

[88] H. Ten Kate, H. W. Weijers and J. M. van Oort, "Critical current degradation in Nb_3Sn cables under transverse pressure," *IEEE Transactions on Applied Superconductivity*, vol. 9, pt. 2, pp. 122–125, June 1993.

[89] D. Dietderich, *et al.*, "Critical current of superconducting Rutherford cable in high magnetic fields with transverse pressure," *IEEE Transactions on Applied Superconductivity*, vol. 9, pt. 2, pp. 122–125, June 1999.

[90] P. Bauer, K. Ewald and J. Ozelis, "Design of a sample holder for measurements of Nb_3Sn critical current under transverse loading conditions," *FNAL, Batavia, IL, USA, Tech. Rep.* TD 99-051, 1999.

[91] G. Amborsio *et al.*, "Design of a sample holder for Nb_3Sn cable test at FRESCA," *FNAL, Tech. Rep.* TD-04-022, 2004.

[92] F. Savary *et al.*, "Progress on the Development of the Nb_3Sn 11T Dipole for the High Luminosity Upgrade of LHC," *IEEE Transactions on Applied Superconductivity,* vol. 27, no. 4, June 2017.

[93] Mitutoyo Europe GmbH, “High-Resolution Digimatic Measuring Unit,” https://ecatalog.mitutoyo.com/cmimages/003/316/2066_Litematic.pdf, 2012.

[94] P. Ferracin, *et al.*, “Mechanical analysis of the collaring process of the 11 T dipole magnet,” *IEEE Transactions on Applied Superconductivity*, vol. 29, no. 5, pp. 1–5, 2019.

[95] FUJIFILM, “Instruction Manual Medium Pressure MS,” https://www.fujifilm.eu/fileadmin/products/prescale/media/Two_Sheet_Type_for_Medium_Pressure_klein.pdf, 2016.

[96] Sensor Products, Inc., “Tactilus Nano-Polymer Core, H-series Sensor” http://www.sensorprod.com/tactile-surface-sensor.php. Sensor Products, Inc, May 2017.

[97] Tekscan, Inc., *I-Scan® Product Selection Guide*, https://www.tekscan.com/sites/default/files/resources/IDL-IScan-SelectionGuide_RevG.pdf, Tekscan, Inc., May 2017.

[98] FUJIFILM, “Product information FujiFilm Pressure Measurement Film”, http://www.fujifilm.com/products/prescale/prescalefilm, 2015.

[99] P. Ebermann and F. Wolf, “Evaluation script for analysing pressure measurement films with office scanners,” tech. rep., CERN, 2017.

[100] Burster GmbH & Co. KG, “Test- and calibration certificate, compression load cell,” January 2016.

[101] GEFRAN, *Konfigurations- und Programmieranleitung.* GEFRAN, July 2012.

[102] Burster GmbH & Co. KG, *Techniche Produktinformationen Typ 8526.*

[103] Burster GmbH & Co. KG, “Test- and calibration certificate, usb-sensor-interface for strain gages,” May 2016.

[104] Burster GmbH & Co. KG, “Digivsion v2017.1.0.0”, https://www.burster.de/en/sensors/load/tension-and-compression-load-cells/p/detail/digivision/,March 2017.

[105] W. C. Young and R. G. Budynas, “*Roark’s Formulas for Stress and Strain*, New York, McGraw-Hill, Seventh Edition, 2002.

[106] M. Fink, *et al.*, “Measurement of mechanical properties of electronic materials at temperatures down to 4.2 K,” *Cryogenics*, vol. 11, pp. 497–510, 2008.

[107] C. Basaran and J. Jiang, “Measuring intrinsic elastic modulus of Pb/Sn solder alloys,” *Mech. Mater.*, vol. 34, no. 379, pp. 349–362, 2002.

[108] R. P. Reed *et al.*, “Tensile strength and ductility of indium,” *Mater. Sci. Eng.*, vol. 102, pp. 227–236, July 1988.

[109] M. P. Davidson, S. Bastian, and F. W. Markley, “Measurement of the elastic modulus of kapton perpendicular to the plane of the film at room and cryogenic temperatures,” *presented at the 4th Int. Ind. Symp. Supercollider*, March 1992.

[110] U. Kelly, *et al.*, “Nb_3Sn wire shape and cross sectional area inhomogeneity in Rutherford cables,” *IEEE Transactions on Applied Superconductivity*, Vol. 28, No. 4, June 2018.

[111] D. Arbelaez, *et al.*, “Cable deformation simulation and hierarchical framework for Nb_3Sn Rutherford cables,” *J. Phys.: Conf. Ser.*, vol. 234, 022002, 2010.

[112] S. Wolff, “Superconducting accelerator magnet design,” *CERN Accelerator School - Fifth General Accelerator Physics Course*, vol. 2, pp. 755–790, January 1994.

[113] D. Dell’Orco, *et al.*, “Fabrication and component testing results for a Nb_3Sn dipole magnet,” *IEEE Transactions on Applied Superconductivity*, vol. 5, no. 2, pp. 1000–1003, 1995.

[114] M. Reytier, *et al.*, “Characterization of the thermo-mechanical behavior of insulated cable stacks representative of accelerator magnet coils,” *IEEE Transactions on Applied Superconductivity*, vol. 11, no. 1, pp. 3066–3069, 2001.

[115] M. Daly, *et al.*, “Multiscale approach to the mechanical behavior of epoxy impregnated Nb_3Sn coils for the 11 T dipole,” *IEEE Transactions on Applied Superconductivity*, vol. 28, no. 3, pp. 1–6, 2018.

[116] R. Bossert, *et al.*, “Recent progress and tests of radiation resistant impregnation materials for Nb_3Sn coils,” *AIP Conference Proceedings*, vol. 1574, no. 132, pp. 132–139, 2014.

[117] D. R. Chichili, *et al.*, “Investigation of cable insulation and thermo-mechanical properties of epoxy impregnated Nb_3Sn composite,” *IEEE Transactions on Applied Superconductivity*, vol. 10, no. 1, pp. 1317–1320, 2000.

[118] C. Fichera, A. Bertarelli, P. Ferracin, *et al.* , “New Methodology to Derive the Mechanical Behavior of Epoxy-Impregnated Nb_3Sn Cables,” *IEEE Transactions on Applied Superconductivity*, vol. 29, pp. 1–12, 2019.

[119] F. Wolf, *et al.*, “Characterization of the stress distribution on Nb_3Sn Rutherford cables under transverse compression,” *IEEE Transactions on Applied Superconductivity*, vol. 28, no. 3, pp. 1–6, 2018.

[120] Epsilon Technology Corp., *Extensometer Catalog.* 3975 South Highway 89, Jackson, WY 83001, USA.

[121] Epsilon Technology Corp., “3442-006m outline drawings,” August 2016.

[122] Mantracourt Electronics Limited, “DSCUSB standard manual,” Mantracourt.com, 2016.

[123] Heinz Maier-Leibnitz Zentrum et al., "STRESS-SPEC: Materials science diffractometer," *Journal of Large-Scale Research Facilities*, vol. A6, 2015.

[124] ASM Handbook Committee, ed., *Metals Handbook - Properties and Selection: Nonferrous Alloys and Special-Purpose Materials*, vol. 2. ASM International, 10th ed., 1990.

[125] COGEBI, Mica cable tapes, "http://www.cogebi.com/mica-products/mica-cable-tapes", July 2018.

[126] I. Composite Technology Development, "CTD-1202 polymer-derived ceramic insulation." Webpage: "http://www.ctd-materials.com", July 2018.

[127] C. Wegst and M. Wegst, *Stahlschlüssel Nachschlagewerk: key to steel.* Stahlschlüssel Wegst KG, 1971.

[128] M. Crouvizier, "Compaction levels of cable stacks," tech. rep., CERN, 2018.

[129] C. Scheuerlein, *et al.*, "Elastic anisotropy in multifilament Nb_3Sn superconducting wires," *IEEE Transactions on Applied Superconductivity*, vol. 25, no. 3, pp. 1–5, 2015.

[130] A. Allen, M. Hutchings, and C. Windsor, "Neutron diffraction methods for the study of residual stress fields," *Advances in Physics*, vol. 34, p. 445, 1985.

[131] L. Pintschovius, *et al.*, "Determination of Residual Stress Distributions in the Interior of Technical Parts by Means of Neutron Diffraction," In: E. Kula and V. Weiss (eds) *Residual Stress and Stress Relaxation. Sagamore Army Materials Research Conference Proceedings*, vol. 28. Springer, Boston, MA," 1982.

[132] M. Bourke, J. Goldstone, and T. Holden, "Measurements of residual and applied stress using neutron diffraction residual stress measurement using the pulsed neutron source at LANSCE," *NATO ASI Series*, 1992.

[133] M. Hofmann, *et al.*, "The new materials science diffractometer STRESS-SPEC at FRM-II," *Physica B: Condensed Matter*, Part 2, pp. 1035–1037, 2006.

[134] L. Muzzi, *et al.*, "Direct observation of Nb_3Sn lattice deformation by high-energy X-ray diffraction in internal-tin wires subject to mechanical loads at 4.2 K," *Supercond. Sci. Technol.*, vol. 25, 2012.

[135] K. Keller and J. Hanak, "Lattice softening in single crystal Nb_3Sn," *Phys. Lett.*, vol. 21, no. 3, pp. 263–264, 1966.

[136] H. Wern, R. Johannes, and H. Walz, "Dependence of the x-ray elastic constants on the diffraction plane," *Phys. Stat. Sol.*, vol. 206, no. 2, pp. 545–557, 1998.

[137] C. Scheuerlein, *et al.*, "Direct measurement of Nb_3Sn filament loading strain and stress in accelerator magnet coil segments," *Supercond. Sci. Technol*, 2018.

[138] E. Barzi, G. Gallo, and P. Neri, "FEM Analysis of Nb-Sn Rutherford-Type Cables," *IEEE Transactions on Applied Superconductivity*, vol. 22, no. 3, 2012.

[139] G. Vallone, B. Bordini, and P. Ferracin, "Computation of the reversible critical current degradation in Nb_3Sn Rutherford cables for particle accelerator magnets," *IEEE Transactions on Applied Superconductivity*, vol. 28, pp. 1–6, June 2018.

[140] Composite Technology Development, Inc., "CTD-101 and CTD-101k epoxy resin system," https://www.ctd-materials.com/wordpress/wp-content/uploads/2013/01/CTD-101-101K-DS-w-nanquq-6-10-09.pdf, 2002.

[141] C. Barth, *et al.*, "Behavior of Nb_3Sn-RRP Rutherford cable under increasing compressive stress applied at RT," *IEEE Transactions on Applied Superconductivity*, to be published in 2020.

[142] F. Wolf, *et al.*, "Characterization and manufacturing validation of CERN capacitive load gauges technology," tech. rep. EDMS: 2330901, CERN, 2020.

[143] K.-H. Mess, P. Schmüser, S. Wolff, "Superconducting Accelerator magnets," *World Scientific*, 1996.

[144] A. Vermulen, "An elastic constants database and XEC calculator for use in XRD residual stress analysis," Philips Analytical, Lelyweg 1, 7602 EA Almelo, The Netherlands, 2001.

[145] R. Hill, "The elastic behaviour of a crystalline aggregate," *Proceedings of the Physical Society. Section A*, vol. 65, no. 5, p. 349, 1952.